ON THE RADIATING AND DYNAMIC PROPERTIES OF THE SOLAR UPPER ATMOSPHERE

A THESIS SUBMITTED TO
THE DEPARTMENT OF PHYSICS AND APPLIED PHYSICS
OF THE UNIVERSITY OF STRATHCLYDE
FOR THE DEGREE OF
DOCTOR OF PHILOSOPHY

By
David Hamilton Brooks
March 1997

Abstract

The spectral variability of the solar upper atmosphere observed from spaceborne satellites has highlighted the need for a reappraisal of the atomic models entering prediction of emission. Solar atmospheric dynamics clearly takes place on timescales shorter than those of ionisation relaxation. Dynamical models of the solar plasma thus require a matching dynamic model at the atomic level to underpin conclusions drawn from the spectral interpretation. The Atomic Data and Analysis Structure (ADAS) (Summers(1994)), used successfully in modelling radiating dynamic plasmas at JET Joint Undertaking, has been extended to astrophysical applications to remove the uncertainty introduced by common oversimplifications. The atomic models are based on generalised collisional-radiative theory. This thesis utilises ADAS in analysis of data from the SOHO satellite while maintaining awareness of the limitations of the analysis methods. Developments are as follows.

Methods to allow flexibility in excited population structure resolution levels, between fusion and astrophysics, have been developed and integrated into the ADAS system.

Methods to calculate experimentally linked derived data including, for example, a metastable resolved density dependent equilibrium ionisation balance, have also been developed. Original results are presented for oxygen, based on a critical review and upgrade of the existing fundamental database and the SOHO instrumentation requirements. This provides an illustration of the atomic modelling analysis path for solar applications.

Extensive investigation of SOHO data and experimental analysis techniques has been undertaken to allow coupling of the data stream to a differential emission measure code in ADAS. Preliminary results from analysis of CDS-NIS data are presented along with a study of the statistical variability of the spectral lines, extending the methods of Lang et al.(1990).

Finally, an outline of the implications for future models of the solar atmosphere is discussed.

Acknowledgments

During the course of completing this thesis I have had the pleasure of meeting and working with many people who I would now like to thank.

I would first, and foremost, like to thank my supervisor Prof. Hugh Summers. His enthusiasm and encouragement were a constant source of motivation and without his innovation the thesis would not have been completed. I would like to thank my joint supervisor from Rutherford Appleton Laboratory Dr. Jim Lang. His encouragement, interest and willingness to help was invaluable. I would like to thank Dr. Alessandro Lanzafame of the Osservatorio Astrofisico di Catania for many helpful discussions and sociable evenings away on working trips. I would like to thank Dr. Peter McWhirter for guidance in the latter stages of this work. Thanks are also due to Dr. Davina Innes for use of her SUMER explosive event data and for being an excellent host during my visit to the Max Planck Institut in Germany.

I would like to thank the Principal Investigators of CDS and SUMER, Dr. Richard Harrison and Dr. Klaus Wilhelm for allowing me to use the observational data presented in this thesis. Thanks also to Gordon Fischbacher and Enrico Landi for taking the data processing load off of me in the final months of this work. I would like to thank Dr. Peter MacNeice from NASA-Goddard who supplied a copy of his hydrodynamic flare code for my use. Thanks also to Dr. Nigel Badnell from Strathclyde University for computing advice and the use of his extensive dielectronic recombination calculations. I am grateful to Dr. Ken Phillips and Dr. Robbie Stewart for helpful suggestions to improve this manuscript.

I would also like to thank the members of my office Harvey Anderson, Dr Costanza Maggi, Mark McPhail, Alan Price, Kevin Smith and Dr Tim Hammond and Dr William Osborn of Tessella Computing Consultants for many interesting discussions not all of which were related to the work of this thesis.

I would like to acknowledge support of the EPSRC and a CASE studentship with Rutherford Appleton Laboratory without which the work would definately not have been completed and the Max Planck Institut for giving me a fellowship to travel to Germany.

On a personal note I would like to thank my mother, father, many friends and

family for their constant interest and encouragement. I would also like to specially mention my brother Nicholas Brooks. Finally I would like to say a special thank you to Ms Eilean P.Kelly. Without her belief, support and affection this work would not have been completed.

Contents

List of Figures

List of Tables

Chapter 1

Introduction

In order to gain a better understanding of Solar-Terrestrial relations, the European Space Agency (ESA), the National Aeronautics and Space Administration (NASA) and the Institute of Space and Astronautical Science (ISAS) agreed to a joint research project called the International Solar-Terrestrial Physics programme. This coordinated project aims to make simultaneous observations and measurements of the solar-terrestrial environment, over an extended period, by using five separate space satellite missions. These are SOHO, Cluster, Geotail, Polar and Wind. With Ulysses and Yohkoh still in orbit, research possibilities are more wide ranging than ever before.

SOHO and Cluster together form ESA and NASA's Solar-Terrestrial Science Programme which is the first cornerstone of ESA's longer term "Space Science Horizon 2000" programme. Cluster consisted of four identical spacecrafts which were to have taken simultaneous measurements of the plasma environment in the immediate vicinity of the Earth in order to map the 3-dimensional geometry and plasma distribution of the magnetosphere. Unfortunately, the satellites were destroyed by the failure of Ariane-5 due to an onboard software error in May 1996. However, it may be possible to realise the original goals of the mission as ESA intend to relaunch aboard Russian launchers under the new name of "Cluster 2".

SOHO was launched successfully aboard AC-121, an Atlas-IIAS rocket, from Cape Canaveral Air Force Station in Florida on December 2nd 1995. After a two and a half

month cruise phase it was inserted into an halo orbit, on February 14th 1996, around the gravitational equilibrium L1 Lagrangian point ($\sim 1.5 \times 10^6$km from the Earth on the sunward side). Since then it has been taking helioseismology measurements and making continuous observations of the solar atmosphere and solar wind for 24 hours each day. The data is telemetered to the ground via NASA's Deep Space Network and there is now a wealth of observations available to support the original objectives of the mission. These are,

1. To study the solar interior.

2. To study the solar corona and explain how it is heated.

3. To investigate the acceleration process of the solar wind.

Observations throughout the '70s and '80s have clearly shown that changes in solar plasma conditions take place on spatial and temporal scales smaller and shorter than previous spaceborne instrumentation has been able to track. A deeper insight into the connection between radiating and dynamic properties of the solar plasma is essential for determination of the mechanisms responsible for its non-radiative heating. The state of the art equipment on SOHO provides a unique opportunity to examine these and other issues in greater detail than before (Fleck, Domingo & Poland (1995)).

Any analysis of spectroscopic data requires to adopt the best available atomic data to assist in interpretation. The problems of standard solar and atomic models in accounting correctly for the solar radiation emission have however suggested the requirements for an improved atomic basis of analysis. The importance of a unified approach to the modelling of atomic processes in plasmas cannot be understressed. To this end, a great deal of work has been done in recent years integrating and extending the quality of atomic modelling for laboratory and astrophysical plasmas. Chief amongst the concerns is the ability to handle the dynamic nature of the plasmas under investigation. At the forefront of this research field is the Atomic Data and Analysis Structure (ADAS). Originally developed at JET Joint Undertaking it has been adopted as the principal spectral analysis software package for the coronal spectrometers on board the SOHO satellite. Due attention is paid to the influence of

metastable states, finite density plasma and the competition of atomic processes in a full collisional-radiative model.

We wish to improve the quality, accuracy and flexibility of atomic modelling to gain new insight into the physical mechanisms of the solar upper atmosphere. The dynamic nature of the solar atmosphere leads us to believe that the assumption of ionisation equilibrium introduces a variability factor that limits the success of commonly used approaches such as differential emission measure analysis (DEM). One of our main objectives is to assess, execute and validate the DEM technique and to identify and quantify the sources of error associated with it.

In this chapter, a brief overview of the coronal instruments is given. Then, an outline of the principles behind the ADAS project is presented. This serves as background and an introduction to the main work of the thesis.

1.1 Outline of Capabilities of CDS and SUMER Spectrometers on SOHO

Details of all the instrumentation on board the SOHO satellite are presented by Fleck, Domingo & Poland(1995). In particular, Harrison et al.(1995) and Harrison & Fludra (1995) present details of the Coronal Diagnostic Spectrometer (CDS) while Wilhelm et al.(1995) and Wilhelm (1993) present details of the Solar Ultraviolet Measurements of Emitted Radiation (SUMER) spectrometer. These instruments deal with the provision of diagnostic information concerning dynamic behaviour such as explosive events and flows, and also the density & temperature structure of the solar atmosphere from the upper chromosphere through to the low corona. Other instruments available for coronal remote sensing are, e.g the Large Angle Spectroscopic COronagraph (LASCO, Brueckner et al.(1995)) and the UltraViolet Coronagraph Spectrometer (UVCS, Kohl et al.(1995)); however these are principally for investigating energy transport, velocities etc. in the upper corona (i.e. $1.1R_{\odot} \rightarrow 30R_{\odot}$). In addition, there is an Extreme-ultraviolet Imaging Telescope (EIT, Delaboudiniere et al. (1995)) on board but this is mainly for feature location and full disc images. Thus

CDS & SUMER are the two principal coronal instruments with which we will be concerned. Here we briefly outline the 'state of the art' capabilities of the two instruments with a comparison to previous and other current spaceborne instrumentation.

1.1.1 Coronal Diagnostic Spectrometer

CDS consists of a Wolter-Schwartzchild type 2 telescope and dual spectrometers fed by an entrance slit behind a scan mirror. The telescope is a full revolution system but only utilises two apertures in front of and light stops behind the telescope to select two components of the telescope beam to illuminate each of the spectrometers. One spectrometer is in normal incidence (NIS) and the other in grazing incidence (GIS). This is because reflection efficiency in normal incidence reduces at decreasing EUV wavelengths (Phillips(1992)). Thus the grazing incidence spectrometer was introduced to make wavelengths below $\sim$ 300Å accessible. The optical layout of the instrument is given in fig.1 of Harrison et al.(1995). The spatial resolution of the telescope is defined by the full width at half intensity maximum (FWHM) of the point spread function. The point spread function is the intensity distribution obtained from observing an infinitely distant point source. For the CDS telescope, the FWHM was measured for both the NIS and GIS apertures in both the direction of wavelength dispersion and the direction perpendicular to it (Harrison et al.(1995)). The results are given in table.1.1.

For NIS the beam is focussed on a pair of toroidal gratings which diffract the image of the entrance slit onto a two-dimensional detector called the Viewfinder Detector Subsystem (VDS). This is an intensified CCD detector (Thompson et al.(1992)). The two gratings are slightly tilted to allow both spectra to be recorded at the same time. The entrance slit is usually aligned North-South during flight unless the spacecraft attitude is changed by a roll manoeuvre. Thus images can be built up by moving the scan mirror in the East-West direction through a small angle in $\sim$2 arcsecond steps.

For GIS the beam hits a spherical grating placed at grazing incidence which disperses the light onto four microchannel plate (MCP) one-dimensional detectors placed

Telescope	Aperture Size	$34.3cm^2$-NIS, $47cm^2$-GIS
	Spatial Resolution	1.2"GIS-wd,1.7"GIS-pwd
		1.2"NIS-wd,1.5"NIS-pwd
NIS	Wavelength Coverage	308-381, 513-633$\mathring{A}$
	Prime Slits(4,5,6)	2×240, 4×240, 90×240 arcsec.^{2}
	Spectral Resolution	0.08$\mathring{A}$-NIS1, 0.14$\mathring{A}$-NIS2
GIS	Wavelength Coverage	151-221, 256-338, 393-493, 656-785$\mathring{A}$
	Prime Slits(1,2,3)	2×2, 4×4, 8×50 arcsec.^{2}
	Spectral Resolution	0.21$\mathring{A}$

Table 1.1: CDS Relevant characteristics. pwd denotes the direction perpendicular to the wavelength dispersion plane and wd denotes the direction of wavelength dispersion.

around the Rowland circle. The resulting spectra are astigmatic (i.e. a focussed image of the slit is not produced on the detector) and so 'pinhole' slits are used. By rastering E-W using the scan mirror and N-S using the slits, images may be formed.

The field of view of the instrument is 4' by 4' and it can be repointed to anywhere on the solar disc. The wavelength coverage of the instrument is from 151$\mathring{A}$ to 785$\mathring{A}$ in the different bands as given in table.1.1. There are 6 slits available for use, nominally three for the GIS and three for the NIS, and these are also given in table.1.1. For NIS the spatial information is retained by the 2-d detector so it utilises slits which are long in the direction perpendicular to that of wavelength dispersion (i.e. 2" by 240", 4" by 240" & 90" by 240"). The 90" by 240" slit is provided to act as a feature locater. For GIS the 'pinhole' slits are square apertures and thus have a spatial extent limited to their size. The 8" by 50" slit can be used to provide a larger throughput. The spectral resolution of the two spectrometers can be obtained from the grating equation,

$$n\lambda = d\,(\sin\theta + \sin\alpha) \tag{1.1}$$

where n is the order, d is the grating spacing, θ is the angle of incidence on the grating and α is the angle of reflection off the grating. On assuming that the angle of incidence is fixed and making use of a trigonometric expansion of $\sin(\alpha + \delta\alpha)$ we

obtain,

$$\frac{\lambda}{\delta\lambda} = \frac{2\lambda R}{dx \cos\alpha} \tag{1.2}$$

which defines the spectral resolving power dependent on wavelength, with R the radius of the Rowland circle and dx the resolution scale. The spectral resolution ($\delta\lambda$) is given in table.1.1. As pointed out by Harrison & Fludra (1995) this argument is also valid for NIS. Finally, the temporal resolution, dictated by engineering capability, is of the order 1s or less.

1.1.2 Solar Ultraviolet Measurements of Emitted Radiation

The SUMER instrument optical layout is presented in fig.2 of Wilhelm et al.(1995). It consists of a telescope containing a parabolic mirror and an enclosed spectrometer utilising another parabolic mirror, a plane mirror and a spherical concave grating. The telescope mirror images the sun into the entrance slit of the spectrometer where the beam is directed onto the second parabolic mirror which collimates the light. The collimated beam is directed onto the plane mirror which deflects it onto the grating. Two two-dimensional detectors are positioned in the focal plane of the grating to collect images of the slit. Spatial information is retained as the images are stigmatic. Two spectral orders are recorded simultaneously over short wavelength ranges. To build a complete spectrum (such as that obtained with CDS) the plane mirror is rotated to scan wavelength ranges. The spatial resolution is close to 1 arcsec. but dependent on wavelength (see table.1.2).

The SUMER field of view covers 64' by 64' and is scanned using the telescope mirror which manoeuvres in 0.38" steps. This can attain a fastest rate of 300 steps s^{-1}. The wavelength coverage is from 660$\mathring{A}$ to 1610$\mathring{A}$ in first order and 330$\mathring{A}$ to 805$\mathring{A}$ in second order. The precise detector ranges are given in table.1.2. Since the instrument uses three normal incidence reflections its sensitivity is very low below $\sim 500\mathring{A}$. This principally affects the detection of lines in second order. Four slits are available and they are narrow in the dimension of wavelength dispersion to provide good wavelength resolution (see table.1.2). As for CDS-NIS the spectrometer is stigmatic so long slits are used to provide spatial information. These are oriented N-S and centred on the

Wavelength Coverage	Detector A : 390-805$\mathring{A}$ (2nd order), 780-1610$\mathring{A}$ (1st order) Detector B : 330-750$\mathring{A}$ (2nd order), 660-1500$\mathring{A}$ (1st order)
Prime Slits(2,4,7,1)	1×300, 1×120, 0.3×120, 4×300 arcsec.^{2}
Spatial Resolution	1.03 arcsec. px^{-1} at 800$\mathring{A}$ 0.95 arcsec. px^{-1} at 1600$\mathring{A}$
Spectral Resolution	0.0228$\mathring{A}$ px^{-1} at 500$\mathring{A}$ (2nd order) 0.0209$\mathring{A}$ px^{-1} at 800$\mathring{A}$ 0.0450$\mathring{A}$ px^{-1} at 800$\mathring{A}$ (1st order) 0.0418$\mathring{A}$ px^{-1} at 1600$\mathring{A}$

Table 1.2: SUMER Relevant characteristics.

detector spatial dimension. Slit 1 is wide in order to increase counts and was intended for off-limb observations. Slit 4 & 7 are available for more intense lines to cut the count rates from both the line and the continuum. Slit 2 is for standard use as it maps larger areas, perpendicular to the spatial dimension, than the others in a set time. A number of other refined slit positions are available and are referred to by separate slit numbers but these are only available to authorised SUMER team members (Wilhelm et al.(1995)).

The spectral resolution is again obtained from the grating equation and is given in table.1.2. The temporal resolution is of the order 1 second but can be as little as 60ms for specific observations of intense lines using the appropriate slit.

1.1.3 Discussion

Previous solar EUV instrumentation has improved our understanding of the solar upper atmosphere and has allowed us to define what exactly is needed to make greater advances. It is clear that the atmosphere is highly dynamic and that attempts to discover the coronal heating mechanism along with a comprehensive description of the atmospheric energy balance and radiating characteristics requires observations on much finer scales than have been available here-to-fore. In addition, measurements are required over a broader wavelength range, especially to shorter wavelengths (below $\sim$ 300$\mathring{A}$) which include emission lines from some of the hottest non-flare coronal

plasmas.

In recent years great advances have been made in instrumentation development and engineering. For example, the spatial resolution of an instrument such as the soft x-ray telescope on YOHKOH, launched in 1991, is about a factor of three better than that available to scientists involved with the Solar Maximum Mission satellite launched in 1980. Missions prior to SOHO have been limited in their impact due to project and instrumentation design. As discussed by Harrison & Fludra (1995), in the context of EUV experiments, observations have been made since the early '60s. The Orbiting Solar Observatory (OSO) series (I-VII) ran from 1962-72 but in many cases used integrated solar disc images or integrated spectral bands. For those that did not, the spatial, spectral and temporal resolution was at least, and usually more than, an order of magnitude coarser than the instruments on SOHO e.g. 20", 0.8$\mathring{A}$ and 120s respectively for the best (e.g. OSO VII in 1972). Certainly also, the wavelength coverage was much less (120-400$\mathring{A}$ for OSO-VII) and usually did not extend adequately to the shorter wavelengths ($\sim$ 300$\mathring{A}$ being typical). Skylab (1973-74) improved the situation with regard to spectral coverage (171-630$\mathring{A}$) and resolution (0.13$\mathring{A}$). However, the spectral and spatial information could not be separated unambiguously as the spatial resolution was dependent on the location and brightness of the feature on the disc and in the spectrum. Since Skylab there have been five short duration solar EUV missions flown on the space shuttle and sounding rockets. Of these only the Coronal Helium Abundance Spacelab Experiment (CHASE) and the Solar Extreme ultraviolet Rocket Telescope and Spectrograph (SERTS) have characteristics comparable with CDS & SUMER. CHASE flew on the space shuttle for nine days in 1985 and SERTS typically observes for $\sim$ 6mins. during its rocket flight. In addition, the spectral and spatial resolution of CHASE were $0.25-0.4\mathring{A}$ and 15" respectively, which is worse than the SOHO instruments. SERTS has spectral and spatial capabilities close to that of CDS but prior to the SOHO launch only used photographic film and thus limited its temporal resolution. Also, its wavelength range is more restricted (170-450$\mathring{A}$). SOHO-CDS & SOHO-SUMER thus provide the first opportunity for a complete investigation of the EUV sun.

CDS and SUMER together provide a wavelength coverage (from 150$\mathring{A}$ to 1600$\mathring{A}$)

which encompasses spectral emission lines produced by ions formed at temperatures from 10^4 to 2×10^6K. These temperatures are appropriate for investigation of the upper chromosphere through to the corona. The shorter wavelengths accessible by CDS allow measurement of the valuable hotter lines.

It has been usual, in solar physics, to assume that the solar atmosphere from the chromosphere through the *transition zone* to the corona is all one continuous structure. However, Feldman(1983) and Feldman(1987) argued that most of the observed solar emission between temperatures of $\sim 40,000- \sim 500,000$ K originates from plasma structures magnetically isolated from the chromosphere and corona. In this model, the true *transition zone* is only responsible for a small part of the emission within these temperature ranges. These structures, which Feldman(1983) named *unresolved fine structures*, should be extremely small and as yet unobserved by spaceborne instrumentation. CDS, and particularly SUMER, have a spatial resolution that will allow investigation of some of the smaller scale structures of the solar atmosphere and will investigate such issues. From the L_1 Lagrangian point, 1 arcsecond corresponds to $\sim$ 715km on the solar surface (Wilhelm (1993)). Typically compact loop structures have a radius of the order of 7 or 8 thousand km (Woodgate et al.(1983)). Therefore, the spatial resolution of an instrument such as SUMER is fine enough to resolve these small structures into $\sim 10 - 20$ segments. Thus due account should be taken of the spectrometer line of sight, for example, when estimating emitting plasma volumes for comparison with models. This has not been necessary for previous missions as the resolution was adequate only for total loop observations e.g. for CHASE the spatial resolution was 15" equivalent to $\sim$11,000km (see also Doschek et al.(1982)).

The temporal resolution of CDS & SUMER is critical in assessing whether dynamics in the transition region and corona are rapid enough to cast doubt on the assumption of ionisation equilibrium. The implications of this are widespread for determination of solar atmospheric structure and predictive studies and are addressed in chap.5 of this thesis. The resolution will also allow investigation of dynamical plasma events such as jets etc. The positioning of SOHO at L_1, conversely, permits long duration studies that can help in the interpretation of measurements of, for example,

growth and decay rates of active region loops and prominences.

Finally, the available spectral resolution of the two instruments is high enough to separate a large number of lines of prime interest for density and temperature diagnosis and also to determine line-of-sight velocities from doppler shifts with an accuracy of $\sim 1km\ s^{-1}$. Such accuracy will facilitate the determination of plasma flow characteristics and velocity field fluctuations around sunspots and prominences, for example.

1.2 Overview of ADAS

1.2.1 The ADAS Project and its Principles

The Atomic Data and Analysis Structure (ADAS) originated at JET Joint Undertaking and is now developed jointly with Strathclyde University, and the sponsoring laboratories, under the direction of Prof. H.P.Summers. ADAS provides an interactive set of computer codes for accessing and displaying important plasma quantities. It is possible to look at large amounts of fundamental atomic collision data and also model dependent derived data more closely linked to the experimental plasma spectroscopy data reduction. In addition, ADAS provides a powerful capability for exploring parameter dependencies, for calculation of original data and for tailoring output to the specific requirements of a particular set of spectral observations.

ADAS draws together the experience and abilities of scientists working in different areas of plasma research. Theorists who calculate detailed reaction cross-sections to spectroscopists at the forefront of plasma experimental research are involved. With the large amounts of atomic data produced presently, and the differing quality standards, it is essential that some record of data sources is used for ease of comparison. In addition, an integrated approach to the atomic modelling of plasmas can only be beneficial to the overall goals of plasma fusion and astrophysical research. ADAS provides this integrated structure by having a centrally managed atomic database where every result is traceable to its source. The adoption of a common modelling approach also provides consistent source functions, for entry to plasma transport

models, with validation through widespread use. Thus leading fusion and solar astrophysical laboratories have sponsored the ADAS project to provide themselves with this capability. The sponsoring laboratories include both of the Principal Investigator Institutes for the European coronal spectrometers on SOHO i.e. Rutherford Appleton Laboratory, Oxford, UK (CDS Team) and Max Planck Institut für Aeronomie, Katlenberg-Lindau, Germany (SUMER Team). The involvement of a Consortium of worldwide research laboratories ensures that it is possible to fill the needs of the database by separating the local atomic tasks, thus avoiding needless duplication of effort.

ADAS was originally written in FORTRAN for the IBM mainframe at JET (Summers (1994)). However, it was decided at an early stage that the future of the project lay with a workstation environment and IDL was chosen to provide the interactive window interface to the subroutines and database. Due to requirements to support the project at JET it was decided that all the processing routines would remain in FORTRAN and that the interface and process management would be written in IDL. For the past two years contracted programmers and research assistants have made the conversion to UNIX-IDL on workstations. ADAS now has three main parts.

1. Centrally controlled Interactive user display.

2. Atomic database.

3. Library of Subroutines.

The user interface helps the informed user to run through the ADAS routines. It adopts central defaults which guide the user to the correctly formatted data types. A description of how to use each routine is generally provided with each updated release of ADAS and for solar astrophysical applications a user manual has been written (Summers et al.(1996)). Individual users' own application software can draw from the database and also the library of subroutines that ADAS has built up during the course of the conversion and development. Again, this avoids duplication of effort. ADAS provides a great deal of data but there are also 'off-line' codes that can be activated for specific gaps that need filled.

Participating Organisations	Contact
JET Joint Undertaking, England	H.P.Summers
IPP Garching, Germany	K.H.Behringer
KFA Juelich, Germany	J.Hey
Oak Ridge Cont. Fusion Atom. Data Centre, USA	D.Schulz
IPF Stuttgart, Germany	K.Hirsch
RAL (SOHO-CDS), England	J.Lang
MPAe Lindau, Germany	D.Innes
INEA Frascati, Italy	R.de Angelis
CEA Cadarache, France	W.Mandl
Tokamak de Varennes, Canada	E.Haddad

Table 1.3: Members of the ADAS consortium

The Consortium

A number of research laboratories worldwide are sponsors of the ADAS project. These make up the ADAS consortium and are are listed in table 1.3.

The Database

The ADAS database is strictly controlled according to various classes each of which have their own ADAS data format number. There are 24 *adf*'s in the database and some examples useful for solar astrophysical applications are shown in table 1.4. These formats must be strictly adhered to and a sample specification of each is given in Summers(1994). These are still valid for the UNIX-IDL version. Further examples of adf04 files are given in chap.3. Although there is some provision for inputting default values, if for example particular data is not available, there is generally not much protection against a faulty dataset. The data comes from a variety of sources. JET has contractual arrangements with Douglas Sampson and co-workers, at Pennsylvania State University, and Queen's University Belfast to name two. There is also a great deal of data taken from the general literature. Lang et al.(1994) compiled a comprehensive critical review of the available atomic data which is generally referred to as the 'green book'. This document includes contributions from many distinguished

Data Class	Description
adf04	Specific ion data
adf07	Direct resolved electron impact ionisation data
adf11	CR ionisation, recombination and power data
adf15	Photon emissivity coefficient data
adf20	G(T_e) functions

Table 1.4: Key ADAS data format numbers for solar applications

Series No.	Title	Description
ADAS1	Atomic Data Entry and Verification	Graphing/Interpolation of individual reaction data & subsequent evaluation of rate coeffts.
ADAS2	General Z data and Population Processing	Coefft. preparation for and evaluation of excited populations of specific ions in a plasma. Calculation of line emission.
ADAS3	Charge Exchange processing	Graphing/processing of charge exchange related data (special interest to fusion).
ADAS4	Recombination and Ionisation Processing	Coefft. preparation for and evaluation of ground and metastable populations in plasma models (dynamic or steady state).
ADAS5	Supplementary Programs	Graphing/fitting of derived data & preparation of G(T_e) DEM precursor files.
ADAS6	Data Analysis Programs	Differential emission measure analysis.

Table 1.5: Summary of ADAS organisation

authors and represents a good 'benchmark' opinion of the best available data. It includes reviews of atomic data for H-like to F-like ions and also SiII-SiIV, SII-SIV and FeI-XVII. The 'green book' developed from an atomic data assessment meeting held at Cosener's House in Abingdon in 1992. Since its publication there have been many improved calculations and it is important to keep aware of these. Lang & Summers (1996) have prepared an ADAS document outlining the data needed to complete the adf04 database for the requirements of SOHO-CDS & SOHO-SUMER.

The Modelling Codes

This thesis is primarily concerned with solar radiation modelling so it is worthwhile to mention the ADAS codes which are of interest here. There are currently six ADAS series and not all are relevant to this topic. Table 1.5 provides a list and brief summary of the purpose of each of them. The modelling approach adopted for ADAS is that of generalised collisional-radiative theory (sec.2.2.2). Most ADAS codes draw from the fundamental database, perform some collisional-radiative modelling appropriate to the study in question, and output derived data that can be confronted with the experimental results. Alternatively, they provide for examination of fundamental or generated derived data. Output data from each program is formatted so it can be passed to other relevant ADAS routines for further investigative studies. Text and graphical output is also provided for the users' convenience. The codes of special relevance to solar astrophysics are listed in table 1.6 and described in great detail by Summers et al.(1996). Some of these are also described in chap.3, with examples of use, and many have been used in the study of oxygen (chap.4). Each of the codes in table 1.6 was completed with the release of ADAS v.1.6 in June 1996, so ADAS now has a fully functioning capability for solar physics. Many studies and analysis of spectroscopic data in the past have been questionable due to uncertainties in the atomic modelling calculations. For example, the ionisation balance, line emission functions and line ratio diagnostic techniques can often be a weakness in the final results. ADAS has a powerful capability for examining such issues and it is hoped that its use will validate certain approaches and eliminate many of these problems. Although many of the codes are complex and can only be handled with practice,

Program	Use
ADAS205	Calculation of metastable & excited state populations
ADAS207	Calculation & display of line emissivities and ratios
ADAS208	Advanced version of ADAS205
ADAS209	Combines rate coefft. data from LSJ coupling to LS
ADAS210	Separates rate coefft. data from LS coupling to LSJ
ADAS405	Calculation of ionisation equilibrium fractions, radiated power & G(T_e)'s-can be metastable resolved
ADAS502	Interrogates ionisation rate coefficients
ADAS503	Interrogates photon emissivity coefficients
ADAS506	Interrogates G(T_e) functions, sets up collection file for DEM analysis
ADAS601	Executes DEM analysis

Table 1.6: Key ADAS routines for solar applications

the tutorial manual used together with the release bulletins should alleviate any difficulties. In addition, it is hoped that the study of oxygen in ch.4 will provide a useful demonstration of the analysis path for solar applications.

ADAS is currently only applicable to optically thin plasmas. However, it is hoped that its success in modelling the radiating properties of such plasmas will encourage a similar structured approach to the investigation of optically thick plasmas. Indeed the flexibility, organisation and modelling approach of ADAS is such that it is well suited to developing new methods for dealing with these and other circumstances. The incorporation of a complete treatment of radiative transfer by simultaneous solution with the equations of statistical equilibrium, the integration of simpler *escape factor* models (McWhirter (1965)) and non-maxwellian electron distributions, are some of the ideas for future development.

Chapter 2

Outline of Atomic Modelling and Spectral Emission from Plasmas

To model the radiative behaviour of atomic species in laboratory or astrophysical plasmas, it is necessary to know a number of key fundamental properties of the atoms, ions and electrons, whose interactions contribute to the spectral emission. The population distribution amongst excited states of the atoms or ions is essential for both predictive spectrum line studies and analysis and therefore must be established. To do this we must take into account all the rate coefficients of every participating atomic process that contributes to the formation of the individual level populations. Since the atomic structure of the atoms and ions is essentially an infinite assembly of levels, it is generally necessary to make certain simplifying assumptions about the nature of the plasma being investigated in order to make the problem tractable. While this prejudices the results of such studies, it can provide a convenient starting point that allows us to focus on the most influential assumptions which should eventually result in convergence on the correct model. Certainly it is possible to include or exclude those assumptions that prove to be far removed from the reality of the conditions in the plasma in question. In the sections that follow, some of the common models are outlined and it is shown that the most appropriate atomic modelling approach is that of *Generalised Collisional Radiative Theory*. In addition, as background, a brief description is given of each of the most important fundamental atomic processes.

Their incorporation into ADAS provides derived atomic data whose applications are focused primarily on individual plasma studies.

2.1 Plasma Modelling

2.1.1 Thermodynamic Equilibrium

Consider a plasma consisting of atoms, ions and electrons with number densities N_i and N_e respectively, where i refers to the state of the atom or ion. Then, if the free electrons and ions are confined within the plasma and no radiation can escape, the system is said to be in *complete thermodynamic equilibrium.* In such circumstances, the atoms, ions and electrons establish equilibrium energy distributions at a particular temperature, and the rate of every individual reaction is balanced by the rate of its inverse reaction.

The electron speed distribution is then referred to as Maxwellian and is given by

$$f(v) = 4\pi \left(\frac{m_e}{2\pi k T_e}\right)^{3/2} v^2 \exp\left(\frac{-m_e v^2}{2kT_k}\right) \tag{2.1}$$

where m_e is the mass of an electron, k is Boltzmann's constant, and T_k is the plasma kinetic temperature. The photon energy distribution of the system is that of a *black body* corresponding to the radiation temperature T_k. Therefore, the radiation field energy density at frequency ν, per unit frequency interval, is given by

$$U(\nu) = \frac{8\pi h \left(\nu^3/c^3\right)}{\exp\left(h\nu/kT_k\right) - 1} \tag{2.2}$$

This is known as Planck's function, where c is the speed of light and h is Planck's constant.

The population distribution of excited states within an ion and between ionisation states can be obtained for the system by means of the Boltzmann and Saha-Boltzmann equations. These are,

$$\frac{N_i}{N_j} = \frac{\omega_i}{\omega_j} \exp\left\{-\left(E_i - E_j\right)/kT\right\} \tag{2.3}$$

and

$$\frac{N_i^z}{N_e N_k^{z+1}} = \frac{\omega_i^z}{\omega_k^{z+1}} \frac{h^3}{2\left(2\pi m_e k T_e\right)^{3/2}} \exp\left(I/kT_e\right) \tag{2.4}$$

respectively, where the superscript z refers to the z times ionised state and $z+1$ to the next higher ionisation stage. In addition, N_i, ω_i and E_i are the population density, statistical weight and transition energy of the level i and there are corresponding expressions for the level j and the level k of the $z+1$ times ionised state.

Complete Thermodynamic Equilibrium is never achieved in laboratory plasmas but may be closely approached in astrophysical plasmas, for example stellar interiors. This is principally because the radiation can usually escape before being reabsorbed, but also because the timescales to reach equilibrium are usually longer than the time taken for the plasma to change in temperature or density. These equilibrium timescales are described in more detail in sec. 2.1.2. Anticipating these results, we see that in general the electrons form a Maxwellian distribution of velocities. The external radiation field, in a real plasma, is unlikely to be a black body but it may be a diluted version of one, for example, in the solar corona.

The excited state populations, in natural and laboratory plasmas, can attain Boltzmann values, but are more likely to correspond to those of statistical balance. Statistical balance assumes that the sum of processes which populate a level can be equated to the sum of processes that depopulate that same level. If this is not so, the sum of these reaction rates defines a particle interaction term (see left hand side of eq. 2.5). This term denotes the integral over all velocities, of the rate of change of the electron distribution, due to collisions with other particles (McWhirter & Summers (1985)).

$$\int \left(\frac{\partial f(N_i^{+z}, \mathbf{v})}{\partial t} \right)_{int} d\mathbf{v} = \sum_j N_e N_j q_{j \to i} - \sum_j N_e N_i q_{i \to j} + \sum_j N_j A_{j \to i} + ... \qquad (2.5)$$

where $A_{j \to i}$ is the spontaneous radiative transition probability and $q_{i \to j}$ and $q_{j \to i}$ are the electron impact excitation and deexcitation coefficients respectively. Eq. 2.5 also contains similar products of rate coefficients with participating species densities for ionising collisions, proton collisions, recombination interactions etc.

We can formulate certain expressions which show the relationships between the reaction rate coefficients. For example, if we consider radiative transitions in our system, we can have

1. Spontaneous Radiative Decay

$$X_j^{+z} \rightarrow X_i^{+z} + h\nu \tag{2.6}$$

2. Photoabsorption

$$X_i^{+z} + h\nu \rightarrow X_j^{+z} \tag{2.7}$$

3. Stimulated Emission

$$X_j^{+z} + h\nu \rightarrow X_i^{+z} + 2h\nu \tag{2.8}$$

The spontaneous radiative transition probability mentioned above is also known as the Einstein A-coefficient and describes eq. 2.6. Similarly, there are Einstein coefficients to describe eq. 2.7 and eq. 2.8 which are denoted $B_{i\rightarrow j}$ and $B_{j\rightarrow i}$ respectively. The statistical balance of these,

$$N_i U(\nu) B_{i\rightarrow j} = N_j \left[U(\nu) B_{j\rightarrow i} + A_{j\rightarrow i}\right] \tag{2.9}$$

together with the assumption of complete thermal equilibrium, eq. 2.2 and eq. 2.3, allow us to derive the following connections between them.

$$\omega_i B_{i\rightarrow j} = \omega_j B_{j\rightarrow i} = \frac{\omega_j A_{j\rightarrow i}}{8\pi h\nu^3/c^3} \tag{2.10}$$

In what follows, we neglect the effects of photon induced transitions such as photoabsorption and stimulated emission. This is equivalent to saying that the plasmas with which we are concerned are optically thin. This is probably a valid assumption for the solar transition region and corona (Zirker (1981)).

Each of the individual processes in eq. 2.5 has an inverse and if their rates equate they are said to be in *detailed balance*. Reaction terms occur in the equation in these detailed balance pairs. In statistical balance the interaction term is zero. Therefore, the dominance of the collisional or radiative processes, in the plasma, is controlled by the interplay between the $N_e N_j q_{j\rightarrow i}$ and $N_j A_{j\rightarrow i}$ terms. This is directly influenced by the plasma electron density. The radiative transition probabilities are generally much larger than the collisional deexcitation coefficients. Therefore, N_e must become large enough to overcome this deficit for collisional processes to take control. It is clear that

for every statistical balance equation, for every level of an atom or ion, there is a fixed N_e where this is true. Above this critical density, the collision processes balance and the spontaneous part of eq. 2.5 becomes negligible in comparison. When this happens, the system is said to be in *local thermodynamic equilibrium* and this is usually denoted LTE (note that the definition of LTE varies between authors and in the case of stellar atmospheres it is usual to define LTE by assuming that the population densities, opacity, emission and thermodynamic properties of a small volume of atmospheric material are the same as the thermodynamic equilibrium values, but at the *local* temperature and electron density (Mihalas (1978)).

In LTE the populations follow the distributions specified by the Boltzmann and Saha-Boltzmann equations. In reality, plasmas are more likely to be in LTE than complete thermodynamic equilibrium. The large cross-sections for collisional transitions between highly excited states makes this a strong possibility at least for them. In these circumstances, it is useful to modify eq. 2.4 by a b factor which gives a measure of the departure from LTE (McWhirter & Summers (1985)). Low lying levels are normally only close to, or in, LTE at extremely high densities. LTE can therefore be viewed as the high density collision dominated behaviour of plasmas. At low density the plasma is radiation dominated and a separate model is required for this regime.

One such model is that of *Coronal Equilibrium*. This is so named because it approximates the behaviour of the solar corona. The assumption is that atoms and ions are excited by electron collisions,

$$X_i^{+z} + e \rightarrow X_j^{+z} + e \tag{2.11}$$

and that they deexcite by spontaneous radiative decay (eq. 2.6). They are collisionally ionised by electron impact,

$$X_i^{+z} + e \rightarrow X_j^{+z+1} + 2e \tag{2.12}$$

and recombine also by electron collision,

$$X_i^{+z} + e \rightarrow X_j^{+z-1} + h\nu \tag{2.13}$$

This model is reasonable if the plasma is of low density and optically thin. The low density ensures that the spontaneous radiative term is greater than the collisional

deexcitation term. In addition, the fact that photons can escape without further interactions ensures that upward radiative transitions (e.g. photoabsorption) can be neglected. Essentially the model predicts that atoms and ions are excited by electron impact, and that they then have time to decay, by photon emission, before they are involved in any other reaction. Similarly, if an atom or ion is ionised, it has time to recombine before further disruptions.

As mentioned above, highly excited states could well be in LTE. This happens above what is termed the *collision limit*, $\bar{\imath}$ say, where the excited state populations are dominated by collisionally induced transitions. States above $\bar{\imath}$ effectively become part of the continuum due to their large cross-sections for transitions to neighbouring states (Burgess(1965) - unpublished, Jordan(1969)). Even at low density this is the case. At increasing density more and more states are in LTE and the collision limit is lowered. It is possible to extend the applicability of the coronal model if we treat ionisation and recombination as including transitions between levels below $\bar{\imath}$ and levels above $\bar{\imath}$. This requires more detailed examination of intermediary states for step-wise ionisation and dielectronic recombination. Discussion of this is deferred until sec. 2.2.2.

We could pose a number of questions. For example, at what densities do collisional processes begin to dominate over radiative ones? At which excited state do collisional processes become important? When does it become necessary to take account of secondary processes that collisionally redistribute the populations before they have time to relax? It is concerns like these that have led to a reevaluation of the different modelling approaches. We wish to adopt an approach which deals with these issues.

2.1.2 Equilibrium Timescales

It is of interest to investigate the different relaxation timescales for the excited states of an atom or ion in a plasma. A comparison of these for low lying levels and highly excited ones, and also with plasma diffusion, transient event and instrument sampling times, enables us to determine our modelling approach. For example, do the low lying levels relax into equilibrium quicker than we can take readings with our instruments?

If so, is there any point in modelling them dynamically? It is interesting also to see whether the plasma itself has time to relax properly. How close is the plasma to thermodynamic equilibrium? Do the electrons generally have time to adopt a Maxwellian velocity distribution? Can we say that the electrons and protons have the same temperature?

First, let us look at these particle-particle equilibration timescales. McWhirter & Summers (1985) provide expressions for these, following the work on encounters between charged particles developed by Spitzer (1956). For a particle of mass m the self collision time is given by,

$$\tau_s c = 0.12 \frac{1}{\alpha c a_0^2} \left(\frac{m}{m_e}\right)^{1/2} \left(\frac{kT_e}{I_H}\right)^{3/2} \frac{1}{N z^4 \ln\Lambda} \tag{2.14}$$

which gives us the following rough estimate for the electron-electron equipartition time.

$$\tau_{ee} \sim \frac{1.96 \times 10^7}{(cm^3 s^{-1})} \left(\frac{kT_e}{I_H}\right)^{3/2} \frac{1}{N_e \ln\Lambda} \tag{2.15}$$

Likewise, the proton-proton equipartition time follows from this due to the $(m_p/m_e)^{1/2}$ mass factor,

$$\tau_{pp} \sim \frac{8.43 \times 10^8}{(cm^3 s^{-1})} \left(\frac{kT_p}{I_H}\right)^{3/2} \frac{1}{N_p z^4 \ln\Lambda} \sim 43\tau_{ee} \tag{2.16}$$

McWhirter & Summers also gave an expression for the equilibration timescale between two different particles, viz.

$$\tau_{eq} = 0.0529 \frac{1}{\alpha c a_0^2} \frac{m_1}{m_e} \frac{m_2}{m_e} \left(\frac{kT_1}{I_H}\frac{m_e}{m_1} + \frac{kT_2}{I_H}\frac{m_e}{m_2}\right)^{3/2} \frac{1}{n^2 z_1^2 z_2^2 \ln\Lambda} \tag{2.17}$$

which leads to the approximate form for proton-electron thermalisation,

$$\tau_{ep} \sim \frac{8.64 \times 10^6}{(cm^3 s^{-1})} \frac{m_p}{m_e} \left(\frac{kT_e}{I_H} + 5.4 \times 10^{-4} \frac{kT_p}{I_H}\right)^{3/2} \frac{1}{n_p \ln\Lambda} \sim 1849\tau_{ee} \tag{2.18}$$

In eqs. 2.14 to 2.18, α is the fine structure constant, a_0 is the first Bohr radius, c is the speed of light, k is Boltzmann's constant, I_H is the first ionisation potential of the hydrogen atom and $\ln\Lambda$ is the coulomb logarithm which generally takes a value ~ 20.

	$N_e(cm^{-3})$	$T_e(K)$	$\tau_{ee}(s)$	$\tau_{ii}(s)$	$\tau_{ie}(s)$
solar corona	$\sim 5 \times 10^8$	$\sim 1 \times 10^6$	~ 0.18	~ 8	$\sim 153 \rightarrow 348$
laboratory	$\sim 1 \times 10^{13}$	$\sim 1 \times 10^7$	$\sim 3 \times 10^{-4}$	1.3×10^{-2}	$\sim 0.3 \rightarrow 0.6$

Table 2.1: Relaxation timescales for selected plasmas

Table 2.1 gives values for these three timescales, using eq. 2.14 to 2.18, by taking typical values of electron density and temperature for the solar corona and a laboratory fusion plasma. For equipartition we have assumed that the electron contribution is dominant. In a fusion laboratory plasma the confinement time is of the order $\sim 1s$. In the solar corona, the plasma is generally assumed to be in a global steady state, although there are localised dynamic events. This last assumption is likely to be reevaluated as a consequence of the initial results from SOHO, as we shall see in later chapters. However, it appears that in both cases the electron velocities are indeed that of a Maxwellian distribution. Furthermore, they will have had time to thermalise before the ions have. It is likely that in both situations the ions will also thermalise, but in a laboratory plasma the equipartition of energy between ions and electrons does not necessarily have time to take place. Therefore, in a lab. plasma, a two temperature treatment is probably appropriate. This is also true for dynamic activity in the solar corona, but is not necessarily the case if we just consider the overall picture.

Turning now to the relaxation times for the excited states of the ions themselves. These timescales determine the lifetimes of the excited states and as such, influence our modelling approach. We can make simple 'order of magnitude' estimates of the relaxation timescales for ordinary excited states. Essentially this is the inverse of the sum of the transition probability and the product of electron density and the collisional rate coefficient i.e.

$$\tau_{ord} \sim \frac{1}{(N_e q_{i \rightarrow j} + A_{j \rightarrow i})} \tag{2.19}$$

This is dominated by the fastest reaction rate between the two levels. Usually this is the radiative transition probability which is typically very large compared to the

collisional rate coefficient. McWhirter & Summers (1985) give an approximate form for the radiative transition probability which reduces to $A_{j\rightarrow i} \sim 10^8 z1^4$, where $z1 = z + 1$. Therefore, the lifetime for an ordinary excited state is approximately,

$$\tau_{ord} \sim \frac{10^{-8}}{z1^4} \tag{2.20}$$

Evidently, the lifetime of the ground state is dominated by collision processes since it has no possibility of radiatively decaying. In this case we should include ionisation and recombination coefficients in eq. 2.19, but we should exclude the transition probability term. In this case, the dominant reaction rate is that involving the excitation rate coefficient. McWhirter & Summers (1985) also give an approximate form for the excitation rate coefficient which reduces to $q_{i\rightarrow j} \sim 10^{-8}/z1$. The lifetime is then inversely proportional to the electron density and can be approximated thus,

$$\tau_g \sim \frac{10^8 z1}{N_e} \tag{2.21}$$

It is possible also to have metastable states whose lifetimes are comparable to the ground state. These are discussed in more detail in sec. 2.2.2 but arise principally due to their small radiative transition probabilities. Radiative decay from them is less likely as the only pathways from them to the ground state are via quantum mechanically forbidden transitions. Metastables can be influenced by recombination and ionisation processes, and despite their longevity will eventually decay to the ground level at low electron density. Eq. 2.19 for metastables would be similar to that for the ground state but with the spontaneous term reactivated. Once again the interplay between the dominance of the collisional and radiative terms is important. The influence of electron density means that metastable states will have long lifetimes at low density, but that above some threshold, the time constant will become dependent on density. They can therefore be viewed as a separate level grouping, midway between ground and excited states.

A final class of excited states to be considered are those that autoionise (sec. 2.2.1). These have extremely short lifetimes ($\sim 10^{-12} s$) and as such are related to the ordinary excited state and metastable state relaxation timescales as,

$$\tau_{auto} \ll \tau_{ord} \ll \tau_g \tag{2.22}$$

In general, the key lifetimes mentioned above will satisfy the following relationship also,

$$\tau_{met} \sim \tau_g \sim \tau_{plasma} \sim \tau_{ion} \gg \tau_{ord} \gg \tau_{ee} \tag{2.23}$$

where τ_{plasma} refers to plasma diffusion and dynamic timescales, and τ_{ion} refers to the ionisation relaxation timescale. A more detailed discussion of the latter is given in chap.2.

From these heuristic estimates a number of properties of the plasma are evident. We have established that the electron velocity distribution is very likely Maxwellian. It is also clear that the dominant populations of the atoms and ions will be in the ground and metastable states. Their lifetimes are comparable to plasma dynamic timescales and may be shorter than that necessary to establish ionisation equilibrium. As a result, these should be modelled dynamically via the equations of plasma transport (sec. 6.1.1). It is possible to make a separation of states between those that must be modelled in this way, and ones whose relaxation times are so short that they are already in equilibrium. The ordinary excited states and autoionising states fall into the latter category. We call this a *quasi-static separation of excited states* and refer to the highly excited states as being in *quasi-equilibrium*. This division of atomic states, between quasi-static and dynamic populations, allows us to separate the atomic modelling tasks. We can first calculate the excited state populations, emission functions and effective source coefficients. These can then be entered into a dynamical transport model. The spatial and temporal non-equilibrium model can then be advanced, and the new populations reassociated with the quasi-static state emission functions at a new local temperature and density. We require to derive a connection between the dynamic populations and the quasi-static ones that will provide us with these effective source coefficients. This leads us neatly into the approach we will adopt, that of *Collisional-Radiative Modelling*. We defer discussion of this until sec.2.2.2.

2.2 Radiating characteristics of plasmas

2.2.1 Relevant Atomic Processes

To complete our preparations it is necessary to discuss the reactions that we include in our atomic model. The assumption is made that we are dealing with a fully ionised hydrogen plasma. This is usually the case for both astrophysical and fusion plasmas. It therefore consists of electrons, protons, hydrogen atoms and minor species. Protons in this context refer to hydrogen ions of any isotope. The minor species are other elements in various stages of ionisation. It is the latter which contribute the greatest to the radiation emission and it is reactions involving these that must be considered. Despite this, we can neglect reactions between the minor species on the grounds that they occur too infrequently. Many body collisions, e.g. multiple ionisation, are also unlikely to be effective in the present context although they may be important for higher densities. We make special reference to three-body recombination here due to its influence on the generalised dielectronic recombination coefficients at low temperature and high density (see chap.4). We discuss the atomic processes in inverse pairs where appropriate.

Collisional Excitation/Deexcitation by Electron/Proton Impact

Consider the electron impact excitation reaction between two excited levels i and j, of an ion X^{+z}, of an element X;

$$X_i^{+z}(E_i) + e(\epsilon_i) \rightarrow X_j^{+z}(E_j) + e(\epsilon_j) \tag{2.24}$$

where E_i (E_j) is the excitation energy of level i (j), and ϵ_i (ϵ_j) is the incident (scattered) electron energy. This reaction will take place if $\epsilon_i \geq \Delta E_{ij}$, where $\Delta E_{ij} = E_j - E_i$. The reaction, (2.24), is described by a cross-section, $\sigma_{i\rightarrow j}(\epsilon_i)$, which is the effective target size of the ion that the electron has to hit. More completely, we can define the cross-section as follows. If we consider a flux of electrons, $f = N_e v_e$, incident on the ion with number density, N_i, then the number of electrons scattered into a small solid angle, $d\omega$, per unit time is $f N_i \sigma d\omega$. The differential cross-section is the

proportionality factor, σ, which is a function of the scattering angle, and the total cross-section is this integrated over all solid angles.

The symmetrical dimensionless quantity, Ω_{ij}, is the collision strength and it is related to the excitation and de-excitation cross sections by,

$$\Omega_{ij} = \left(\frac{\sigma_{i\to j}(\epsilon_i)}{\pi a_0^2}\right)\omega_i\left(\frac{E_i}{I_H}\right) = \left(\frac{\sigma_{j\to i}(\epsilon_j)}{\pi a_0^2}\right)\omega_j\left(\frac{E_j}{I_H}\right) \tag{2.25}$$

where $\omega_i(\omega_j)$ are the statistical weights of the lower (upper) level, πa_0^2 is the atomic unit of cross-section ($= 8.7974 \times 10^{-17} cm^2$) and I_H is the Rydberg unit of energy ($= 13.6058eV$). When considering reaction kinetics in plasmas the effective collision strength is often used, and this is a function of Ω_{ij} such that,

$$\Upsilon_{ij} = \int_0^\infty \Omega_{ij}(\epsilon_j)\exp(-\epsilon_j/kT_e)d(\epsilon_j/kT_e) \tag{2.26}$$

for excitation from level i to level j at electron temperature T_e, where k is Boltzmann's constant and ϵ_j is the scattered electron energy after excitation. Υ_{ij} is sometimes also written as γ_{ij}. The excitation rate coefficient for this transition can also be obtained from the effective collision strength, viz.,

$$q^e_{i\to j}(T_e) = 2\pi^{1/2}\alpha c a_0^2\left(\frac{I_H}{kT_e}\right)^{1/2}\frac{\Upsilon_{ij}}{\omega_i}\exp(-\Delta E/kT_e) \tag{2.27}$$

where α is the fine structure constant, c is the velocity of light and $2\pi^{1/2}\alpha c a_0^2 = 2.1717 \times 10^{-8} cm^3 s^{-1}$. The de-excitation rate coefficient can be calculated from detailed balance,

$$q^e_{j\to i}(T_e) = q^e_{i\to j}(T_e)\frac{\omega_i}{\omega_j}\exp(\Delta E/kT_e) \tag{2.28}$$

The various approximate forms and asymptotic behaviours, for the different transition types, are discussed in more detail in sec.3.1.4.

A similar excitation reaction takes place involving protons,

$$X_i^{+z} + p \to X_j^{+z} + p \tag{2.29}$$

In general, electrons are more effective than protons at causing collisional transitions due to their larger reaction rate coefficients. These coefficients are products of the

collision cross-section and the velocity. Therefore, this is true in conditions where there is an equipartition of kinetic energy between the protons and electrons. In such circumstances, the electron velocities will be much larger due to the electron to proton mass factor. However, proton collisions can be better at redistributing electrons amongst the fine structure levels of a minor species ion. This is principally because the cross-sections for proton induced transitions between levels with small energy separations, can sometimes become sufficient to overcome the low velocity disadvantage. This is also true for transitions between high n-shells because the l-subshells are nearly degenerate.

Collisional Ionisation by Electron Impact / Three Body Recombination

Consider the electron impact ionisation reaction,

$$X_{\rho}^{+z} + e(\epsilon_1) \rightarrow X_{\tau}^{+z1} + e(\epsilon_2) + e(\epsilon_3) \tag{2.30}$$

This is the direct state resolved total ionisation reaction where the individual electron initial inner shell, ρ, and final target states, τ, are known. It occurs when $\epsilon_1 > \chi_{\tau}$, i.e. the incident electron energy is greater than the ionisation potential of the ion. Alternatively, it can occur through stepwise excitation to an autoionising level, e.g.,

$$X_{\rho}^{+z} + e \rightarrow X_{i}^{+z} + e \rightarrow X_{\tau}^{+z1} + e + e \tag{2.31}$$

In either case it is described by a reaction cross-section, $\sigma_{\rho\rightarrow\tau} \equiv \sigma_{\tau\rho}$. This in turn can be expressed in terms of the two alternative pathways i.e.

$$\sigma_{\tau\rho} = \sum_{nl} \zeta_{nl}\sigma_{\tau(nl,\rho)} + \sum_{i} q^{e}_{\rho\rightarrow i} \tag{2.32}$$

where the $q^{e}_{\rho\rightarrow i}$ is the excitation rate coefficient to the autoionising level i and ζ_{nl} is the number of electrons in the shell nl i.e. the number of equivalent electrons. $\sigma_{\tau(nl,\rho)}$ is the direct ionisation coefficient from the shell nl. Expression 2.32 assumes that excitation to the level i is always followed by autoionisation. This is not necessarily the case and a modification which omits the second sum in 2.32, to take account of this, is described by Burgess, Summers, Cochrane & McWhirter (1977). Autoionisation can

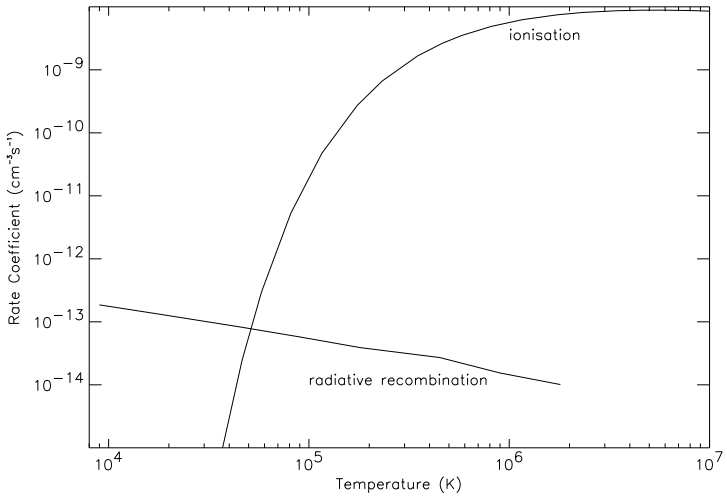

Figure 2.1: Ionisation and Radiative Recombination coefficients for $C^{+2} \leftrightarrow C^{+3}$. Data taken from Abel-Van Maanen(1982)

contribute a substantial amount to the total ionisation cross-section for moderately ionised atoms. For highly ionised systems, the competition with radiative stabilisation means that it is less important. It is described by the radiationless transition probability A^a.

The total ionisation rate coefficient is obtained by integrating over a Maxwellian distribution of electron velocities, i.e.,

$$S_{\tau\rho}^{z\to z1}(T_e) = 2\sqrt{\pi}\alpha c a_0^2 \left(\frac{kT_e}{I_H}\right)^{1/2} \int_{\frac{I_{\rho\tau}}{kT_e}}^{\infty} \frac{\sigma_{\tau\rho}^{z\to z1}(\epsilon_{\rho\tau})}{\pi a_0^2} \left(\epsilon_{\rho\tau}/kT_e\right) \exp\left(-\epsilon_{\rho\tau}/kT_e\right) d\left(\epsilon_{\rho\tau}/kT_e\right) \tag{2.33}$$

where $\epsilon_{\rho\tau}$ is the excitation energy separation between the levels ρ and τ. The typical behaviour of an ionisation rate coefficient is illustrated in fig.2.1.

The inverse process in eq. 2.30 is that of three body recombination. The rate coefficient for this process can be obtained from detailed balance, i.e. by equating the reaction rate for ionisation, $N_e N_\rho S_{\tau\rho}^{z\to z1}$, and the reaction rate for three body recombination, $N_e^2 N_\tau \alpha_{\tau\to\rho}^3$. Note that three body recombination has a reaction rate proportional to N_e^2. This effectively means that, although the rate coefficients for this

reaction are generally very small, it becomes the dominant recombination process at very high electron density. Typically this begins to occur at electron densities above $\sim 10^{14} cm^{-3}$ and becomes more evident as the density increases.

Spontaneous Radiative Decay

Spontaneous radiative decay allows an electron to deexcite from one bound state of an ion, to another bound state of the same ion. This is achieved by the emission of a photon.

$$X_i^z \rightarrow X_j^z + h\nu \tag{2.34}$$

$h\nu$ is the usual term to describe the energy of the emitted photon, and this produces a single spectral emission line at the wavelength corresponding to the frequency ν. As mentioned in sec.2.1.1, the rate coefficient for this reaction is called the transition probability or Einstein coefficient and is denoted by $A_{j\rightarrow i}$. Accurate calculations of them are extremely important as particular transition types have substantially different Einstein coefficients, and this can result in wildly differing relaxation lifetimes (see sec.2.2.2). Consequently, the LTE limit will be approached for some levels much more easily than for others. Three types of transition are generally distinguished.

1. Electric Dipole
2. Non-Dipole
3. Spin changing

Electric dipole transitions have the largest probabilities and these are typically at least $3 \rightarrow 4$ orders of magnitude greater than those for non-dipole and spin changing transitions i.e.$\sim 10^7 - 10^{10} s^{-1}$ compared with $\sim 10^2 - 10^4 s^{-1}$. For electric dipole transitions the Einstein coefficient can be approximated as,

$$A_{j\rightarrow i} = \frac{16\alpha^4 c}{3\sqrt{3}\pi a_0} \frac{g^I}{n_j n_i \left(n_i^2 - n_j^2\right)} \frac{z1^4}{w_j} \tag{2.35}$$

due to McWhirter & Summers (1985), where g^I is the bound-bound Gaunt factor ~ 1, and the $n_{j(i)}$ represent the effective principal quantum numbers of the level j(i).

As discussed earlier, there is a $z1^4$ dependence. This is true for transitions between principal quantum shells, although the dependence is more like $z1$ for transitions within n shells. The other transition types are much more strongly dependent on $z1$. For type 2 this may be $\sim z1^6 - z1^{10}$ and for type 3 $\sim z1^7 - z1^{10}$, again conditional on whether the transition is within the same n shell, or not. As a result, spectral lines for transitions of types 2 and 3 are much weaker than for type 1 in neutral atoms and near neutral ions, but can become dominant for highly ionised ones.

Finally each of the different transition types are identified by specific quantum mechanical selection rules. For electric dipole transitions, the total orbital angular momentum quantum number L must change by 1. Transitions between levels with different total spin angular momentum S are disallowed and the total angular momentum, quantum number J, cannot change by > 1. In addition, $J = 0 \rightarrow J = 0$ transitions are forbidden and the parity selection rule stops transitions within configurations. The parity of an excited state is described as *odd* or *even* and can be calculated as $(-1)^{\sum_i l_i}$, where l_i is the angular momentum quantum number of the ith electron. If the result is -1 the parity is odd and this is denoted by a superscript o on the total angular momentum quantum number of the term e.g. P^o. Spin changing transitions take place between levels with different S quantum numbers. This is only possible in relativistic theory, some mention of which is made in sec. 2.2.2. There are a number of different transitions of type 2. Magnetic dipole transitions take place between levels which do not require a change in their total angular momentum. In this case, $\Delta J = 2$ transitions are also forbidden. It is also possible to make an electric quadrupole transition. The electron, in this transition type, must either change its total orbital angular momentum by 2 or not at all. Also, $L = 0 \rightarrow L = 0$ transitions are disallowed.

Radiative Recombination

The radiative recombination reaction is,

$$X_\rho^{z1} + e(\epsilon_1) \rightarrow X_{\rho,nl}^{z} + h\nu \tag{2.36}$$

where the incident electron loses enough energy, by photon emission, to be captured into some principal quantum shell, n. The recombining ion is sometimes referred to as the *parent* ion. McWhirter & Summers (1985) give an approximate form for the associated radiative recombination coefficient. This is based on the assumption that the energies of the highly excited states are approximately hydrogenic (i.e. degenerate).

$$\alpha^r_{\rho j} = \frac{128}{3}\sqrt{\frac{\pi}{3}}\alpha^4 c a_0^2 z 1^4 \left(\frac{I_H}{kT_e}\right)^{3/2} \frac{1}{\omega_{nl} n} \exp\left(\frac{\chi_n}{kT_e}\right) \int_{\frac{\chi_n}{kT_e}}^{\infty} \frac{g^{II}\exp(-(E/kT_e))}{(E/kT_e)} d(E/kT_e) \tag{2.37}$$

where $j \equiv \rho, nl$ and g^{II} is the bound-free Gaunt factor, which is usually taken to be equal to one. The ionisation energy of the nl shell is χ_{nl} and E is the recombining electron energy. Asymptotically the coefficient behaves like,

$$\begin{aligned} \alpha^r_{\rho j} &\rightarrow \exp(s) Ei(s) \rightarrow 1/s \text{ as } s \rightarrow \infty \\ &\rightarrow -\ln s \text{ as } s \rightarrow 0 \end{aligned} \tag{2.38}$$

where $Ei(s) = \int_s^\infty \frac{\exp(-w)}{w} dw$. The first of these is generally more appropriate since the temperature is usually much smaller than the ionisation energy, in an equilibrium plasma (Hutchison (1987)). An example of the typical behaviour of the radiative recombination coefficient is given in fig.2.1. The inverse photon induced processes are not considered in the present context.

Charge Exchange Recombination

The charge transfer reaction takes place between an ion and neutral hydrogen as follows,

$$X_j^{z1} + H^0 \rightarrow X_i^z + p \tag{2.39}$$

where the proton, p, represents singly ionised hydrogen. Generally, the number of neutral hydrogen atoms, with which charge exchange can occur, is much less than the number of electrons. Evidently then, collisional processes involving electrons are much more likely to dominate than charge exchange. In the solar transition region and corona, sufficient numbers of neutral hydrogen atoms are not likely to be present. In contrast, in fusion plasmas, neutral hydrogen beams are actively injected

into the plasma in order to generate heat and also to work as a localised spectroscopic diagnostic. A charge transfer reaction with helium beams is also important in fusion plasmas but, due to the even smaller quantities of the species in the solar atmosphere, it is even less likely to be of importance there.

One effect of charge exchange is to reduce the overall ionisation state of an element. This occurs because the charge exchange recombination coefficient is much larger than the radiative recombination coefficient, and therefore, produces a substantial increase in the total recombination rate. This has consequences for the associated ionisation balance etc. Expressions for charge transfer cross-sections and rate coefficients are dominated by contributions from different physical processes. The change in the relative speeds of the target and projectile species has an influence on the controlling process. For an in depth overview see Janev & Winter(1985) and references therein.

Dielectronic Recombination / Autoionisation

Dielectronic recombination occurs if an incident electron excites an electron in the target parent ion, X_i^{z1}, while simultaneously losing sufficient energy to be captured into a bound state, nl.

$$\begin{aligned} X_\rho^{z1} + e(\epsilon) &\leftrightarrow X_{j,nl}^{z} \\ X_{j,nl}^{z} &\rightarrow X_{\tau,nl}^{z} + h\nu \end{aligned} \tag{2.40}$$

Here ρ denotes the metastable states of the parent ion, τ denotes the metastable states of the recombined ion, j is an ordinary excited state and nl is a bound orbital with n and l large. In general, this occurs if the incident electron has an energy slightly less than the excitation energy required. As a result, the condition is inherently unstable and may only be transient. That is, it can easily break-up in an *Auger* reaction which returns the individual electrons to their initial states; the leftward arrow in the first part of eq. 2.40. However, it is possible that the ion will rid itself of its excess energy by emitting a photon before this has time to occur. In that case, the incident free electron is 'properly captured' and the ion recombines. The captured electron makes no contribution to the stabilisation phase. The spectrum line associated with the radiated photon is called a *satellite line* and can be useful

for temperature diagnostics. Its wavelength is $\sim \frac{hc}{\Delta E_{\rho j}}$. The two processes in the dielectronic recombination reaction are usually referred to as *resonant capture* and *radiative stabilisation*. The Auger decay is also referred to as *autoionisation* and this has been discussed above.

We can distinguish total and partial zero density dielectronic recombination coefficients. Expressions for these have been given by Burgess(1964,65) and a useful review was presented by Seaton & Storey (1976). Here we follow these authors and express the partial dielectronic recombination coefficient as,

$$\alpha^d_{\rho k} = \frac{\omega^z_k}{\omega^{z1}_\rho} \frac{h^3}{2(2\pi m_e k T_e)^{3/2}} \sum_\tau A_{j,nl\rightarrow\tau,nl} \sum_{nl} \exp\left(\frac{-E}{kT_e}\right) A^{cap} \tag{2.41}$$

where $k \equiv \tau, nl$ and the statistical weight, ω^z_k, is the product of ω_j and ω_{nl}. A^{cap} is the capture cross-section which estimates the probability of dielectronic capture into nl; taking account of the possibility of autoionisation. It is expressed as,

$$A^{cap} = \frac{\sum_f A^a_{j,nl\rightarrow\rho,f}}{\sum_f A^a_{j,nl\rightarrow\tau,f} + \sum_\tau A_{j,nl\rightarrow\tau,nl}} \tag{2.42}$$

where the A^a's are autoionisation transition probabilities. It is likely that the most efficient dielectronic recombination rate will be obtained when $\rho = \tau$. This is because returning to the initial metastable state means that the final state energy is low enough to avoid the Auger break up reaction (Burgess(1964)). The total dielectronic recombination rate coefficient can be obtained by summing over all possible intermediary states j,nl thus

$$\alpha^{dtot.}_{\rho k} = \sum_{j,nl} \alpha^d_{\rho k} \tag{2.43}$$

These potentially transient states are referred to as *doubly excited*, and the summation extends from the lowest energetically accessible one to infinity. The lowest accessible state corresponds to the case where nl satisfies,

$$E_\rho = E_{\tau,nl} + h\nu \tag{2.44}$$

Only at zero density do all resonant captures cascade to the ground level and contribute to the effective dielectronic recombination coefficient. At increasing density secondary collisional redistribution is more likely to intervene in the process before

radiative stabilisation has had time to occur. At some critical density, collisional ionisation will dominate over radiative stabilisation. The main effect of this is to suppress the dielectronic recombination coefficient at high density. Therefore, dielectronic recombination has a more important role to play in low density plasmas. Burgess(1964) also showed that dielectronic recombination was extremely important in high temperature plasmas. At high temperature, the mean electron energy, kT_e, can be comparable to the resonant excitation energy, ϵ. As a result, the exponential term in eq. 2.41 is much larger than usual and this results in an enhancement in the dielectronic recombination coefficient itself, typically $\sim 10-20$ times larger than the radiative recombination coefficient.

In this work we are considering solar plasmas which can be high temperature and low density, for example, the corona. Burgess & Seaton (1964) showed that by including dielectronic recombination they were able to remove the previously existing discrepancy between the coronal temperature deduced from ionisation equilibrium calculations, and the temperature inferred from spectral measurements, e.g. doppler line widths. We should note that dielectronic recombination is now regarded as the dominant recombination process in the solar corona.

2.2.2 Collisional-Radiative Theory

The original concept of Collisional-Radiative modelling was developed by Bates, Kingston & McWhirter (1962). It encompasses both the low density coronal equilibrium approximation and the high density LTE model. It takes full account of the shifting influence of collisional and radiative processes dependent on the electron density and the excitation energy of the principal quantum shell. All radiative and electron collisional processes are included in the model. Photon induced ones e.g stimulated emission, photoionisation etc., are not.

The ion in the plasma is assumed to consist of a complete set of levels with collisional and radiative couplings between each of them. In addition, direct *'state resolved'* ionisation and recombination coefficients to and from the next ionisation stage are included. The quasi-equilibrium assumption is then invoked to *condense*

the influence of the highly excited states onto the dominant states. In this way effective contributions to the evolution of the dominant populations, from the sub-dominant ones, can be identified. At finite plasma densities these contributions may include direct transitions to the dominant states, but can also include transitions via indirect pathways. Examples of the latter are, recombination into highly excited states followed by recombination cascade or stepwise excitation leading to ionisation. Bates et al. (1962) named these contributions collisional-radiative recombination and ionisation coefficients. Following this, Burgess & Summers (1969) included dielectronic recombination in the specification of the collisional radiative recombination coefficient. This allowed them to introduce *collisional-dielectronic* recombination and ionisation coefficients, which Summers (1973) later extended to be dependent on density as well as temperature. These coefficients give the connection between different ionisation stages. In this work it is these latter coefficients that are used. If the dominant populations include metastable states, the coefficients are said to be *generalised*. Collisional-radiative theory also makes a distinction between levels that exist below the collision limit, and those that do not.

It is worthwhile, as background, to present an outline of the theory which establishes the effective recombination and ionisation coefficients used in the time dependent calculation of the dominant populations. This includes the technique of *population condensation*, referred to earlier, which can be generalised to arbitrary level sets. It is clear that different situations require different modelling approaches. For example, the dominant spectrum line emission tends to come from low-lying levels for which a complete specification of the level structure is required. Conversely for highly excited states a much less detailed description is necessary, perhaps dealing with principal quantum shells only. Chap.3 addresses a number of these issues more completely.

Effective Coefficients and Population Condensation

If we consider an ion X^{+z} with arbitrary levels $1 \leq i, j \leq \infty$ below the continuum and recombining ion X^{+z1}, then the statistical balance equations for the level i are,

$$\begin{aligned}\frac{dN_i}{dt} = \sum_\sigma N_e N_\sigma^{z1} \left(\alpha_i^r + \alpha_i^d + N_e\alpha_i^3 + \left(\frac{N_H}{N_e}\right)\alpha_i^{cx}\right) \\ + \sum_{j>i} N_j \left(N_e q_{j\to i}^e + N_e q_{j\to i}^p + A_{j\to i}\right) \\ + \sum_{j<i} N_j \left(N_e q_{j\to i}^e + N_e q_{j\to i}^p\right) \\ - N_i \left(\sum_{j>i} \left(N_e q_{i\to j}^e + N_e q_{i\to j}^p\right) \right. \\ + \sum_{j<i} \left(N_e q_{i\to j}^e + N_e q_{i\to j}^p + A_{i\to j}\right) \\ \left. + \sum_\sigma \left(N_e s_{i\to\sigma} + A_{i\to\sigma}^a\right)\right) \end{aligned} \tag{2.45}$$

where we have included all rate coefficients for the relevant processes in an optically thin low density thermal plasma (see sec.2.1) and we have implicitly assumed that the electron, involved in the four recombination processes, is fully captured although this has not been explicitly noted in the expressions for the α's. The subscript σ refers to the metastable states of the recombining ion, N_e is the electron density, N_H is the hydrogen density and N_i is the population density of the level i. Let us express eq. 2.45 differently by gathering together the recombination, ionisation, excitation and deexcitation terms and defining them more helpfully i.e.

$$\frac{dN_i}{dt} = \sum_{j\neq i} C_{j\to i} N_j + \sum_\sigma N_e N_\sigma^{z1} r_{\sigma i} - \sum_\sigma N_i S_{i\sigma} - \sum_{j\neq i} C_{i\to j} N_i \tag{2.46}$$

The new coefficients are defined as,

$$C_{j\to i} = A_{j\to i} + N_e \left(q_{j\to i}^e + q_{j\to i}^p\right) \tag{2.47}$$

$$C_{i\to j} = A_{i\to j} + N_e \left(q_{i\to j}^e + q_{i\to j}^p\right) \tag{2.48}$$

$$r_{i\sigma} = \alpha_i^r + \alpha_i^d + N_e\alpha_i^3 + \left(\frac{N_H}{N_e}\right)\alpha_i^{cx} \tag{2.49}$$

$$S_{\sigma i} = N_e s_{i\to\sigma} + A_{i\to\sigma}^a \tag{2.50}$$

This allows us to define a total loss coefficient C_{ii} for the level i, viz.

$$-C_{ii} = C_{i\to j} + \sum_{\sigma} S_{\sigma i} \tag{2.51}$$

which, combined with the populating term,

$$-C_{ij} = C_{ii} + C_{j\to i} \tag{2.52}$$

defines the usual collisional-radiative matrix previously used by, amongst others, Summers (1973), Burgess & Summers (1976), Spence (1987) and Dickson (1993). Therefore, we can rewrite eq. 2.46 as,

$$\frac{dN_i}{dt} = \sum_{\sigma} N_e N_{\sigma}^{z1} r_{i\sigma} - \sum_{j} C_{ij} N_j \tag{2.53}$$

This equation provides us with a mechanism for calculating arbitrary level populations. By substituting for the N_j we can recover the dominant populations N_i, be they ground or metastable states. First we must calculate the N_j. This is readily done by invoking the quasi-equilibrium assumption which allows us to set the left hand side of eq. 2.53 equal to zero. It is clear also that the recombination term could be split to its component parts. It is often usual to do this in order to separate out the contribution due to charge exchange recombination (Summers (1994)).

For simplicity, we will illustrate here, the procedure adopted assuming that only the ground states of the X^{+z} and X^{+z1} ion, are heavily populated. We denote the ground state of the X^{+z} ion by ρ, and the ground state of the parent ion by τ. This approach can be generalised to include the effects of the metastable states in the collisional-dielectronic coefficients (see Dickson (1993), Summers (1994)). As such it introduces the effective metastable cross-coupling coefficients and parent-parent metastable cross-coupling coefficients (see sec.3.2.1).
If we now partition the ground states exclusively out of eq. 2.53, we obtain,

$$\frac{dN_\rho}{dt} = -\sum_{j>\rho} C_{\rho j} N_j - C_{\rho\rho} N_\rho + N_e N_\tau r_{\rho\tau} \tag{2.54}$$

For the quasi-static excited populations we have,

$$\frac{dN_i}{dt} = 0 = -\sum_{j>\rho} C_{ij} N_j - C_{i\rho} N_\rho + N_e N_\tau r_{\tau i} \tag{2.55}$$

which gives, in equilibrium,

$$N_j^{eq} = -\sum_i C_{ji}^{-1} C_{i\rho} N_\rho + \sum_i C_{ji}^{-1} N_e N_\tau r_{\tau i} \tag{2.56}$$

Substituting into eq. 2.54 we get,

$$\frac{dN_\rho}{dt} = -\left(C_{\rho\rho} - \sum_j \sum_i C_{\rho j} C_{ji}^{-1} C_{i\rho} \right) N_\rho + \left(r_{\rho\tau} - \sum_j \sum_i C_{\rho j} C_{ji}^{-1} r_{\tau i} \right) N_e N_\tau \tag{2.57}$$

This allows us to specify the collisional-dielectronic recombination coefficient,

$$\alpha_{CD} = r_{\rho\tau} - \sum_j \sum_i C_{\rho j} C_{ji}^{-1} r_{\tau i} \tag{2.58}$$

and the collisional-dielectronic ionisation coefficient,

$$S_{CD} = \left(C_{\rho\rho} - \sum_j \sum_i C_{\rho j} C_{ji}^{-1} C_{i\rho} \right) / N_e \tag{2.59}$$

so that the time dependent equation for the ground state ρ finally becomes,

$$\frac{dN_\rho}{dt} = N_e N_\tau \alpha_{CD} - N_e N_\rho S_{CD} \tag{2.60}$$

These coefficients are now density dependent also and include contributions from their simpler temperature dependent individual reaction forms. The method of assuming a quasi-static situation for the excited states and solving for the dominant populations, is the explanation for the term condensation. In principal, this excited state partition could take place anywhere, although it is usual to to keep this decision on a firm physical basis. The effective coefficients provide a measure of the influence of the highly excited levels, projected onto the low lying ones. As such, they provide convenient parameters for data storage which can be throughput to dynamical transport models.

Metastable states

Metastable states have been briefly mentioned above, but it is helpful at this stage, to provide an explicit example. If we adopt the commonly used Russell-Saunders, or LS, coupling scheme, then there are quantum mechanical selection rules which

decide what spontaneous radiative transitions are possible. Mention of these was briefly made in sec.2.2.1. The net effect of these is to promote or inhibit a particular transition and these are generally termed *allowed* or *forbidden*. In general, a state becomes metastable if it is forbidden to decay easily to the ground state. This may arise if it has to decay via a *non-electric dipole* transition. As we have seen, in LS coupling, a change in the *total spin angular momentum*, quantum number S, is not allowed. Therefore, *exchange* transitions between different spin systems are forbidden. More specifically, the selection rule disallows $\Delta S \neq 0$ transitions. In addition, transitions between the same configurations are forbidden by the parity selection rule. Metastable states will form if they have to break either of these rules to make a transition to the ground state.

Fig. 2.2 shows the Grotrian diagram of Be-like C^{+2} for transitions amongst the twelve lowest lying levels. These include some $n = 2 \rightarrow 3$ transitions. The left hand side of the diagram identifies the levels that occur in the singlet spin system, while the right hand side shows those from the triplet system. It is easily seen that the only metastable term for Be-like ions is that of the $1s^2 2s2p\ ^3P$, due to its inability to decay from the triplet spin system. There is no metastable term in the singlet system as electrons can cascade quite freely to the $1s^2 2s2p\ ^1P$ term, which has an electric dipole pathway to the ground. This inability of metastable states to relax, allows them to collect populations which may be of the same order as that of the ground level. We have already seen that their lifetimes can be comparable to that of the ground level, so it is clear that they must be identified and modelled dynamically in the plasma transport equations The complete set of metastable states for oxygen is presented in chap.4 sec.4.3.1. This partition holds true also for all H-like to O-like ions.

In relativistic theory it is possible for metastable states to relax more freely. This occurs because it is necessary to take account of spin-orbit interactions in the Hamiltonian. The latter is done by adding a spin-orbit term as a perturbation to the electrostatic Hamiltonian, producing the Breit-Pauli Hamiltonian (see Berrington, Eissner & Norrington (1995)). When these perturbations are non-negligible, LS coupling breaks down into intermediate coupling. The perturbations split the LS terms

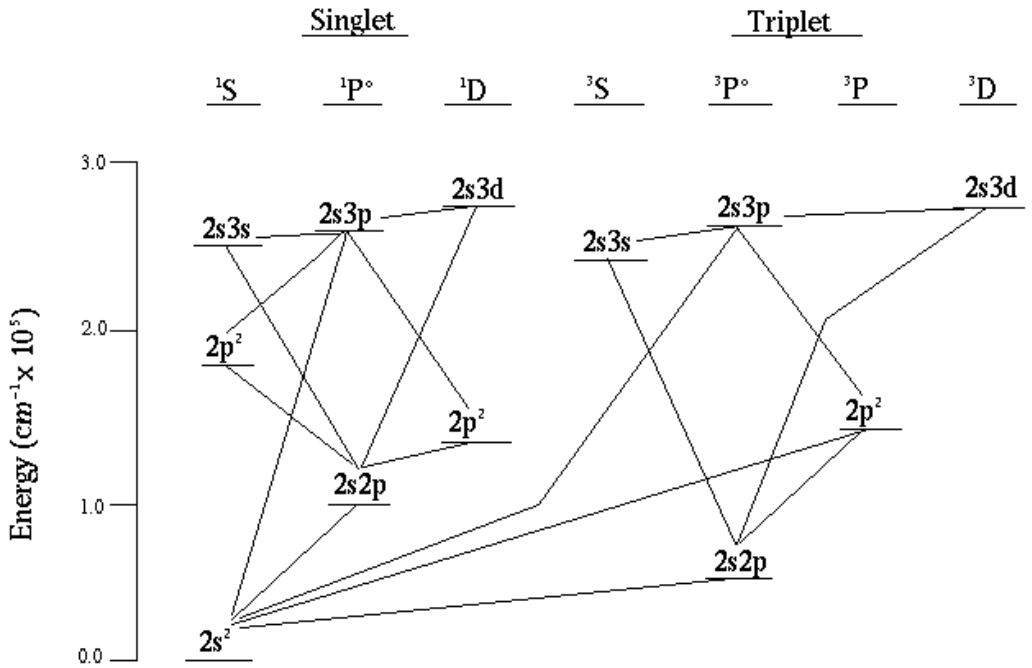

Figure 2.2: Grotrian Diagram for Be-like CIII

into fine structure levels, according to their J quantum numbers. It is then possible for intersystem transitions, via the J-resolved levels, to allow the metastables to decay to the ground. For example, an intercombination transition from $2s2p\ ^3P_1$ to the $2s^2\ ^1S_0$ ground level becomes weakly allowed. Also, a magnetic quadrupole transition from $2s2p\ ^3P_2$ to the ground becomes active.

2.2.3 Derived Atomic Data and their Application to Spectroscopic Diagnostics

In order to gain understanding of the behaviour of plasmas it is important to develop methods for diagnosing their properties. In laboratory plasmas, powerful techniques are in use to measure parameters such as electron density and temperature. These can involve passing laser beams into the plasma to measure the backscattered light (LIDAR - LIght Detection And Ranging) or to compare the beam with one that traverses the same distance, but not through the plasma (infra red interferometry). See Dickson (1993) for a discussion. In addition, placing magnetic probes in the plasma or attaching particle samplers to the plasma container walls, are extremely useful techniques for investigating magnetic field geometry and strength and for diagnosing temperature and density, respectively. Acquiring diagnostic information through spectroscopy is commonplace, but it is rarely necessary to rely solely on the radiation emission to infer plasma parameters and the physical processes at work. For example, neutral beam injection also provides information on the magnetic field through Stark splitting due to the electric field and a prior knowledge of the beam velocity (Wolf (1993)), but this is mainly used with known electron densities and temperatures to diagnose the physical processes at work.

The high temperature solar corona is optically thin. Therefore, radiation is one of the main energy loss mechanisms from the solar upper atmosphere. Here, it is essential to calculate radiation signatures observable by spectroscopic instrumentation. Current technology makes it impractical to consider releasing a solar probe into the hostile environment. Therefore, in remote sensing of the solar atmosphere the only potential diagnostic information we can obtain is this radiation.

We should be aware of the potential limitations of this approach. For example, the intensity of a spectral line emitted by a column of optically thin plasma resulting from a transition $i \rightarrow j$ is formally expressed as

$$I_{i \rightarrow j} = \int \int k(T_e, N_e) \phi(T_e, N_e) dT_e dN_e \tag{2.61}$$

The $\phi(T_e, N_e)$ function is the emission measure differential in temperature and density and represents the most information on the plasma that we can obtain without making any more assumptions. The $k(T_e, N_e)$ is the kernel function which contains the contribution function and the elemental abundance. Recent work by Hubeny & Judge (1995) and Judge, Hubeny & Brown (1997) has shown that the information content of the spectrum is very small and that, due to the ill posed nature of the problem, it is extremely difficult to infer anything about the temperature and density structure of the plasma given the errors associated with the observations and the kernel functions. Indeed, they suggest that with realistic errors information on the density dimension becomes lost in the spectral data noise, making it unrealistic to expect to determine density distributions in addition to temperature distributions.

The usual approach in the astrophysics community has been to proceed by making a number of simplifying assumptions about the nature of the plasma under investigation until eventually arriving at the formulation of Eq.2.62.

$$I_{i \rightarrow j} = \frac{1}{4\pi} \frac{N_{tot}}{N_H} \int_{t_1}^{t_2} G_{i \rightarrow j}(T_e, N_e) \phi(T_e) dT_e \tag{2.62}$$

where $\frac{N_{tot}}{N_H}$ is the abundance of the element, $\phi(T_e)$ is the emission measure differential in temperature and the limits t_1 and t_2 represent the two temperature extremes of the plasma volume contributing to the line. The assumptions are as follows. The elemental abundance is assumed constant over the plasma depth. This allows us to separate the kernel function into the abundance, $\frac{N_{tot}}{N_H}$, and the contribution function $(G(T_e, N_e))$. The abundance is subsequently taken outside of the intensity integral. Here we have also explicitly noted the slight dependence of the contribution function on density. The plasma pressure is assumed constant over the temperature width of significant values of the $G(T_e, N_e)$ function. This method assumes a relationship between temperature and density, allowing us to change the variable of the integral

from the viewing volume to the electron temperature (Craig & Brown (1976)). Therefore, under these simplifications, we avoid the bi-variate integral dependent also on density and the $G(T_e, N_e)$ function can be assumed effectively dependent only on temperature. Finally, the function $\phi(T_e)$ is the average value of the differential emission measure over the viewed region and tells us something about the structure of the atmosphere at the temperature T_e. It is mathematically equivalent to the integral of the differential emission measure in density i.e.

$$\phi(T_e) = \int \phi(T_e, N_e) dN_e \tag{2.63}$$

If we have a series of line intensity observations and their corresponding $G(T_e, N_e)$ functions, we can attempt to invert the integral (2.62) to obtain the differential emission measure. Many inversion algorithms have been developed to do just this (Harrison & Thompson (1992)). As mentioned above, it is extremely difficult to produce meaningful results in the bi-variate case and the solution for the temperature dependent case is of limited value. (See chapter.5 for a discussion on the differential emission measure in temperature and its validity with regard to the solar atmosphere).

The predictive approach is more secure. If we have a plasma model we can produce a $\phi(T_e, N_e)$ function and combine it with calculations of $G(T_e, N_e)$'s to predict spectral line intensities. These can then be compared to the observations. In this way, we can gain physical insight into the processes which contribute to the formation of the individual spectral line intensities. Consequently, we can refine our theoretical models and attempt, ultimately, to match the observations. Note that a complete match will only ever tell us that our model provides one possible solution to the problem, not that it is correct.

Whichever approach is used, the line emission contribution function is required and this is expressed as,

$$G_{i\rightarrow j}(T_e, N_e) = A_{i\rightarrow j} \frac{N_H}{N_e} \sum_{\sigma=1}^{m_z} \frac{N_i^z}{N_e N_\sigma^z} \mid_{q.s.} \frac{N_\sigma^z}{N_{tot}} \mid_{eq.} \tag{2.64}$$

where $A_{i\rightarrow j}$ is the spontaneous transition probability for the transition $i \rightarrow j$, N_H is the hydrogen density and N_e is the electron density. $\sum_{\sigma=1}^{m_z} \frac{N_i^z}{N_e N_\sigma^z}$ represents the collisional-radiative calculation of the population dependence of the level, i, on the

metastables of the ionisation stage, z. This is computed in the quasi static approximation (see sec.2.2.2) and assumes that effective contributions to the population of the level i come only by excitation from the metastables, such that,

$$N_i^z = \sum_{\sigma=1}^{m_z} N_e N_\sigma^z f_{i\to\sigma}^{exc.} \tag{2.65}$$

The final part of eq. 2.64 describes the population distribution of the different ionisation stages using the assumption of equilibrium. It is possible to include a time dependent calculation here but this would be dependent on a temporal model and consequently would restrict the applicability of the contribution function and the differential emission measure. The temperature corresponding to the peak of the ionisation stage curves is often used as an estimate of the formation temperature for spectral lines emitted by an ion. An exploration of the influence of metastable states on the ionisation balance is conducted in chap.4.

The 'derived' quantities we refer to here, are calculated from the fundamental atomic collision cross-sections by taking account of level population density and collisional-radiative effects. Therefore, on final computation, they may be model dependent. Contribution functions ($G(T_e, N_e)$ functions) and equilibrium ionisation stage populations are included and photon emissivity coefficients are another example. Leaving aside problems associated with the spectrometer interpretation, e.g. errors in the intensity calibration, we can establish theoretical expressions that we can couple with our models to confront the spectral measurements.

In the astrophysics community it has often been the case that line intensity ratios are used as diagnostics of plasma density and temperature. For estimates of electron temperature, two lines which are sensitive to temperature are chosen. Then, the assumption is made that the temperature of the plasma is uniform over the region of emission. In theory this allows us to take the $G(T_e, N_e)$ function outside the integral in eq. 2.62, so that the intensity ratio becomes a ratio of excitation coefficients only, i.e.,

$$\frac{I_{i\to j}}{I_{k\to l}} = \frac{q_{g\to i}}{q_{g\to k}} \tag{2.66}$$

The excitation rate coefficients are not 'derived' in the same sense as described above

but are model dependent in that it is assumed that the distribution of electron velocities in the plasma is Maxwellian. Bearing this in mind we can proceed to recover a plasma temperature. The physical meaning of this temperature is probably obscured by the assumptions involved in the derivation. As pointed out by Lang, Mason & McWhirter (1990) the formulation of eq. 2.62 has already implicitly assumed something about the temperature dependence, for example, through the ionisation balance. It is also based on the assumption that the atmosphere is composed of concentric surfaces of constant temperature and pressure. Hubeny & Judge (1995) state that it is simply "the single temperature of an isothermal plasma that reproduces the observed intensity ratio". Whether the plasma is indeed isothermal is open for debate. Also, the technique may be uncertain due to the dependence on the ionisation balance fractions used. Therefore, it is more appropriate to consider the ratio between lines as being that between the full integrals of eq. 2.62. Evidently, the ratio is then independent of the abundance and is usually fairly insensitive to the ionisation balance calculations. As a result, moderate uncertainties in the technique can be partially removed.

For estimates of electron density it has been usual to take the ratio between lines, one of which arises from a metastable. Since metastables are collisionally disrupted, above some critical density, the ratio will also be sensitive to electron density. Collisional deexcitation of the metastables is much faster than radiative decay so lines originating from a metastable become more intense. Conversely, transitions terminating in a metastable have associated lines which are weaker. Eq. 2.66 is usually used for this also, except that the excitation coefficients are now density dependent. Our earlier assumption of constant pressure ensures that this line ratio technique can be used but once again the physical interpretation of the result is uncertain. Indeed, the work of Judge et al.(1997), mentioned above, implies that the inferred density is likely to be wrong and that more information on the structure being observed is needed to go any further. Nevertheless, line ratio techniques are still in widespread use. Order of magnitude estimates of plasma parameters can be useful in some circumstances, although more detailed studies are likely to benefit only from a predictive modelling approach. Clearly, the applications of the $G(T_e, N_e)$ function are widespread. For

astrophysical work it is of use to archive them at a range of plasma pressures, for use in differential emission measure and line ratio analyses.

Since it is often the line intensity that is required for observational comparison, we might ask whether mass production and collection of these is appropriate. In general, this is less helpful since they depend on both the metastable state populations of the individual ionisation stage, and also the stage to stage ionisation balance. The former may be computed from the quasi-equilibrium assumption and effective contributions to the dominant populations (see eq. 2.56) archived. This assumption is justified and is assured when an initial model for the dominant populations is specified. The assumption of ionisation balance is less secure. Generally it requires some model assumption about the nature of the plasma under investigation. It is probably more appropriate to treat this point as a reasonable cut-off between the calculation of purely fundamental atomic parameters, and subsequent model dependent data. In this work we treat photon emissivity coefficients as an intermediary class of data which facilitates the transfer from pure to applied data. These are temperature and density dependent (i.e. they are also derived) but are appropriate for archiving over suitable temperature and density ranges that are applicable to solar and fusion studies.

It is possible to identify photon emissivity coefficients for each process by extracting their contribution to the evolution of the dominant populations from eq. 2.65 (e.g. as in eq. 2.56 and see Summers et al.(1996) for a complete description). We can derive an expression for the line emissivity which allows us to pick out the photon emissivity coefficients. This proceeds as follows. If the line emissivity for a transition $i \rightarrow j$ is given by,

$$\epsilon_{i \rightarrow j} = A_{i \rightarrow j} N_i \tag{2.67}$$

then using eq. 2.65, with individual reaction components included, we get,

$$\epsilon_{i \rightarrow j} = A_{i \rightarrow j} \left(\sum_{\sigma=1}^{m_z} N_e N_\sigma^z f_{i \rightarrow \sigma}^{(exc)} + \sum_{\tau=1}^{m_{z+1}} N_e N_\tau^{z+1} f_{\tau \rightarrow i}^{(rec)} + \sum_{\tau=1}^{m_{z+1}} N_H N_\tau^{z+1} f_{\tau \rightarrow i}^{(cx)} + \sum_{\rho=1}^{m_{z-1}} N_e N_\rho^{z-1} f_{\rho \rightarrow i}^{(ion)} \right) \tag{2.68}$$

where the f's are effective contributions to the population of the excited state i due to excitation from the metastables, recombination from the parent ion, charge exchange

recombination from neutral hydrogen and ionisation from the $z-1$ ion. ρ, σ and τ index the metastable states of the $z-1, z$ and $z+1$ ions respectively. As a result the photon emissivity coefficients are defined as,

$$\mathcal{PEC}^{(exc)}_{\sigma,i\to j} = \frac{\left(A_{i\to j} f^{(exc)}_{i\to\sigma}\right)}{N_e} \tag{2.69}$$

for excitation

$$\mathcal{PEC}^{(rec)}_{\tau,i\to j} = \left(A_{i\to j} f^{(rec)}_{\tau\to i}\right) \tag{2.70}$$

for recombination

$$\mathcal{PEC}^{(cx)}_{\tau,i\to j} = \left(A_{i\to j} f^{(rec)}_{\tau\to i}\right) \tag{2.71}$$

for charge exchange recombination

$$\mathcal{PEC}^{(ion)}_{\rho,i\to j} = \left(A_{i\to j} f^{(ion)}_{\rho\to i}\right) \tag{2.72}$$

for ionisation. Examples of the behaviour of such coefficients are provided in chap.4.

Chapter 3

New Developments for Data Handling and Production within ADAS

3.1 Methods for Handling Data Entry

3.1.1 Bundling and Unbundling of Levels and Parents

In recent years the volume of fundamental atomic data output from large collision cross-section and atomic structure calculations has increased the requirements for computer storage space while placing a premium on methods for easing its use and also for allowing a physical focus to be maintained. For example, ADAS data format files *adf09* contain state selective dielectronic recombination coefficients for all terms up to principal quantum shell 7 supplemented with n-shell totals up to principal quantum shell n=1000 (see for example Badnell et al.(1993)). Given that the main interest in a particular study may well be in transitions involving highly populated low lying metastable states it seems sensible to provide some way of focusing attention on the transition in question, but at the same time, attempting to maintain the effects of the more sophisticated treatment of highly excited levels provided by these calculations.

The *condensation* methods of *collisional-radiative* theory, see for example Summers (1994), Summers & Hooper (1983), Dickson (1993) and sec.2.2.2, allow computation of metastable level populations by projecting on to them the influence of quasi-static equilibrium calculations of highly excited levels. As shown in chapter 2, and by the above authors, this technique can be generalised to arbitrary high and low level sets which, in effect, are bundled together. This allows compression of large data collections to more manageable sizes. Levels can be bundled in different ways. For example, grouping together according to the recombining parent ion on which they were built, by the spin system to which they belong or by levels of the same term. These techniques can be beneficial to users in handling large quantities of data when studying the excited populations of complex ions.

However, bundling without a physical basis is unrealistic and any method must pay great attention to the atomic processes contributing to spectral emission. Summers & Dickson (1992) pointed out the conflicting requirements of a full theoretical description of recombination in plasmas. Evidently, as is obvious from the example above, very high n-shells can contribute to the total effective recombination coefficient. This is principally due to dielectronic recombination and its efficiency in populating very highly excited states. At such high quantum shells the effects of fields and other particles cannot be ignored (Burgess & Summers (1969)). A proper theoretical treatment of dielectronic recombination therefore requires detailed calculation for these highly excited levels. When dealing with the population structure of an ion these results can only be included using many level handling techniques such as *'bundle-n'* and *'matrix condensation'* (Summers (1974)). However, sophisticated treatment of emitting states is essential for spectroscopic studies and these transitions generally involve low lying levels labelled by an explicit coupling scheme. Here, *'bundle-n'* is not appropriate but it may be useful to perform some grouping of minor populations especially if they have little influence on the spectra being studied.

The key issue here is awareness of the physical model. Whether the study is of dielectronic recombination coefficients or population distributions of low lying levels any bundling method must maintain consistency between the requirements of the atomic structure models, the data handling and prediction of the dominant emission.

Bundling need not be confined to levels. In ionisation and recombination reactions it is proper to distinguish metastable states as well as ground states as potential initial states for recombination and final states for ionisation. Parent states of the recombining ion, which drive the population structure calculations, should be identified and included explicitly in any ionisation balance. These parents could be bundled together in order to focus attention on the parent ground state. This might be useful if there was a wish to ignore the complexities of metastables, or if full account was being taken of J-resolved metastable components in the input dataset but LS term resolution was required.

Evidently during transient events in dynamic plasmas the dominant emission from a heavy impurity ion, such as molybdenum, is principally that due to the highest ionisation stages of the ion (Badnell et al.(1996)). In such a case it is computationally unnecessary to attempt to model the ground and metastable population distributions for every ionisation stage. It is more appropriate to concentrate on the stages that are observed and to bundle together lower charge states. In addition, it may be beneficial to bundle together terms of the same principle quantum shell which are likely to be ionised simultaneously, for example those which have roughly similar ionisation potentials.

Resolution of the dominant populations is an important consideration. For light ions the metastables are LS terms, whilst for highly ionised ions the excitation energy separations between J components are such that they may be true levels. Our work, developed in the fusion context at JET, takes account of LS resolved metastable states and parents. Consequently derived quantities such as ionisation balance are treated in LS coupling. However, in the astrophysical context J-resolved datasets are sought even for light species. This situation is motivated by the available spectral resolution in the two regimes. The spectral resolution of the Normal Incidence Spectrometer on the CDS instrument is ~ 0.08Å depending on the wavelength (Domingo, Fleck & Poland(1992)). This compares favourably with KT7 the VUV spectrometer at JET which has a spectral resolution of between 0.5 and 4Å also dependent on the wavelength (Maggi(1996)). Therefore CDS will actually see J-resolved subcomponents of emission lines and they may require appropriate data to assist them.

Generation of such data is another concern. However, resolution of all transitions between J-components does not necessarily imply the need for a full J-resolved treatment of ionisation balance. Some awareness of consistency between fundamental and derived data is desirable here. Generation of LS coupled data collections is often performed by reassembling the J-resolved counterparts. The LS resolved datasets are then consistent with the J-resolved ones and duplication of effort in the atomic collision calculations can be avoided. The reassembling is done by bundling together J-resolved levels of the same term.

Bundling in this way can be of great value, to fusion plasmas, by making use of high quality calculations of effective collision strengths in the J-resolved form which are produced primarily for astrophysical use. Computer codes to calculate these, by transforming the reactance matrices obtained from LS coupling or including relativistic terms in the Hamiltonian before solution of the time independent Schroedinger equation, are now widespread. The first method referred to is that used in the JAJOM code of Saraph(1972) & Saraph(1978), and the second method is that of Scott & Burke (1980) which is now possible with RMATRX1 (Berrington, Eissner & Norrington (1995)).

In one direction then the capability exists to take a dataset and alter its resolution to the benefit of another application. However, there are broader applications and issues to be considered. The CDS and SUMER communities wish to have J-resolved data but would it be useful to have an approximate reverse '*unbundling*' routine to take advantage of calculations targeted at JET and the fusion community? If so, how accurate would the technique be compared to other calculations, in producing J-resolved effective collision strengths? How can the bundling methods outlined be extended to coping with J-resolved metastable parents or ionisation stage populations?

Essentially the answer to the first question is yes. The Abingdon atomic data assessment meeting (Lang et al.(1994)) recommended producing J-resolved data for all ions of all species. Clearly this is an enormous computational task. However, 'fill in' data, especially if the technique is proven to be fairly accurate, would be very welcome in astrophysical circles. Approximate data accurate to within 30% say

could be used as effectively for spectroscopic diagnostics as **R**-matrix data which normally has comparable errors. Within ADAS 'top up' Born approximation data (Summers(1992)) has already proven to be in surprisingly good agreement with **R**-matrix data (Brooks et al.(1997)).

Apart from the ability to react to the observational data from CDS and SUMER, unbundling of terms to produce level data allows us to have a 'quick look' at new data and see whether a J-resolved treatment is necessary. Rather than blindly mass produce atomic data for everything, we can make our studies more specifically targeted towards the astrophysics and fusion communities' needs, and, as a consequence, connect more closely with experimental results.

As for the third question, coping with J-resolved parents when the data are available is not a serious problem. An alteration to the information conventions in the ADAS specific ion file should allow the use of not only J-resolved parents but also arbitrary ones. This has already been implemented in the ADAS codes (for a full description of the specific ion file (adf04) see Summers, Brooks et al.(1996)). A detection routine flags the parent type (LS, LSJ or arbitrary) to the other routines and some minor modifications to the data gathering codes deal with the alteration. A more serious concern is in resolving the initial recombining J-parent or the final ionisation target in the first place.

Bundling together ionisation stages to focus on the more important populations has not been included as yet. However, it does not present a serious computational problem and can also be used to enable 'unresolved' ionisation stage population data to be reconstructed from the metastable resolved counterpart.

As a first step towards implementing such ideas as data entry utilities within ADAS, two codes have been developed. ADAS209 is a general purpose level bundling program which assists in controlled grouping of effective collision strengths for levels and/or parents (provided parent information is available in the adf04 files). ADAS210 is a general purpose level unbundling program which does the reverse i.e. it assists in splitting effective collision strengths for levels and parents.

Our approach has an advantage over an automatic splitting and grouping routine in that it introduces a level of flexibility which would otherwise be unavailable.

This flexible bundling and unbundling ability allows us to target specific studies by controlled expansion and contraction of data collections and by partially merging resolution levels to the degree we require. In this way we can take advantage of the best available data while reducing the computational load. In addition, bundling and unbundling of the parent metastable states helps us to retain control of the resolution employed in derived calculations and hence to achieve our objective of consistency. As with the level calculations it makes it easier for us to switch between coupling schemes and to 'work at different resolution levels'.

Background Theory

Consider again the electron impact excitation reaction defined in chapter 2.

$$X_i^{+z}(E_i) + e(\epsilon_i) \rightarrow X_j^{+z}(E_j) + e(\epsilon_j) \tag{3.1}$$

If we now consider a transition I to J in LS coupling, then the *'LS bundled'* effective collision strength is a summation over the effective collision strengths between J-resolved fine structure levels, such that,

$$\Upsilon_{IJ} = \sum_{i \in I} \sum_{j \in J} \Upsilon_{ij} \tag{3.2}$$

Spontaneous emission coefficients (Einstein A-values) corresponding to the new *'bundled'* transitions are given by,

$$A_{J \rightarrow I} = \sum_{i \in I} \sum_{j \in J} \omega_j A_{j \rightarrow i} / \omega_J \tag{3.3}$$

where,

$$\omega_J = \sum_{j \in J} \omega_j \tag{3.4}$$

The new bundled parent energies, relative to the lowest level of the recombining ion, are calculated in the same way as for the excitation energies of each of the excited levels of the X^{+z} ion, such that,

$$E_{J \rightarrow I} = \sum_{i \in I} \sum_{j \in J} \omega_j E_{j \rightarrow i} / \omega_J - E_{shift} \tag{3.5}$$

where E_{shift} denotes the relative change in energy between the original and bundled ground states of the X^{+z} ion. The statistical weights are summed as for the levels above. Now consider the reaction

$$X_I^{+z}(E_I) + e(\epsilon_I) \rightarrow X_J^{+z}(E_J) + e(\epsilon_J) \tag{3.6}$$

this time between two excited terms I and J, of an ion X^{+z}, of an element X. In this case, E_I (E_J) is the excitation energy of level I (J), and ϵ_I (ϵ_J) is the incident (scattered) electron energy. If we have high precision calculation data for the effective collision strength associated with this transition, we can obtain an *'LSJ resolved'* effective collision strength corresponding to the fine structure transition, $i \in I$ to $j \in J$, in intermediate coupling. We should note that while a proper representation of the angular momentum of the terms of the ion, X^{+z}, is possible in LS coupling (for low charge ions) or jj-coupling (for high charge ions), this is not true of intermediate coupling. The Hamiltonian of the system is not nearly diagonal and so off-axis contributions to the eigenvalues must be included to specify the level energies (Cowan (1981)). However, it is still possible to obtain an approximation of the angular momentum characteristics of the J-resolved levels, since the total angular momentum, J, is still a good quantum number. This can only serve as a label since the true wavefunction will be a mixture of pure coupling functions and it will be assigned by choosing the eigenvector whose contribution dominates. Notwithstanding that, we find LSJ a convenient choice for intermediate coupling in our circumstances, and will use hereafter.

Returning to our problem. We can use two methods to calculate the J-resolved effective collision strength. Firstly, we may already have lower quality data at LSJ resolution. If so, we can bundle this data and then form a ratio with our new data to use as a premultiplier to our lower quality data i.e. we normalise the J proportions of our lower quality data to that of our higher quality data. Therefore,

$$\Upsilon_{ij}^{Jn} = \Upsilon_{ij}^{Jo}\Upsilon_{IJ}^{LS}/\Upsilon_{IJ}^{BLS} \tag{3.7}$$

where Υ_{ij}^{Jn} denotes the new LSJ effective collision strength, Υ_{ij}^{Jo} denotes the lower quality LSJ value, Υ_{IJ}^{LS} is the high quality LS resolved value and Υ_{IJ}^{BLS} is the bundled

lower quality value and is given by,

$$\Upsilon_{IJ}^{BLS} = \sum_{i\in I}\sum_{j\in J}\Upsilon_{ij}^{Jo} \tag{3.8}$$

The spontaneous emission coefficients (Einstein A-values), can be calculated in a similar manner such that,

$$A_{j\to i}^{Jn} = A_{j\to i}^{Jo}(A_{J\to I}^{LS}/A_{J\to I}^{BLS}) \tag{3.9}$$

where,

$$A_{J\to I}^{BLS} = \sum_{i\in I}\sum_{j\in J}A_{j\to i}\omega_j^{Jo}/\omega_J^{BLS} \tag{3.10}$$

with Jo and Jn referring to the lower quality J-resolved data and the new data respectively, and, superscript LS referring to the higher quality LS resolved data. In this case, the statistical weights have been included with similar markings, and

$$\omega_J^{BLS} = \sum_{j\in J}\omega_j^{Jo} \tag{3.11}$$

Secondly, if we do not have any LSJ data for a particular transition, it is appropriate to use a statistical splitting method similar to that of Saraph, Seaton & Shemming (1969). The A-values are zeroed in this case and the upsilons are given by,

$$\begin{aligned}&\Upsilon(^{2S+1}L_J,{}^{2S'+1}L_{J'})\\ &= \sum_J\sum_{J'}\left(\frac{2J+1}{(2L+1)(2S+1)}\right)\left(\frac{2J'+1}{(2L'+1)(2S'+1)}\right)\Upsilon(^{2S+1}L,{}^{2S'+1}L')\end{aligned} \tag{3.12}$$

To unbundle the parent metastables we require an additional LSJ resolved dataset for the recombining ion. If available, the parent energies and statistical weights pass directly from it. The energies are always adjusted to account for the energy shift relative to the lowest level of the ion.

3.1.2 Overview of ADAS209 (General Level Bundling)

Summary of Program and Processing Linkages

ADAS interactive programs make use of an IDL widget based interface to FORTRAN algorithms and subroutines. The schematic of the ADAS209 code (Fig. 3.1) shows

the linkages between the two processes. ADAS209 has a standard three screen structure, file selection, processing of user choices and output of results. These screens correspond to the three boxes down the left of the diagram. Communications between the two processes take place via a bidirectional UNIX pipe set up by IDL as an interface buffer from the standard input/output units of FORTRAN to variable free logical units located by IDL. The IDL procedure spawns the FORTRAN process and then performs repeated checks on its status and on the interactions between them. This is in order to prevent any 'hanging' of the program due to *'unsynchronised communication'*.

After selecting ADAS209 from the main system menu the standard ADAS dataset entry widget appears (see fig.3.2). Here a specific ion file of type adf04 is entered either from the central ADAS database or alternatively from the users' own space. The data root is displayed in a text widget which becomes editable after selecting '*Edit Path Name*' with the mouse cursor. Data files and subdirectories contained within the directory entered in this field, are displayed in a data file selection window below. Scroll bars appear if the number of files exceeds the window size. A data file is selected by highlighting with the mouse cursor. The name of the chosen file is displayed in the selection window above, and once it has been read in, the comments appended to the dataset can be viewed by clicking on the *'Browse Comments'* button with the mouse. All adf04 type files contain information about the data they hold and how, and by whom, it was prepared. ADAS209 itself generates information about the processing options chosen by the user and appends it to the tail of its own output file which is of type adf04 also (see fig.3.6). Clicking on *'Done'* instructs the code to proceed to the next window.

The next 'pop-up' is the *'Processing Options'* widget (see fig.3.3). This displays information from the selected adf04 file and allows the user to enter their bundling allocations. At the top left of the screen are the processing option switches, level or parent bundling. Below this the adf04 file name is displayed for information followed by a *'Browse Comments'* button which repeats the facility of the previous window. Below this, the ion and charge and the nuclear charge of the atom, are also displayed. A transcript of the level list obtained directly from the adf04 file, is presented with

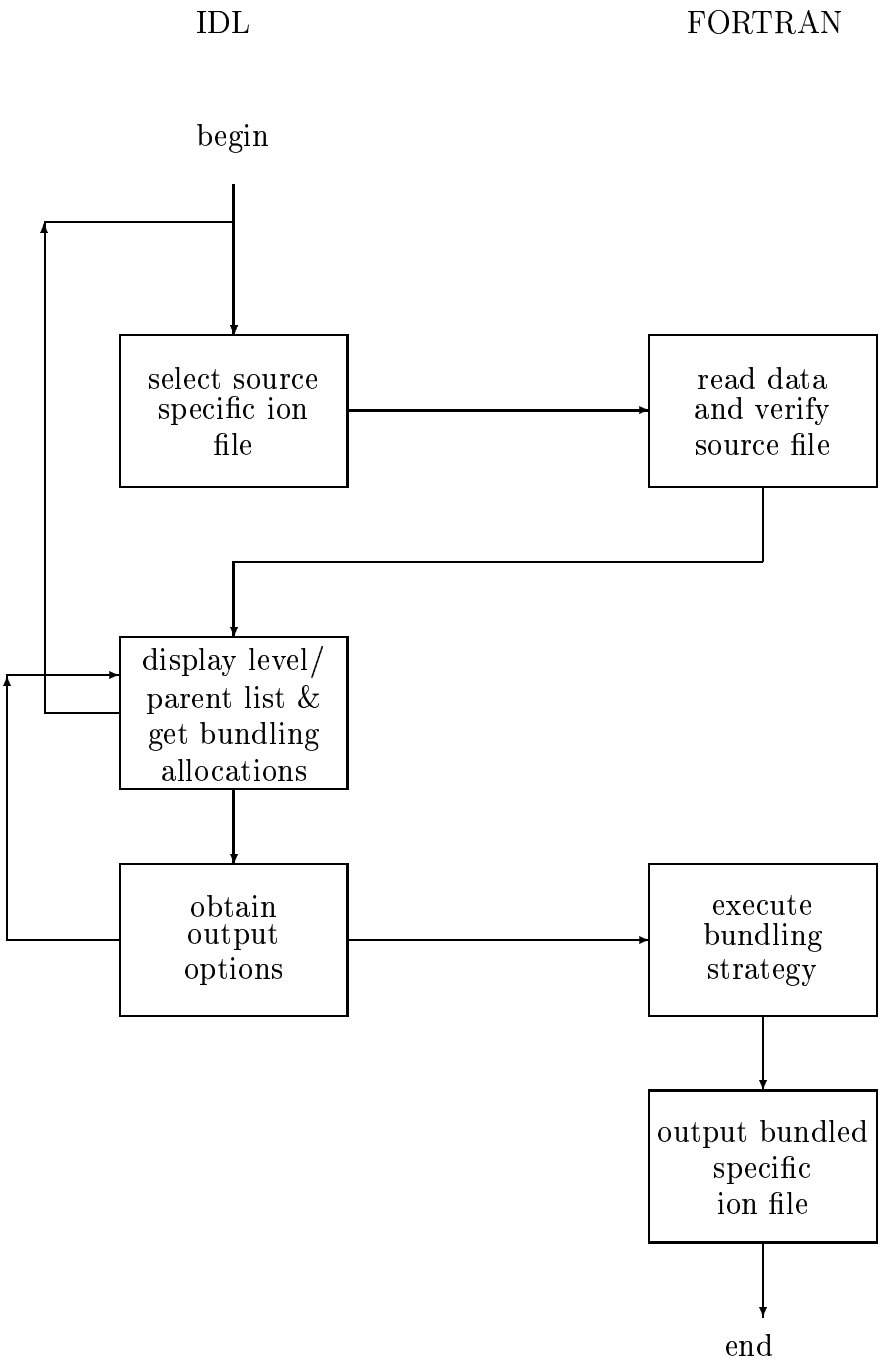

Figure 3.1: Schematic of ADAS209 program and processing linkages. The left hand boxes correspond to the IDL user interface windows. The right hand ones correspond to the FORTRAN processes.

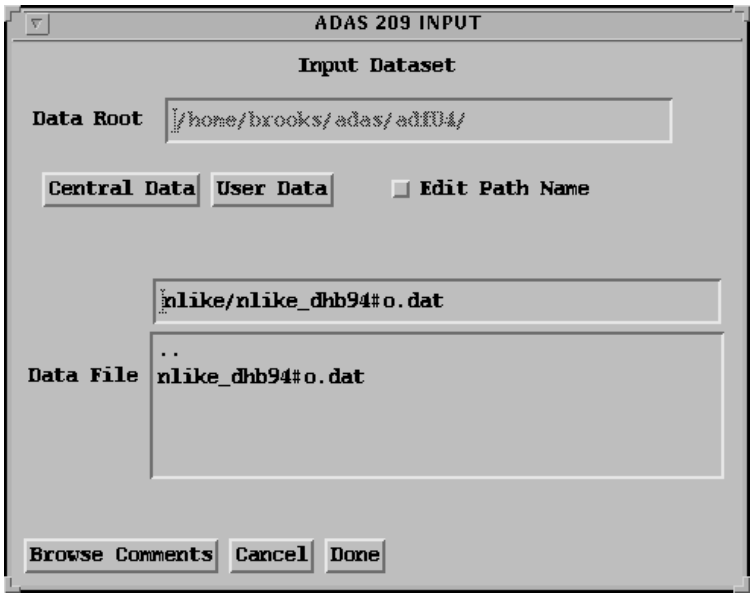

Figure 3.2: ADAS 209 input options - example widget screen. See text for explanation of use.

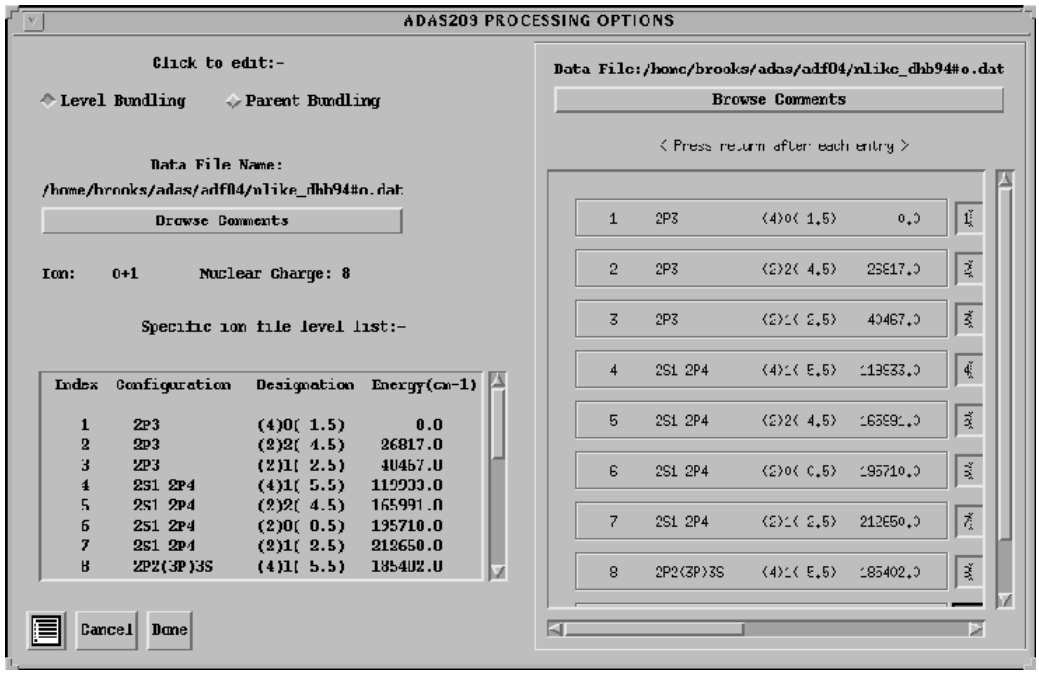

Figure 3.3: ADAS 209 processing options - example widget screen. See text for explanation of use.

a moveable slider, to its right, which allows quick scanning. For ADAS209 the level list is only present for supplementary information. In ADAS210 it is essential to the processing choices. Below this list are the *'Cancel'* and *'Done'* buttons. The bitmap icon to the left of the *'Cancel'* button is an automatic return to ADAS series 2 menu button. On the right hand side of the screen the data file name and *'browse comments'* button are again present. Below them are multiple columns containing the entire level list from the adf04 source file. Each level is displayed with its ordered list index, the configuration, the designation and the level energy. The designation is the usual (2S+1)L(J) quantum numbers of the Russel-Saunders specification for the level. The energy is displayed in cm^{-1}. To the right of each level is an editable text entry box. A decision is made here as to which levels to group together and a group index number is entered in each box along side each of the chosen levels. Thus levels to be bundled together are given the same group index. If no entry is made, it implies that the level is to be retained as an individual and it is allocated a default group value of zero.

If the Parent bundling option is chosen, the window changes to a display of information about the recombining ion parent metastables in the dataset. The new window is almost identical in appearance to that which is displayed for the level list(see fig.3.3). However, this time each parent is shown with an index, its term in brackets, its statistical weight and finally its energy relative to the lowest level of the recombined ion (in cm^{-1}). Thus, in the case of a single parent it is just the ionisation potential. This information is present on the top line of the adf04 data set from which it is obtained. Such data are present only in the advanced adf04 specification. An example is given in fig.3.6. Up to four parent entries are allowed. There is only one, the default, if the advanced adf04 file specification is not being used. Each parent is displayed with its parent energy and must belong to one of three strictly formatted resolution types. These are *'term parents'* with code '*<2S+1>L*', *'level parents'* with code *'<2S+1>L<2J+1>'* and unidentified parents with code *'<statistical weight>'*. The latter occur when mixed symmetry metastable parents are combined for example when the configuration interaction is strong. The recombining ion parent metastables

can be bundled with no direct influence on the standard adf04 file as it contains transition probability and electron collisional excitation coefficients for transitions only between the low level set of a single ionisation stage. However, in advanced population structure studies it is essential to do this properly in order to assemble effective coefficients for calculating stage to stage quantities correctly. In the advanced specification adf04 files, effective zeta parameters assign proportions of ionisation from each of the levels to each of the identified parents. Practical operation of the widget is as for the level bundling. It is not essential to select *'Parent Bundling'* but if this option is ignored a default (^1S) is entered and this may be incorrect. In these circumstances it is advisable to check the top line of the output adf04 file.

N.B. It is essential to press return after each entry in order to register selections with the widget event handling routines. Also, grouping together levels with the value zero clashes with the default options and results in no bundling taking place.

After completing the processing options, clicking on *'Done'* proceeds to the *Output Options* window (see fig.3.4). This window simply allows naming and placing of the output file. Once again the source data file name is displayed accompanied by a *'Browse Comments'* button. Below this is an 'activation' button labelled *'File Output'*. Clicking on this button sensitises the other buttons in the widget. Any filename and directory can be entered in the *'File Name :'* editable text box, but the usual ADAS convention is to store the data in a *'bundle.pass'* file. This is the default file which appears on clicking the '*Default File Name*' button. The code attempts to place this file in the directory '/home/user/adas/pass', so users must create a directory '/pass' to enable use of this facility. The *'Replace'* button only comes into effect when the user already has a file of the same name. Activating *'Replace'* overwrites the older file, while not activating it produces a pop-up warning if the file already exists. Clicking on *'Done'* completes the program and returns the user to the ADAS system menu.

The levels/parents are bundled according to the entries given and information about the options chosen is written in the output adf04 file. The adf04 file produced is fully structured and can immediately enter the ADAS database. It follows the advanced adf04 formatting if the source file was of this specification. The code is

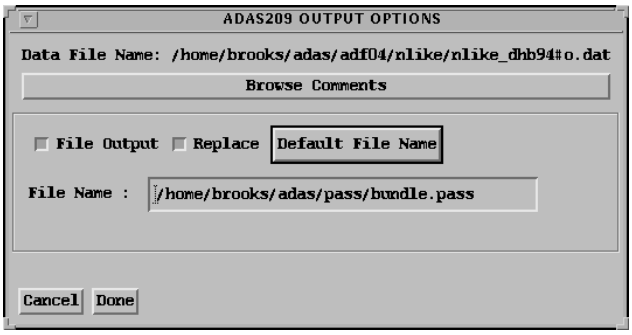

Figure 3.4: ADAS 209 output options - example widget screen

arranged to allow bundling of any levels. However, this can lead to a number of technical complexities. The principal problem occurs if the energies of the levels of a bundle occur on either side of the energy of a target level for spontaneous emission. In these circumstances the output adf04 file should be checked and ADAS209 issues a warning. The code outputs two divisions of the transition with reversed upper and lower indices: firstly, bundled transitions from the target level to lower energy levels of the group; secondly, bundled transitions from higher energy levels, of the group, to the target level. Due to the symmetry of Υ these can simply be added, but the spontaneous emission coefficients will be incorrect in the latter case. This is due to wrong assignment of the 'true' bundled upper statistical weight. Therefore, these should be deleted.

Example of Use

As an example, consider the LSJ resolved dataset for *Be-like* O^{+4} shown in fig.3.5. The file contains effective collision strengths calculated from the fit parameters to **R**-matrix data provided by Kato, Lang & Berrington (1990). The object in this example was to produce an LS resolved dataset using ADAS209. Therefore, all LSJ levels have been bundled together to form LS terms e.g. $2s2p\ ^3P_{0,1,2} \rightarrow 2s2p\ ^3P$. The output file is shown in fig.3.6.

The convention is to preserve the configuration label of the lowest level contributing to the bundle. In addition, a $*$ is added at the start of the designation to indicate this. At the tail of each output file the original indexing of levels is shown and below this the grouping selections are displayed. For parent metastables, the original terms are given along with the selection vector. Information about the program, the source file, and the date that the file was produced are also given. Since, as in this example, we would normally be bundling a J-resolved file to produce an LS resolved one, a header is printed with this additional information. The producer id is generally entered by hand.

Note that the parent metastable on the top line is (^1S). This is the default which is entered if no further information is available and is incorrect in this case. It is essential to check the parent configurations in an output dataset when the full parent options in the processing codes ADAS209 or ADAS210 are not used.

A further example is shown in fig.3.7. This shows both input and output datasets. The original file contains **R**-matrix data, in LS coupling, from McLaughlin & Bell (1994) for *N*-like O^{+1}. There are four parent metastable terms for this ion which are $1s^22s^22p^2\ ^3P$, ^1D, ^1S and $1s^22s2p^3\ ^5S$. The file is laid out according to the advanced adf04 specification. Thus, to the right of each level of the list are final parent indices and effective zeta parameters. The parent indices are the numbers in brackets and refer to the index of the final parent metastable state after ionisation from the level. The adjacent numbers give the proportions of the total electron count available, which go to particular parents. The last part of the transition list of the file contains radiative and dielectronic recombination data with the code 'R' in the first column. These data are bundled consistently with the parents in like manner.

```
O + 4         8         5        918657.
   1  2S2(1S0)     (1)0( 0.0)          0.0
   2  2S2P(3P0)    (3)1( 0.0)    81942.5
   3  2S2P(3P1)    (3)1( 1.0)    82078.6
   4  2S2P(3P2)    (3)1( 2.0)    82385.3
   5  2S2P(1P1)    (1)1( 1.0)   158797.7
   6  2P2(3P0)     (3)1( 0.0)   213462.5
   7  2P2(3P1)     (3)1( 1.0)   213618.2
   8  2P2(3P2)     (3)1( 2.0)   213887.0
   9  2P2(1D2)     (1)2( 2.0)   231721.4
  10  2P2(1S0)     (1)0( 0.0)   287910.3
  11  2S3S(3S1)    (3)0( 1.0)   546972.7
  12  2S3S(1S0)    (1)0( 0.0)   561276.4
  13  2S3P(1P1)    (1)1( 1.0)   580824.9
  14  2S3P(3P0)    (3)1( 0.0)   582806.4
  15  2S3P(3P1)    (3)1( 1.0)   582843.1
  16  2S3P(3P2)    (3)1( 2.0)   582920.3
  17  2S3D(3D1)    (3)2( 1.0)   600748.9
  18  2S3D(3D2)    (3)2( 2.0)   600758.9
  19  2S3D(3D3)    (3)2( 3.0)   600779.2
  20  2S3D(1D2)    (1)2( 2.0)   612615.6
  -1
 5.00    3             2.50+04 5.00+04 1.25+05 2.50+05 5.00+05 1.25+06 2.50+06 5.00+06
   2   1   1.00-30    6.79-02  5.99-02  4.99-02  4.23-02  3.40-02  2.27-02  1.52-02  9.18-03
   3   1   2.17+03    2.04-01  1.80-01  1.50-01  1.27-01  1.02-01  6.81-02  4.55-02  2.75-02
  ...
  19  17 1.00-30     1.55+00 1.57+00 1.25+00  9.33-01 6.54-01  3.85-01   2.52-01  1.62-01
  19  18 1.00-30     3.30+00 3.26+00 2.90+00 2.41+00 1.85+00 1.17+00  7.79-01  4.93-01
  -1
  -1  -1
C-----------------------------------------------------------------------------------------------------------------
C
C  The effective collision strengths are calculated using the fit
...
C  this comparison (above) is unaffected.
C
C                                D.H.Brooks 16.08.95
C-----------------------------------------------------------------------------------------------------------------
```

Figure 3.5: ADAS 209 example input dataset. This is of adf04 type as are fig.3.6 and fig.3.7 and a description of the format is given in Summers et al.(1996)

```
O + 4        8       5  918657.0(1S)
   1 2S2(1S0)      *(1)0( 0.0)          0.0  {1}1.000
   2 2S2P(3P0)     *(3)1( 4.0)    82233.9  {1}1.000
   3 2S2P(1P1)     *(1)1( 1.0)   158797.7  {1}1.000
   4 2P2(3P0)      *(3)1( 4.0)   213750.2  {1}1.000
   5 2P2(1D2)      *(1)2( 2.0)   231721.4  {1}1.000
   6 2P2(1S0)      *(1)0( 0.0)   287910.3  {1}1.000
   7 2S3S(3S1)     *(3)0( 1.0)   546972.7  {1}1.000
   8 2S3S(1S0)     *(1)0( 0.0)   561276.4  {1}1.000
   9 2S3P(1P1)     *(1)1( 1.0)   580824.9  {1}1.000
  10 2S3P(3P0)     *(3)1( 4.0)   582881.9  {1}1.000
  11 2S3D(3D1)     *(3)2( 7.0)   600766.4  {1}1.000
  12 2S3D(1D2)     *(1)2( 2.0)   612615.6  {1}1.000
  -1
 5.00    3            2.50+04 5.00+04 1.25+05 2.50+05 5.00+05 1.25+06 2.50+06 5.00+06
   2   1  7.23+02    6.12-01  5.39-01  4.49-01  3.80-01  3.06-01  2.05-01  1.37-01  8.26-02
   3   1  2.86+09    2.63+00 2.67+00 2.81+00 3.02+00 3.36+00 4.03+00 4.68+00 5.44+00

  11   4 3.00-30     2.13+00 1.85+00 1.33+00  9.09-01 5.53-01  2.55-01  1.38-01  7.50-02
  11  10 3.00-30     5.25+01 5.70+01 8.07+01 1.06+02 1.32+02 1.61+02 1.77+02 1.89+02
  -1
  -1  -1
C-----------------------------------------------------------------------------------------------------------------------
C
C  File generated by compression of a J-resolved file
C
C  Program: ADAS209
C
C  Source file: /export/home/adas/adas/adf04/belike/belike_dhbj95#o.dat
C
C  Original level indexing:
C     1   2   3   4   5   6   7   8   9  10
C    11  12  13  14  15  16  17  18  19  20
C  Selection Vector:
C     1   2   2   2   3   4   4   4   5   6
C     7   8   9  10  10  10  11  11  11  12
C
C  Original parent metastables:
C    (1S)
C  Parent bundling vector:
C     0
C  Insert producer id here: D.H.Brooks
C  Date: 19/03/96
C-----------------------------------------------------------------------------------------------------------------------
```

Figure 3.6: ADAS 209 example output dataset

```
O + 1        8        2      283244.0(3P) 303310.(1D) 326222.(1S) 343357.(5S)
   1    2P3          (4)0( 1.5)           0.0   {1}3.00   {4}1.250
   2    2P3          (2)2( 4.5)    26817.0   {1}2.250 {2}0.622 {3}0.128
   3    2P3          (2)1( 2.5)    40467.0   {1}2.250 {2}0.622 {3}0.128
   4    2S1 2P4      (4)1( 5.5)   119933.0   {1}1.500 {4}2.500
   ...
  23    2P2(3P)3D             (2)3( 6.5)   232889.0   {1}1.00
  -1
 2.00    3             8.00+03 2.00+04 4.00+04 8.00+04 2.00+05 4.00+05 8.00+05
   2   1   9.70-05     1.37+00 1.40+00 1.46+00 1.53+00 1.58+00 1.51+00 1.27+00
   3   1   4.80-02     4.10-01  4.31-01 4.61-01  4.97-01  5.28-01  5.05-01  4.15-01
   ...
  10   7  1.00-30     4.44-03   5.19-03 5.65-03  6.02-03  6.27-03  6.17-03  5.69-03
R  1   +1              5.58-13   3.99-13 2.59-13  1.90-13  1.40-13  9.13-14  6.30-14
   ...
R 21   +4              1.00-30   1.00-30 1.00-30  1.00-30  1.00-30  1.00-30  1.00-30
  -1
  -1  -1
C-----------------------------------------------------------------------------------------------------
C  LS-resolved effective collision strengths for OII
C  ------------------------------------------------------------
C  This file contains new effective collision strength data for all transitions ...
C  ...Radiative & Dielectronic recombination data from wjd92#o.dat unchanged.
C                                                    DH Brooks         22.11.94
C-----------------------------------------------------------------------------------------------------
```

```
O + 1        8        2   305437.7(3P)
   1   2P3          (4)0( 1.5)           0.0   {1}4.250
   2   2P3          (2)2( 4.5)    26817.0   {1}3.000
  ...
  22   2P2(3P)3D  (2)2( 4.5)   234434.0   {1}1.000
  23   2P2(3P)3D  (2)3( 6.5)   232889.0   {1}1.000
  -1
 2.00    3             8.00+03 2.00+04 4.00+04 8.00+04 2.00+05 4.00+05 8.00+05
   2    1 9.70-05      1.37+00 1.40+00 1.46+00 1.53+00 1.58+00 1.51+00 1.27+00
  ...
  10   7 1.00-30      4.44-03  5.19-03  5.65-03  6.02-03   6.27-03 6.17-03  5.69-03
  -1
  -1  -1
C-----------------------------------------------------------------------------------------------------
C  File generated by compression of a J-resolved file
C  Program: ADAS209
C  Source file: /home/brooks/adas/adf04/nlike/nlike_dhb94#o.dat
C  Original level indexing:
C    1   2   3   4   5   6   7   8   9  10
C   11  12  13  14  15  16  17  18  19  20
C   21  22  23
C  Selection Vector:
C    0   0   0   0   0   0   0   0   0   0
C    0   0   0   0   0   0   0   0   0   0
C    0   0   0
C  Original parent metastables:
C   (3P)   (1D)   (1S)   (5S)
C  Parent bundling vector:
C    1      1      1      1
C  Insert producer id here:D.H.Brooks
C  Date: 19/03/96
C-----------------------------------------------------------------------------------------------------
```

Figure 3.7: Output example of bundled parents

In this case, the aim was to show parent bundling, therefore, all the parents have been grouped together to obtain only an effective ground state, ^3P. The first line of the output file contains the resolution type label discussed above. This will include a weight parameter for LSJ and arbitrary resolution types. However, in this case the parent metastables are LS terms. The labelling convention for bundling parents is to preserve the 'resolution type'. Therefore, in this example, since the aim was to group together all parent metastables to obtain only an effective ground state, the output bundled parent label is an LS term ^3P. The effective ionisation potential of the bundled parents is given for all resolution types. Finally, the selection details are presented at the tail of the file, as above.

3.1.3 Overview of ADAS210 (General Level Unbundling)

Summary of Program and Processing Linkages

A schematic of the linkages between the FORTRAN and IDL processes, for the ADAS210 code, is shown in fig. 3.8. ADAS210 presents a very similar appearance to ADAS209. It has the standard ADAS three screen structure, file selections, processing of user selections and output of results. However, there are additional requirements for this code. Since a template dataset is required to provide the approximate J-resolved split up fractions, there are two input datasets, namely, the one to unbundle, and the template. In addition, to unbundle the parent metastables, a further J-resolved template dataset relating to the parent ion is required. A facility within ADAS210 seeks to locate this automatically. The code checks the user's own space and if no data is available the central ADAS database. For example, if the template file *copss#be/copss#be_ss#o4j.dat* is selected then the code searches for *copss#li/copss#li_ss#o5j.dat*. It first looks in */home/<username>/adas/adf04* and afterwards in */home/adas/adas/adf04/*.

In the diagram, the three boxes of solid outline to the left correspond to the three screens. The dashed box on the left represents the search mechanism. It is possible to omit the parent template file, provided no attempt is subsequently made to unbundle the parents. The dashed box on the right represents the optional reading of this file.

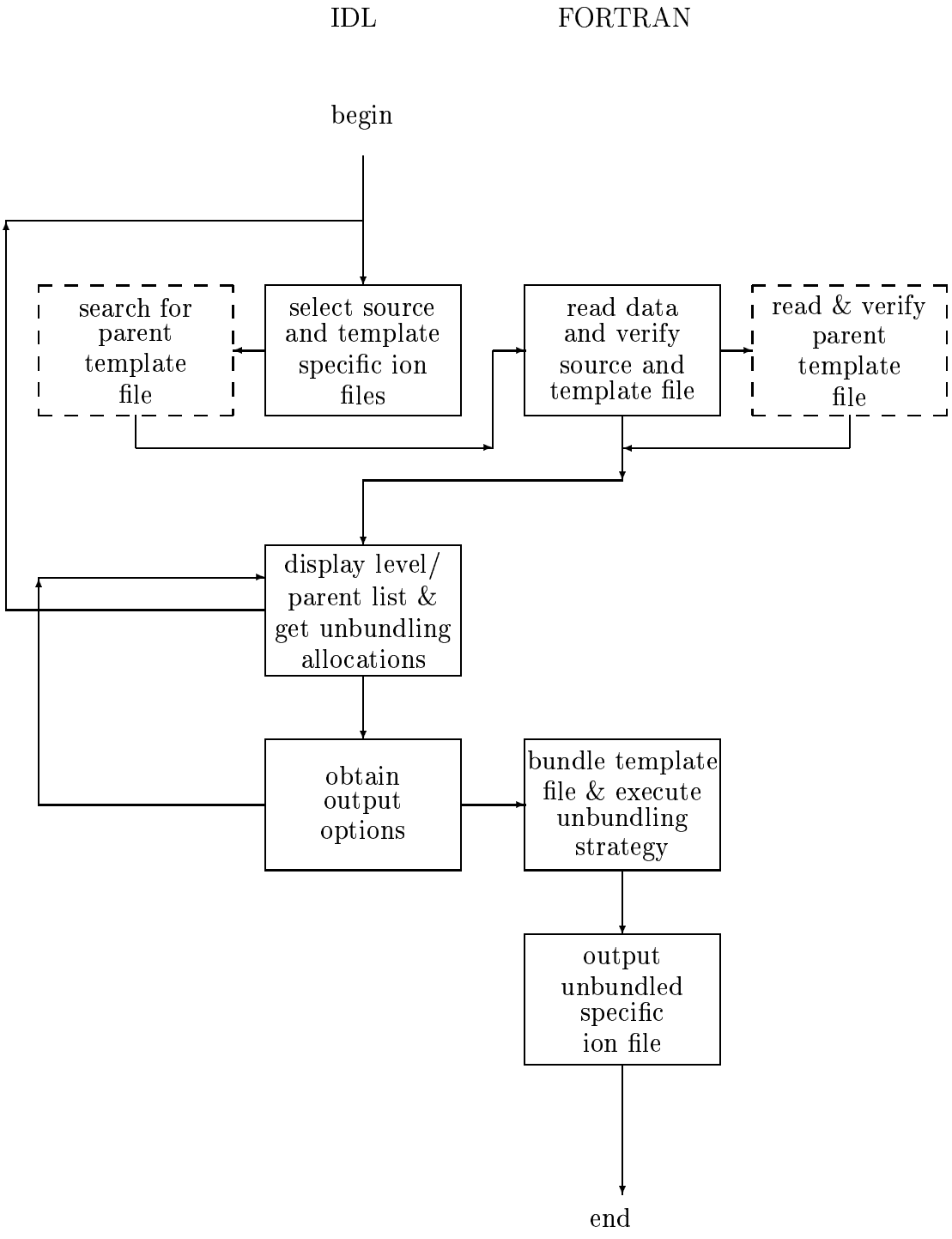

Figure 3.8: Schematic of ADAS210 program and processing linkages. The left hand boxes correspond to the IDL user interface windows. The right hand boxes correspond to the FORTRAN processes. The dashed boxes represent the parent template search.

Since we require to select two datasets, the input options screen for ADAS210 contains two data entry widgets. Each follows the standard individual widget used in ADAS209, except that a *'browse comments'* button appears for each dataset (see fig.3.9).

The upper widget is used for entry of the specific ion file to be unbundled. Access to the central ADAS database or individual user spaces follows the same operation as described for ADAS209. The *'Browse Comments'* button below the selection list refers to this dataset. The lower widget is used for entering the J-resolved dataset to be used as the template for splitting the file. Source file collections for this normally come from mass produced high resolution SUPERSTRUCTURE files, hence the information line *'Select Superstructure file for Template'*. Such files are present in the central adf04 directory in subdirectories according to isoelectronic sequence (e.g.*copss#b*). Intermediate coupling files have the termination 'j.dat'. It is not essential to use files produced by the SUPERSTRUCTURE code but the file naming conventions must be strictly adhered to for the search mechanism to locate the parent template correctly. After selecting the files, clicking on *'Done'* proceeds to start the automatic parent template search and if the parent file is located the program proceeds without interruption. A 'pop-up' warning will appear if the search fails, but it is possible to continue regardless.

The *'Processing Options'* widget is similar in appearance to that of ADAS209. The options are to unbundle the levels or the parents. The same information as in ADAS209 is displayed in the left side window. The *'Browse Comments'* button here refers to the file the user wishes to unbundle, as does the level list below it. The right side window is different from ADAS209. Firstly, the *'Browse Comments'* button now refers to the template file. In the case of level unbundling, the multiple columns are filled with the level information from the template file. As with ADAS209, group indices are entered in the editable text boxes next to each level. In this case the index of the level to unbundle is entered in the boxes adjacent to each of the J-resolved levels to be used for the split up fractions (see example screen). No entry implies that the level is to be left alone. Fig.3.10 is an example of the parent unbundling screen,

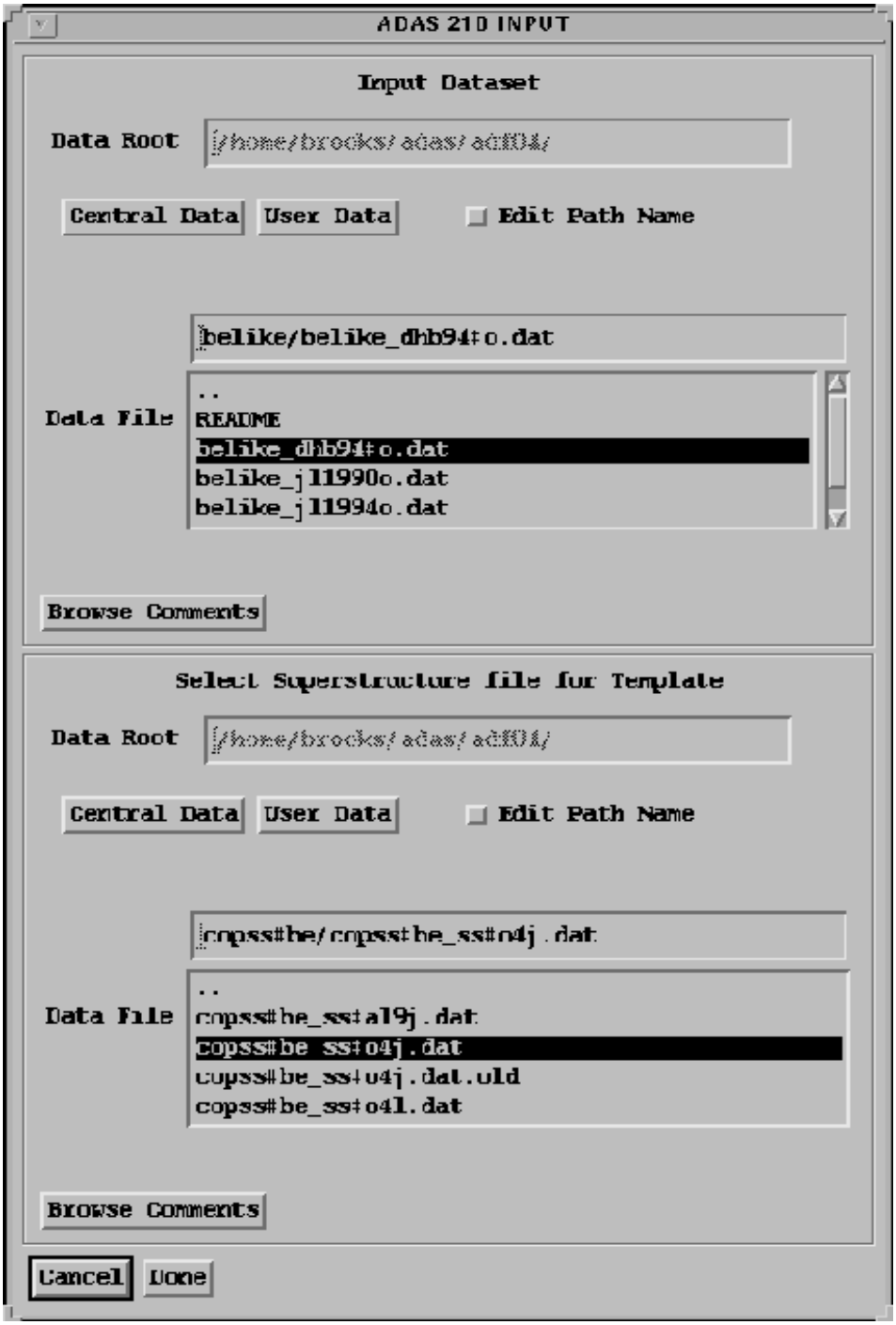

Figure 3.9: ADAS 210 input options - example widget screen. See text for explanation of use.

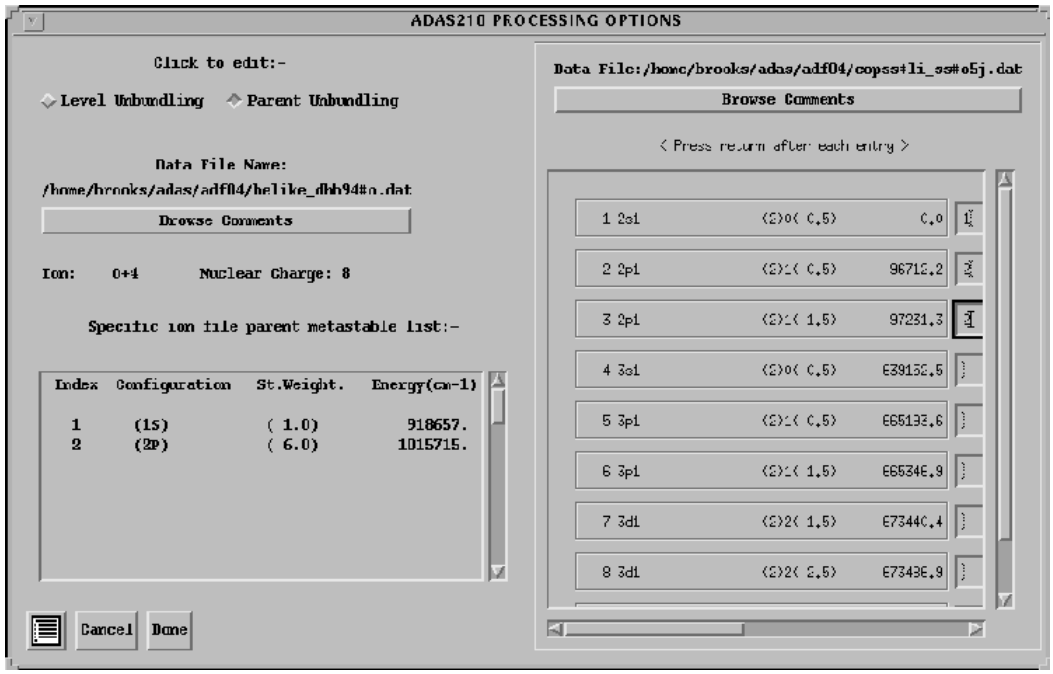

Figure 3.10: ADAS 210 processing options - example widget screen. See text for explanation of use.

and the difference applies here too. The multiple columns contain the level information from the parent template dataset rather than the input file, as was the case in ADAS209. The example screen also shows that the parent level list is transcribed directly from the parent template file. Therefore, the information presented is exactly the same as in the level list i.e. index, configuration, designation and energy. **N.B.** Expanding the number of parent metastables to greater than five is not supported by the ADAS structure. If the user attempts to do this a 'pop-up' warning will appear.

The final screen displayed is for entry of the *'Output Options'*. This widget is the same as in ADAS209 (see fig.3.4). There is no graphical display so only naming and placing of the output file is required. In this case the default output file name is *unbundle.pass*. The code attempts to place this in the directory */home/<username>/adas/pass* so it is essential to create this directory in advance.

The levels/parents are unbundled according to the processing entries and information about the options chosen is written in the output adf04 file. This file is suitable for entry to other ADAS routines such as ADAS205 etc, and is of the advanced formatting type if the source adf04 file was too. **N.B.** In some cases it may appear that transitions have disappeared from the file on output. In fact, the SUPERSTRUCTURE code does not contain forbidden transitions, such as $J = 0 \rightarrow 0$ or $\Delta J = 2$, with very small cross-sections. ADAS210 deliberately splits terms according to the data available in the high resolution file so, in this case, it omits these transitions.

Examples of Use

The example in fig.3.11 shows unbundling of an LS resolved dataset for *Be-like* O^{+4} to produce an LSJ resolved *'unbundle.pass'* file. The input file was created by bundling an LSJ resolved one. In fact it is the output file from the first *Example of Use* for ADAS209 (see fig.3.6). Notice the mix of configuration types in the level list. Some are preserved from the input file e.g. $2s^2\ ^1S$ and others are transcribed from the template dataset e.g. $2s12p1$. The latter type are the ones that have been unbundled. At the tail of the file, information is given about the selections made. The *Source file* is the input dataset and the *Template file* is the high resolution SUPERSTRUCTURE dataset. The *Template File indexing* and the *Source File Assignment* vectors provide

```
O + 4        8        5   918657.0(1S)
   1 2S2(1S0)     (1)0( 0.0)           0.0
   2 2s1 2p1      (3)1( 0.0)    82544.5
   3 2s1 2p1      (3)1( 1.0)    82698.1
   4 2s1 2p1      (3)1( 2.0)    83007.2
   5 2S2P(1P1)    (1)1( 1.0)   158797.7
   6 2p2          (3)1( 0.0)   215600.0
   7 2p2          (3)1( 1.0)   215755.1
   8 2p2          (3)1( 2.0)   216059.3
   9 2P2(1D2)     (1)2( 2.0)   231721.4
  10 2P2(1S0)     (1)0( 0.0)   287910.3
  11 2S3S(3S1)    (3)0( 1.0)   546972.7
  12 2S3S(1S0)    (1)0( 0.0)   561276.4
  13 2S3P(1P1)    (1)1( 1.0)   580824.9
  14 2s1 3p1      (3)1( 0.0)   582531.6
  15 2s1 3p1      (3)1( 1.0)   582569.6
  16 2s1 3p1      (3)1( 2.0)   582640.4
  17 2s1 3d1      (3)2( 1.0)   601247.4
  18 2s1 3d1      (3)2( 2.0)   601262.9
  19 2s1 3d1      (3)2( 3.0)   601286.1
  20 2S3D(1D2)    (1)2( 2.0)   612615.6
  -1
 5.00    3          2.50+04 5.00+04 1.25+05 2.50+05 5.00+05 1.25+06 2.50+06 5.00+06
   3   1 2.17+03   6.12-01  5.39-01 4.49-01  3.80-01  3.06-01  2.05-01  1.37-01  8.26-02
   5   1 2.86+09  2.63+00 2.67+00 2.81+00 3.02+00 3.36+00 4.03+00 4.68+00 5.44+00
   ...
  18  15 2.26-30  1.31+01 1.42+01 2.01+01 2.65+01 3.30+01 4.02+01 4.42+01 4.72+01
  18  16 7.44-31  4.38+00 4.75+00 6.74+00 8.84+00 1.10+01 1.34+01 1.47+01 1.57+01
  19  16 3.00-30  2.45+01 2.67+01 3.77+01 4.95+01 6.17+01 7.52+01 8.28+01 8.83+01
  -1
  -1  -1
C-----------------------------------------------------------------------------------------------------------------------
C  File generated by expansion of an LS-resolved file
C  Program: ADAS210
C
C  Source file: /disk2/brooks/adas/adf04/belike/belike_dhbl95#o.dat
C  Template file:
C  /disk2/brooks/adas/adf04/copss#be/copss#be_ss#o4j.dat
C
C  Template File indexing:
C     1    2    3    4    5    6    7    8    9   10
C    11   12   13   14   15   16   17   18   19   20
C    21   22   23   24   25   26   27   28   29   30
C    31   32   33   34   35   36   37   38   39   40
C    41   42   43   44   45   46
C  Source File Assignment:
C     0    2    2    2    0    4    4    4    0    0
C     0    0    0   10   10   10   11   11   11    0
C     0    0    0    0    0    0    0    0    0    0
C     0    0    0    0    0    0    0    0    0    0
C     0    0    0    0    0    0
C  Original parent metastables:
C  Parent unbundling vector:
C
C  Insert producer id here:D.H.Brooks
C  Date: 08/02/96
C-----------------------------------------------------------------------------------------------------------------------
```

Figure 3.11: ADAS 210 example output dataset. This is of adf04 type as is fig.3.12 and a description of the format is given in Summers et al.(1996)

a complete record of the unbundling selections made. If any selections were made, the *Original parent metastables* and the *Parent unbundling vector* are printed. If an LSJ parent level is selected then the configuration and statistical weight are printed on the top line. Note that in this case the statistical weight is equal to 2J+1. Finally, the identifier of the user should be entered by hand and the current date is printed for completeness.

Next we illustrate the use of ADAS209 and ADAS210 together to vary the resolution levels in a particular study. The object is to identify which transitions dominate. We have used the same dataset for O^{+4}, at LS resolution, as in the earlier example for ADAS210. In this case, since we might expect the metastable level $2s2p\ ^3P$ to have a significant influence, we have unbundled it to determine the possible effects of J-resolution. In addition, we have bundled all the levels above $2p^2\ ^3P$, to see whether we can avoid treating them in any greater detail.

The layout of the file is the same as before. Note that the bundled level 6 retains the configuration specification of the lowest level and that the bundled statistical weight is now very large (25.0). From the file we can see that electrons captured into level 6 will find it relatively easy to decay by spontaneous emission, or electron collisions, to the levels $2s2p\ ^3P_1$ and $2s2p\ ^1P_1$, from which they have an intercombination and electric dipole pathway to the ground level, respectively. In LS coupling, the levels that are significantly populated are the ground ($2s^2\ ^1S$) and metastable ($2s2p\ ^3P$), but at a first glance, in LSJ we might suggest that, due to their inability to decay to the ground level, $2s2p\ ^3P_0$ and $2s2p\ ^3P_2$ are likely to become the dominant levels of the metastable.

Finally, it is interesting to compare the results of the unbundling code ADAS210 with a high quality LSJ resolved calculation. From the 'Example of use' in ADAS210, we can compare our unbundle.pass file with the original LSJ data. Fig.3.13 shows a comparison between the unbundled effective collision strengths and the original ones for some transitions whose spectrum lines are identified as useful for studies by CDS and SUMER. In most cases they will be used for differential emission measure analysis of the quiet sun but the $2s2p\ ^3P_1$-$2s^2\ ^1S_0$ transition is useful for dynamic studies and observations of sunspot oscillations since it is sensitive to the electron

```
O + 4        8            5    918657.0(1S)
   1 2S2(1S0)         (1)  0( 0.0)           0.0   {1}1.000
   2 2s1 2p1          (3) 1( 0.0)      82544.5   {1}1.000
   3 2s1 2p1          (3) 1( 1.0)      82698.1   {1}1.000
   4 2s1 2p1          (3) 1( 2.0)      83007.2   {1}1.000
   5 2S2P(1P1)        (1) 1( 1.0)     158797.7   {1}1.000
   6 2P2(3P0)        *(3) 1(25.0)     483048.0   {1}1.000
  -1
 5.00    3          2.50+04 5.00+04 1.25+05 2.50+05  5.00+05  1.25+06 2.50+06  5.00+06
   3   1 2.17+03 6.12-01  5.39-01  4.49-01  3.80-01  3.06-01   2.05-01  1.37-01   8.26-02
   5   1 2.86+09 2.63+00 2.67+00 2.81+00 3.02+00  3.36+00 4.03+00  4.68+00  5.44+00
   6   1 1.72+09 8.78-01  8.46-01  7.90-01  7.52-01  7.44-01   7.86-01   8.57-01  9.49-01
   ...
   6   3 4.63+08 1.77+01 1.75+01 1.75+01 1.85+01 2.00+01  2.30+01  2.54+01  2.76+01
   6   4 1.00+09 3.74+00 3.57+00 3.23+00 2.96+00 2.85+00  3.13+00  3.67+00  4.39+00
   6   5 4.62+09 1.54+01 1.49+01 1.48+01 1.54+01 1.68+01  1.94+01  2.16+01  2.38+01
  -1
  -1  -1
C-----------------------------------------------------------------------------------------------------------------------------
C  File generated by compression of a J-resolved file
C
C  Program: ADAS209
C  Source file: /disk2/brooks/adas/pass/unbundle.pass
C
C  Original level indexing:
C     1   2   3   4   5   6   7   8   9   10
C    11   12   13   14
C  Selection Vector:
C     0   0   0   0   0   1   1   1   1   1
C     1   1   1   1
C
C  Original parent metastables:
C    (1S)
C  Parent bundling vector:
C     0
C  Insert producer id here:D.H.Brooks
C  Date: 13/02/96
C-----------------------------------------------------------------------------------------------------------------------------
```

Figure 3.12: Example of Merged Resolution Levels

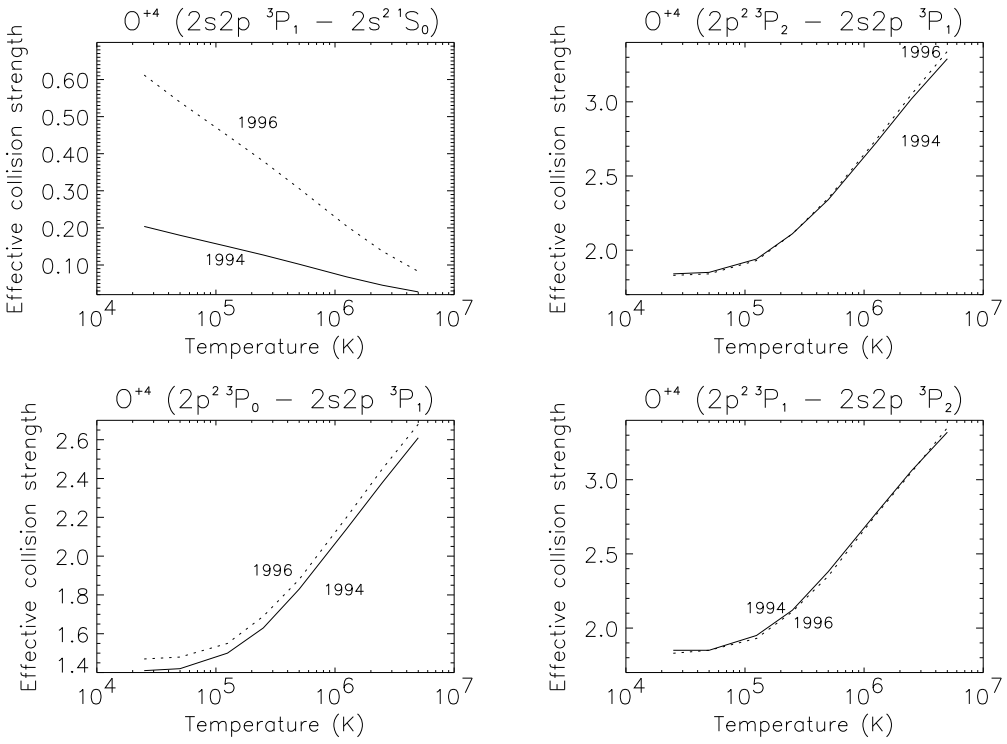

Figure 3.13: Comparison of Effective Collision Strengths produced by ADAS210 to higher quality calculation. The solid lines labelled 1994 are the higher quality data in this case from Kato et al.(1990). The dotted lines labelled 1996 are the results using the unbundling code ADAS210.

density due to its low radiative transition probability. In fact, it is this transition which is the least accurate of the examples shown. However, this is exactly as we would expect. Spin changing transitions are forbidden in LS coupling so the SUPERSTRUCTURE code does not contain this transition. Hence, using data output from it as the template will not allow us to unfold such transitions. However, for a light ion such as oxygen, the configuration interaction between the $2s2p\ ^1P$ and $2s2p\ ^3P$ levels is such that the $2s2p\ ^3P_1 - 2s^2\ ^1S_0$ transition has a slight dipole contribution. Therefore, SUPERSTRUCTURE will 'fill in' approximately with less accurate values roughly following this effect. In this case it mimics this behaviour by using the $2s2p\ ^1P_1$-$2s^2\ ^1S_0$ electric dipole transition data. We can 'see' this if we return to

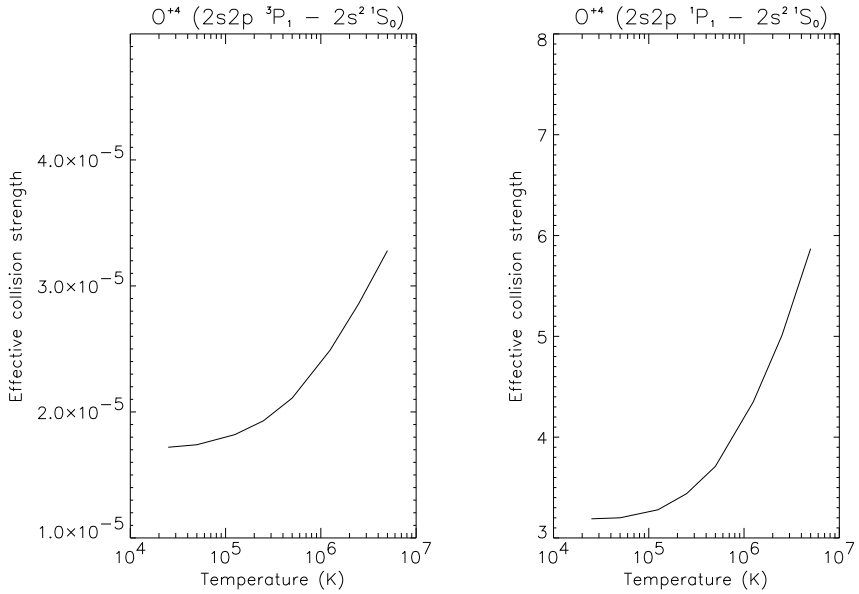

Figure 3.14: Original SUPERSTRUCTURE data

the SUPERSTRUCTURE dataset. Fig.3.14 shows the effective collision strengths for these two transitions plotted against temperature. The data comes from the file *copss#be_ss#o4j.dat*. For a spin changing transition we would expect the value of Υ to fall off at high temperature. Instead notice the broadly similar behaviour for both transitions imposed by SUPERSTRUCTURE. The upturn at high temperatures is typical of dipole transitions and behaves like $dln(4\epsilon_i^2/\Delta E_{ij})$, where $d = 4\omega_i f_{ij}/\Delta E_{ij}$, ϵ_i is the incident electron energy, ΔE_{ij} is the transition energy, ω_i is the statistical weight of the level i and f_{ij} is the optical oscillator strength (Henry (1981)). The unbundled effective collision strength for this transition only reproduces the original data to within a factor of 3 (see top left graph in fig.3.13).

The largest discrepancy for the three other transitions presented in fig.3.13 is for the $2p^2\ ^3P_0 - 2s2p\ ^3P_1$ transition at low temperature ($\sim 3.10^4 K$)(see bottom left graph in fig.3.13). Here the disparity is still only 4.2%, and in the other two transitions (see top right and bottom right graphs) it is less than 2% for all temperatures. These are all magnetic dipole transitions since the total orbital angular momentum does

not change. We can conclude from this that, as expected, using the SUPERSTRUCTURE data is a good method for unbundling electric dipole allowed transitions but inappropriate for unbundling spin changing ones.

3.1.4 Atomic Data Verification

Introduction

Appropriate handling of large quantities of data is essential for general studies and for focusing attention on dominant transitions, but there are many circumstances in which it is necessary to assess and check the validity of individual atomic collision cross-sections in greater detail. In procuring data from the general literature it is often a source of annoyance to find transcription errors and inconsistencies between data generation and publication. Simple methods for determining data accuracy, comparing with previous calculations and uncovering errors can be extremely useful.

For example, it is important when assessing new data to ensure that any extrapolation procedures used, correctly describe the high energy behaviour of the cross-sections. One method of doing this is to remove the energy dependence completely by plotting a comparison ratio between the data and an adjustable expected approximate form. Such a ratio is sometimes referred to as the *'reduced* Ω*'*, where Ω refers to the collision strength. A *'reduced* Ω*'* plot of this type is generally slowly varying and any unusual resonance or bad point appearance should be more easily detectable. Henry (1981) discussed the limiting behaviour of cross-sections for different transition types and through his work we can obtain reasonable approximate forms.

Another problem is that at high energies the number of partial waves which have an influence on the calculation of the total cross-section increases. This happens through their contribution to the individual partial cross-sections in the expansion of the total cross-section. A lack of convergence of the expansion results and the total cross-section falls off too rapidly at high energy if insufficient partial cross-sections are included in the calculation.

An example of each of these two effects was given by Burgess & Tully (1992). Firstly, they looked at the Υ data of Pradhan, Norcross & Hummer (1981). These

authors failed to reproduce the expected high energy limit point as they did not ensure that the coefficient of the dominant logarithmic term was correctly related to the gf value (see eq. 8 in Burgess & Tully (1992) and also the expression for the limiting behaviour used for electric dipole transitions below). Secondly, they mention the paper by Christensen, Norcross & Pradhan (1985) who corrected the lack of convergence in their distorted wave calculation, of the cross-section for the $Fe^{+14}(3s^2\ ^1S - 3s3d\ ^1D)$ transition, produced by only including partial waves up to $l = 11$. After including partial waves up to $l = 50$ their results changed from 'dropping off' at high energy and instead tended more accurately to the Born limit calculated by Burgess & Tully (1992).

Finally, it is usual when modelling the excited populations of ions in astrophysical and laboratory plasmas to assume that the electron distribution is Maxwellian. In such circumstances the excitation and de-excitation rate coefficients are expressible as functions of the Maxwell averaged collision strength Υ (also referred to as the *'effective collision strength'* or *'rate parameter'*, see chap.2, eq. 2.26). Therefore, it is convenient, at this point, to calculate Υ and to perform a check on its validity.

ADAS series 1 implements techniques to tentatively verify cross-sections and rate coefficients. It also provides a mechanism to flexibly enter data, in the variety of forms present in the literature, into a standard archiving structure for future entry to the central ADAS database. ADAS101 deals with entry and validation of electron impact excitation cross-sections and display and conversion to effective collision strengths. It also includes an ADAS graph editor for quick removal of bad points and immediate updated processing of alterations by the user. ADAS102 similarly allows validation of the calculated Υs and was recently included in ADAS.

Opinions differ on the best way to verify atomic data individually so ADAS101 has been set up to allow the use of different analysis methods. Presently, two have been included. The first is the type of analysis used at JET (the *'ADAS option'*) and the second is an implementation of the technique developed by Burgess & Tully (1992) (the *'Burgess option'*). The interactive capabilities of IDL prove very appealing when confronted with problems associated with quick plot adjustments and immediate updating of interpolated splines.

Background Theory

It is only possible for the electron impact excitation reaction (2.24) to take place if $\epsilon_i \geq \Delta E_{ij}$, where $\Delta E_{ij} = E_j - E_i$. Therefore, we can introduce a *'threshold parameter'*, $X = \epsilon_i / \Delta E_{ij}$ which ranges from 1, at the excitation energy threshold, to ∞. The reaction, (3.1), is described by a cross-section which is expressible either in terms of the incident electron energy, ϵ_i, the scattered electron energy, $\epsilon_i - \Delta E_{ij}$, or the threshold parameter.

Cross-section data can be obtained from the literature in many forms. ADAS internally converts all types into collision strengths, Ω_{ij}, tabulated as a function of X using the relationships defined in sec.2.2.1. In subsequent ADAS routines, rate coefficients are stored as effective collision strengths. It is common also in the literature to provide the atomic transition probabilities in the form of the *'line strength'*, the *'absorption oscillator strength'* or the *'spontaneous emission coefficient'*. These are related by

$$A_{j \to i} = \frac{\alpha^4 c}{2a_0} \left(\frac{\Delta E_{ij}}{I_H} \right)^2 \frac{\omega_i}{\omega_j} f_{i \to j} = \frac{\alpha^4 c}{6a_0} \left(\frac{\Delta E_{ij}}{I_H} \right)^3 \frac{1}{\omega_j} S_{ij} \tag{3.13}$$

where $\alpha^4 c / 2a_0 = 8.0323 \times 10^9 s^{-1}$. ADAS accepts each of these forms. For our comparison graph we can identify three types of transition for which we have simple approximate forms which show the correct asymptotic behaviour. These are dipole, non-dipole and spin change, and the functions we use are,

1. dipole: $\Omega_{ij} \approx F_3 S_{ij} \ln(X + F_2)$
2. non-dipole: $\Omega_{ij} \approx F_3 + F_2 / X$
3. spin change: $\Omega_{ij} \approx F_3 / (X + F_2)^2$

where F_2 and F_3 are constants. For the dipole case $F_3 = 4/3$. A plot of the ratio of our data to our approximate form, should therefore have a value ~ 1. It is convenient also to map our threshold parameter directly onto the range [0,1] by introducing a *'reduced X'* such that $X_r = 1 - 1/X$.

The theory behind the method of Burgess & Tully (1992) is described in great detail in their paper. However, the reduced comparison plots and transition type high

energy behaviours are broadly similar to those discussed above. Reduced collision strengths and energies are calculated using transition type specific scaling rules and the asymptotic behaviours are expressed as functions of electron energy. The main difference is the introduction of an adjustable parameter C which allows a more accurate least squares fit to the simplified data to be obtained essentially by rescaling in the x-direction. The authors' idea was to provide data compaction by reducing the data to five points obtained by a representative spline fit. They also wished to extend this technique to calculation and storage of Upsilons (see the ADAS manual for details of this). Here we are only concerned with the fitting of Ω_{ij} and computation of Υ_{ij}.

Burgess & Tully (1992) distinguish four transition types which also correspond to those identified in ADAS. The fourth, not mentioned so far, is referred to as *'semi-forbidden'* or *'other'* and is associated with very small oscillator strengths. The limiting behaviours are

1. electric dipole: $\Omega_{ij} \approx const.\ln(E)$
2. non electric dipole, non exchange: $\Omega_{ij} \approx const.$
3. exchange: $\Omega_{ij} \approx const./E^2$

And, the scaling rules are,

Type 1 : Dipole

$$x = 1 - \frac{\ln C}{\ln\left(E_j/E_{ij} + C\right)}$$
$$y(x) = \frac{\Omega_{ij}}{\ln\left(E_j/E_{ij} + e\right)}$$

such that $x \in [0,1]$ for $E_j \in [0,\infty]$, $y(0) = \Omega_{ij}(0)$ and $y(1) = 4\omega_i f_{ij}/E_{ij}$.

Type 2 : Non-Dipole

$$x = \frac{\left(\frac{E_j}{E_{ij}}\right)}{\left(\frac{E_j}{E_{ij}} + C\right)}$$
$$y(x) = \Omega_{ij}$$

such that $y(0) = \Omega_{ij}(0)$. Burgess & Tully(1992) also point out that $y(1)$ can be obtained through Born approximation.

Type 3 : Exchange

$$y(x) = \left(\frac{E_j}{E_{ij}} + 1\right)^2 \Omega_{ij} \tag{3.14}$$

here x is as for type 2 and $y(0)$ again equals $\Omega_{ij}(0)$ and $y(1)$ is difficult to obtain.

Type 4 : Other

$$y(x) = \frac{\Omega_{ij}}{\left(\frac{E_j}{E_{ij}} + C\right)} \tag{3.15}$$

here x is as for type 1 and $y(0) = \Omega_{ij}(0)/\ln C$ and $y(1)$ is as for type 1.

Adjustment of C will alter the approximate form and re-evaluation of the least squares fit is necessary. In the case of type 1, $C > 1$, while in types 2,3 & 4 $C > 0$.

3.1.5 Overview of ADAS101 (Electron Impact Excitation Cross Section)

Summary of Program and Processing Linkages

A schematic diagram of the linkages between the FORTRAN and IDL processes, in ADAS101, is shown below. Due to the complexity of the code and the number of potential pathways through it, this diagram appears quite intricate. However, it does follow the standard ADAS sequential structure discussed previously. The boxes down the left hand side of the diagram represent each of the IDL interactive screens. The first is the archive option selection screen which replaces the usual input screen although it is broadly similar in appearance and use. The second is the processing options screen, which acts as the primary data entry utility. The third is the output options screen, at which point selection of an analysis option must be made. The fourth is the interactive editable graph screen, which replaces the usual plot screen, and finally, a display plot of the calculated upsilons. The dashed boxes in the diagram show the alternative path taken when the Burgess analysis is chosen.

The input options screen has the same data file entry widgets as discussed previously for ADAS209 and ADAS210. However, its functionality and purpose are slightly different and it has an additional feature in that data file selection can be over-ridden. The main point is that users enter data, analyse it, and decide how to store, maintain

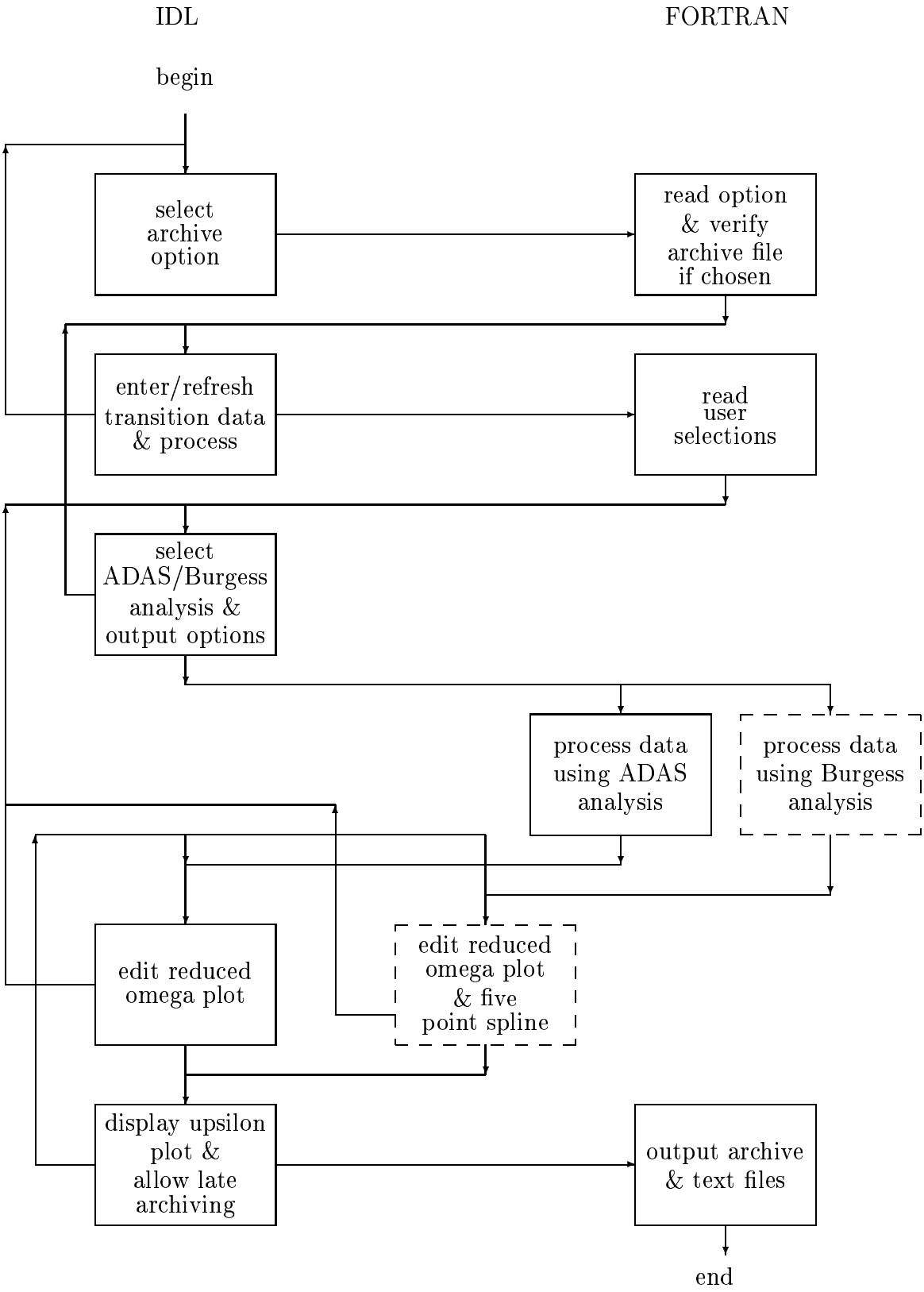
IDL
FORTRAN
begin
select archive option
read option & verify archive file if chosen
enter/refresh transition data & process
read user selections
select ADAS/Burgess analysis & output options
process data using ADAS analysis
process data using Burgess analysis
edit reduced omega plot
edit reduced omega plot & five point spline
display upsilon plot & allow late archiving
output archive & text files
end

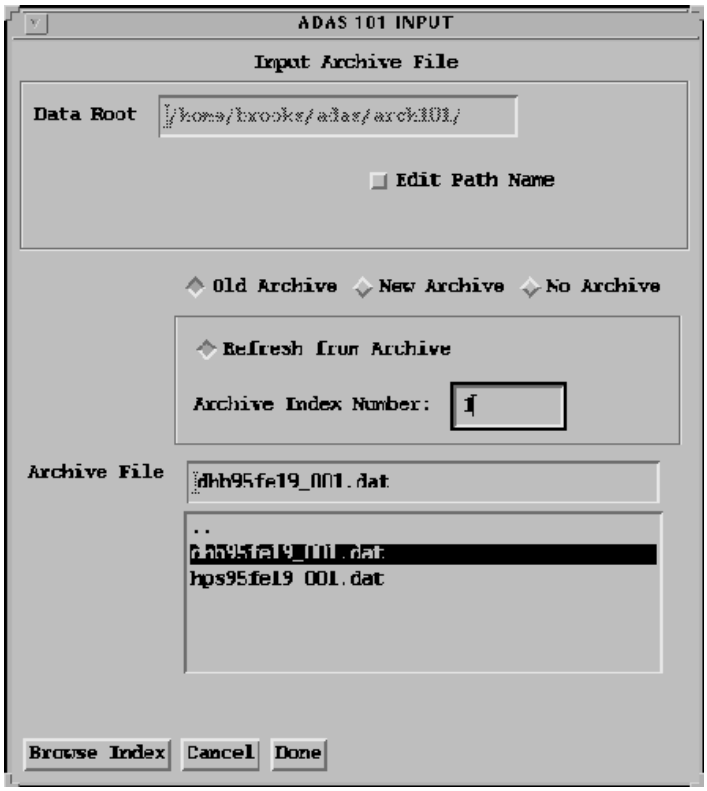

Figure 3.16: ADAS 101 input options - example widget screen. See text for explanation of use.

and update their individual databases. ADAS101 provides an archiving facility to deal with this need but there is no central ADAS database for this routine. There are three archiving options to choose from (see fig.3.16), *'Old Archive'*, *'New Archive'* or *'No Archive'*.

It is possible to reload and re-analyse data from an old archive. Archive files created by ADAS101 consist of sequentially indexed transition data, and recovery of data for a particular case is made by reference to its *'Archive Index Number'*. Selecting *'Old Archive'* allows this and will sensitise the framed area and selection list below. An archive file is then chosen from the selection list display window. In this particular case it will operate in the usual manner. Once a file is selected the *'Browse Index'* button becomes active and it is important to use this to obtain the correct index number for the transition being analysed. Clicking on *'Refresh from Archive'* makes the *'Archive Index Number:'* entry box editable. The index number of the data to load is entered here. If refreshing from an old archive the defaults in subsequent windows will come from this file.

When entering new data, it is possible to save it to an old archive file. In this case, the user would follow the same procedure as above but avoiding the *'Refresh from Archive'* button. Archive files can be stored and created anywhere by using the *'Edit Path Name'* button. This performs in the same manner as for ADAS209 and ADAS210. However, the usual ADAS practice is to make a directory *'/home/<username>/adas/arch101'* and create files with the naming convention *'<user initials><year><element><charge+1>_<no.>.dat'*, e.g. *'dhb95fe19_001.dat'*.

Clicking on *'New Archive'* will start a fresh archive file. The file is created by entering a name in the 'selected file' window which appears above the selection list. This field becomes editable for this particular case. It is also possible to completely ignore archiving and analyse a transition perhaps only keeping a printout file as record. To do this select *'No Archive'*, at which point nothing more can be done on this screen. Clicking on *'Done'* will advance to the *'Processing Options'* screen.

N.B. It should be noted that no actual archiving is done until the final output screen, but all the selections made here will determine how the code deals with the archiving later. Also, there is no data replacement or substitution capability in

ADAS101; any new analysis, which requires archiving, is appended to the existing data contained within the archive file and given a new index number.

The next screen is the *'Processing Options'* one. All the data about the transition for analysis is entered here. If the refresh from an old archive option was selected then everything on this screen will be obtained from the chosen file. In fig.3.17 the values shown are for the Fe^{+18} $2p^4\ ^3P - 2p^5\ ^3P$ transition. The data were taken from Mann(1983) and were recovered from an old archive. The *'Data File Name:'* and *'Browse Index'* button are displayed again. Below this are editable text boxes for entering the *'Nuclear Charge'*, *'Ion Charge'* and *'transition type'*. The latter correspond to the types specified earlier. In the case of dipole transitions the *'Transition Probability'* must be entered. This can be in one of three forms; the line strength (S), the absorption oscillator strength (f) or the Einstein A-value (A). Clicking on the buttons here will calculate the correct values for the other parameters. The details of the lower and upper levels of the transition are then entered. These are the chosen lower and upper level *'Index'*, *'Statistical Weight'* and *'Level Energy'*, followed by the units that are being used for the energies. The latter are altered by clicking *'Select Energy Form:'*.

Finally, the input cross-sections, energies and output temperatures for the transition are entered by means of the ADAS table editor (for a complete description see Summers et al.(1996)). This is activated by clicking on *'Edit Table'* with the mouse. Clicking on *'Default Temperature Values'* will insert a standard set of temperatures, between $2.5 \times 10^4 K$ and $5.0 \times 10^6 K$. Confirmation is required here and is made by responding to a 'pop-up' prompt which asks whether to *'Confirm Overwrite Values with Defaults'*. If an old archive is being refreshed then the table will already be filled with the values from the archive. The units used for the energies, cross-sections and temperatures are also displayed on the screen. When working with the table editor data can be entered using a wide array of units i.e. Kelvin, eV, scaled and reduced temperatures, Omega, scaled omega, $exc. : \pi a_0^2$ and $dexc. : \pi a_0^2$ for cross-sections and $E_j k^2$, $E_i k^2$, $E_j (k/z_0)^2$, X and $E_j (k/z_{eff})^2$ for energies. This is to ease the problems of unit variation between different data sources. However, if a quantity of data is refreshed from the archive it will always appear in the form of the collision strength Ω_{ij}

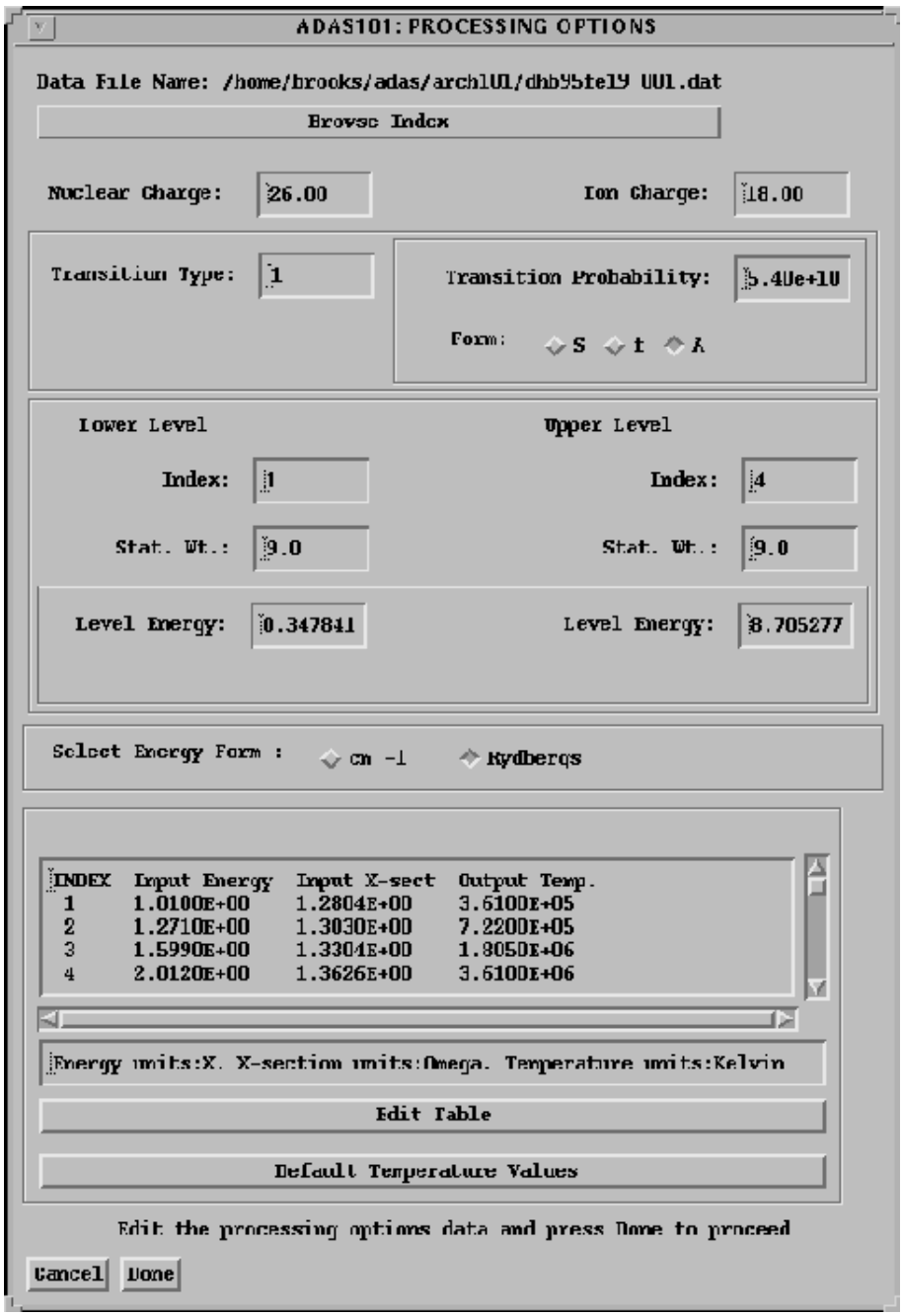

Figure 3.17: ADAS 101 processing options - example widget screen. See text for explanation of use.

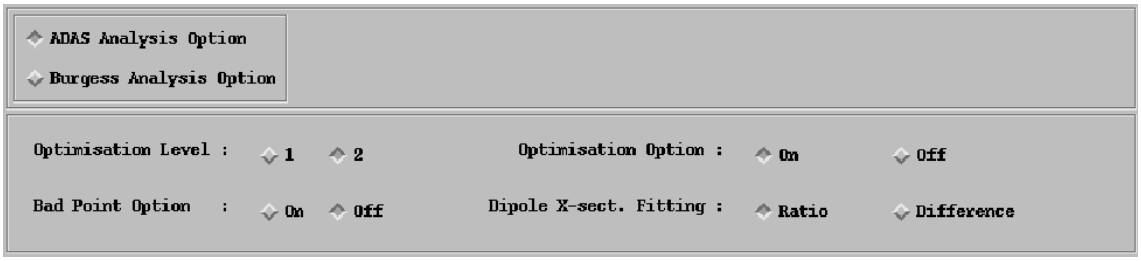

Figure 3.18: ADAS 101 output options - example segment of widget screen. See text for explanation of use.

and the threshold parameter, X. When all the editing and data entry is completed clicking on *'Done'* will proceed.

The *'Output Options'* screen enables selection of the analysis method and also allows control over the graph scalings, positioning of output files etc. An example diagram of the screen is available in the ADAS July 1995 bulletin. A segment of it is shown in fig.3.18. As with the previous displays the *'Data File Name:'* is presented along with a *'Browse Index'* button. Below this are the actual analysis option buttons discussed above, *'ADAS Analysis Option'* and *'Burgess Analysis Option'*, see fig.3.18. In fig.3.18 we have chosen the ADAS option. Below these buttons is a 'switching widget base' which offers different options depending on the analysis method selected. In practice this area will be blank when the output screen first appears. There is a practical reason for this. When switching between analysis methods on old archive data processed by one technique, ADAS101 has no way of knowing what options

would be best suited for the data using the alternative method. Therefore, it is best to set default values and these are, obviously, not suited to all transition types. However, wildly differing results can be obtained using different options and analysis methods, so it was felt best to force selection of a method to ensure consideration of the various options rather than allowing the user to blindly accept the defaults.

The four buttons for the ADAS option are *'Optimisation Level:'*, *'Bad Point Option:'*, *'Optimisation Option:'* and *'Dipole X-sect. Fitting:'*. A full explanation of these is given in the ADAS manual (Summers (1994)). However, briefly, the *'Optimisation Option'* should generally be switched on with 1 or 2 chosen as the *'Optimisation Level'*. The *'Optimisation Level'* uses either the first data point, or the first and last data points, to set an approximating form for the data. The *'Bad Point Option'* should be switched on when there are only a few points or the data includes unrealistic values. This option will help to avoid overshooting of the interpolating spline. The *'Dipole X-sect. Fitting'* determines whether the spline is fitted to the difference, or the ratio, of the input data and the approximate form. In the case of the Burgess Option, the only active entry is an initial estimate of the adjustable C-parameter. A second button *'Insert Non-dipole Point at Infinity'* is not in use at this time.

The actual output screen then presents various graphical and text optional selection facilities. For example, there is a *'Graphical Output'* button which allows entry of a working *'Graph Title'* and default scaling ranges for the scaled omega and final upsilon plots. An *'Explicit Scaling'* button, associated with this, is used for entering minimum and maximum values for the x and y ranges of the editable omega and final upsilon plots. A printout of both the subsequent graphs can be obtained by using an *'Enable Hard Copy'* option and entering a *'File Name'*, usually *'graph.ps'*. If the file already exists then ADAS101 issues a warning and an option to *'Replace'* the file is given. The output device can be chosen by clicking on a member from a small selection list. ADAS101 supports three choices at present, *Post-script*, *HP-PCL* and *HP-GL*. A hard copy of the output is also available and is printed in a similar form to how it appears in any archive file. This operates using a *'Text Output'* button similar to that which appears in ADAS209 and ADAS210. Once all the selections are complete, clicking on *'Done'* will process the data using the chosen analysis option

and bring up the editable graph screen.

The example in fig.3.19 is of the Burgess analysis graph editor. It is broadly similar to and encompasses all the features of the ADAS graph editor, but it also has some additional specific amenities. The common features are *'Move Point'*, *'Delete Pt.'*, *Add X-pt.'* , *'Add Any Pt'* and *'Insert Point by Value:'*. While the Burgess option also allows movement of the 5 knot points of the Burgess spline, *'Move Knot'*, constant display of the R.M.S. error, and immediate adjustment of the scalable C-parameter, *'Adjust C-value'*. In fig.3.19, the diamonds represent the original data and the dashed line is a best fit line drawn through them. The five knot points appear as crosses on the vertical lines and the solid line is the spline through the five knots. In this example, the C-value chosen is not particularly accurate, so that the data points and spline are visually separated on the graph. In the ADAS graph editor, the data points are also represented by crosses and the spline is a solid line. In this case there are no knot points. The editor has five different modes of operation. In general, the left hand mouse button is used for selecting and the right hand one for exiting.

'Move a point mode:' This is activated by selecting the *'Move Point'* button on the widget display. The overall widget is desensitised and the plot area becomes active. A data point is then selected with the left mouse button and is dragged around by holding this button down. To place the point in a new position, the mouse button is released. This process can be repeated any number of times. Pressing the right hand mouse button exits from this mode.

'Delete point mode:' Clicking on *'Delete Pt.'* will activate this mode. Once again, the plot area becomes editable and a point can be removed by selecting it with the left mouse button. The right mouse button is the exit button here also.

'Add x-point mode:' This can be done in two ways. Either, selecting *'Add X-Pt.'* on the display, or, entering values in the boxes provided. To add a point with the mouse we simply decide where to place it and click the left mouse button. Clicking the right hand one will again exit. To add explicitly, we enter the coordinates in the *'X-Val:'* and *'Y-Val:'* boxes and then select *'Click to Insert'*. The precision of this method can be greatly improved by noting the on screen x and y coordinates, which are displayed when moving a point, and making use of the *'Refresh'* button. When

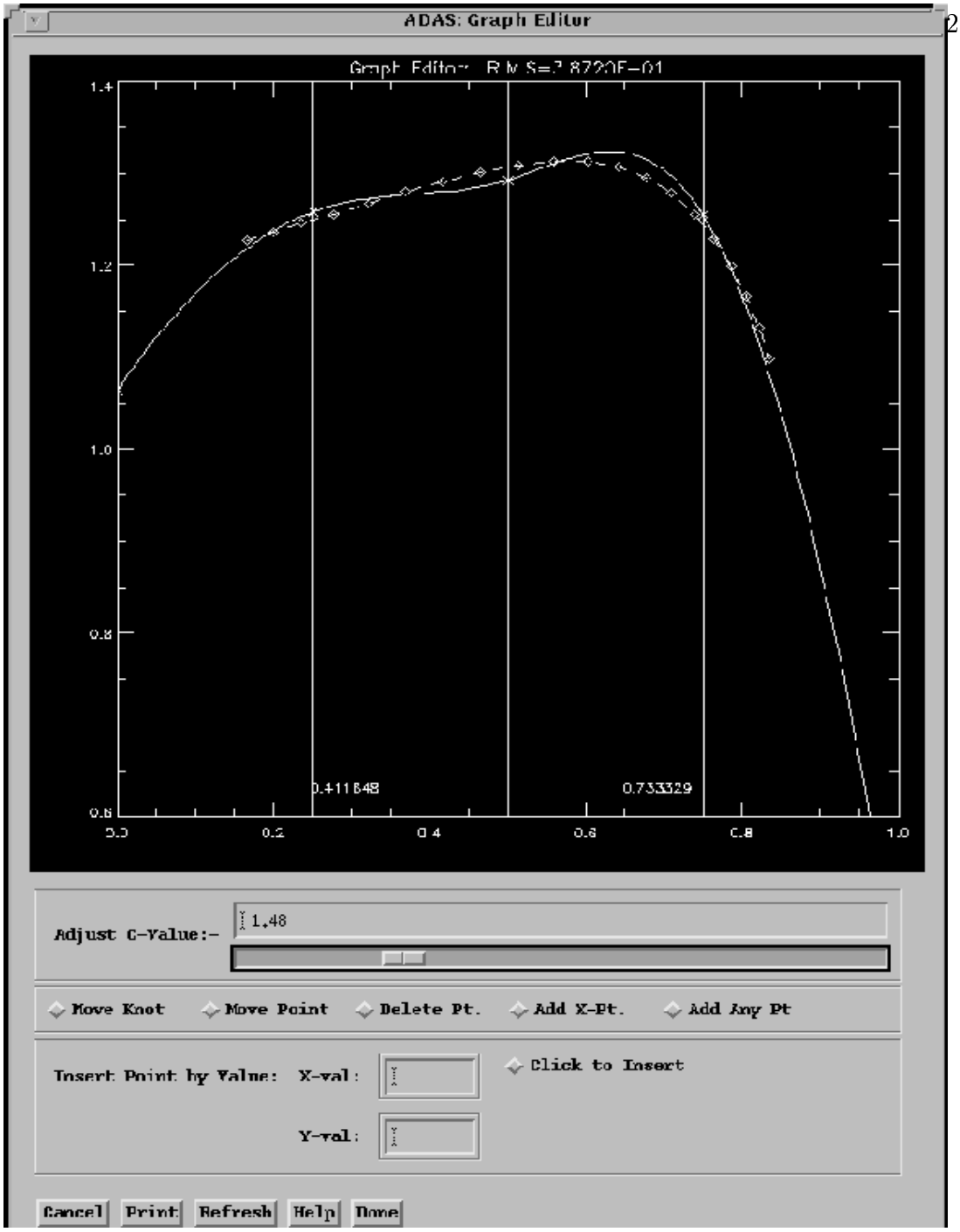

Figure 3.19: ADAS graph editor - example of Burgess option widget screen showing data from the $Fe^{+18}(\ 2p^4\ {}^3P - 2p^5\ {}^3P)$ transition. See text for explanation of use. The diamonds are the data points, the dashed line is a spline fit to them. The stars are the Burgess knot points and the solid line is the spline fit through them. The x and y positions of the cursor are given on the screen also.

selected, *'Refresh'* restores the graph by replotting the original unaltered data. This is helpful if any errors are made during editing. Therefore, moving the point to its best position, recording the displayed x and y values and refreshing the plot so the code doesn't record them, allows entry of significantly more accurate values.

The above two methods will add the point between the nearest two x-values to maintain the x vector as monotonically increasing. However, the following method will add a point anywhere. This is physically unreasonable, but is added for completeness.

'Add anywhere mode:' This is activated by clicking on *'Add Anywhere'* with the mouse cursor. It is a slightly more complex mode than the others. First, we select the point we wish to add after with the left had mouse button. Then, we click the left mouse button again to place the points. The points are then inserted after the one originally chosen, and this will continue for unlimited points until we press the right hand button. Therefore, no matter where the point is placed, it will be inserted after the original point, and splines, plot lines etc. will pass through it in that order. Theoretically a circle could be drawn in this way. To add more data we simply choose a second starting point. In this mode the right hand button must be pressed twice to exit; once to stop adding after a particular point and then again to exit completely.

'Move a Burgess knot mode:' This mode is executed by clicking on *'Move Knot'* and it is performed in the same manner as with the *'Move a point'* mode. However, it is unique to the Burgess analysis option. In this way repositioning and visual adjustment of the five spline knot points calculated by this method is possible. Only vertical motion of the points is allowed so that they remain at the five x-coordinates specified by Burgess & Tully (1992). Once again selection is with the left button and exit is by the right one.

When moving, adding or deleting a point it is the actual data that is altered. Therefore, if any changes are made, the program will re-process the approximate forms and fits. Hence, moving a point and then clicking *'Done'* will cause the *'Output Options'* screen to re-appear, rather than continuing forward as it usually does. Alteration of the five Burgess knot points does not have this effect as their technique allows for a final visual check on the spline.

As mentioned above, the other feature unique to the Burgess option is the ability

to re-adjust the scalable parameter C. A widget slider is available, *'Adjust C-value'*, which allows quick and easy adjustment without the laborious task of continually cancelling and reprocessing. When the slider is moved the value is recorded, the data is reprocessed and the new R.M.S. is computed and immediately updated. The graph is also replotted and this makes any analysis much easier. Finally, there are some extra buttons along the bottom row of the screen. The *'Cancel'* and *'Done'* buttons have their usual meaning and the *'Refresh'* button has already been discussed. The *'Print'* button writes the edited plot into a file suitable for printing. This is only possible if an output device was selected on the *'Output Options'* screen. Finally, it was decided that although the graph editor was fairly straight forward to use, it could appear quite daunting at first sight and problems could be generated easily by moving too fast and getting out of step between the buttons and the IDL processing. Therefore, it was thought desirable to have some information available to clearly explain its use. Clicking on *'Help'* displays instructions on which buttons to press etc. similar to those given above. The *'Help'* screen can be left up as a display while using the graph editor. In addition to this there is a reminder present on the screen, in the position of the title, which explains how to start each process e.g. in *' Delete point mode'* it will display *'left button selects point to delete'*.

The final screen is a plot of the calculated upsilons. It is displayed with information about the time, date, ADAS release and file used. The graph itself is plotted against $\log_{10}(T_e(K))$. Once again a printout of the graph can be obtained by clicking on *'Print'*. Finally, there is an option to archive the analysed data. Clicking on *'Archive'* will do this no matter which options were chosen on the first screen. The original options only open old or create new files and prepare their format but do not actually write anything to them. This is because we often wish to try reprocessing several times before deciding on the best fit. However, clicking on *'Archive'* when originally choosing *'No Archive'* is a contradiction and ADAS101 will 'pop-up' a warning accordingly. However, the data will be archived anyway, in this case, and the default is to create a file *'archive.dat'* in the users' *'arch101'* directory.

Example of Archive File

Fig.3.20 shows an example of the archive file produced by ADAS101. Both the *'ADAS analysis'* and the *'Burgess analysis'* options have been used to create the two differing output formats. The data shown is again for the $Fe^{+18}(2p^4\ ^3P - 2p^5\ ^3P)$ transition. The first line of the file identifies the index number of the data block and also the analysis option chosen. *'A'* corresponds to the *'ADAS analysis'* and *'B'* to the *'Burgess analysis'*. Between these, some information about the transition and also the date are given. In fact, this area is filled with the graph title from the ADAS101 run. Lower down in fig.3.20 the same information is repeated. This is the start of the Burgess data block where the index number is increased and the analysis code updated. Data blocks in the archive file end with the terminator '-1' in the first column.

The data archived using the *'ADAS analysis'* is fairly self explanatory and more details are given in the ADAS manual (Summers (1994)). In the case of the *'Burgess analysis'* the data block has been set up to maintain the precise formatting output from Burgess's own codes, except that the data has been shifted along by one space to allow the ADAS search routines to identify index numbers, and that all the data is merged in one file rather than two separate ones for Ω and Υ. Due to this alteration it was thought unnecessary to repeat the information on statistical weights etc. Also, ADAS has two routines (101 & 102) to do the fitting of Ω and Υ, so the final Υs are output in the archive file but the Burgess spline fit is not. These would appear in the archive file for ADAS102. The FORTRAN and IDL routines which output this data were coded up from the original BBC BASIC program provided by Alan Burgess. Below the information header, the Ω data is displayed. Below this is the *ion charge* then the *nuclear charge*. Underneath these are the lower level *energy*, in cm^{-1}, and *statistical weight* followed on each line by those for the upper level. Next is the *transition energy*, the *transition type*, the gf value and the adjustable *C-parameter*. Following this are the five y-coordinates of the spline knot points, two parameters which indicate the range of the upsilons and the lower and upper level indices. The producer program is then printed as a reference and finally the number of cross-sections followed by the *reduced energies* and the actual Ω values. After this the Υ information, truncated from the Burgess file, is given. Essentially this is just

```
I  1  FE+18 2P4(3P)-2P5(3P) MANN(1983) 26/2/93                    A
 NUCLEAR CHARGE = 26.00   ION CHARGE = 18.00   EFFECTIVE ION CHARGE = 19.00
 LOWER  INDEX =     1              UPPER  INDEX  =     4
 LOWER ENERGY =     0.347841       UPPER ENERGY =     8.705277
 LOWER WEIGHT =   9.0              UPPER WEIGHT =   9.0
 ACOEFF =   5.4000E+10     S =  3.1095E-01      FABS =   9.6251E-02     ENERGY DIFFERENCE =     8.357436
 XSECT TYPE=  1    XSECT OPT.FACTORS, FXC2 =  6.9706E+00   FXC3 =  1.9825E+00   IXOPS = 1   IBPTS = 0
IFPTS =  2   IDIFF = 0
    X                OMEGA         APPROX. OMEGA          DIFFERENCE
 1.0100E+00          1.2804E+00          1.2804E+00          2.2204E-16
 ...
 7.9472E+01          2.7491E+00          2.7491E+00         -1.6645E-07
 TE(K)               GAMMA         APPROX. GAM          EX. RATE          DEXC. RATE          GBARF
 3.6100E+05          1.3027E+00          1.3001E+00          5.3754E-11          2.0791E-09          8.3365E-02
 ...
 3.6100E+09          4.5342E+00          4.5342E+00          7.2341E-11          7.2367E-11          2.9017E-01
-1
I  2  FE+18 2P4(3P)-2P5(3P) MANN(1983)08/03/96                    B
 OMEGA
 18.00
 26.00
     38171.080       9.0
    955292.288       9.0
    917121.208
   1
 0.8663E+00
 1.68000
  0.117E+01   0.127E+01   0.131E+01   0.116E+01   0.415E+00
   0.00E+00    0.32E+00
 1  4
  ADAS101
  20
  0.101E+01   0.128E+01
  ...
  0.795E+02   0.275E+01
 UPSILON
  13
 0.3610E+06  0.3641E-01
 ...
 0.3610E+10  0.3220E+00
-1
C-------------------------------------------------------------------------------------------------------------------------------
C INDEX  CODE  ION     TRANSITION      SOURCE              DATE
C   1           A     FE+18  2P4(3P)-2P5(3P)    MANN(1983)          26/02/93
C   2           B     FE+18  2P4(3P)-2P5(3P)    MANN(1983)          08/03/96
C-------------------------------------------------------------------------------------------------------------------------------
```

Figure 3.20: ADAS 101 example archive file. See text for a complete description.

the number of points followed by the temperatures, in Kelvin, and the calculated Υs.

3.2 Methods for Derived Data Production

3.2.1 Ionisation Balance

Introduction

In sec.2.2.3 the applications of derived data to plasma spectroscopy and research were outlined. Central to these applications was the use of the line emission contribution function otherwise known as the $G(T_e, N_e)$. As can be seen from eq. 2.64, equilibrium abundance fractions for each of the ionisation stages normalised to the total abundance of the element in question contribute to the make up of the $G(T_e, N_e)$ function. The importance of calculating these can also be seen from sec.2.2.3. It is usual in astrophysics to assume the plasma under investigation is in equilibrium. Therefore, for derived data to be of widespread use, these fractions should be computed as accurately as possible. A discussion of the validity of this assumption is deferred until later in this chapter.

We require values of these fractions for all minor species contributing to the radiation emission from the solar atmosphere. A complete study must include processes such as dielectronic recombination in detail which can shift the temperature dependence of the peak of the ionisation stages. Also, it is important to evaluate the effect of finite plasma density and the influence of metastable states. Usually when describing the ionisation state of ions of an element only the abundances of complete ionisation stages are considered. However, plasma dynamic and atomic relaxation timescales are such that metastables can accumulate large populations and that they may evolve on long timescales (see sec.2.2.2 and 2.1.2). In these cases, the metastables are important to population calculations, contributing substantially to refined dielectronic recombination and ionisation computations. The make up of the $G(T_e, N_e)$ function can be significantly influenced also, as can the total radiative power functions, since

they contain the ion fraction in their representation, (eq. 3.16).

$$P_{tot} = \sum_{z=0}^{z_0} \sum_{\sigma=1}^{m_z} P^z \frac{N_\sigma^z}{N_{tot}} \tag{3.16}$$

where P^z can be separated into radiated power coefficient contributions from each of the individual metastables. Consequently composite radiative power loss functions for the solar atmosphere (Summers & McWhirter(1979)) may be altered as a result. Calculations of ionisation balance are common in astrophysics. The calculations of Summers(1974) used a full collisional-radiative model to produce effective ionisation and recombination coefficients dependent on density and temperature. With improvements in fundamental atomic data generation, calculations must be revised. The results of Arnaud & Rothenflug (1985) are currently the most widely used but do not include metastable states or the effects of finite density plasma. Exclusion of collisional-radiative effects has been justified for solar coronal densities by suggesting that zero density calculations only are necessary since its electron density is low $\sim 5.4 \times 10^8 cm^{-3}$. In reality, this is not so. In particular, it is clear that the collisional dielectronic recombination coefficients will be significantly altered even at low density. This occurs through their influence on the individual dielectronic recombination coefficients (see chap.2.2.1). Also, when moving to the chromosphere, the low temperature enhancement of the collisional dielectronic coefficients, due to the influence of three body recombination at higher density, can play a more significant role.

Summers & McWhirter (1979) discussed the possibility of including metastables in a collisional-radiative model, while Summers & Hooper (1983) developed a method to incorporate them consistently. Kato, Lang & Berrington (1990), while not including recombination processes, showed that spectral line intensities were altered by up to 60% when the effects of metastable states were included. In the fusion context, Dickson (1993) performed a study of metastable resolved ionisation balance and its influence on derived data. In so doing, he found that metastables contribute substantially to calculations of radiated power.

We wish to make an improvement in the precision of our ionisation balance calculations by introducing the ability to treat metastable states explicitly. In doing this, we add a degree of complexity to the population distribution calculation. However,

it is ultimately of interest for studying the role of significantly populated levels in different plasma environments and essential for realistic dynamic studies. Therefore, a method to incorporate metastable states in the ionisation balance eqs. 3.18 is developed below. The first 'in-depth' study, directed at astrophysical plasmas, including also the influence of finite density plasma, is presented in chap.4 and also in Brooks et al.(1997).

Background Theory

For an element X, evolving with time in a thermal plasma, with nuclear charge z_0, the population of the ion X^{+z} is denoted by N^z, where $z \in [0, z_0]$. To evaluate N^z we construct an equation describing its time evolution due to populating and depopulating collisional and radiative processes. Therefore,

$$\begin{aligned} \frac{d}{dt}N^z = N_e S_{CD}^{z-1\to z} N^{z-1} \\ - \left[N_e S_{CD}^{z\to z+1} + N_e \alpha_{CD}^{z\to z-1} + N_H C_{CD}^{z\to z-1}\right] N^z \\ + N_e \alpha_{CD}^{z+1\to z} N^{z+1} + N_H C_{CD}^{z+1\to z} N^{z+1} \end{aligned} \tag{3.17}$$

where the S_{CD}'s, α_{CD}'s and C_{CD}'s are the collisional dielectronic coefficients for ionisation, recombination and charge-exchange recombination respectively (see chap.2).

In equilibrium ionisation balance the time derivative in equation 3.17 is set to zero and the stage populations can be calculated by solution of the matrix equation,

$$N_e \begin{bmatrix} \ddots & 0 & 0 & 0 \\ \ddots & \alpha_{CD}^{z\to z-1} + \left(\frac{N_H}{N_e}\right) C_{CD}^{z\to z-1} & 0 & 0 \\ S_{CD}^{z-1\to z} & -\left(S_{CD}^{z\to z+1} + \alpha_{CD}^{z\to z-1} + \left(\frac{N_H}{N_e}\right) C_{CD}^{z\to z-1}\right) & \ddots & 0 \\ 0 & S_{CD}^{z\to z+1} & \ddots & \ddots \\ 0 & 0 & \ddots & \ddots \end{bmatrix} \begin{bmatrix} \vdots \\ \vdots \\ N_z \\ N_{z+1} \\ \vdots \end{bmatrix} = 0 \tag{3.18}$$

and subsequent normalisation to the total population,

$$N_{tot} = \sum_{z=0}^{z_0} N^z \tag{3.19}$$

where N_{tot} is the total number density of all ions of the element X . From Eq.3.18and 3.19 we can obtain the equilibrium fractional abundances, N^z/N_{tot} at a grid of temperature and density points. This is the usual *unresolved* or *stage to stage* picture and assumes ionisation and recombination takes place only from and to the ground states of each ion.

To include metastable states, we partition the population of each stage N^z into ground and metastable levels denoted by N^z_σ where $\sigma \in [1, m_z]$. Eq. 3.17 then becomes,

$$\begin{aligned}\frac{d}{dt}N^z_\sigma = N_e \sum_{\rho=1}^{m_{z-1}} S^{z-1\to z}_{CD,\rho\to\sigma} N^{z-1}_\rho + N^{z+1}_\tau \left(N_e \sum_{\tau=1}^{m_{z+1}} \alpha^{z+1\to z}_{CD,\tau\to\sigma} + N_H \sum_{\tau=1}^{m_{z+1}} C^{z+1\to z}_{CD,\tau\to\sigma} \right) \\ + N^z_\sigma \left(N_e \sum_{\sigma'=1;\sigma'\neq\sigma}^{m_z} Q^{z\to z}_{CD,\sigma'\to\sigma} + N_e \sum_{\sigma'=1;\sigma'\neq\sigma}^{m_z} X^{z\to z}_{CD,\sigma'\to\sigma} \right) \\ - N^z_\sigma \left(N_e \sum_{\tau=1}^{m_{z+1}} S^{z\to z+1}_{CD,\sigma\to\tau} + N_e \sum_{\rho=1}^{m_{z-1}} \alpha^{z\to z-1}_{CD,\sigma\to\rho} + N_H \sum_{\rho=1}^{m_{z-1}} C^{z\to z-1}_{CD,\sigma\to\rho} \right. \\ \left. + N_e \sum_{\sigma'=1;\sigma'\neq\sigma}^{m_z} Q^{z\to z}_{CD,\sigma\to\sigma'} + N_e \sum_{\sigma'=1;\sigma'\neq\sigma}^{m_z} X^{z\to z}_{CD,\sigma\to\sigma'} \right) \quad (3.20)\end{aligned}$$

which describes the population evolution of each metastable σ of each ionisation stage z. The symbols ρ and τ index the metastables of the $z-1$ and $z+1$ ions respectively i.e. $\rho \in [1, m_{z-1}]$ and $\tau \in [1, m_{z+1}]$. Also, $\sigma' \in [1, m_z]$ indexes the metastables of the zth ionisation stage, with $\sigma' \neq \sigma$. The collisional radiative coefficients now correspond to those of the *metastable resolved* case. Two new coefficients are introduced which link metastables of the same stage; contributions to populating and depopulating processes via metastable cross-coupling reactions, Q_{CD}, and recombining ion parent to parent metastable cross coupling reactions, X_{CD}. It is convenient to separate them because of their different origin in calculation. X_{CD} is that part of the cross-coupling which occurs through capture+autoionisation and is best associated with dielectronic recombination. In this case the $X^{z\to z}_{CD}$ coefficients refer to the parents of the $z-1$ stage. The left hand side of Eq. 3.18 then becomes,

$$N_e \begin{bmatrix} \ddots & 0 & 0 & 0 \\ \ddots & \mathbf{A}_{CD}^{z\to z-1} + \left(\frac{N_H}{N_e}\right)\mathbf{C}_{CD}^{z\to z-1} & 0 & 0 \\ \mathbf{S}_{CD}^{z-1\to z} & -\left(\mathbf{S}_{CD}^{z} + \mathbf{A}_{CD}^{z} + \left(\frac{N_H}{N_e}\right)\mathbf{C}_{CD}^{z} + \mathbf{Q}_{CD}^{z\to z} + \mathbf{X}_{CD}^{z\to z}\right) & \ddots & 0 \\ 0 & \mathbf{S}_{CD}^{z\to z+1} & \ddots & \ddots \\ 0 & 0 & \ddots & \ddots \end{bmatrix} \begin{bmatrix} \vdots \\ \vdots \\ N_z \\ N_{z+1} \\ \vdots \end{bmatrix} \tag{3.21}$$

where each bold faced letter in eq. 3.21 is an individual matrix describing reactions between the ground and metastable levels of the ionisation stages involved. Therefore, the ionisation coefficient matrix is given by,

$$\mathbf{S}_{CD}^{z-1\to z} = \begin{bmatrix} \cdot & \vdots & \vdots & \cdot \\ \cdots & S_{CD,\rho-1\to\sigma-1}^{z-1\to z} & S_{CD,\rho-1\to\sigma}^{z-1\to z} & \cdots \\ \cdots & S_{CD,\rho\to\sigma-1}^{z-1\to z} & S_{CD,\rho\to\sigma}^{z-1\to z} & \cdots \\ \cdot & \vdots & \vdots & \cdot \end{bmatrix} \tag{3.22}$$

and the $\mathbf{S}_{CD}^{z}$ matrix contains the summed values of the ionisation coefficients corresponding to ionisation out of the stage z, such that,

$$\mathbf{S}_{CD}^{z} = \begin{bmatrix} \cdot & \vdots & \vdots & \cdot \\ \cdots & \sum_{\tau=1}^{m_{z+1}} S_{CD,\sigma-1\to\tau}^{z\to z+1} & 0 & \cdots \\ \cdots & 0 & \sum_{\tau=1}^{m_{z+1}} S_{CD,\sigma\to\tau}^{z\to z+1} & \cdots \\ \cdot & \vdots & \vdots & \cdot \end{bmatrix} \tag{3.23}$$

The recombination coefficient is given by,

$$\mathbf{A}_{CD}^{z\to z-1} = \begin{bmatrix} \cdot & \vdots & \vdots & \cdot \\ \cdots & \alpha_{CD,\sigma-1\to\rho-1}^{z\to z-1} & \alpha_{CD,\sigma\to\rho-1}^{z\to z-1} & \cdots \\ \cdots & \alpha_{CD,\sigma-1\to\rho}^{z\to z-1} & \alpha_{CD,\sigma\to\rho}^{z\to z-1} & \cdots \\ \cdot & \vdots & \vdots & \cdot \end{bmatrix} \tag{3.24}$$

and it also has a corresponding matrix which contains the summed components of

recombination out of the stage z, viz.

$$\mathbf{A}^{z}_{CD} = \begin{bmatrix} \cdot & \vdots & \vdots & \cdot \\ \cdots & \sum_{\rho=1}^{m_{z-1}} \alpha^{z\to z-1}_{CD,\sigma-1\to\rho} & 0 & \cdots \\ \cdots & 0 & \sum_{\rho=1}^{m_{z-1}} \alpha^{z\to z-1}_{CD,\sigma\to\rho} & \cdots \\ \cdot & \vdots & \vdots & \cdot \end{bmatrix} \tag{3.25}$$

A similar definition applies for the C_{CD}'s.

For completeness, we should note also that the matrix containing the metastable cross-coupling coefficients also includes the summation of components populating the metastables of stage z by processes that depopulate those same metastables i.e. a transition out of a metastable of stage z will move into a metastable of stage z. Similarly, the matrix containing the parent to parent metastable cross-coupling coefficients includes the summation of components populating the parent metastables of stage z-1 due to processes which depopulate those same parent metastables.

$$\mathbf{Q}^{z\to z}_{CD} = \begin{bmatrix} \cdot & \vdots & \vdots & \cdot \\ \cdots & -\sum_{\sigma'=1;\sigma'\neq\sigma}^{m_z} Q^{z\to z}_{CD,\sigma'\to\sigma-1} & Q^{z\to z}_{CD,\sigma-1\to\sigma} & \cdots \\ \cdots & Q^{z\to z}_{CD,\sigma\to\sigma-1} & -\sum_{\sigma'=1;\sigma'\neq\sigma}^{m_z} Q^{z\to z}_{CD,\sigma'\to\sigma} & \cdots \\ \cdot & \vdots & \vdots & \cdot \end{bmatrix} \tag{3.26}$$

and

$$\mathbf{X}^{z\to z}_{CD} = \begin{bmatrix} \cdot & \vdots & \vdots & \cdot \\ \cdots & -\sum_{\sigma'=1;\sigma'\neq\sigma}^{m_z} X^{z\to z}_{CD,\sigma'\to\sigma-1} & X^{z\to z}_{CD,\sigma-1\to\sigma} & \cdots \\ \cdots & X^{z\to z}_{CD,\sigma\to\sigma-1} & -\sum_{\sigma'=1;\sigma'\neq\sigma}^{m_z} X^{z\to z}_{CD,\sigma'\to\sigma} & \cdots \\ \cdot & \vdots & \vdots & \cdot \end{bmatrix} \tag{3.27}$$

Finally, to obtain the equilibrium metastable fractional abundances the normalisation (eq. 3.19) now becomes

$$N_{tot} = \sum_{z=0}^{z_0} \sum_{\sigma=1}^{m_z} N^{z}_{\sigma} \tag{3.28}$$

Outline of Solution Method

We employ a progressive elimination algorithm to solve the tridiagonal matrix eq. 3.18. However, there is a practical problem. For a particular N^z we have,

$$N^z = N^{z+1}\left[\alpha_{CD}^{z+1\rightarrow z} + \left(\frac{N_H}{N_e}\right) C_{CD}^{z+1\rightarrow z}\right] / S_{CD}^{z\rightarrow z+1} \tag{3.29}$$

which has the ionisation coefficient as the denominator. McWhirter & Summers (1985) give the following expression for the ionisation coefficient,

$$S_{CD}^{z\rightarrow z+1} = 16\sqrt{\pi}\alpha c a_0^2 \frac{(kT_e)^{1/2}}{(z+1)^4 I_H^{1/2}} \nu_p^4 F exp\left(-\frac{(z+1)^2 I_H}{kT_e \nu_p^2}\right) \tag{3.30}$$

where ν_p^z is the effective principal quantum number of the level p, of the ionisation stage z, from which the reaction takes place and F is a factor approximately equal to one. This equation includes an exponential dependence on $-T_e^{-1}$ which results in a rapid 'drop-off' of the ionisation coefficient at low temperature. As a result of these extremely small values, it is possible to obtain *overflows* during the numerical solution of eq. 3.18. This generally occurs when attempting to form the population ratio of ionisation stages in 3.29 using the abundance of an ionisation stage formed at a radically different temperature. This problem would appear in reverse if the alternative elimination route was chosen. Therefore, to circumvent this problem the algorithm employs a *'double pass'* technique. By simultaneously solving towards the predicted dominant ionisation stage, from the fully ionised and neutral stages, we can recover the population densities by back substitution in eq. 3.29 once the dominant stage's actual value is known.

An equivalent algorithm is used for the *metastable resolved* case (eq. 3.21) but matrix manipulations are used to replace the usual arithmetic operations. A 'first guess' at the target dominant stage is made by a simple comparison of the effective ionisation and recombination coefficients. Selection is made at the ionisation stage where these coefficients are deemed to be most similar subject to the constraint that the stage is not too close to a region of rapid population 'drop-off'. On solution of eq. 3.21 the equilibrium fractional abundances are checked and, if the dominant stage is wrong, the algorithm is re-run with the correct one.

ADAS405 and scripts for observational sequences

The above solution method for eq. 3.20 has been implemented in ADAS series 4, as ADAS405 (Summers et al.(1996)). ADAS405 computes the equilibrium population distribution amongst the ionisation stages of an element, in both the metastable resolved and unresolved approximations. In addition, it calculates the radiated power function, P_{tot} (see eq. 3.16), and also the contribution function, $G(T_e, N_e)$ (see eq. 2.64) for a temperature and density model. As such, it provides a complete capability for exploring the temperature and density dependence of these quantities as well as the ionisation balance and the influence of metastables.

ADAS405 draws from collections of the collisional-radiative coefficients required to solve eq. 3.21. These are stored in adas data format files *adf11*. Selection of these is made to be consistent with the intention of the calculation, e.g it is not necessary to include metastable cross-coupling data if the computation is to be unresolved.

Computation of the line emission functions, $G(T_e, N_e)$, is controlled by a user specified '*script file*'. This allows us to explore emission function ratios between the specified lines, and also between lines originating from different ions of the same element. A sample script file showing the OV and OVI lines associated with the suggested SOHO observing sequence of McWhirter (PTCOR in Harrison & Fludra (1995) also known as the Blue Book) to measure the coronal temperature versus height, is given in fig.3.21. The script specifies the element (SPECIES), the number of lines (NLINE) and the number of line ratios (NRATIO), for the study. ADAS405 accesses photon emissivity coefficients from the ADAS database (see chap.2) and the names of the files for the study are entered below NFILE. The coefficients are stored in ADAS datafiles of type *adf15*. NFILE itself is the number of files being accessed. ILINE indexes the number of lines, NCOMP is the number of component parts of the line, IZION is the charge to which the components belong and ICOMP indexes the components. IMET indexes the the metastables of the ion to which the component is attached and INDPH is the selection index of the component photon emissivity coefficient in the *adf15* file. The letter 'E', to the right of this index, identifies the coefficient as being driven by electron collisions or charge exchange if it is replaced by an 'H'. The file in the list, to which the index INDPH refers, is given by IFILE.

```
SPECIES  =  O
NLINE    =  5
NRATIO   =  1
NFILE    =  2
PHOTON EMISSIVITY FILE NAMES = /disk2/adas/adas/adf15/pec93#o/pec93#o_pjr#o4.dat
                               /disk2/adas/adas/adf15/pec93#o/pec93#o_pjr#o5.dat

 ILINE   NCOMP   IZION   ICOMP   IMET    INDPH   IFILE    TITLE
-------------------------------------------------------------------------------
   1        2       4       1       1       2E      1     OV   172.17A
                    4       2       2      14E      1
-------------------------------------------------------------------------------
   2        2       4       1       1       1E      1     OV   629.73A
                    4       2       2      13E      1
-------------------------------------------------------------------------------
   3        1       5       1       1       6E      2     OVI  173.08A
-------------------------------------------------------------------------------
   4        1       5       1       1       5E      2     OVI  184.12A
-------------------------------------------------------------------------------
   5        1       5       1       1       1E      2     OVI  1033.8A
-------------------------------------------------------------------------------
 IRATIO  ILINE   JLINE    TITLE
-------------------------------------------------------------------------------
   1        1       2      OV (172.17A)/OV (629.73A)
-------------------------------------------------------------------------------
C-------------------------------------------------------------------------------
C ANALYSIS OF OXYGEN EMISSION
C
C   LINES INCLUDED:
C              1.  OV  (2s2 1S - 2s3p 1P)    172.17A
C              2.  OV  (2s2 1S - 2s2p 1P)    629.73A
C              3.  OVI ( 2p 2P -  3d 2D)     173.08A
C              4.  OVI ( 2p 2P -  3s 2S)     184.12A
C              5.  OVI ( 2s 2S -  2p 2P)     1033.8A
C
C
C
C-------------------------------------------------------------------------------
C  CODES:
C       IMET   - Trailing '+'          => IZION+1 metastable
C                <blank>               => IZION   metastable
C                Trailing '-'          => IZION-1 metastable
C
C       INDPH  - Trailing 'E' or  <blank>  => Electron coll. driven
C                 Trailing 'H'             => Hydrogen  CX   driven
C
C-------------------------------------------------------------------------------
```

Figure 3.21: Sample script file for oxygen. See text and Summers et al.(1996) for a complete description.

The TITLE field is usually filled with the ion, in spectroscopic notation, followed by the wavelength of the emitting line. IRATIO indexes the number of line ratios in the *script* while ILINE and JLINE give the line indices of the numerator and denominator of the ratio to be formed. There is an arbitrary information field at the bottom of each *script* which is for the convenience of the user.

Users should create their own script file suitable for analysing the spectral emission from whichever ion is of interest to them. The expectation is that the lines and line ratios present in the script file will reflect those chosen for a particular observing sequence using SOHO-CDS or SOHO-SUMER. Therefore, a direct comparison can be made between the predicted emission and the actual observations, once the observing study has been run.

Validity of Equilibrium Assumption

It has been usual, in astrophysics, to assume that steady state ionisation balance is a reasonable approximation when investigating radiation from the outer atmosphere of the Sun. However, this hypothesis is unsound when looking at dynamic activity, such as flares, and may also be invalid for the quiet Sun.

The steady state assumption is only valid if the atomic relaxation timescales, for the ground and metastable states, are short enough to allow the plasma to reach equilibrium. We can make a simple estimate of this timescale by looking at the summation, over all ionisation stages of an element, of the reciprocal of the sum of the collisional dielectronic recombination and ionisation coefficients. We call this $\tau_{transient}$ and define it as

$$\tau_{transient} = \sum_{z=0}^{z_0} \frac{1}{N_e(S_{CD}^{z\rightarrow z+1}(T_e) + \alpha_{CD}^{z+1\rightarrow z}(T_e))} \tag{3.31}$$

Hence, we can obtain an estimate for the minimum amount of time required for a particular species to relax into equilibrium in a plasma of given electron temperature and density. In this simple approximation, we have assumed that the rate coefficients are independent of density. This is a reasonable assumption since they are generally only slowly varying.

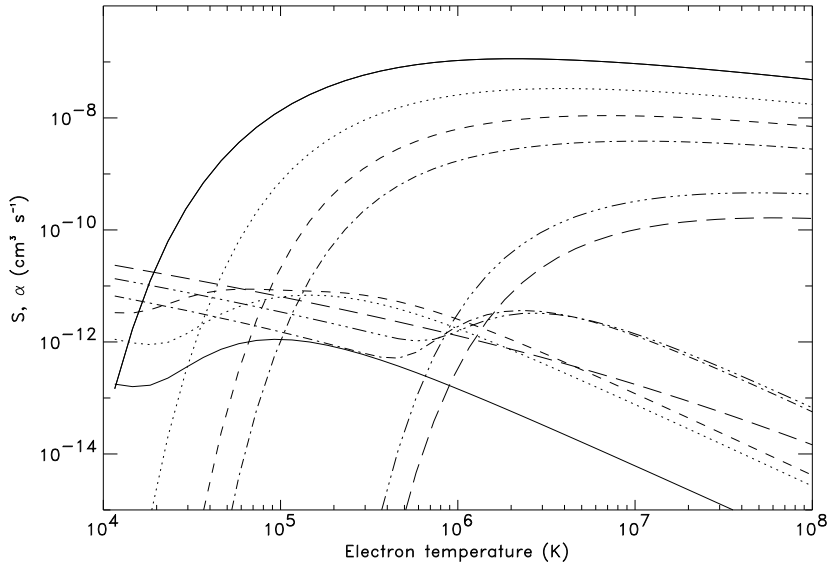

Figure 3.22: Collisional-Dielectronic Recombination and Ionisation coefficients for carbon ions, $N_e = 10^{10} cm^{-3}$

Fig. 3.22 shows the collisional dielectronic recombination and ionisation coefficients for each ionisation stage of carbon, plotted over a range of electron temperatures at an electron density of $10^{10} cm^{-3}$. The data was taken from Abel-Van-Maanen (1982) Recombination and ionisation processes balance where $S_{CD}^{i \rightarrow i+1} = \alpha_{CD}^{i+1 \rightarrow i}$ i.e. where each line of the same style crosses. McWhirter (1960) treated the minimum $\tau_{transient}$ as being independent of the recombination coefficient and, therefore, controlled by the ionisation coefficient for the highest ionisation stage present in the plasma; since this would provide the largest term in the summation expansion. However, if we wish to include the possibility that the plasma may be recombining, we use eq. 3.31. Fig. 3.23 shows the variation with temperature of $N_e \tau_{transient}$. The behaviour of the curve indicates the temperature regions in which carbon is ionising or recombining in the plasma. For a fixed electron density, the time taken to relax into equilibrium diminishes with increasing temperature as the element ionises from the neutral stage through to the He-like one. Then, as the He-like stage dominates

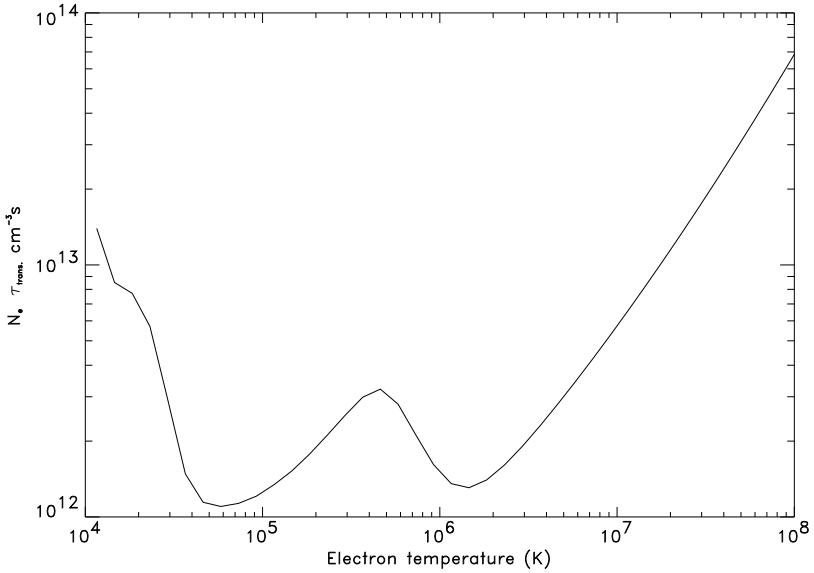

Figure 3.23: Function $N_e\tau_{transient}$ for Carbon

and the plasma begins to recombine, the time increases with temperature until it is hot enough to strip open the closed $n = 1$ shell. Thereafter, the timescale drops until the ion is fully stripped when recombination again dominates. A similar dip and rise would be expected at the Ne-like stage, for an element of nuclear charge ≥ 10, in order to open the $n = 2$ shell. Dividing by typical electron densities for the solar atmosphere, allows us to identify approximate relaxation timescales for the different temperature/density regimes.

The same type of analysis can be made for other ions and fig.3.24 shows a general plot of $N_e\tau_{transient}$ against T_e for Beryllium, Carbon, Nitrogen, Oxygen and Neon. Broadly similar behaviour can be seen for each element. However, the region, at which the effects of the He-like stage set in, shifts to a higher temperature for elements of higher nuclear charge. This would be reflected in the width of the He-like stage, in the ionisation balance, at correlated electron temperatures.

For a particular plasma environment, we expect *transient* or *nonequilibrium* effects to be important if the time to pass through a temperature scale height is shorter

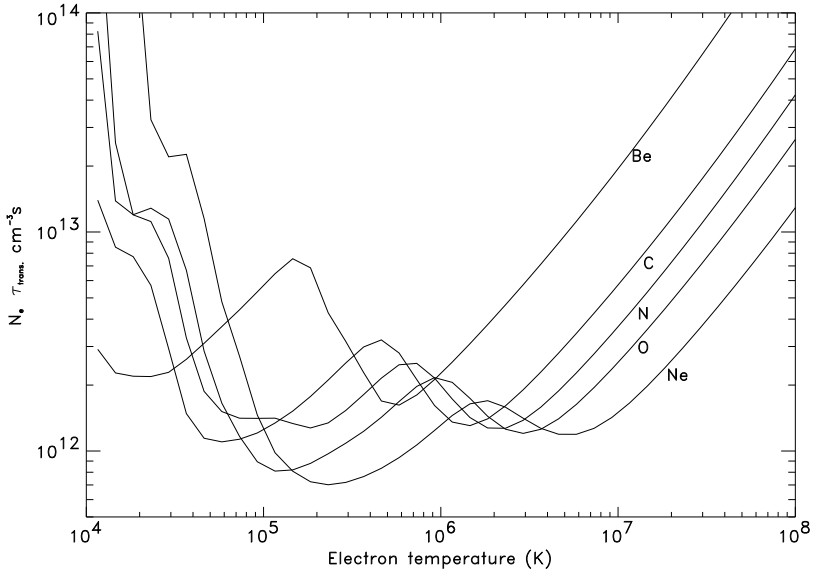

Figure 3.24: $N_e\tau_{transient}$ for some prominent radiators in the solar atmosphere

than $\tau_{transient}$ (Noci, Spadaro, Zappala & Antiochos (1989)). If this is true, the left hand side of eq. 3.20 cannot be set to zero and the problem becomes more complex, requiring a suitable choice of boundary conditions to solve the differential equations. Noci et al.(1989) did just this. They evolved carbon ions through a temporal variation of plasma electron density, temperature and velocity computed by a numerical hydrodynamic model of a steady siphon flow along a coronal magnetic loop. They computed the population distribution amongst the ionisation stages and their results show that, even for plasma flows of only a few km s^{-1}, nonequilibrium effects can make an appreciable difference.

It should be noted that these differences are not necessarily better able to resolve the discrepancies between theoretical models and spectroscopic observations. Spadaro, Noci, Zappala & Antiochos (1990) continued the work of Noci et al.(1989), computing UV emission lines for carbon from their siphon flow model. This was an attempt to explain the persistent red shifts observed in some transition region lines (Doschek, Bohlin & Feldman (1976)). Then, Spadaro, Antiochos & Mariska (1991)

	$N_e(cm^{-3})$	$T_e(K)$	$\tau_{transient}(s)$
upper chromosphere	3.7×10^{10}	2×10^4	~ 160
transition region	$1.3 \times 10^{10} \rightarrow 1.3 \times 10^9$	$5 \times 10^4 \rightarrow 5 \times 10^5$	$\sim 75 \rightarrow 2300$
corona	5.4×10^8	1×10^6	~ 2800

Table 3.1: Carbon relaxation times for the solar atmosphere

extended the research to include oxygen and investigated an asymmetrically heated magnetic loop, with and without the assumption of ionisation equilibrium. Generally they found that nonequilibrium tended to alter and smooth out the ion density distribution through the steep temperature gradients in the loop. Also, they found that the calculated line widths were changed and that the doppler shifts were significantly reduced; by greater than a factor three for OVI $(2p\,^2P_{3/2} \rightarrow 2s\,^2S_{1/2})\lambda 1031.9\mathring{A}$. However, in the case of Spadaro et al.(1990), the main results predicted that blue shifts would dominate the emission lines. Also, in Spadaro et al.(1991), they conclude that the nonequilibrium results were less able to account for the observed red shifts than the equilibrium ones.

Transient effects should certainly play a role in violent events with sudden energy releases and large temperature gradients, but, it is an open question whether the 'quiet Sun' is in a constantly dynamic state. It is worthwhile to take representative solar parameters and use them to investigate quiet sun relaxation timescales. As an illustration consider table 3.1. This shows approximate values of $\tau_{transient}$, for carbon, from the chromosphere through the transition region to the corona. The solar parameters were taken from Gabriel (1976) and the suggested boundaries and regions from Athay (1981). Clearly the effect of the He-like recombination phase plays a role in lengthening the relaxation time in the transition region, despite an initial downward trend faster than the density drop trying to offset it. In the diffuse corona the density effect eventually wins causing long relaxation times even though $N_e\tau_{transient}$ has entered its final rising phase. We can conclude that fluctuations and dynamics on timescales shorter than those shown would suggest that carbon ions should be treated as being out of equilibrium for the plasma in question. Similar

results would be expected for the other species shown in fig. 3.24. Recent evidence from SOHO-CDS & SOHO-SUMER suggests that timescales, for quiet sun activity, may indeed be shorter than those given (see chap.5).

Chapter 4

The Oxygen Derived Database and Its Application to the Solar Atmosphere

In observational studies of characteristics of the solar chromosphere and transition region, planned for the SOHO spacecraft, spectral emission by ions of oxygen will be of major importance. Determination of the coronal peak temperature, studies of differential emission measure, abundance separation, sunspot velocity fields and other dynamic flows, are all dependent, to some degree, on spectral measurements of oxygen ion emission line intensities (Harrison & Fludra(1995), Wilhelm (1993)). In previous studies, interpretation of data has often been confused by uncertainties in the accuracy of the atomic collision database underpinning the spectral reduction and in the appropriateness of simplifying assumptions in excited ion population and ionisation state models. Here, a critical review is given of the completeness and precision of the fundamental atomic collision data entering prediction of emission. This is based on the recommendations of Lang et al.(1994). Analysis of the reproduction of atomic data, from fitting procedures presented in the general literature, is also undertaken. A detailed examination of derived atomic data is presented which includes analysis of the influence of metastable states and finite plasma electron density. The importance

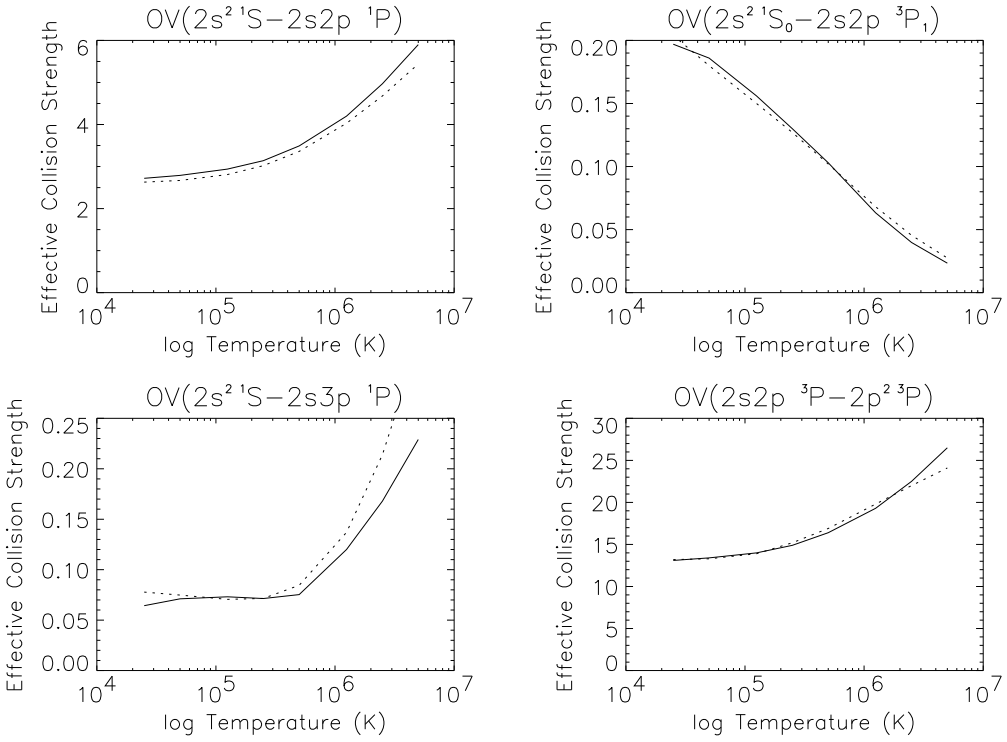

Figure 4.1: Comparison of the effective collision strength data from Kato et al.(1990) and the ADAS database for potential diagnostic transitions. The data of Kato et al.(1990) is the solid line and the older ADAS data (see text for details) is the dotted line.

of this type of approach was outlined in chap. 2. In fact, it is stressed that a complete description of light ion emission from plasmas must include these effects and that this is only possible through the adoption of a generalised collisional-radiative model. A paper is in preparation (Brooks et al.(1997)) which makes comparative analysis with existing derived atomic data, used in spectral analysis, and includes the effects of dynamic ionisation. Re-examination from this viewpoint allows us to quantify systematic errors introduced to the analysis by common simplifications and assumptions.

For practical application, and especially for the spectrometers on board the SOHO

satellite, certain contribution functions, diagnostic line intensity ratios, photon efficiencies etc. are of special importance and general interest in the astrophysical community. Scientific interest will focus around diagnostic spectral analysis of ions formed in the high temperature/low density transition zone. OII has been identified as occurring in this region but ions such as OIII, OIV, OV and OVI have greater prevalence and consequently greater diagnostic impact. Accuracy in the interpretation of SOHO data and in probing the key physical mechanisms present in the solar atmosphere can only be maintained through detailed quantitative modelling of the relevant atomic physics. A comprehensive basis of derived atomic data for analysis of oxygen ion emission and for modelling oxygen ion population distributions has been prepared, and is continually being updated, which spans both these and also laboratory fusion needs. Confidence in the results of our atomic modelling is based on its ability to account correctly for the influence of density, and excited state lifetime variations, between the different plasma regimes to which it is applied. The derived data are archived within ADAS. The oxygen data represents the most complete availability at the present time and provides a prescription for modelling the radiating characteristics of atoms and ions in solar plasmas using ADAS.

4.1 Upgrade of Oxygen Fundamental Database

We seek the best possible derived emissivity data to support the objectives of the SOHO mission. To this end it has been necessary to review and upgrade the fundamental electron impact collision cross-section data which enters our derived calculations. This is a rapidly changing situation.

4.1.1 Quality and Accuracy of Electron Impact Excitation Data - Comparison to Previous Work

Using the publication of Lang et al.(1994) as a benchmark, we have updated the existing ADAS database for oxygen ions. In addition, more recent calculations, presented in the general literature, have been incorporated where appropriate.

Transition	Comments on accuracy
OV($2p^2\ ^3P - 2s^2\ ^1S$)	27.6% more at $2.5 \times 10^4 K$ reducing to 2% at $5 \times 10^4 K$ then increasing to 143% at $5 \times 10^6 K$.
OV($2p^2\ ^1S - 2s^2\ ^1S$)	48.3% more at $2.5 \times 10^4 K$ increasing to a max. at $2.5 \times 10^5 K$ of 87.8% then reducing eventually to 20.8% less at $5 \times 10^6 K$.
OV($2p^2\ ^1S - 2s2p\ ^3P$)	27.3% more at $2.5 \times 10^4 K$ increasing to a max. at $2.5 \times 10^5 K$ of 106.0% then reducing to 61.4% at $5 \times 10^6 K$.
OV($2s3s\ ^3S - 2s2p\ ^3P$)	60% more at $2.5 \times 10^4 K$ reducing to 1% at $1.25 \times 10^6 K$ then increasing to 100% at $5 \times 10^6 K$.
OV($2s3s\ ^1S - 2s2p\ ^3P$)	58% more at $2.5 \times 10^4 K$ reducing to 2% at $5 \times 10^5 K$. Dips then increases to 56% at $5 \times 10^6 K$.
OV($2s3p\ ^1P - 2s2p\ ^3P$)	57% more at $2.5 \times 10^4 K$ reducing to 3% at $5 \times 10^5 K$. Increasing to 32% at $5 \times 10^6 K$.
OV($2p^2\ ^3P_2 - 2p^2\ ^3P_0$)	51% less at $2.5 \times 10^4 K$ reducing to 25% at $5 \times 10^5 K$ then increasing to 52% at $5 \times 10^6 K$.
OV($2p^2\ ^3P_2 - 2p^2\ ^3P_1$)	73% less at $2.5 \times 10^4 K$ reducing to 35% at $5 \times 10^5 K$ then increasing to 60% at $5 \times 10^6 K$.
OV($2p^2\ ^1S - 2s2p\ ^3P$)	Increases to 46.9% at $5 \times 10^5 K$ then reduces to 29% at $5 \times 10^6 K$.

Table 4.1: Comments on the accuracy of the effective collision strength data of Kato et al.(1990) as compared to the ADAS database for lines which show deviations of greater than 20%.

Berrington (1994) reviewed and assessed the current state of the fundamental atomic collision data for beryllium like ions. This included OV and he recommended the results of Kato, Lang, & Berrington (1990). These authors published parameters of an analytic fit to effective collision strengths among the $n = 2$ and $n = 3$ levels, including fine structure transitions. These were obtained from an **R**-matrix calculation involving the 26 lowest lying states (Berrington & Kingston -unpublished). We followed the prescribed method for calculating the effective collision strengths suggested by Kato et al., and then made a detailed comparison of the results with the OV data archived within ADAS. The older data consisted of results from the **R**-matrix calculations of Berrington et al.(1979), Berrington et al.(1985), Widing et al.(1982) and Tayal et al.(1982) and was supplemented by Born calculations (Summers (1992)-unpublished). The results of the comparison for four of the most important transitions of diagnostic interest to CDS and/or SUMER are displayed in fig.4.1. The solid line is the newer data of Kato et al. while the dotted line is the older data. The OV resonance line ($2s^2\ ^1S - 2s2p\ ^1P$) is within 8% of the older data at all temperatures. The intersystem fine structure transition OV($2s^2\ ^1S_0 - 2s2p\ ^3P_1$) is within 7%, of the older data, until $\sim 2.5 \times 10^6 K$ where the disparity begins to increase, eventually rising to 17.5% at $\sim 5 \times 10^6 K$. The OV($2s^2\ ^1S - 2s3p\ ^1P$) shows this same behaviour except that it has a greater overall deviation, i.e. $\sim$20% until the gap begins to increase, at the same temperature, rising to $\sim$41%. The OV($2s2p\ ^3P - 2p^2\ ^3P$) transition data is within 3% all the way up to $\sim 5 \times 10^6 K$ where it diverges by up to $\sim$ 9%. Comments on the transitions which showed the greatest deviations from the older data are given in table 4.1. The effective collision strengths for all the other transitions were found to agree with the older data to within 20%, except at high temperatures, and in many cases far better than 15%. We should note that the deviations at the highest temperatures ($\sim 5 \times 10^5 K$) were principally due to the nature of the ADAS extrapolation routine used on the older data. This automatically flattened off the effective collision strengths at high temperature when no data was available for a particular transition. In fact, this may also explain why smaller upturns were often found (see fig.4.1). Discrepancies at low temperatures were generally not seen, but in one case, the $2s2p\ ^3P$ to $2s3p\ ^3P$ transition, there was a deviation of $\sim$ 40%.

The largest deviation, from the older data, we discovered was in the OV($2s2p\ ^3P - 2s3s\ ^3S$) transition. This was due to an error in the fit parameters of Kato et al.(1990). The discrepancy was considerably reduced after amendment Kato(1994). We also found that the fit parameters supplied for transitions between the fine structure levels of the $2p^2\ ^3P$ term produced effective collision strengths that compared well with the older data, but that the excitation rate coefficients derived from them, using the formula suggested by Kato et al., did not correspond to the published graphs. Kato(1994) confirmed that this was a publishing mistake. Following these private communications it was decided to obtain the original Belfast calculations and compare every effective collision strength with those calculated using the published fit parameters. As a result, other publishing mistakes were identified involving the following transitions.

$$2s3p\ ^3P_2 - 2s3p\ ^3P_2$$
$$2s3s\ ^1S - 2s2p\ ^1P$$
$$2s3s\ ^3S - 2s^2\ ^1S$$
$$2s3d\ ^1D - 2s3s\ ^1S$$

In addition, it was found that a number of fine structure transitions were reproduced to worse than 10% by the approximate fit method of Kato et al. These have been noted in the adf04 file and are within 25% with the exception of the $2p^2\ ^3P_2$ to $2p^2\ ^3P_0$ and $^3P_1$ transitions which are $\sim 38\%$ and $\sim 53\%$ respectively.

In the case of nitrogen like ions, Kato (1994) was the reviewer and assessor and she made recommendations as to which sources should be used for certain transitions amongst the excited states of OII. However, since the review McLaughlin & Bell (1994) have completed a calculation of effective collision strengths in LS coupling for OII using an **R**-matrix approximation which takes account of the eleven lowest lying states of the ion. They provide a table of the coefficients of a chebyshev polynomial approximation to their calculated effective collision strengths. The fit accuracy is stated to be better than 1% for most transitions, and better than 2% at worst.

ADAS contains an adf04 file consisting of close-coupling data from Ho & Henry (1983), Pradhan (1976) and Born approximation calculations of Summers (1992). We

Transition	ADAS data source	Comments on associated spectral line
OII($2p^3\ ^2D - 2p^2(^3P)3s\ ^2P$)	Summers	CS
OII($2p^3\ ^2P - 2s2p^4\ ^2S$)	no previous data	CS
OII($2p^3\ ^2D - 2s2p^4\ ^2D$)	no previous data	CS
OII($2p^3\ ^4S - 2s2p^4\ ^4P$)	Ho & Henry	S
OII($2p^3\ ^4S - 2p^3\ ^2D$)	Pradhan	diagnostic
OII($2p^3\ ^4S - 2p^3\ ^2P$)	Pradhan	diagnostic
OII($2p^3\ ^2D - 2p^3\ ^2P$)	Pradhan	diagnostic

Table 4.2: Selected transitions of interest in OII. The data source are those prior to the work of McLaughlin & Bell (1994). CS denotes that the line is within the CDS & SUMER spectrometer wavelength ranges. The ratios of the three lines marked 'diagnostic' are sensitive to electron density and temperature and are useful for studies of planetary nebulae (Kingsburgh & English (1992)).

have updated this file to include the results of McLaughlin & Bell, adding new data and replacing older data that has been superseded. However, we have retained data for transitions that were not calculated by McLaughlin & Bell. A comparison was also made between transitions for which old and new data were available.

Four transitions between excited terms of OII give rise to spectral lines within the observable range of either the CDS or SUMER instrument (see table.4.2, which also shows potential diagnostic transitions for planetary nebulae). No values prior to those of McLaughlin & Bell were available for the OII($2p^3\ ^2P - 2s2p^4\ ^2S$) and OII($2p^3\ ^2D - 2s2p^4\ ^2D$) transitions. A comparison between the results of Ho & Henry (1983) for the OII($2p^3\ ^4S - 2s2p^4\ ^4P$) transition and Pradhan (1976) for the OII($2p^3\ ^4S - 2p^3\ ^2D$), OII($2p^3\ ^4S - 2p^3\ ^2P$) and OII($2p^3\ ^2D - 2p^3\ ^2P$) transitions, with the results of McLaughlin & Bell (1994) has already been discussed by McLaughlin & Bell (1993); however, fig.4.2 shows these deviations. It can be seen that the Ho & Henry results are within 18% at all temperatures, although they slightly overestimate below 2×10^5K and then underestimate above this threshold. Pradhan's data, for the two transitions to the ground state, are generally diverging from that of McLaughlin & Bell until $\sim 4 \times 10^5$K. This divergence is never more than ~20% below $\sim 8 \times 10^4$K

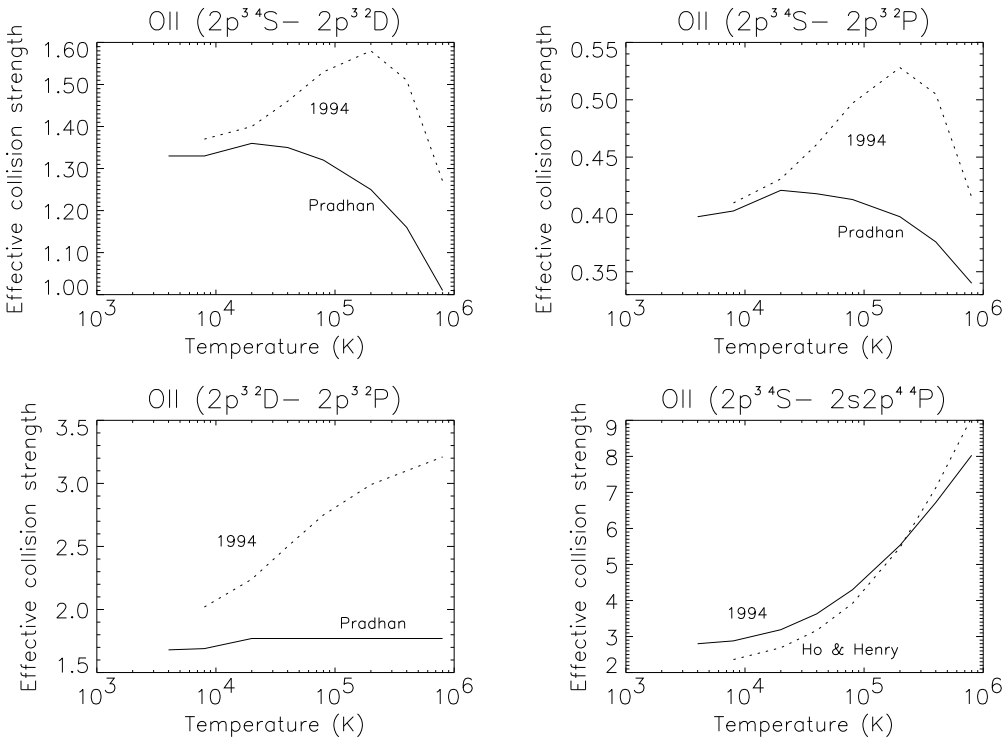

Figure 4.2: Comparison of the effective collision strength data of Ho & Henry (1983), Pradhan(1976) and McLaughlin & Bell (1994), for selected transitions. 1994 refers to the data of McLaughlin & Bell.

and takes its' peak value of 34% at 4×10^5K, for the $^2P - {}^4S$ transition. The new data for the $^2P - {}^2D$ transition appears to be significantly larger than that of Pradhan. It is already 19.5% larger at 8×10^3K and the disparity continues to grow until the newer data is $\sim 81\%$ greater at the highest temperatures.

For the OII($2p^3\ ^2D - 2p^2(^3P)3s\ ^2P$) transition we found that the Born approximation calculations of Summers were surprisingly close to the higher quality calculations of McLaughlin & Bell. At low temperatures ($\sim 8 \times 10^3 K$) the results of Summers overestimate by about 30%, thereafter, the results converge until those of McLaughlin & Bell become larger at $\sim 1 \times 10^4 K$. The two calculations subsequently diverge until

those of Summers underestimate by about 57% at $\sim 8 \times 10^5 K$. The only other transitions for which a comparison could be made were the OII($2p^3\ ^2P - 2p^2(^3P)3s\ ^2P$) and OII($2p^3\ ^4S - 2p^2(^3P)3s\ ^4P$) transitions. In the older dataset, the former transition was again Born approximation data from Summers, and the latter transition originated from Ho & Henry (1983). Once again the Born approximation data proved to be reasonably accurate. This time within ~51-61% at all temperatures. For the other transition, the results of Ho & Henry were within $\sim 16\%$ above $\sim 2 \times 10^4 K$. Initially they underestimated but above $\sim 2.5 \times 10^4 K$ they always overestimated.

New transition probabilities have also been calculated, for some transitions, using the length values for the relativistic oscillator strengths given in Table.VI of Bell, Hibbert, Stafford & McLaughlin (1994). If no new data was available, the older data (Luken & Sinanoglu (1976), Weise, Smith & Glennon (1966) and Summers (1992)) was retained.

The current state of the ADAS atomic collision database, for the rest of the ions along the oxygen isonuclear sequence, is summarised in tables.4.3 and 4.4.

Recently Aggarwal (1993) published new effective collision strengths for transitions amongst 26 LS-coupled states of the following configurations,

$$(1s^2)2s^2 2p^2, \quad (1s^2)2s2p^3$$
$$(1s^2)2p^4, \quad (1s^2)2s^2 2p3s$$
$$(1s^2)2s^2 2p3p, \quad (1s^2)2s^2 2p3d$$

with transitions amongst the latter three being reported for the first time. Aggarwal used the R-matrix method with total angular momentum $L \leq 12$ for forbidden transitions with an extension to higher partial waves, $12 \leq L \leq 40$, for optically allowed and semi-forbidden (spin allowed, parity forbidden) transitions by means of the no-exchange R-matrix code of Burke, Burke & Scott (1992). Contributions from resonances were also included. Aggarwal estimates these new results to be accurate to 10% for transitions amongst the lower excited states and about 20% for those amongst the higher excited states. Aggarwal also states that agreement with his previous calculations (see table) is generally better than 25%. He finds some differences for individual transitions due to the inclusion of resonances and proposes to assess

Ion & Reviewer	Recommendations	ADAS data sources
OI-Lang & Summers	Experimentally determined cross-sections recommended by Laher & Gilmore(1990), between the $2s^2 2p^4\ ^3P$ ground and $2s^2 2p^4\ ^1D$, ^1S, $2s^2 2p^3 3s\ ^5S$, ^3S, $2s^2 2p^3\ ^5P$, ^3P and $2s^2 2p^3 3d\ ^5D$, ^3D	As recommended. Supplemented with data from Summers(1992).
OIII-Monsignori-Fossi & Landini	R-matrix results for optically allowed transitions (Aggarwal(1985)), and forbidden transitions (Aggarwal(1983)) between $2s^2 2p^2$, $2s2p^3$ and $2p^4$. Distorted wave calculations of Bhatia et al.(1979) for transitions not covered in above two papers.*	As recommended, supplemented with data from Summers(1992) for transitions involving levels of $2s^2 2p(^2P)3l$
OIV-Sampson, Zhang & Fontes	Close coupling R-matrix results of Blum & Pradhan(1992) for fine structure transitions between levels of the $2s^2 2p$, $2s2p^2$ & $2p^3$ terms, except the 1-2 transition, where the calculations of Hayes & Nussbaumer (1983) are preferred. They also suggest a supplemental calculation to higher energies.**	Contains close-coupling calculations of Hayes (1983) from $2s^2 2p\ ^2P$ & $2s2p^2\ ^4P$ to the 8 lowest lying levels Robb (1980) for transitions between $2s2p^2\ ^2S$, ^2P & ^2D. Supplemented with Summers data for n=2-2, 3-3, & others involving n=2.

Table 4.3: Current state of the ADAS atomic data library for the low charge oxygen ions not discussed in the text. For more details see Summers(1996), Lang & Summers (1995)-ADAS document. *See text. **Zhang(1994) has now completed this calculation and the results are due for inclusion.

Ion & Reviewer	Recommendations	ADAS data sources
OVI-McWhirter	Relativistic distorted wave calculations of Zhang et al.(1990) altered to include resonance effects (for 2s-3s,3p & 2p-3s,3p) and to converge with close-coupling results (for 2s-3p, 2p-3s,3p,3d), following the work of Bhadra & Henry(1982).	As recommended. Supplemented with data from Summers(1992).
OVII-Dubau	Data from the review by Kato & Nakazaki(1989) for $1s^2 - 1s2l$, Zhang & Sampson (1987) for transitions within $1s2l$, Tayal & Kingston(1984) & Sampson, Goett & Clark(1983) for $1s^2 - 1snl$ n=3 and above.	As recommended except amongst $1s2l$ where the results of Pradhan et al.(1981) were used.*
OVIII-Callaway	Close coupling results of Abu-Salbi & Callaway(1981) for 1s-n=2 transitions.	Born Approximation data of Summers (1992)

Table 4.4: Current state of the ADAS atomic data library for the moderately high charge oxygen ions not discussed in the text. For more details see Summers(1996), Lang & Summers (1995)-ADAS document. *-Under review.

λ1302Å, λ1305Å, λ1306Å	SUMER: detailed study of fine loop structures in the corona.
λ1152.1Å, λ1355.59Å, λ1358.5Å	Within SUMER range 1st order.

Table 4.5: OI emission lines and their application to SOHO-CDS and/or SUMER

their accuracy in due course. These results have been incorporated into an updated adf04 file and will be included in the central ADAS database after the inclusion of radiative recombination data has been completed. Lennon & Burke(1994) also published Maxwellian- averaged collision strengths. However, Dere et al.(1996) found no appreciable differences from the results of Aggarwal(1983).

4.2 The use of Oxygen Data for SOHO-CDS and SOHO-SUMER Spectroscopy

Brief descriptions and associated references for more information on CDS & SUMER were given in chap.1. Based upon their spectral wavelength coverage and sensitivities, sets of observable spectrum lines have been identified which have diagnostic impact on the solar atmospheric structure. These spectrum lines are forming the basis of coordinated observing sequences. Using the Blue Book and the Red Book (Wilhelm et al.(1993)), we have identified important emission lines of oxygen ions that have been selected for observing sequences. Tables 4.5 to 4.11 summarise these lines and their applications.

The majority of lines mentioned in tables 4.9 and 4.10 are expected also to be used in a CDS campaign to check on the atomic physics of the OV ion.

In practice, sub-selections of the above lines are made to form observing sequences with specific diagnostic purposes such as identification of high velocity events or differential emission measure analysis of the quiet sun. It is convenient in the preparation

λ833.34Å	Within SUMER range 1st order.
λ644.1Å	Within SUMER range 2nd order.
λ616.6Å	Within CDS range and SUMER range 2nd order.
λ718.5Å	Within CDS range and SUMER range 2nd order.

Table 4.6: OII emission lines and their application to SOHO-CDS and/or SUMER

λ702.9Å, λ525.8Å	Within CDS range and SUMER range 2nd order.
λ703.9Å	CDS: Study of He enhancement in the transition zone, study of line broadening as an indicator of MHD waves
λ599.6Å λ1015.36Å	High velocity events. SUMER: relationship between high/low density structures in the solar atmosphere.
λ507.6Å	Within SUMER range 2nd order.
λ718.5Å	Within CDS range and SUMER range 2nd order.
λ834.46Å	Within SUMER range.

Table 4.7: OIII emission lines and their application to SOHO-CDS and/or SUMER. Note that the OIII(λ599.6Å/λ703.9Å) line ratio is a CDS temperature diagnostic.

λ790.2Å	CDS: dynamic analysis.
λ553.34Å, λ554.08Å, λ555.28Å, λ608.40Å, λ609.8Å	CDS: differential emission measure study of quiet sun.
λ554.5Å	CDS: solar mass ejection studies, evolution of large scale structures, velocity fields near sunspots, high velocity events, granulation in coronal holes.
λ1249.28Å	SUMER: relationship of coronal & transition region emission line profiles.
λ787.7Å	Within SUMER range 2nd order.
λ1407.39Å	Within SUMER range 1st order.

Table 4.8: OIV emission lines and their application to SOHO-CDS and/or SUMER. Note that the OIV(λ625Å/λ790.2Å) line ratio is a CDS density diagnostic and that the OIV(λ1407Å/λ1404Å) & OIV(λ790Å/λ554Å) ratios are density and temperature diagnostics for SUMER, respectively. The OIV(λ1397.2Å, λ1399.77Å, λ1407.39Å, λ1401.16 Å) SUMER lines with the OIV(λ555.28Å) CDS line supporting, produce density sensitive ratios. Finally, the OIV/SIV(λ1404.8Å) ratio is also density sensitive.

λ629.73Å	CDS: differential emission measure study, dynamics, coronal temperature, high velocity events, flows in the vicinity of prominences, also supports SUMER study of line profiles in transition zone & corona. SUMER: line broadening as a signature of hydromagnetic waves.
λ172.17Å λ758.68Å, λ760.45Å, λ761.13Å, λ762.0Å	CDS: coronal temperature study. CDS: differential emission measure study.
λ760Å	SUMER/CDS: He enhancement in transition zone.
λ1218.34Å	SUMER: dynamics, oscillations of sunspots.
λ1259.46Å	SUMER: study of line profiles in transition zone and corona.
λ1371.3Å	Within SUMER range 1st order.
λ672.6Å, λ675.7Å	Within SUMER range 2nd order.

Table 4.9: OV emission lines and their application to SOHO-CDS and/or SUMER.

λ760Å/λ629.73Å*	SUMER prime candidate for density diagnostics.
λ1218Å/λ629.73Å	Density diagnostic.
λ192.9Å/λ248.46Å	Density diagnostic.
λ215.25Å/λ220.35Å	Density/temperature diagnostic.
λ172Å/λ630Å	CDS prime candidate for temperature diagnostics.
λ760Å/λ630Å	SUMER prime candidate for density diagnostics.
λ193Å/λ760Å	Temperature diagnostic.
λ215Å/λ193Å	Density/temperature diagnostic.
λ193Å/λ172Å	Density diagnostic.
λ220Å/λ248Å	Temperature diagnostic, also slightly density sensitive.
λ220Å/λ172Å	Slightly density/temperature sensitive.
λ270.98Å/λ215Å	Density diagnostic.
λ271Å/λ215Å	Density diagnostic.
CaIV/OV(λ669.6)Å	Within CDS range.

Table 4.10: OV emission line ratios which are potential diagnostics of temperature and density and are within CDS and/or SUMER wavelength ranges. Wavelengths with places after the decimal point are LSJ resolved the others are summed multiplets. * denotes that fine structure transitions of the OV(λ760Å) line, which are quantum mechanically allowed, also produce density sensitive line ratios.

λ183.9Å	Within CDS range.
λ172.93Å	CDS: study of temperature gradient in a coronal hole.
λ173.1Å, λ184.1Å	CDS: study of peak temperature of the corona.
λ1031.9Å	SUMER: dynamic events, supports CDS peak temperature of corona study, detailed analysis of fine loop structures, flows near prominences, temperature gradient in coronal holes, full sun disc image.
λ1037.6Å	SUMER: dynamic events, peak temperature of corona, flows near prominences, temperature gradient in coronal holes, full sun disc image.

Table 4.11: OVI emission lines and their application to SOHO-CDS and/or SUMER. Note that the SUMER observed OVI(λ1031.9Å, λ1037.6Å) to the CDS observed OVI(λ172.93Å, λ173.1Å) ratios are temperature sensitive.

of the theoretical emissivity coefficients, effective contribution functions etc. associated with these measurements, to form a similar grouping called a 'script'. The script steers the theoretical calculations which prepare these data allowing choice of ionisation balance, contributions to a line from various metastables, recombination etc. A detailed discussion of the specification format is given in sec.3.2.1 and an example (fig. 3.21) is also shown. The script draws from photon emissivity collections stored in ADAS data files of format adf15. In practice, parallel scripts for other elements are also prepared to complete the targeted study. For this work, in which we are primarily concerned with the precision of the atomic basis of analysis, we have prepared a general script that takes account of all the considerations outlined in tables 4.5 to 4.11.

4.3 Collisional-Radiative Modelling

4.3.1 Metastable Resolved Equilibrium Ionisation Balance and Effective Radiated Power

As mentioned in section.2.2.3, it has been usual in describing the ionisation state of ions of oxygen, to assume that the population density is distributed amongst the lowest (ground) levels of each ionisation stage only. Many calculations are available which adequately describe the spectral emission from oxygen ions in many circumstances. Despite this discrepancies do still exist so it is desirable to attempt to explain these by adopting a more complete approach. In accordance with the discussion in chapter.3 sec.3.2.1 we note that the ions of oxygen do have metastable states whose influence should be investigated. For example, the $O^{+4}(2s^2\ ^1S)$ ground and the $O^{+4}(2s2p\ ^3P)$ metastable terms have a population ratio ~ 1.0 in equilibrium at $T_e = 8.1 \times 10^5 K$ and $N_e = 1 \times 10^{10} cm^{-3}$. The high population of a metastable such as $O^{+4}(2s2p\ ^3P)$ is due to its slow collisional relaxation time compared with a normal freely cascading excited population such as that of $O^{+4}(2s3p\ ^1P)$. The result of allowing for this second metastable explicitly is to improve the accuracy of the ionisation balance calculation. This is because, for example, the marked difference in

z	m_z	σ			
		1	2	3	4
0	4	$2s^2 2p^4\ ^3P$	$2s^2 2p^4\ ^1D$	$2s^2 2p^4\ ^1S$	$2s^2 2p^3 3s\ ^5S$
1	3	$2s^2 2p^3\ ^4S$	$2s^2 2p^3\ ^2D$	$2s^2 2p^3\ ^2P$	
2	4	$2s^2 2p^2\ ^3P$	$2s^2 2p^2\ ^1D$	$2s^2 2p^2\ ^1S$	$2s 2p^3\ ^5S$
3	2	$2s^2 2p\ ^2P$	$2s 2p^2\ ^4P$		
4	2	$2s^2\ ^1S$	$2s 2p\ ^3P$		
5	1	$2s\ ^2S$	*		
6	2	$1s^2\ ^1S$	$1s 2s\ ^3S$		
7	1	$1s\ ^2S$			
8	1	^1S			

Table 4.12: Metastable partition of oxygen in LS-coupling. z is the ion charge, m_z is the number of metastables for the z times ionised stage and σ is the metastable index. *At very high densities when $2s\ ^2S$ and $2p\ ^2P$ become closely coupled collisionally, it is useful, in some contexts, to treat 2p as a metastable.

dielectronic capture by $O^{+4}(2s^2\ ^1S)$ and $O^{+4}(2s2p\ ^3P)$ can be included (see below). As pointed out in chapter.3 sec.3.2.1 and chapter.2 sec.2.1.2, if the timescale of (diffusive) transport across a temperature gradient is of the same order as the collisional timescale then this metastable resolved picture is mandatory. The metastables of O^{+1} and O^{+2} are typically in this situation in the edge of a tokamak. For this work, we solve the metastable resolved equilibrium ionisation balance matrix equation for oxygen as given in eq.3.21. The ground state is also a 'metastable' in this notation.

For oxygen, the metastable 'partition' is given in table 4.12. The effective coefficients, linking the metastable populations, are also as described in chapter.3 sec.3.2.1. For example, $S^{3\to4}_{2s^2 2p\ ^2P\to 2s2p\ ^3P}$ is the coefficient linking the $O^{+3}(2s^2 2p\ ^2P)$ ground state to the $O^{+4}(2s2p\ ^3P)$ metastable, and in the case of O^{+4}, there is a collisional-radiative coefficient $X^{4\to4}_{2s^2\ ^1S\to 2s2p\ ^3P}$ coupling the two metastable terms.

For a plasma of fixed electron density, N_e, and electron temperature, T_e, with no influx or efflux of oxygen ions, the equilibrium ionisation balance fractional abundances are,

$$\left.\frac{N^z}{N_{tot}}\right|_{equil} \equiv \frac{N^z(t\to\infty)}{N_{tot}} \tag{4.1}$$

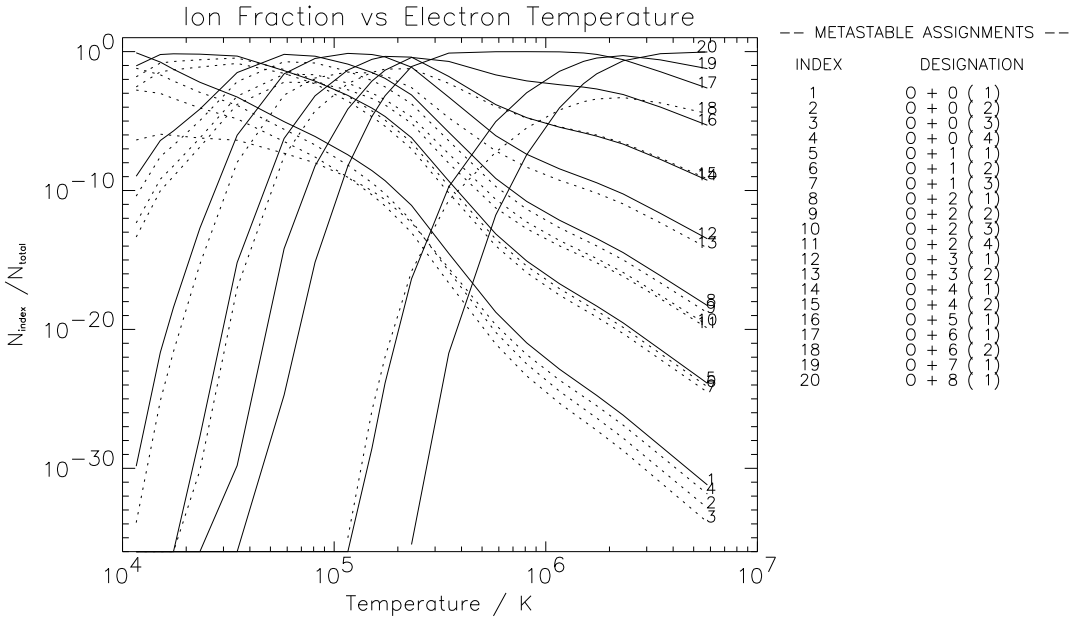

Figure 4.3: Metastable resolved equilibrium ionisation balance for oxygen. $N_e = 1.0 \times 10^{10} cm^{-3}$. Metastable index designations on the right hand side correspond to the partition of table.4.12. Solid line - ground state, dotted lines - metastable states.

where $N_{tot} = \sum_{z=0}^{8} N^z = const.$ in the usual metastable unresolved picture. Similarly, in the resolved picture, the ionisation fractional abundances are $\frac{N^z_\sigma}{N_{tot}}\Big|_{equil}$ where $\sigma = 1, ...m_z$ and are as illustrated in fig.4.3.

The instantaneous effective radiated power coefficient associated with metastable σ of ionisation stage z, is P^z_σ. It is commonly separated as $P^z_{\sigma,LT} + P^z_{\sigma,RB}$ which distinguishes the parts of the power driven by excitation followed by line emission and the part driven by recombination. Bremsstrahlung is usually incorporated with the latter. The equilibrium radiated power function, P_{tot}, obtained by combining

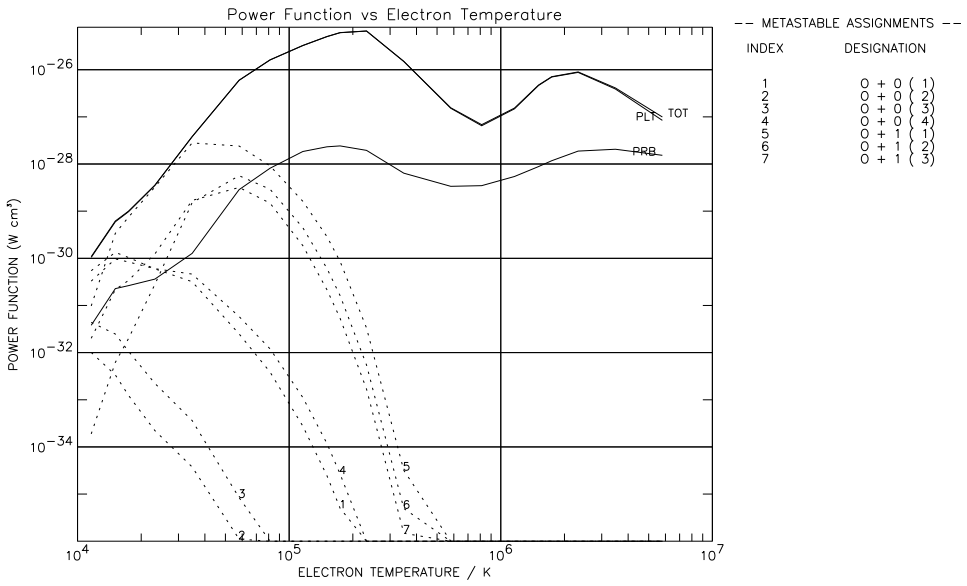

Figure 4.4: Contributions to the radiated power function of oxygen from low ionisation stage metastables i.e. O^{+0} and O^{+1}. $N_e = 1.0 \times 10^{10} cm^{-3}$.. Solid upper line - total, solid middle line - line power, solid lower line - Bremsstrahlung power, dotted lines - metastable contributions.

these coefficients with the equilibrium ionisation balance is,

$$P_{tot} = \sum_{z=0}^{8} \sum_{\sigma=1}^{m_z} \left[P_\sigma^z \left. \frac{N_\sigma^z(t \to \infty)}{N_{tot}} \right|_{equil} \right] \tag{4.2}$$

The contribution in square brackets for the low ionisation stage metastables of oxygen is illustrated in fig.4.4.

An important quantity in fusion plasma studies, which plays a role also in the solar atmosphere, is the excess or deficit of radiated energy compared with that which would have been radiated in equilibrium. For example, the radiated energy from an inflowing O^{+0} atom, released from a limiter and entering a local high temperature plasma, which experiences a time dependent ionisation from its initial neutral state until equilibrium. For fixed electron density and temperature, the energy excess function is,

$$W_{excess} = \int_{t=0}^{\infty} \sum_{z=0}^{z_0} \sum_{\sigma=1}^{m_z} P_\sigma^z \frac{N^z(t) - N^z(t=\infty)}{N_{tot}} \tag{4.3}$$

with simpler equivalent quantities in the metastable unresolved piture.

4.3.2 Oxygen Excited Populations

Consider the O^{+3} ion. The adjacent ionisation stages are O^{+4} and O^{+2}. The levels of the O^{+3} ion can be separated into *metastable levels* O_σ^{+3}, where the Greek index σ spans the number of metastables, m_z, corresponding to two in this case i.e. $2s^2 2p\ ^2P$ and $2s2p^2\ ^4P$. Let the excited levels be denoted by O_{nl}^{+3}, where $nl = 1, ...\infty$ and n and l are themselves the usual principal quantum number and orbital angular momentum quantum number respectively. The driving mechanisms considered for populating the excited levels are, excitation from the metastable levels O_σ^{+3}, recombination from the metastable levels of the adjacent ion O_τ^{+4} and ionisation from the metastable levels of the adjacent ion O_ρ^{+2}, where ρ and τ index the metastable levels of these ions as given in table 4.12. The dominant population densities of the ions in the plasma are those of the levels O_σ^{+3}, O_τ^{+4} and O_ρ^{+2}, denoted by N_σ, N_τ^+ and N_ρ^- respectively. The ratios of these dominant populations to N($2s^2 2p\ ^2P$), the ground level, are assumed known from a separate calculation of a dynamical ionisation balance. The other populations

of significance in the plasma are the electron density N_e, the proton density N_p and the neutral hydrogen density N_H. A *quasi-static equilibrium* of the excited populations, with respect to these dominant populations, gives the connection between them as discussed in sec.2.2.2. Evaluation of the excited populations locally in the plasma, for this specific ion, is computed from the following equation,

$$N_{nl} = f^{(exc)}_{nl,2s^22p\ ^2P} N_e N_{2s^22p\ ^2P} + f^{(exc)}_{nl,2s2p^2\ ^4P} N_e N_{2s2p^2\ ^4P} + f^{(rec)}_{nl,2s^2\ ^1S} N_e N^+_{2s^2\ ^1S} + f^{(rec)}_{nl,2s2p\ ^3P} N_e N^+_{2s2p\ ^3P} \tag{4.4}$$

where, for simplicity, terms arising from ionisation and charge exchange recombination have been omitted. The $f^{(exc)}_{nl,\sigma}$ and $f^{(rec)}_{nl,\tau}$ are the effective contributions to the excited populations from excitation from the metastables and from free electron capture by parent metastables respectively. The coefficients depend on density as well as temperature. This allows specification of the *excitation* photon emissivity coefficient,

$$\mathcal{PEC}^{(exc)}_{2s^22p\ ^2P,nl\rightarrow n'l'} = (A_{nl\rightarrow n'l'} f^{(exc)}_{nl,2s^22p\ ^2P})/N_e \tag{4.5}$$

and the *recombination* photon emissivity coefficient

$$\mathcal{PEC}^{(rec)}_{2s^2\ ^1S,nl\rightarrow n'l'} = A_{nl\rightarrow n'l'} f^{(rec)}_{nl,2s^2\ ^1S} \tag{4.6}$$

and similar coefficients for the other metastables. That is each of these coefficients is associated with a particular metastable σ or τ of the O^{+3} or O^{+4} ions respectively. By combining these emissivity coefficients with the equilibrium ionisation balance metastable fractional abundances the *contribution functions*, $G_{nl\rightarrow n'l'}(T_e, N_e)$, are obtained. Specifications of these contribution functions differ slightly between solar astrophysical plasma and laboratory plasma usages. For astrophysical applications we define the contribution function to include the relationship between electron and hydrogen (ion+neutral) densities in the solar atmosphere. Thus, for our specific example,

$$G_{nl\rightarrow n'l'} = \frac{N_e}{N_H} \left[\mathcal{PEC}^{(exc)}_{2s^22p\ ^2P,nl\rightarrow n'l'} \frac{N^{+3}_{2s^22p\ ^2P}}{N_{tot}} \right|_{equil}$$

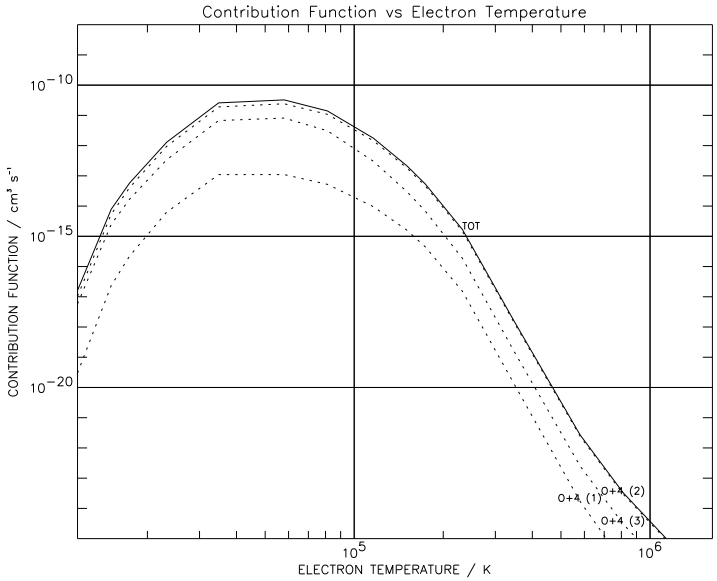

Figure 4.5: Contribution function for the OII($2p^3\ ^2D - 2s2p^4\ ^4P$)λ718.5Å transition showing the parts arising from the different metastables.

$$+\mathcal{PEC}^{(exc)}_{2s2p^2\ ^4P,nl\rightarrow n'l'}\ \left.\frac{N^{+3}_{2s2p^2\ ^4P}}{N_{tot}}\right|_{equil}$$
$$+\mathcal{PEC}^{(rec)}_{2s^2\ ^1S,nl\rightarrow n'l'}\ \left.\frac{N^{+4}_{2s^2\ ^1S,nl\rightarrow n'l'}}{N_{tot}}\right|_{equil}$$
$$+\mathcal{PEC}^{(rec)}_{2s2p\ ^3P,nl\rightarrow n'l'}\ \left.\frac{N^{+4}_{2s2p\ ^3P,nl\rightarrow n'l'}}{N_{tot}}\right|_{equil}\Bigg] \qquad (4.7)$$

An illustration showing the localisation of the contribution function in temperature and the varying influence of metastable levels is given in fig.4.5.

4.4 Derived Recombination/Ionisation Rate Coefficients and the Resultant Ionisation Balance

In this work we use new calculations of dielectronic recombination in preparation of the generalised collisional dielectronic recombination coefficients. These data are incorporated from large structured datafiles in two ways. Firstly, direct state selective capture to identified low levels are extracted, combined with state selective radiative recombination data and added as an extension to the complete collisional rate coefficient/A-value/energy level data collection for these low levels. This is called a *specific ion file* which we have also referred to by its ADAS data format number, adf04. Secondly, dielectronic data grouped according to parent metastable and recombined ion principal quantum shell/spin system are drawn by a very many (bundle-nS) quantum shell collisional radiative calculation (see Burgess & Summers(1976)). Then in a final step, the bundle-nS results are projected onto the specific ion file low level data and the low level population calculation is completed. This yields also the metastable final ion/metastable initial parent ion collisional dielectronic coefficients (see chap.2, sec.2.2.2). The key issue is the accuracy and behaviour of these coefficients. Fig.4.6 shows the behaviour of the collisional-dielectronic coefficients with density. Capture from the beryllium-like (O^{+4}) $2s^2\ ^1S$ and $2s2p\ ^3P$ metastables is contrasted. Note the relatively small coefficient for the $2s2p\ ^3P$ metastable, due to the Auger break-up to the $2s^2\ ^1S$ parent. This coefficient is insensitive to the density until it gets very high, due to the secondary Auger process already depleting the excited states which for a non-metastable parent would be vulnerable to collisional re-ionisation. The collisional-dielectronic coefficient for capture from the $2s^2\ ^1S$ parent shows the usual density induced reduction at quite moderate densities and high temperatures. Note the increase with density of the coefficient at low temperatures in the radiative/three-body regime. Although for the densities of the solar chromosphere/transition region, the finite density results are required, most previous workers have used the total dielectronic recombination coefficient and thus limit their results to the case of zero density (e.g. Hahn(1985)). On some occasions an imprecise density dependent reduction is applied to the total zero-density coefficient, but this takes no true account

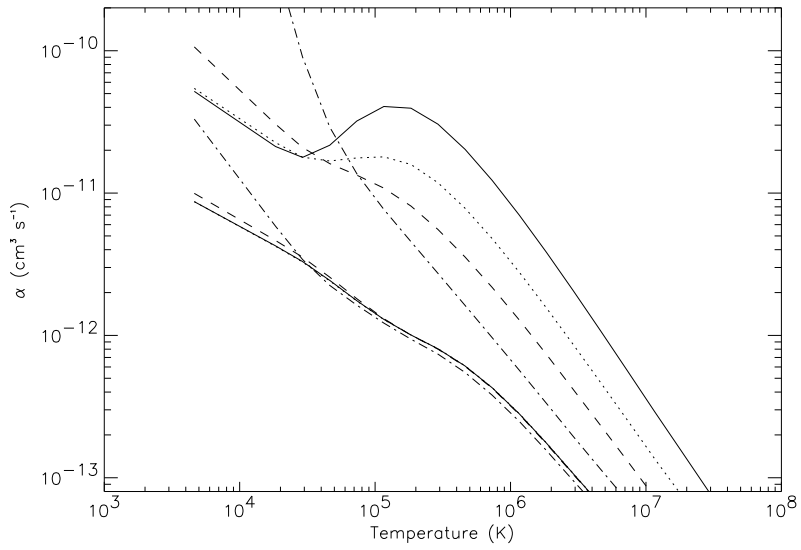

Figure 4.6: Generalised collisional dielectronic recombination coefficient example for $O^{+4}(2s^2\ ^1S \rightarrow 2s^2 2p\ ^2P$ (upper solid line) and $O^{+4}(2s2p\ ^3P \rightarrow 2s^2 2p\ ^2P)$ (lower solid line) as a function of temperature, for densities $N_e = 10^4$ - solid line, 10^{10} - dotted line, 10^{13} - dashed line and $10^{16} cm^{-3}$ - dash dot line.

of the distribution of recombination into excited states of the particular ion.

There is a problem at very low temperatures, $< 1.0 \times 10^4 K$, when very few low autoionising levels contribute to the dielectronic coefficient and their precise energies are critical. The present calculations are based on LS-coupling and theoretical energy level calculations and so are inaccurate in this regime. At the temperatures of the transition region, the high temperature dielectronic recombination is more relevant. Corrections can be introduced to take account of low temperature dielectronic recombination (Storey et al.(1990)) but are not relevant here.

For the metastable resolved picture, resolution of ionisation rate coefficients by initial and final states is also required. Such data have not been available generally in the past. Ionisation cross-sections and rate coefficients are sometimes presented according to initial metastable but invariably summed over final states. In the work presented here, we have compensated for this deficiency by imposing a 'resolution' of

the total coefficient using the principles discussed by Burgess et al.(1977) and Summers & Hooper (1983). In a new development, we have commenced more detailed calculations of resolved ionisation rate coefficients and have established an organisation of the direct state resolved ionisation coefficients analogous to that used for state selective dielectronic and radiative recombination coefficients. These data may then be mapped into the low level specific ion files in like manner and then used in production of the generalised collisional dielectronic ionisation coefficients.

For $O^{+0} \rightarrow O^{+1}$, the rate coefficients involving ionisation from the 2p subshell were determined using the experimental data of Brook et al. (1978), for $O^{+1} \rightarrow O^{+2}$, that of Aitken et al.(1971) and for $O^{+2} \rightarrow O^{+3}$, that of Gregory et al.(1985). Details of the theoretical calculations and approximations used are given in Griffin(1995). In the general case, a substantial part of the task relates to excitation/autoionisation pathways (complementary to the dielectronic recombination situation). For the ions of oxygen, this appears less important. The extensions mentioned above have not yet been fully implemented in the central ADAS codes. They are scheduled for inclusion in mid 1997 together with a new very low temperature enhancement.

Of primary importance for solar astrophysics is the result of combining the recombination and ionisation data to form an equilibrium ionisation balance. As pointed out in sec.4.3.1, our primary ionisation balance is a metastable-resolved one. For assessment of the significance of the present developments and future comparison with earlier work we have used the equilibrium metastable to ground fractions, for each ionisation stage in the resolved picture, to reassemble a stage to stage ionisation balance.

It is to be noted that the ionisation balance is density dependent at moderate densities due to the dielectronic part, and at relatively high densities due to the stepwise ionisation part. Fig.4.7 contrasts the zero density balance with the balance at electron density $N_e \sim 5.0 \times 10^9 cm^{-3}$, representing the upper solar transition region. The shifts of the stage abundance peaks compared with the zero density cases are given in table 4.13. The final definitive position on the ionisation balance and comparison to previous workers (e.g. Arnaud & Rothenflug (1985)) will not be presented until the extension defined above is completed. However, no substantive error is indicated

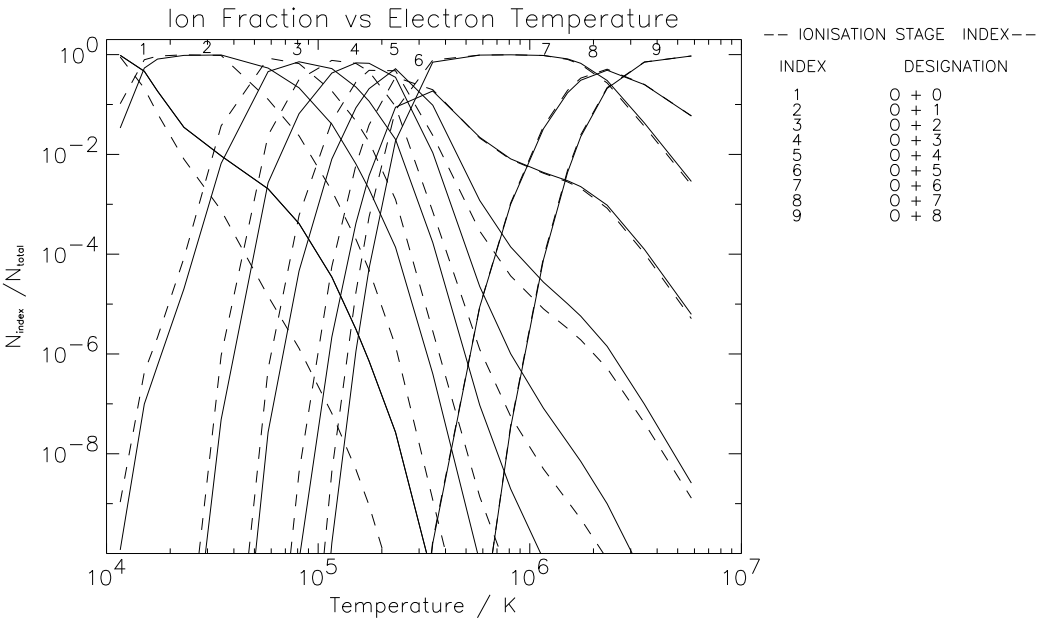

Figure 4.7: Comparison of reconstructed stage to stage ionisation balance at electron densities $N_e = 0.0$ (solid line) and $5.0 \times 10^9 cm^{-3}$ (dashed line).

Ion	Temperature Displacement (K)	Ion	Temperature Displacement (K)
O^{+0}	s	O^{+5}	6.6×10^4
O^{+1}	3.0×10^3	O^{+6}	s
O^{+2}	2.1×10^4	O^{+7}	s
O^{+3}	4.7×10^4	O^{+8}	s
O^{+4}	2.7×10^4		

Table 4.13: Temperature displacement of the ionisation balance fractional abundance peaks as a result of density. An 's' denotes that the shifts were smaller than the temperature grid separations or that the peaks were so broad that the shifts were too small to notice (see fig.4.7).

in the present work.

4.5 Derived Populations and Emissivities

Turning to the spectroscopy of oxygen ions, we consider the influence of various factors on the populations of the excited states and then the emissivities. The individual electron impact excitation and deexcitation rate coefficients are of course fundamental in determining the final accuracy of any calculated emissivity. We have already explored the absolute precision of these cross-sections in sec.4.1.1. Here we examine rather the importance of finite plasma electron density, including or ignoring metastables and the coupling of low levels to the infinite higher n-shell populations for step-wise ionisation. Such examination is possible within our resolved picture. Fig.4.8 shows the emissivity coefficient for the transition $O^{+5}(5s\ ^2S - 2p\ ^2P)\lambda 117.4\mathring{A}$ as a function of electron density. This line illustrates the case of no metastables. Note that at an electron density $N_e = 1.0 \times 10^{14} cm^{-3}$, the $2p\ ^2P$ is already 10% of the ground population. Note the moderate decrease at higher electron densities and the increase due to the inclusion of step-wise ionisation pathways.

For emissivity coefficients of lines from an ionisation stage with metastables, the separate effective emissivities associated with each metastable are relevant. Effective coefficients are also present, associated with recombination and inner shell ionisation driven by the metastables of the adjacent stages. As in the ionisation balance case, we can reconstruct an unresolved emissivity coefficient by using the equilibrium metastable to ground fractions for each ionisation stage. Fig.4.9 illustrates these effects for $O^{+4}(2s3d\ ^3D - 2s2p\ ^3P)\lambda 192.9\mathring{A}$. Note that the excitation energies from the ground and metastable states to the $2s3d\ ^3D$ state are similar. Therefore, the spin changing contribution is smaller and the $2s2p\ ^3P$ metastable is more efficient at exciting the $2s3d\ ^3D$ state. Note also that the equilibrium reconstructed coefficient contains excitation contributions from both metastables. Exploration of other effects, for example the inclusion of excited state ionisation and recombination contributions to the line emission will be presented by Brooks et al.(1997).

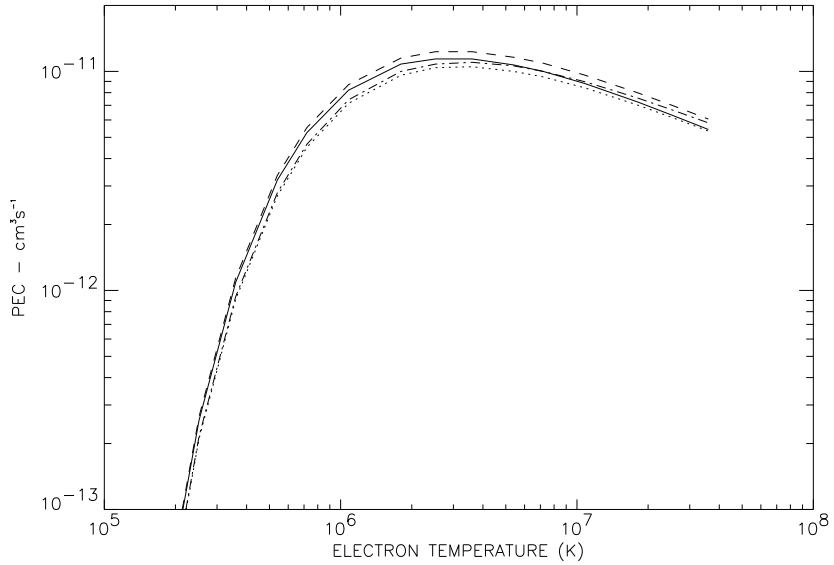

Figure 4.8: Influences on the $O^{+5}(5s\ ^2S - 2p\ ^2P)\lambda 117.4$Å line emissivity coefficient. Solid line - *llu* - low level metastable unresolved at $N_e = 10^{11} cm^{-3}$. Dotted line - *llu* at $N_e = 5 \times 10^{14} cm^{-3}$. dashed line - *pju* - high level pathways to ionisation and redistribution included, at $N_e = 10^{11} cm^{-3}$. Dash dot - *pju* at $N_e = 5 \times 10^{14} cm^{-3}$.

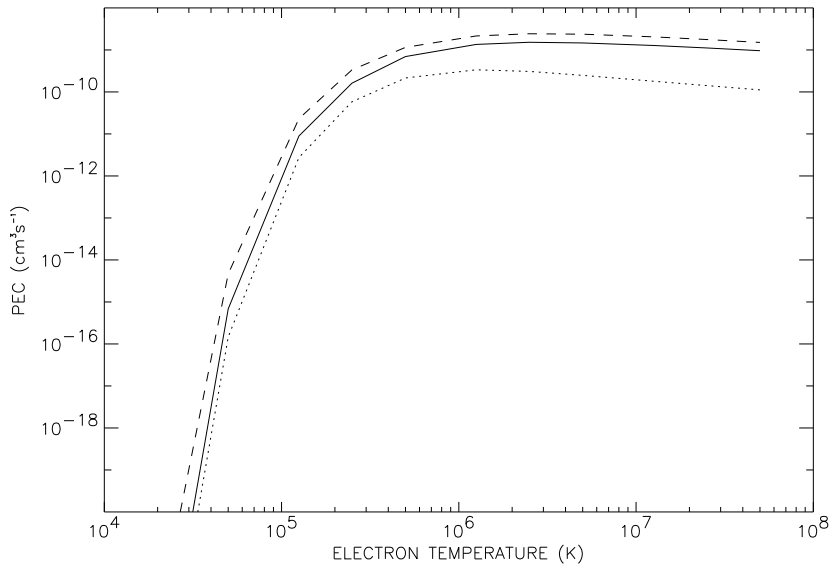

Figure 4.9: Effective emissivity coefficients for the $O^{+4}(2s3d\ ^3D - 2s2p\ ^3P)\lambda 192.9\mathring{A}$ line, from the $O^{+4}(2s^2\ ^1S)$ and $O^{+4}(2s2p\ ^3P)$ metastables. The results are presented at an electron density of $7.81 \times 10^{10} cm^{-3}$. The contribution from the $2s2p\ ^3P$ metastable is the dashed curve. The contribution from the $2s^2\ ^1S$ ground state is the dotted curve. The reconstructed stage emissivity for the excitation part is the solid curve.

4.6 Applications to Solar Atmospheric Structure

The important lines of oxygen ions for SOHO-CDS & SOHO-SUMER have been identified from our general script (see sec.4.2) with the aid of the review of sec.4.2). Data collections of $G(T_e)$ functions and spectrum line intensities of these lines are under preparation for solar atmospheric models, that is, linked pairs of electron density and electron temperature associated with height in the atmosphere. This is possible for, say, the various atmospheric models of Vernazza et al.(1981). For more general convenience, $G(T_e)$ functions for many transitions have been calculated and are stored in the central ADAS database for specific constant densities and constant pressures. The location of the $G(T_e)$ functions with temperature indicates the importance of particular spectrum lines for different parts of the atmospheres. Such considerations are of paramount importance if a differential emission measure analysis is to be attempted.

The effect of finite plasma electron density is again of paramount importance. For advancement of solar atmospheric studies to differential emission measures in density as well as temperature, it is of interest to know also the location of the $G(T_e, N_e)$ functions in density. This again can be linked to particular model heights in the atmosphere. More importantly, calculation of contribution functions dependent on density is essential for bi-variate DEM studies unless advantageous lines with weak density dependences have already been chosen. This however is a dangerous pastime as, anticipating the discussion of chap.5 sec.5.6.5, density dependences can be found in lines where it is not altogether expected. Fig. 4.10 shows the locations of the contribution functions for the OII($\lambda 833.8\mathring{A}$) and OV($\lambda 760.36\mathring{A}$) lines. The shifted positions in temperature are familiar and correspond roughly to upper chromosphere/ lower transition region and upper transition region temperatures for OII and OV respectively. Note that the density dependence increases the line emission for OV and shifts it to lower temperatures before decreasing again at $1 \times 10^{15} cm^{-3}$. In the case of OII, the density dependence acts to decrease the line emission and shift it to lower temperatures while 'peaking' the function and decreasing the range of emission. The reduction is continuous for increasing density.

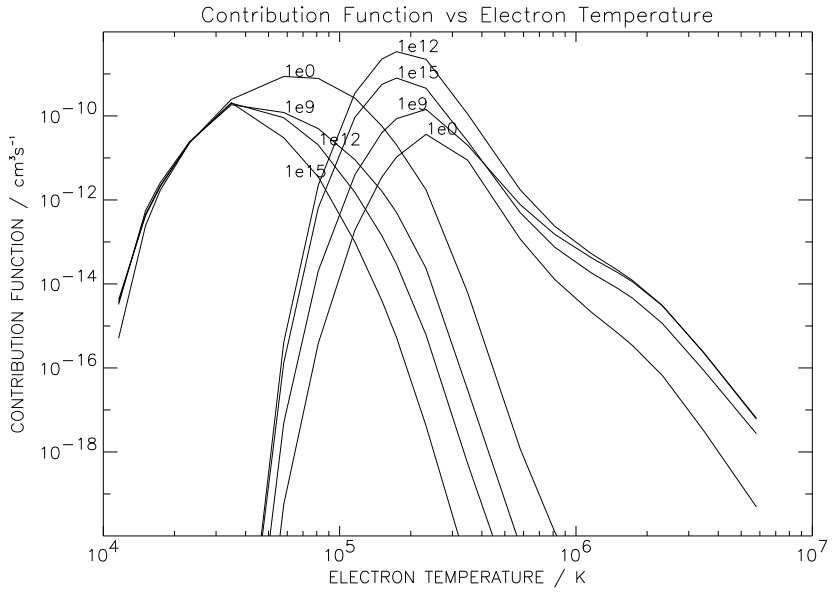

Figure 4.10: Contribution function for the OV($2s2p\ ^3P - 2p^2\ ^3P$)λ760.36$\mathring{A}$ and OII($2p^3\ ^4S - 2s2p^4\ ^2D$)λ833.8$\mathring{A}$ lines and the effect of finite plasma electron density.

4.7 Concluding Remarks

An extensive review of the fundamental electron impact excitation data for oxygen has been undertaken and the recommended data integrated into the ADAS database. These data have been combined with generalised collisional dielectronic recombination and ionisation data to calculate a metastable resolved equilibrium ionisation balance for oxygen using the numerical technique outlined in chap.3 sec.3.2.1. This allowed detailed examination of the role of metastable states in the ionisation balance and spectral emissivities.

We have shown that non-ground state metastables can contribute substantially to contribution functions, equilibrium photon emissivities and radiated power. In addition, they can attain populations comparable to ground states. Previous work in the fusion context has also shown that metastable states can shift the reconstructed ionisation stage peaks in temperature due to their effects on ionisation coefficients

(Dickson (1993)). From chap.2 sec.2.1.2 we see that metastable states have lifetimes comparable with timescales for plasma transport. As pointed out in sec.4.3.1 the metastable resolved picture is mandatory here. To model radiated power and spectral intensities in such environments also requires a metastable resolved transient ionisation model. ADAS provides a capability to calculate a transient ionisation balance for a system evolving from a dynamic state until equilibrium and computes associated radiated energy and emission excesses/deficits. Investigation of these effects is part of our paper study.

By inclusion of the dielectronic data we allowed investigation of the associated effects of finite plasma density on the ionisation balance, contribution functions etc. It is clear that even at moderate alterations from zero density the ionisation balance and contribution function peaks shift and the shapes can change substantially. Incorporation of density dependencies to spectral emission prediction is essential for furthering solar analysis by development of commonly used methods such as differential emission measure. We will return to this topic in the discussion section of the next chapter.

Chapter 5

Analysis of Observational Data from the SOHO Spacecraft

5.1 Introduction and Objectives of the Analysis

Our studies focus on the temperature/density structure of the solar atmosphere and its dynamic nature, taking advantage of the high spatial, temporal and spectral resolution of the CDS and SUMER spectrometers. The first stage is to use the most accurate derived atomic data, produced by ADAS, and couple it with calibrated line intensity measurements to investigate the differential emission measure distribution from the chromosphere through to the corona. The high quality of the atomic data will allow us to investigate and quantify the sources of error associated with this type of analysis more precisley than here-to-fore and determine whether it is a realistic approach for studying the structure of the solar atmosphere. The solar atmosphere's clearly dynamic nature leads us to believe that the technique may be limited. Subsequently, we wish to synthesize dynamic solar models linked to the observations by making geometrically valid spectrometer line of sight calculations to use in predictive studies.

In a preliminary study of the observations we develop critically the analysis techniques which will be used in all future work. Thus we seek to gain an understanding of the analysis problems and the peculiarities of the instruments. Also, it is essential to

do this to provide feedback for refinement of the observing sequences. In this chapter, we develop techniques of data handling and analysis that will be used principally for computing the differential emission measure with line intensities obtained by both CDS and SUMER. In so doing, we test key software components for the DEM analysis and propose baseline software modifications to deal more effectively with various aspects of the observational data. A critical study is also made of the statistical variability of the spectrum line intensities obtained by the CDS spectrometer. This latter study follows that applied to the CHASE spectrometer which flew aboard Spacelab 2 in 1985 (Lang, Mason & McWhirter (1990)). Finally, a reconstruction of the DEM using CDS-NIS data is presented to demonstrate the validity of the analysis procedures and the coupling of the different aspects of the problem. In doing this, some comment is made on the sensitivity of the normal incidence detectors. The presentation is however preliminary. The intensity calibration issue for CDS-NIS remains undecided and so our definitive differential emission measure study remains on 'hold'. However, reexamination of potential blended lines, back checks on the atomic physics of particular lines etc. have been commenced on the basis of this preliminary work.

5.2 Spectral Line Profile Fitting Procedure

Central to the aims of our work is the analysis of spectral line intensities. To obtain the fluxes observed in the lines we fitted a theoretical spectrum to the observed one. The method used is to fit multi-Gaussian line profiles and a background using a maximum likelihood method together with statistical analysis to calculate the total integrated counts under the line profiles along with their estimated standard errors and 95% confidence limits. The basic procedure is due to Lang et al.(1990) and was used in their analysis of data from the CHASE experiment. It has been adapted here to extend its capabilities while retaining its simplicity and flexibility. A major modification was to integrate the routine to both the SOHO-CDS and SOHO-SUMER data acquisition software. In this section a brief outline of the statistical methods used is presented for completeness followed by an overview of the modifications, associated tests and capabilities of the latest IDL version.

5.2.1 Overview of Line Fitting Method

A full explanation of the statistical methods used was presented by Lang et al.(1990). Here we restrict ourselves to outlining the main features and note the different observational mechanisms of CDS compared with CHASE. CHASE built up a profile of a particular line at a number of grating positions while CDS gives the whole spectrum at one position. The observed spectrum is represented by the form below,

$$I_k = b0 + b1x_k + b2x_k^2 + \sum_{i=1}^{L} h_i \exp - \left(\frac{(x_k - xo_i)}{w} \right)^2 \tag{5.1}$$

where I_k is the observed counts at integer bins, L is the number of lines to be fitted, b0 is the flat component of the background, b1 introduces a linear slope to that background, b2 introduces a curve to that background, x_k gives the pixel positions, h_i gives the peak of each line, w is the width to fit for each line and xo_i is the fitted positions of the lines which may be to fractions of a pixel. The statistical variation in the observed counts in the line, I_k, is assumed to have a normal distribution with variance proportional to the mean. The true mean at any I_k is unknown but if it is equal to the expected value of I_k, denoted $E(I_k)$, then an estimate of the variance of I_k follows from $\sigma_k^2 = \sigma^2 E(I_k)$. Here, σ^2 is an unknown constant of proportionality and σ_k^2 is the unknown statistical variance. As defined by Lang et al(1990) the natural logarithm of the likelihood function is

$$\log L = \sum_{k=1}^{P} - \log \sigma_k (2\pi)^{1/2}$$

$$-\frac{1}{2} \sum_{k=1}^{P} \frac{1}{\sigma_k^2} \left[I_k - \left(b0 + b1x_k + b2x_k^2 + \sum_{i=1}^{L} h_i \exp - \left(\frac{(x_k - xo_i)}{w} \right)^2 \right) \right]^2 \tag{5.2}$$

where k=1,...,P and P is the number of pixels in the range of the data. We maximise the likelihood function by maximising eq.5.2. That is, minimise the negative part of the right hand side of eq.5.2,

$$\sum_{k=1}^{P} \left[\frac{I_k}{\sigma_k} - \frac{1}{\sigma_k} \left(b0 + b1x_k + b2x_k^2 + \sum_{i=1}^{L} h_i \exp - \left(\frac{(x_k - xo_i)}{w} \right)^2 \right) \right]^2 \tag{5.3}$$

In Lang et al.(1990) this was done by a NAG library routine. However, we removed the dependence on NAG for portability and compatibility with ADAS by using an

adapted version of the MINPACK routine XXDER1. This minimises a sum of squares of functions provided, so we write eq.5.2 in the form $F(x) = \sum_{i=1}^{P} [f_i(x)]^2$ and specify the functions $f_i(x)$ along with their first derivatives. An initial estimate must be supplied and the code then iterates to find the solution that minimises eq.5.3. The parameters required for this initial estimate are dependent on options outlined below but usually include the number of lines, their centroid positions, estimated widths and an expected background level. The code obtains estimates of the unknown quantities, σ_k, by dividing the estimated value of I_k by the exposure time. This was retained for compatibility with CHASE. Finally, the estimated standard error of the individual quantities (e.g. b0, b1, b2, w etc.) and estimated 95% confidence limits are computed by standard methods of maximum likelihood. See Lang et al.(1990) and Lang & Payne (1987) for further description.

5.2.2 Integration with Existing Instrument Software

In the subsequent text we refer to the line profile fitting routine by its name, *mlcds*. To merge *mlcds* with the CDS and SUMER software it was necessary to develop first an IDL interface. This is because all the CDS software is written in IDL and the data, although archived in FITS format, is accessible only through this path. In addition, there are plans to archive the SUMER data in the same format and using the same organisation as that for CDS. This has not yet been done. The present recommended method for obtaining corrected SUMER data is directly from the CD ROM disks relayed to the Max Planck Institute in Lindau, Germany. The form of these data are IDL save/restore files and so are easily manageable by the IDL interface as for CDS. With this last point in mind, the original strategy was to take the SUMER data and streamline it into the form that *mlcds* expected from the way it was used for CHASE. Thus we had to specify an array containing the spectrum, the minimum and maximum pixel numbers over the range of the spectral segment and the exposure time of the observations. The exposure time was needed for CHASE as the count rates were recorded in quarter seconds and so had to be readjusted. Here, it is just used to divide the data to produce quarter seconds, before passing to the original code,

and is then used to multiply up again at the end. For DEM studies the exposure time is redundant as the data are calibrated and come as a count rate. Therefore, the option of specifying the exposure time was made into a keyword (/exptime) to allow flexibility between the two cases.

We sought to retain full use of the available baseline CDS and SUMER software. Therefore, we returned all the output information from the fitting program in the form of a structure with individual tags referencing the information. The original data and references to the source were maintained within this organisation to allow immediate reconstruction of the spectrum. The contents of the structure and their meaning are given in table.5.1.

5.2.3 Illustrative Examples and Outline of Analysis Options

During the course of the investigations presented in the next sections it became necessary to make a number of improvements to the original program to extend its' applicability. Table.5.2 provides an overview of the IDL keywords currently implemented. The most important capabilities, are as follows. *mlcds* can use an initial fit to one line to fit automatically the same line repeatedly through multiple datasets. For the extremely large datasets generated by the observing sequences it is unrealistic to treat them all individually, especially if the data are of regions where the behaviour of the emission is expected to be similar. A switch is provided (/autoloop) which invokes the repeat facility. The ability to fit individually is of course retained and is most useful for lines that show dynamic behaviour, for example. The (/oldstr) keyword allows specification of an initial structure, normally taken from the fit to another dataset, that can then be used to supply the information for the current fit, to the code. This was implemented, during a visit to MPAë Lindau, where it is usual to do automatic fitting as a background job. /oldstr works in conjunction with the /noprompt keyword for background jobs.

A number of routes in the analysis are allowed following user response to specific prompts from the code. After start up, the number of lines for fitting is entered, to a maximum of ten, and then the number with fixed centroid positions is specified.

Variable	Type	Meaning
B0	Floating	Flat part of background
ESEB0	Floating	Estimated standard error in B0
ECLB0	Floating	Estimated 95% confidence in B0
B1	Floating	Sloped part of background
ESEB1	Floating	Estimated standard error in B1
ECLB1	Floating	Estimated 95% confidence in B1
B2	Floating	Curved part of background
ESEB2	Floating	Estimated standard error in B2
ECLB2	Floating	Estimated 95% confidence in B2
W	Double Array(10)	Fitted widths of lines
ESEWL	Floating	Estimated standard error in W(fixed)
ECLWL	Floating	Estimated 95% confidence in W(fixed)
XO	Double Array(10)	Fitted positions of lines
ESEXO	Double Array(10)	Estimated standard error in XO
ECLXO	Double Array(10)	Estimated 95% confidence in XO
H	Double Array(10)	Fitted heights at centroid of lines
ESEH	Double Array(10)	Estimated standard error in H
ECLH	Double Array(10)	Estimated 95% confidence in H
ESEWV	Double Array(10)	Estimated standard error in W(variable)
ECLWV	Double Array(10)	Estimated 95% confidence in W(variable)
FLUX	Double Array(10)	Counts under line profile
ESEF	Double Array(10)	Estimated standard error in flux
ECLF	Double Array(10)	Estimated 95% confidence in flux
GETFIT	Integer Array(6)	Options selected(see next table)
EXPTIME	Floating	Exposure times
INFO	Integer	Error flag from MINPACK routine
HEADER	String	Editable comment
XMIN	Integer	Minimum pixel of spectrum
XMAX	Integer	Maximum pixel of spectrum
X	Integer Array(nsize)	Pixels
Y	Double Array(nsize)	Spectrum
YA	Double Array(nsize)	Fitted spectrum
NSIZE	Long	Range of pixels
NUMLINE	Integer	No. of lines fitted
NFXL	Integer	No. lines with fixed positions
BCHL	Floating	Initial guess at background
BCHR	Floating	Initial guess at background
LINEID	String Array(10)	Preliminary line identifications

Table 5.1: Contents of the 'Fitted' structures returned from *mlcds*.

Keyword	Use	Default
EXPTIME	Specify the exposure time for the data and divide by it.	Off.
DATA	Specifies the spectrum array for one dataset.	Either data or loopdata must be set.
XMIN	Specifies the minimum pixel of the data range.	Left hand range of plot window.
XMAX	Specifies the maximum pixel of the data range.	Right hand range of plot window.
PSYM	Allows alteration of the plot type.	Histogram.
AUTOLOOP	Allows automatic processing of fits to many datasets.	Off.
LOOPDATA	Specifies the spectrum array for many datasets.	Either data or loopdata must be set.
HEADER	Allows entry of a comment (usually source data and username).	Empty.
NOBACK	No background in the data.	Background present.
NOPROMPT	Omit *Print to screen* prompt.	Prompt given.
POST	Make a postscript file of plot.	No postscript file.
OLDSTR	Fit data using a previous set of parameters.	New fit.

Table 5.2: Keyword options implemented in mlcds.

jl-ju	M+G (A)	Pixel^V	Flux^V	ESE^V	Pixel^F	Flux^F	ESE^F
1-2	1174.933	836.26	27440.1	2.2	836.26	27382.0	2.7
0-1	1175.263	844.14	22061.2	2.6	844.09	22618.3	3.0
1-1	1175.590	850.99	15648.1	11.3	851.85	19560.7	5.8
2-2	1175.711	854.70	73526.8	2.5	854.72	68494.8	2.2
1-0	1175.988	861.40	22520.5	2.7	861.30	22761.1	3.3
2-1	1176.370	870.36	25240.6	2.4	870.36	25372.7	3.0

Table 5.3: The results of the test on the SUMER CIII multiplet data of the alteration to allow fixed line positioning. M+G denotes Moore(1993 - Edited by Gallacher) of the wavelengths used. The superscript V refers to the variable positions and F to the fixed ones. The estimated standard errors are given as percentages of the total fluxes.

This latter option is essential to allow use of laboratory wavelengths in defining the separations of overlapped components of multiplets, for example. Before entering the fixed positions of the lines, an option is available to make a preliminary identification of them. This is recorded in the output data structure for use in subsequent analysis routines. It is envisaged that the fixed position option will be used mainly with known wavelengths but a facility to correct wrongly entered values or to confirm estimates of line centres is available at this point. The introduction of lines with fixed positions required a separation of the final term in eq.5.1 as,

$$\sum_{i=1}^{L-nfxl} h_i \exp - \left(\frac{(x_k - xo_i)}{w} \right)^2 + \sum_{i=L-nfxl+1}^{L} h_i \exp - \left(\frac{(x_k - xo_i)}{w} \right)^2 \qquad (5.4)$$

where the variables are defined as before excepting *nfxl* which is the number of fixed lines. This modification was coded into the original FORTRAN.

Extensive tests were carried out on a series of selected multiplets comparing the derived intensity values with the expected values from ratios of transition probabilities and making a comparison of the variation in the errors of the fits. As an example, we used the data from the SUMER study OPAC_1. This sequence targets specific multiplets and tracks their variation in intensity as the instrument rasters across the solar limb. The component line intensity ratios arising from transitions from the same upper level alter due to the effects of opacity. We used the CIII($2s2p\ ^3P - 2p^2\ ^3P$)

transition in a dataset recorded on the solar disc. The dataset was chosen by viewing movies of limb brightening to confirm the selected one was indeed on the disc and to ensure the data was free from optical distortion. We first fitted the six members of the multiplet by allowing the line positions to vary, all lines to be the same width and the background to have a linear slope. This gave pixel positions for the six lines. From the graph of pixel versus wavelength a straight calibration line was drawn. Then best fixed pixel positions of the lines were estimated. The total counts of the lines found at the fixed positions were then obtained using the fitting program. The transitions and wavelengths, fitted pixel positions, fitted fluxes and estimated standard errors are given in table.5.3. The fit parameters are given for the case of fixed and variable line positions. The fixed positioning reduced the uncertainty for the blended pair 1-1 and 2-2 (1175.590$\mathring{A}$ and 1175.711$\mathring{A}$ or 851.85 and 854.72 fixed pixel position respectively) from 11.3% and 2.5% to 5.8% and 2.2% respectively, at the expense of about 0.5% accuracy in the others. An example plot of the fixed position fit to this multiplet is given in fig.5.1. We then compared the theoretical optically thin branching ratios with the observed intensity ratios obtained by the fitting program. The theoretical A-values were taken from ADAS which contains the best currently available data (Allard et al.(1990)). We estimate that these A-values are uncertain to at least 5%. Then, the theoretical ratio $I(2-2)/I(1-2)$ should be 3.00 $\pm$0.21 and the ratios $I(0-1)/I(1-1)$, $I(2-1)/I(1-1)$ and $I(2-1)/I(0-1)$ should be 1.34$\pm$0.09, 1.67$\pm$0.12 and 1.250.09 respectively in optically thin plasma. The results for free positions give 2.68$\pm$0.09 for $I(2-2)/I(1-2)$, 1.41$\pm$0.16 for $I(0-1)/I(1-1)$, 1.61$\pm$0.19 for $I(2-1)/I(1-1)$ and 1.14$\pm$0.04 for $I(2-1)/I(0-1)$. While the results of the fixed positions give 2.50$\pm$0.09 for the $I(2-2)/I(1-2)$, 1.16$\pm$0.08 for $I(0-1)/I(1-1)$, 1.30$\pm$0.08 for $I(2-1)/I(1-1)$ and 1.12$\pm$0.05 for $I(2-1)/I(0-1)$.

The results of this test on the fitting program of fitting lines at fixed positions was satisfactory. The fixed position option was more accurate in evaluating fluxes from the blended lines as expected. In comparison with the theoretical line intensity ratios the results with the free fit were slightly better but less accurate. Intensity ratios calculated from the fixed position fits to the other lines had errors comparable with the free fit and were about the same at matching theoretical line intensity ratios.

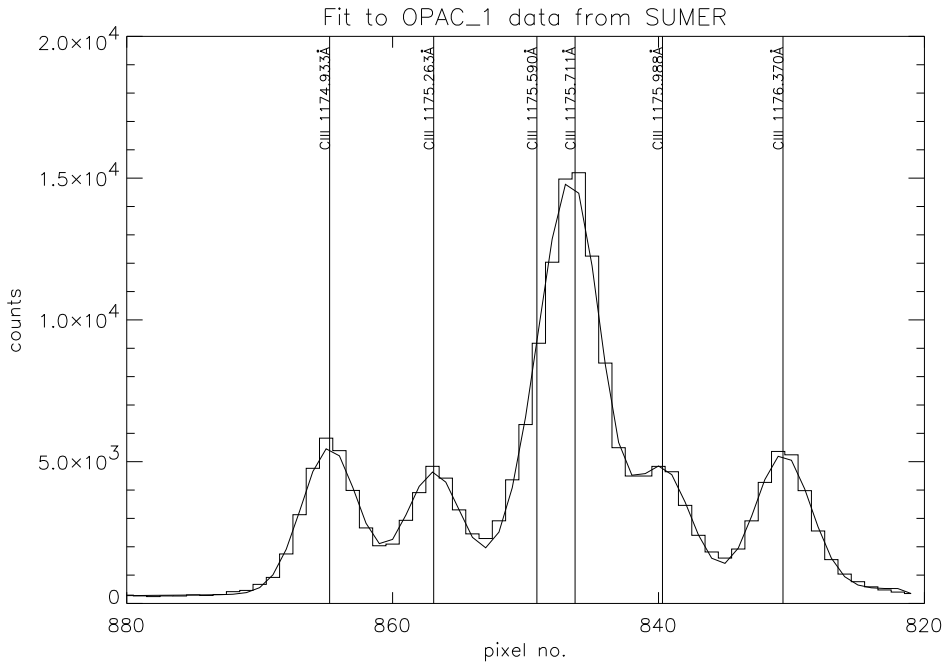

Figure 5.1: Example of fixed position fit to the CIII multiplet in OPAC_1 SUMER data.

Such success with this multiplet is essential for full analysis of opacity with the OPAC data.

During the other tests on CDS data the main problem arising was that blended lines were often closer together than the spectral resolution of the spectrometer i.e. they were often within one data pixel while the data were binned at one pixel. This is a fundamental limitation in the data that affects our ability to separate the lines. However, for optically thin plasmas, calculation of theoretical line ratios using ADAS together with spectral fitting of well separated lines will allow progress to be made in identification and inference of the make up of overlapped line intensities.

mlcds requires an estimate of the widths of each line. This is done using the mouse cursor by clicking on the left and right hand sides of the lines at about full width half maximum. In fact, the calculated widths are not the full widths at half maximum but are $\sim \frac{3}{5}$ of them (Lang (1996) - private communication). The treatment of the line widths has been made quite flexible for application to differing data requirements. An option is available to fix the widths of every line to be the same (answer 0(=No) to *line widths to vary ?*). Alternatively, one can allow the program to fit the widths but make them all the same (answer 1(=Yes) to *line widths to vary ?* and 0(=No) to *Fit different widths to lines*) or to fit them, but allow them to be different (line widths to vary and fit different widths to lines). These changes required alterations to the FORTRAN code to re-order the vectors containing the free parameters but the final terms in eq.5.1 are still those of eq.5.4. The vector w will contain the values of the variable widths or the widths that the program finds, but when using fixed widths for all lines it becomes a scalar quantity. In this case the exponential terms are constant and their derivatives drop out.

The ability to fit variable line widths was introduced because of a preliminary analysis on explosive event data from SUMER. The explosive components initially appear weak and then grow in intensity to dominate the central line. As first pointed out by Innes et al.(1997) these events are probably bi-directional jets of plasma created following magnetic reconnection in the chromosphere. Fig.5.2 shows the line width variation with time, along with intensity and position, in observations taken by SUMER in May. The solid line is the central unshifted non-explosive component

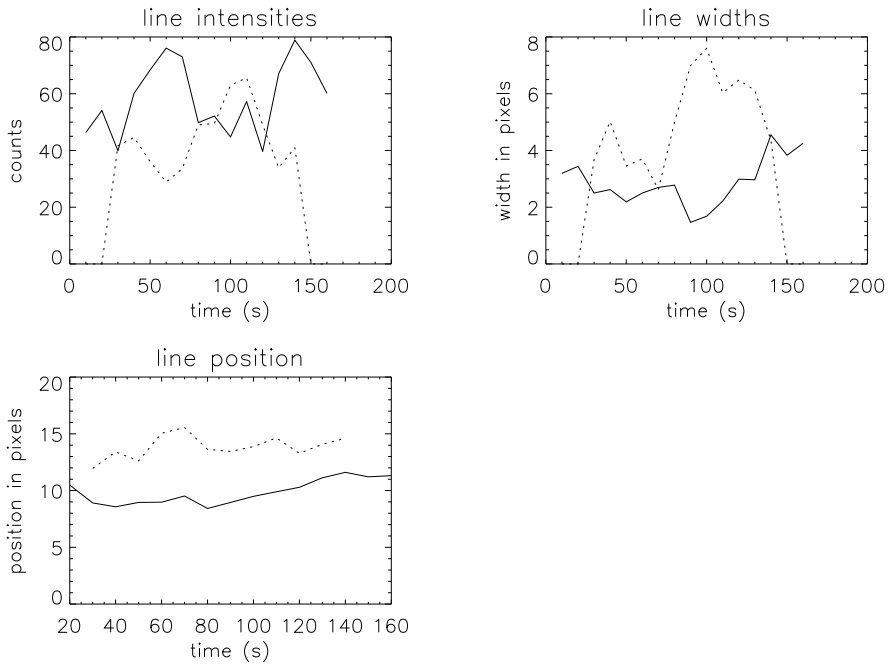

Figure 5.2: Example of application of variable widths option to SUMER explosive event data. In each case the solid curve refers to the stationary component and the dotted curve refers to the explosive component.

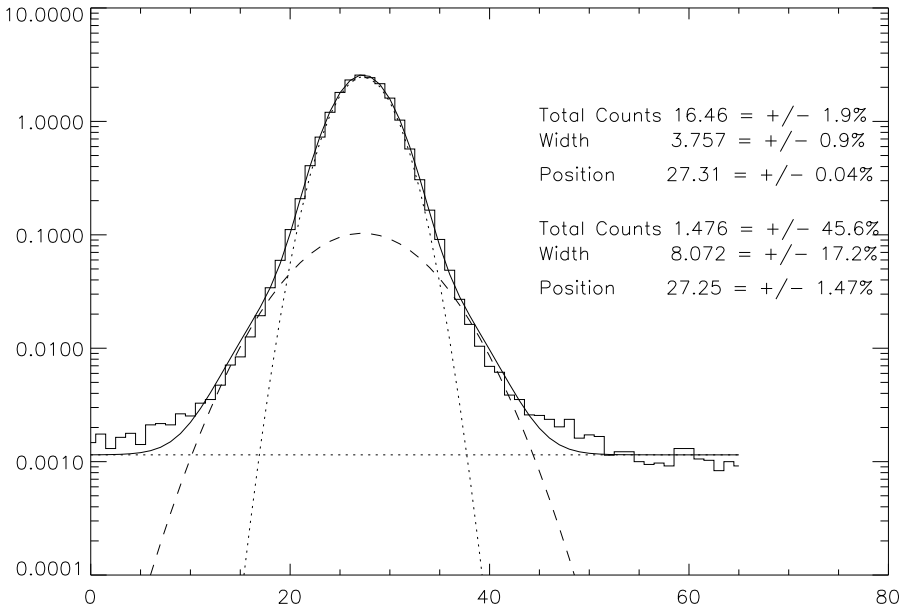

Figure 5.3: Example of variable width fit of two Gaussians to an OVI line taken while scanning above the limb. The x-coordinate is the pixel number in the wavelength direction. The y-coordinate is the number of counts.

and the dotted line is the explosive component. Note that the central component width remains relatively constant, between ∼3-4 pixels, as does the central position. The non-explosive component intensity appears to fluctuate substantially as the explosive component develops. This is due principally to imperfect separation of the fitting program at each time. The width of the explosive component varies over a much larger scale, ∼0-8 pixels, than the stationary component. This example illustrates the effectiveness of the variable width option in separating two components of different width. Another example is shown in fig.5.3. SUMER data from a scan off the limb is used to separate double Gaussians thus giving the contribution to the line from thermal broadening. The line used was OVI 1032$\mathring{A}$. Once again the variable width option was effective. Despite the much smaller number of counts the fit is within 45%.

Three options are available for specifying the shape of the background for which *mlcds* needs two initial estimates. These estimates are used to calculate the linear slope or curve to be added to the flat background dependent on the background choice. Once again the vector containing the free parameters had to be reordered and the various contributions to the $b0 + b1x_k + b2x_k^2$ part of eq.5.1 are dropped out dependent on the user choices.

The fitting procedure normally performs a fit to the counts in each line using a weight function which is the square root of the number of counts. In the case of the GIS 'fixed' patterns we found that this was not satisfactory. We implemented a *non-weighted* option which seemed more robust in handling the data from GIS. A prompt from *mlcds* allows a choice between the two weighting options in the code. An illustration of fitting the fixed patterns is given in sec.5.3.2.

5.3 Background on the Observations and Problems Associated with the Analysis Methods

5.3.1 The Normal Incidence Spectrometer Spectral Atlas Data

The Coronal Helium Abundance Spacelab Experiment (CHASE) instrument consisted of a grazing incidence telescope and spectrometer with a spectral resolution of $0.7\mathring{A}$, in first order, within the spectral range 160 to $1344\mathring{A}$. The instrument had 15 wavebands which could scan sequentially in 10 to $20\mathring{A}$ ranges by rotating the grating mechanism through an angle. The instruments' entrance slit corresponded to a spatial area on the Sun's disc of 15" by 180" arcsec.

The data used for this initial study was taken from a series of observations given the acronym NISAT_S. This study is run fairly frequently by the CDS team and by early June about 50 datasets were already available. We required about 10 sound datasets and so 20 were chosen for investigation (accepting that there could be cause for rejection). The details of the observing sequence are given by Harrison & Fludra (1995) but the main points are as follows. NISAT_S only utilises the Normal Incidence spectrometer and its purpose is to obtain a spectral atlas covering the entire wavelength range of the instrument. Atlases are recorded NIS windows 1 and 2. The observations use the 2" by 240" arcsec slit which is moved to the immediately adjacent area on the quiet sun after each 50 second exposure. The slit is stepped 10 times so scanning a total spatial area of 20" by 240" arcsecs in a total observing time of 8 minutes and 20 seconds.

In order to be able to duplicate the method of analysis used in CHASE, the CDS data was organised to match, as closely as possible, the area picked out on the Sun by the size of the CHASE slit. Therefore, the datasets were first summed over half the rasters and then over half the slit with the final data segments corresponding to 10" by 120" arcsecs. This is approximately the same as that observed by CHASE.

Since we wish to apply the differential emission measure technique to quiet sun locations, we want to examine the variability of spectrum line intensities only in such regions. Therefore, we analysed the created data segments in an attempt to identify

any presence of active regions in our field of view. The procedure was to sum the data arrays over the dimension corresponding to wavelength and then to examine the variation in line intensity along the length of the slit. The reasoning here was that active areas would reveal a much more pronounced variation from location to location than their inactive counterparts and so be detectable. There was a separate problem with data signal transfer from the spacecraft whereby signal dropouts occurred at single pixels. As an example, fig.5.4 shows the intensity variation with pixel no. along the slit for one of the NISAT_S observations. Note the sudden single point drop of approximately 18.5% between position 30 and 40. Our method for identifying active regions effectively pointed out these signal dropouts too. This technique also reveals intensity spikes due to cosmic ray hits (note the spikes at positions 10 and 80 for example). Standard CDS software is available for removal of cosmic ray spikes but not for signal count replacement. As a result, all the data segments that showed signal dropouts were rejected from the analysis.

During analysis we noticed that there were about 15 redundant pixels at each end of the slit. These were removed from the chosen datasets. Also, we noticed that the spectra were not square to the detector. This can be corrected for using standard CDS software (*vds_rotate*).

Our objectivity in rejecting regions that apparently show active contributions is questionable. Fig.5.5- 5.7 show surface plots of intensity variation with space and time. The x-axis is the spatial dimension corresponding to pixels along the slit (where the edge pixels have been removed) while the y-axis is raster number. The data is from file no. *s3436r00* so there are 9 rasters of 100 second exposures and cosmic ray spikes have been 'cleaned'. The z-axis is the total counts integrated under the line profiles. Note that a photometric calibration was not used at this time. The chosen lines are HeI 515.617$\mathring{A}$ (fig.5.5), CaX 574.01$\mathring{A}$ (fig.5.6) and OV 629.732$\mathring{A}$ (fig.5.7) which cover formation temperatures of $\sim 1.2 \times 10^4 K$, $\sim 1.6 \times 10^6 K$ and $\sim 2.5 \times 10^5 K$ respectively. These correspond, roughly, to the temperatures of the chromosphere, corona and transition zone. The lower and higher temperature regions appear to have a common appearance. The spatial and temporal structure and count ranges are fairly similar. However, the OV line varies much more widely than the other two.

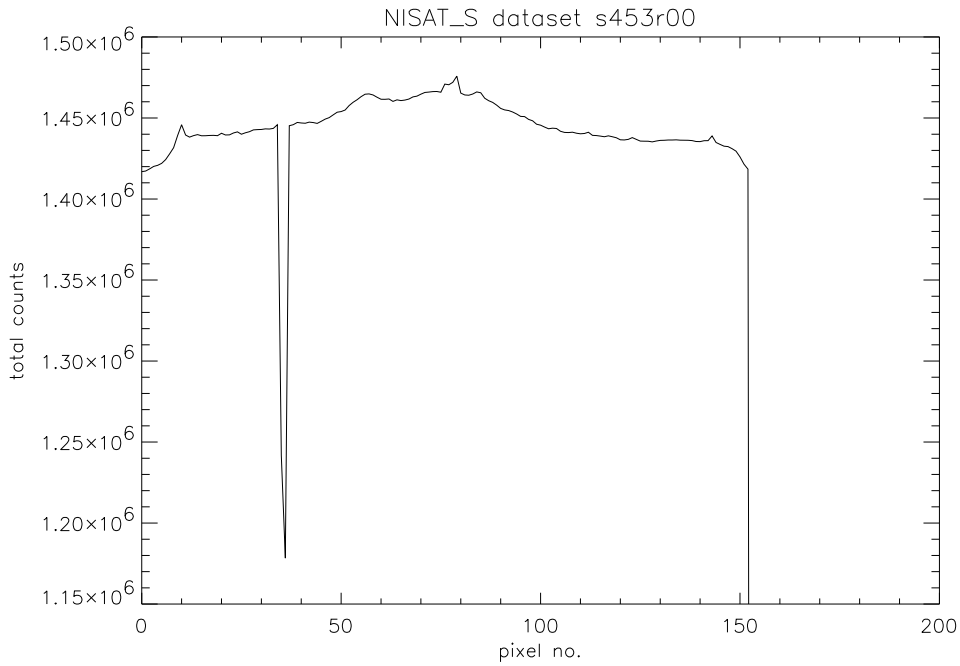

Figure 5.4: Intensity variation with pixel position in the y-direction along the slit. The data is from the NIS2 spectral atlas observations. Rasters 5 to 9 were extracted and the wavelength dimension summed over to produce this plot.

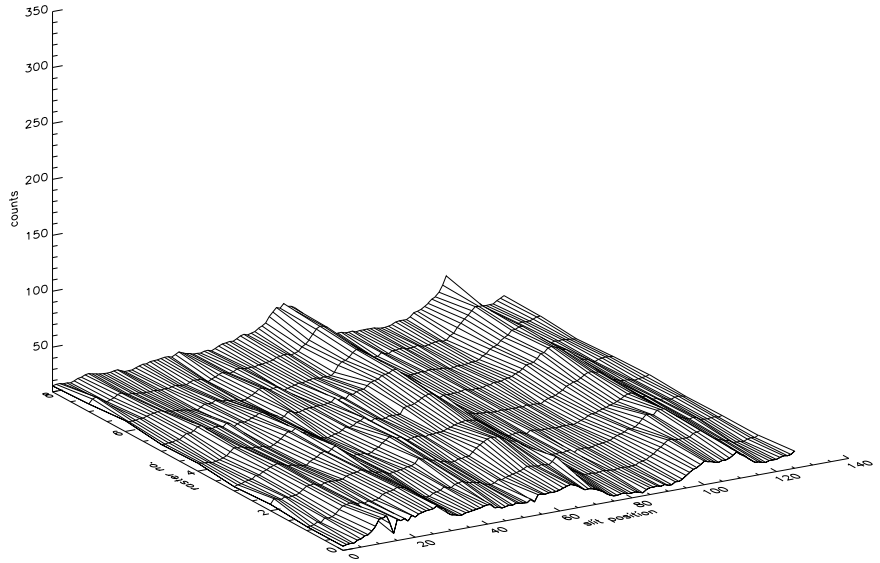

Figure 5.5: Spatial and temporal variation of HeI 515.617$\mathring{A}$ line emission. The x-coordinate is the spatial dimension along the y-direction of the slit. The y-coordinate is the temporal dimension denoted by raster number. The z-dimension is the number of counts.

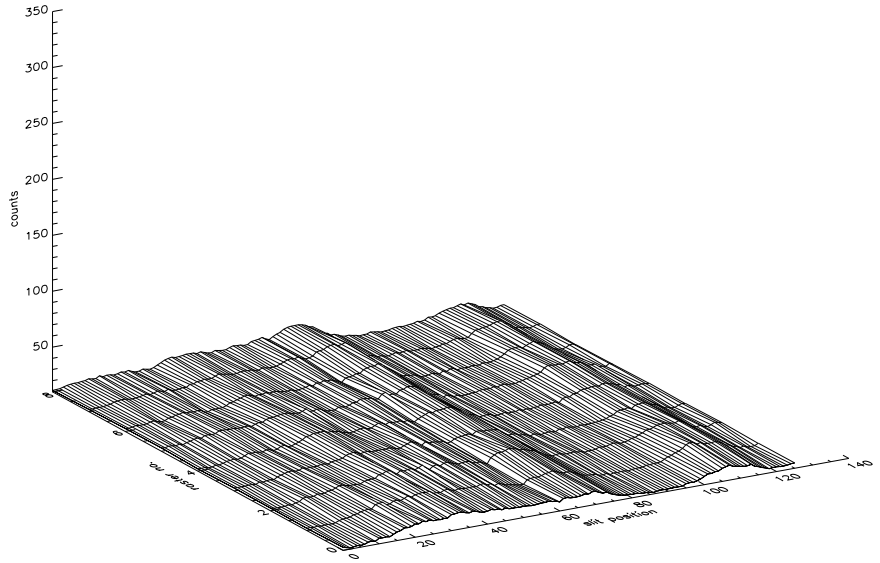

Figure 5.6: Spatial and temporal variation of CaX 574.01$\mathring{A}$ line emission. The x-coordinate is the spatial dimension along the y-direction of the slit. The y-coordinate is the temporal dimension denoted by raster number. The z-dimension is the number of counts.

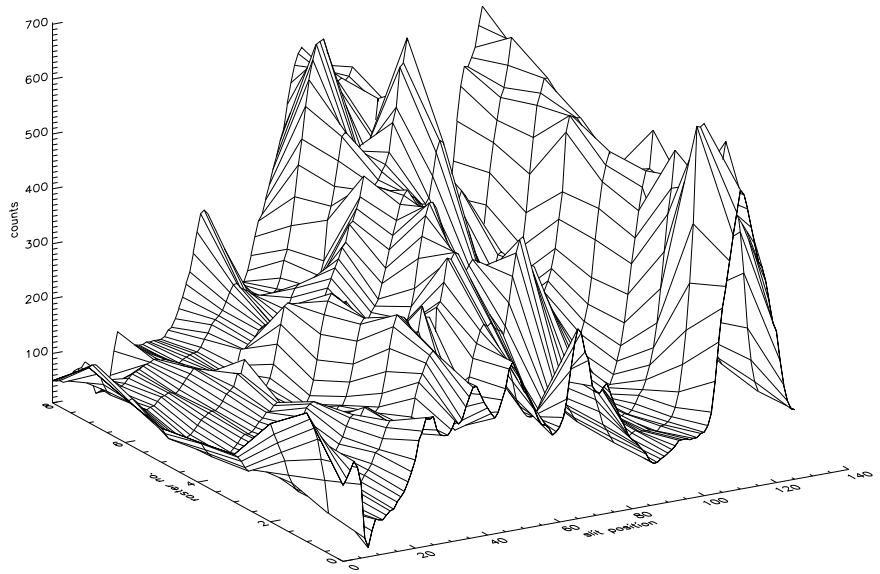

Figure 5.7: Spatial and temporal variation of OV 629.732$\mathring{A}$ line emission. The x-coordinate is the spatial dimension along the y-direction of the slit. the y-coordinate is the temporal dimension denoted by raster number. The z-dimension is the number of counts.

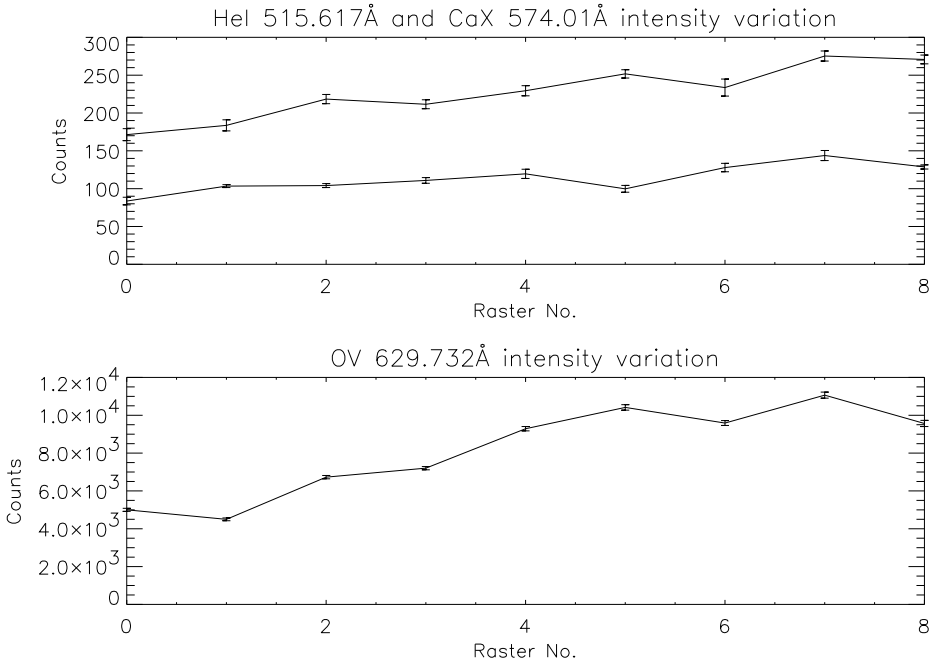

Figure 5.8: Temporal variation of intensities of the HeI, CaX and OV lines. The data is from the NIS2 spectral atlas observations. Rasters 5 to 9 were extracted and the wavelength dimension summed over to produce this plot. In the upper diagram, the HeI variation is the top line and the CaX variation is the bottom line.

Note that the HeI and CaX plots appear on an intensity scale that is half that of the OV plot. In addition, despite some similarities the spatial structure appears more changeable. Fig.5.8 shows the intensity variation with time of each of these three lines at pixel locations 60 to 80 i.e. averaged over that area of the slit. Again, we can see that the OV line varies much more widely than the other two.

Information like this clearly shows the dynamic nature of the solar atmosphere and also shows that intensity variations and 'hot-spots' can come and go on time scales close to ionisation relaxation times. Using the estimates for carbon ions presented in sec.3.2.1 we see that both the transition region and the corona are fluctuating over timescales that are too short to have allowed carbon ions to relax to equilibrium. This raises the question as to what is the quiet sun? In the CHASE pattern analysis in

Position	Dataset	Set of Rasters	Portion of Slit
1	s453r00	B	2
2	s454r00	B	2
3	s505r00	A	1
4	s505r00	B	2
5	s633r00	B	2
6	s747r00	A	1
7	s747r00	B	1
8	s747r00	A	2
9	s747r00	B	2

Table 5.4: The final list of NISAT_S observations selected. The letter A refers to rasters 0-4 and B to rasters 5-9. Index 1 refers to the lower portion of the slit with the ends removed (i.e. pixels 15-77) and index 2 refers to the upper portion (i.e. pixels 78-140).

sec.5.5.1 a number of spatial locations are relatively bright but our selection criterion (i.e. less than a factor 3 variation about the mean) accepts them as quiet sun. A number of such files had been marked as active regions by the observer. We rejected these datasets on this basis but decided that it was statistically unsound to reject others of this type. The purpose of our analysis is to quantify the variation of intensities in the quiet solar atmosphere and we did not wish to be biased.

The final list of datasets and segments used is given in table.5.4 along with the letter (a or b) to identify whether the segment corresponds to the first five or second five raster steps in the sequence and the index number (1 or 2) to specify whether the data comes from the lower or upper part of the slit. All the data were stored in IDL save/restore format.

The Earth's magnetosphere normally acts to shield spacecraft from direct bombardment by cosmic rays. SOHO's position at the L1 Lagrangian point is outside the influence of the magnetosphere so it is more susceptible to cosmic rays than Earth orbiting satellites such as YOHKOH. Thus cosmic ray detector activation is a major problem, in particular for the normal incidence spectrometer, which must be addressed. Fig.5.9 shows a normal incidence spectrum from spectral band 1. Cosmic

ray events appear as dots and are widespread. We can see that it is not unusual for these events to activate more than one pixel. This presents another problem discussed in section.5.3.3. Note also the appearance of a detector blemish in the lower left portion of the spectrum. In the spectral display mode, the cosmic rays appear as thin bright line-like features. For example, fig.5.10 shows features that are difficult to distinguish from spectrum lines. Note in particular the events at 541 & 593$\mathring{A}$. One must seek to remove each of these spurious features as they disturb the spectral line fitting procedure. Fig.5.11 shows the same data segment as fig.5.4 after the removal of cosmic ray features by the CDS IDL code. Note that the peaks at positions 10 & 80 have been smoothed. This cosmic ray cleaning code was applied to all the datasets although its effectiveness was dependent on the type of observation that had been made, so it was not always applied in this form (see section.5.3.3). All the data were stored in IDL save/restore format to be compatible with the CDS analysis software.

As mentioned, the NISAT_S observations were originally intended to provide a spectral atlas for the normal incidence spectrometer. For our work an atlas is very helpful for identifying lines that we can use for the analysis of statistical variance. In fact the atlas had not been fully assembled and so as part of this work we completed a spectral atlas for NIS1 and NIS2 including the cosmic ray cleaning. Many spectral lines were identified and a list of those chosen for the study is given in section.5.5.1 table.5.7.

The line fitting code, *mlcds*, was then used to fit Gaussian profiles to each of the selected lines in each of the selected data segments.

5.3.2 Integration of the Grazing Incidence Spectrometer to the Analysis and Refinement of Observing Sequences

Results of the 'CHASE type' analysis for NISAT_S data are presented in sec.5.5.1. Although the NISAT_S data proved suitable, it does not correspond exactly to the pattern of observations made with CHASE. In the CHASE experiment, the first observing sequence moved the spectrometer over eight adjacent positions across the limb, then returned it to the original viewing position. This raster was repeated a

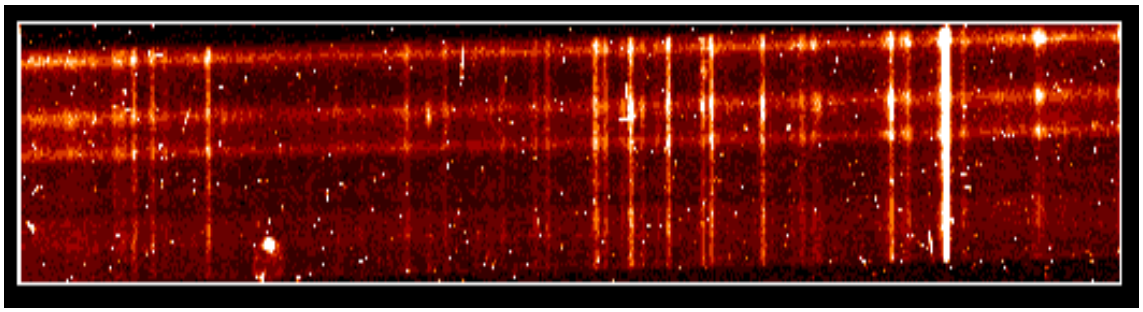

Figure 5.9: Example of how cosmic ray events appear on a typical NIS spectrum. The data is from NIS1 and from the DEMST_1 observations fits file no. s4878r01. The cosmic rays appear as dots and small streaks all over the spectrum.

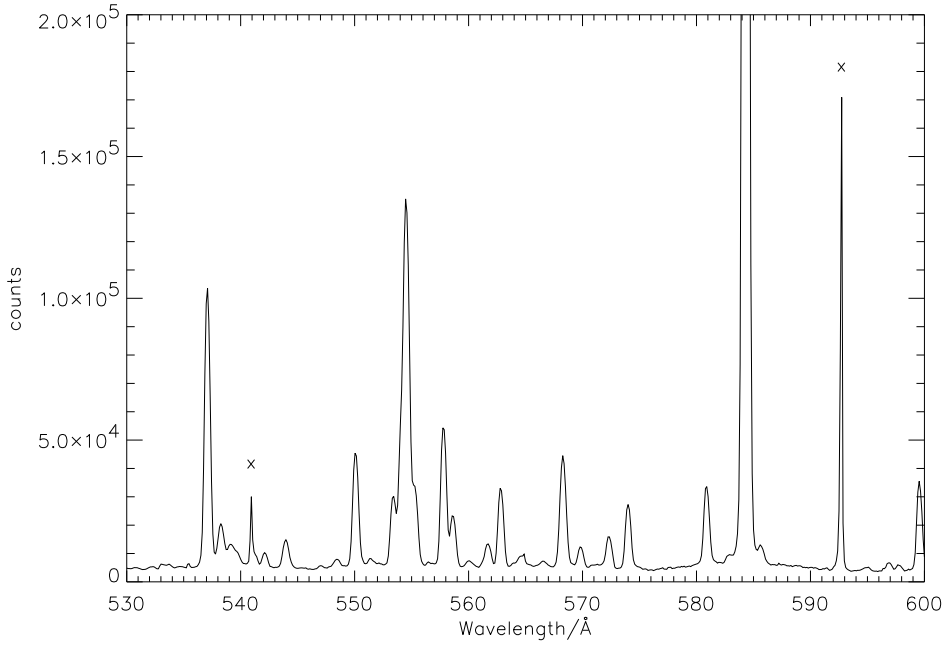

Figure 5.10: Example of how cosmic ray events appear on a typical NIS spectrum. The data is from NIS2 and from the NISAT_S observations fits file no. s350r00. Two cosmic rays are prominent at $\sim$ 541Åand $\sim$ 593Åand are marked with crosses.

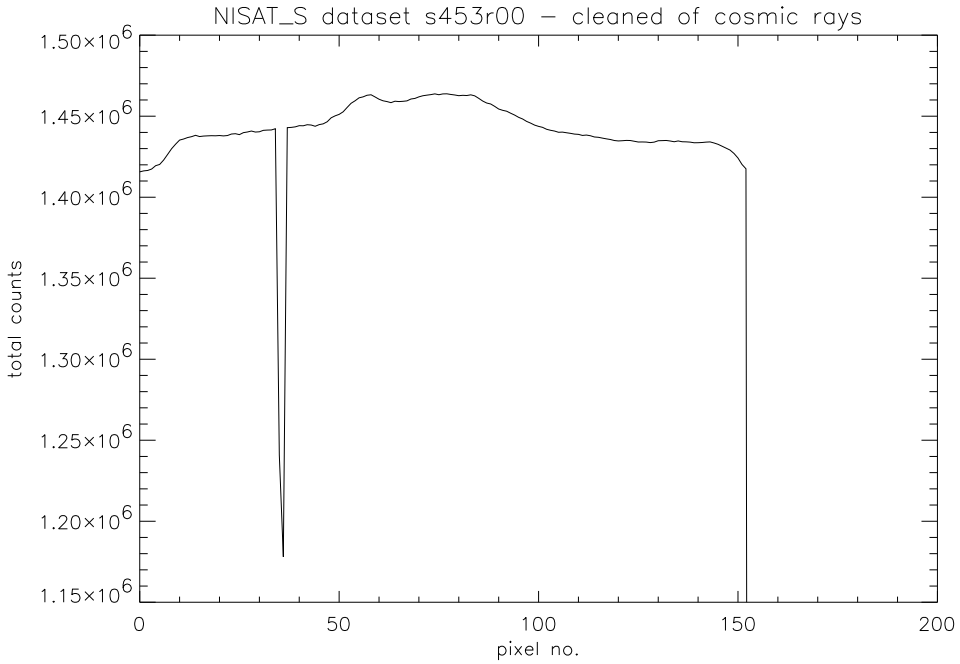

Figure 5.11: Intensity variation with pixel position in the y-direction along the slit after the removal of cosmic rays.

further 3 times. In the second study eight widely separated positions over the solar disc were selected and observed in turn. The purpose of these studies was to observe the temporal variation in intensity coming from the same region of the Sun and then to examine the variation of intensity between different positions. The NISAT_S data was similar to the second CHASE study. We analysed these data but then proceeded to a dedicated study of the temporal variations in a new set of observations. We gave these the acronym RWPM_2. Our main objective was not simply to repeat the CHASE analysis but to establish the statistical uncertainty of the line intensities for the DEM study. Spectrum lines from the Grazing Incidence Spectrometer wavelength region are essential for DEM studies and so the new observations encompassed both NIS and GIS. NIS and GIS cannot observe simultaneously and so the distinct set of observations made for GIS are given the acronym RWPM_1. Both observations were run on 1996 July 7 and were specifically designed to match characteristics of the CHASE ones e.g. rastered area and overall count rates.

Three rasters were made by each spectrometer and these were interleaved to ensure that variations in the solar atmosphere were picked up by both. The GIS observations used the 4" by 4" slit and this was stepped in the NIS slit direction 60 times to cover a total area of 4" by 240". This corresponds to the size of the NIS slit number 5 which was subsequently used for NIS observations. Each exposure of the GIS detector lasted 60 seconds and so the observations took 1 hour to complete. We then switched to the NIS spectrometer whose detector was exposed 9 times for 100s at the same location (allowance was made for solar rotation). This took a total of 15 minutes. The observations were repeated twice more and the complete study lasted a little over 7 hours. The Grazing Incidence Spectrometer observations provided us with the first opportunity to look into the complexities associated with it and also to plan for possible use of the long slit with GIS to precisely match CHASE.

In sec.5.5.2 a complete analysis of the observational accuracy and presence of patterns is given for the NISAT_S data. However, the finalised observations that precisely match those of CHASE are those given the acronym GISAT_S. This sequence was designed using the experience of the data from RWPM_1 and the GIS detector problems discussed in sec.5.3.2 and sec.5.3.2. In addition, new NISAT_S observations

are being run concurrently with the GISAT_S ones and pointed at the same location. The main development with GISAT_S is that it utilises the long slit (i.e. 2" × 240"). Therefore, it exactly matches NISAT_S by rastering 10 times in the x-direction. A problem arises. To match the spectral segments used for NISAT_S we require to sum the GISAT_S data over half the rasters. Since GIS is astigmatic there is no spatial dimension to split these over and we do not wish to split the wavelength range. Therefore, the final spatial area covered will be 10" by 240" which is double the length of the NISAT_S segments. Also, it becomes extremely difficult to determine whether data dropouts exist as our previous method of totalling over wavelength effectively reduces the data to one point for each raster. One possibility might be to look at adjacent rasters and try to estimate whether one region contained manifestly less counts than another. However, since the dropouts may be as little as 18% (see fig.5.4) it is possible that they fall within the normal variation between rasters due to the quiet sun.

It was necessary also to design the DEM observing sequence. This was loosely based on the sequences used before. CDS rastered over a 40" by 240" area using the 2" by 240" slit and moving in 2" steps to cover the 40". In addition, it alternated between the normal incidence and grazing incidence spectrometers. At each position the detector was exposed for 200s. This sequence was designed in conjunction with the SUMER team who performed observations covering a 300" by 3" area with the 300" by 1" slit. The CDS part encompassed the same region as SUMER saw and also allowed for errors in the co-pointing. The sequence was named DEMST_1.

Investigation of Detector Anomalies and Aberrations

There are many problems associated with detector response, blemishes etc. which were taken care of and need attention in all observations. However, there are two main difficulties presented by the GIS detector system, namely,

1. The appearance of ghosted lines in the spectrum.

2. Fixed patterning in the line profiles.

Information about the GIS detectors is given by, for example, Breeveld et al.(1992), Harrison et al. (1995) and Kent et al.(1997). Here, we briefly outline the causes of the problems. The detector consists of a stack of micro channel plates (MCP) which produce a charge cloud of electrons when receiving a single photon. The charge cloud varies in number depending on the position of the incident photon. An EUV photon produces $\sim 4 \times 10^7$ electrons and this is the gain of the event. This gain has a normal distribution called the pulse height distribution (PHD). The cloud passes onto a spiral anode detector (SPAN) which consists of strips containing three electrode elements. Digital signals are produced from two of the electrode elements by an analogue to digital converter (ADC). The third element is used as a reference. The magnitude of the first two signals is dependent on the position of the photon event. An on-board look up table (LUT) is used to determine the corresponding pixel position. Separate LUT's are used for different observations dependent on the expected count rates. Raw anode signals are shipped to the ground and fitted by a data spiral pattern to select parameters necessary for re-building the LUT correctly. The spiral pattern takes account of flat fielding effects etc.

The SPAN electrodes are in the form of damped sine waves. Consequently, a large charge cloud covers more 'waves' in the anode pattern than a small cloud. This has the effect of introducing a damped sine wave fluctuation to the spiral pattern. As a result, positions determined on the spiral overlap in some areas and the uniqueness of the solution is lost. This results in transference of data to other areas of the spectrum by movement of lines between spiral arms. Thus spectral lines have ghost companions at different wavelengths and the determination of line positions is affected. The intensity and location of the 'ghosts' varies from observation to observation depending on the voltage and position of the photon event as these affect the size of the charge cloud. However, they can be determined from a knowledge of the detector LUT set up. Software to deal with ghosts is being developed by Mullard Space Science Laboratory.

For detectors which digitise the signals before determining the position, sampling of the continuous function is done at integer values. Clearly this undersamples and introduces an error. This produces a 'fixed pattern' in the line profile. That is, counts are shifted between bins producing an excess in some and a deficit in others. However,

the total counts are conserved. Fixed patterning can also be seen on YOHKOH data (see Culhane et al.(1991) and Lang et al.(1992)) but is much less pronounced than that seen with the GIS. We decided to investigate the degree and structure of fixed patterning in the RWPM_1 observations to determine whether we were able to perform spectral fitting in a meaningful way.

In principle the pattern should remain the same for all observations which use the same look up table (LUT) and have similar count rates (Breeveld(1996) - private communication). We decided to check this for our observations since the validity of the LUT may degrade with time (Pike(1996) - private communication). Also, we sought to verify how 'fixed' was the nature of the pattern. Does it vary from line to line? Does a particular line exhibit the same characteristics if we look at different spatial locations? If the pattern is not random, we might hope to reverse the process and recover the original profile.

We extracted the GIS1 data from the RWPM_1 observations. These correspond to the FITS file numbers s3435r00, s3437r00 and s3439r00. The header information in each FITS file contains a parameter GSET_ID which records which LUT was used. For our three sets of observation the GSET_ID was 42. The data arrays extracted spanned three dimensions, wavelength, raster dimension (x) and the 60 movements in the y-direction covering the area of the NIS slit.

Firstly, we looked at the pattern of the strongest line at pixel number 610 along the wavelength dimension and compared it over four different exposures in the y-direction along the slit. The results are shown in fig.5.12. This line was tentatively identified as FeIX 171Å. We see that although there is some variation in the pattern, it is constant enough between the different spatial locations to warrant more detailed investigation. We then split the data into two portions spanning half of the y dimension (slit) and averaged over the x dimension (wavelength). These totalled patterns showed a greater similarity. Hence, despite the variability of the individual pattern we were encouraged to believe that the 'total' patterns would have fixed characteristics. To confirm this we averaged the data over both dimensions, of the slit, for each of the RWPM_1 datasets and found that the patterns matched very closely. Fig.5.13 shows the similarity of the totalled patterns of individual lines in each of the three datasets.

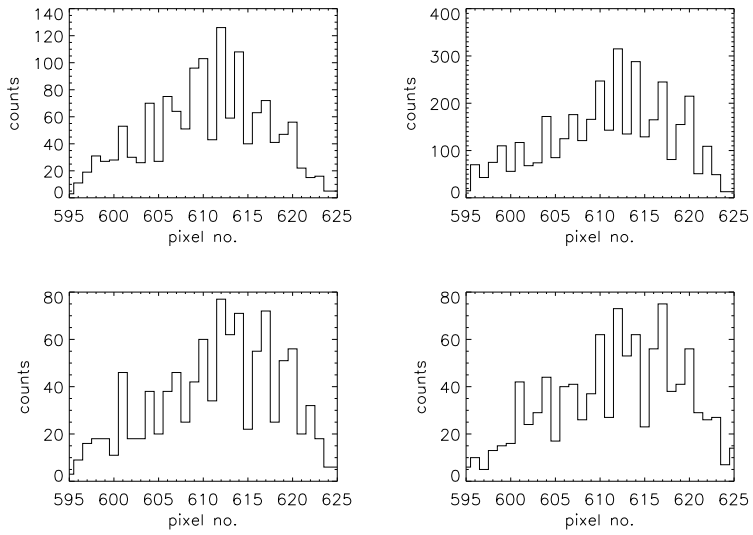

Figure 5.12: Plots of a spectral line at 610 pixels (in the wavelength dimension) which was tentatively identified as FeIX 171Å. The x-coordinates are pixel numbers along the wavelength dimension. The y-coordinates are recorded counts. The four graphs show the pattern of the same line varying at four randomly selected unknown y-pixel positions along the slit dimension.

This is what we would expect since the LUT numbers were the same for each dataset. Also, since the observations spanned 7 hours, we can conclude that any degradation in the applicability of the LUT's is not important over the period of these observations.

Note also that the two lines in fig.5.13 show different fixed patterns. This is consistent with the variability we found over spatial locations even for a single line. However, this does not appear to have much influence on our analysis. The main concern was that we would be unable to say conclusively that the same LUT's give us the same patterns but it appears from fig.5.13 that they do. Differences between individual lines are actually of less concern as the main purpose was to see if it was feasible to apply some retrospective-correction to each line profile.

Each position on the spiral pattern corresponds to a value of the event gain function. Therefore, the sampling grid needs to be fine enough to map every point. After discussions with Pike & Lang (1996 - private communication) it became clear that the resolution of the on-board sampling grid was the main problem and a retrospective-correction was not possible. That is, the only proper solution would be to attempt to obtain the raw data from the spacecraft and apply a finer sampling grid ourselves to reproduce the gain function and obtain the photon position. This is impracticable as the data telemetry rate is such that to get a reasonable signal to noise ratio the transfer time would have to be two to three orders of magnitude longer. Also, the normal planning and on-board pre-analysis software would have to be bypassed. In any event, for this type of detector, there is a fundamental limitation to the resolution obtainable. For a particular charge, falling on the anode, the digitised results will differ by an absolute minimum of 1/charge (Geesman et al.(1991)). Therefore, it is necessary to handle the patterns as they are.

Finally, we should mention one more restriction. The GIS to command and data-handling system (CDHS) link only operates up to a maximum constant rate of 8.9×10^4 counts/s. However, the detector readout electronics can operate up to 1×10^5 counts/s. Therefore, it is possible that count rates above the capabilities of the CDHS are sent to it. If this happens, half the data from the detectors are lost. In addition, above 5×10^4 counts/s the actual total count rate is unknown (Kent et al.(1997)).

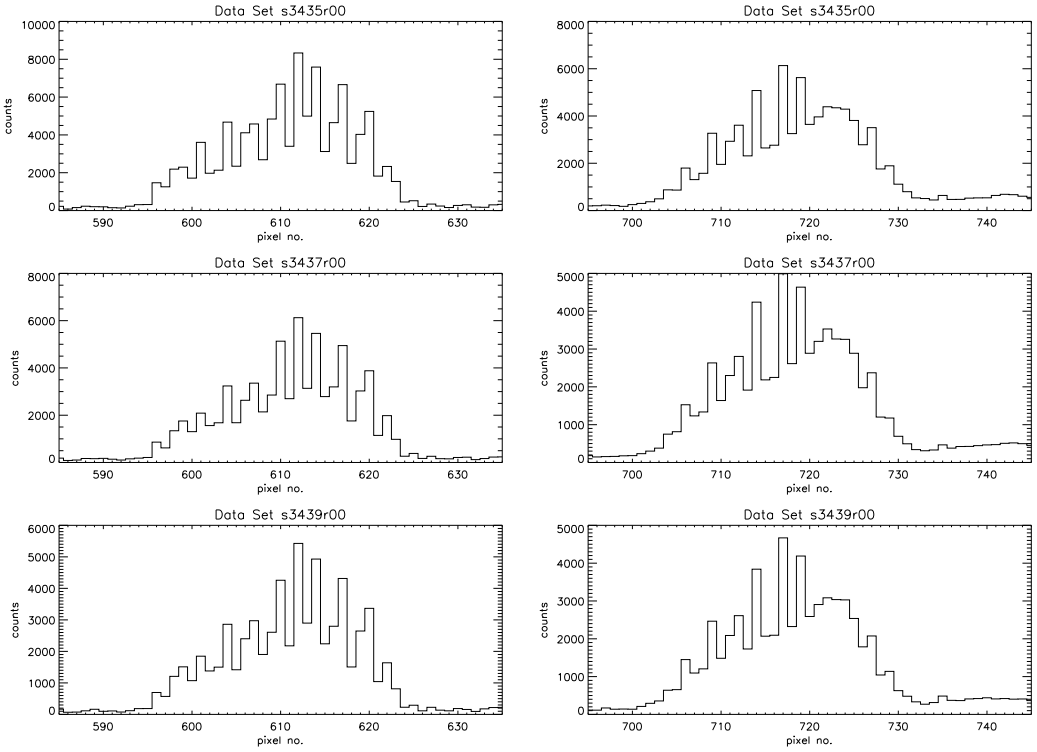

Figure 5.13: Example showing the similarity of individual lines' patterns when the counts from all 3 datasets have been totalled. Note also the pattern variation between the two different lines. The x-coordinates are pixel numbers along the wavelength dimension. The y-coordinates are recorded counts. The line in the 3 left hand diagrams is the line previously identified as FeIX 171Å(see text). The line in the 3 right hand diagrams was unidentified.

Test of Gaussian Line Profile Fitting to Fixed Patterns

We determined their wavelengths using the available wavelength calibration in the CDS software (*pix2wave*). Then, we attempted to find the options in *mlcds* that would allow us to get the optimum fit, regardless of whether the fit was good. Hence, in the results that follow, the same options have not necessarily been used for each pattern and, in some cases, two lines have been fitted instead of one. Evidently, handling the GIS lines is more time intensive than NIS and the development of automatic procedures is not necessarily of benefit here. As discussed in sec.5.2.3 *equal weighting* was introduced solely for this purpose, therefore, results are presented for each chosen line with and without this option. The total flux count from the line profile fitting routine was compared to a hand count. The results are given in table.5.5. We selected 8 lines spanning the four GIS detectors which showed different types of pattern.

It is clear that the program's ability to handle the data is determined by the pattern type and the fit options chosen. Fig.5.14 shows an example of attempts to fit two types of pattern using the intensity weighted and equal weighted fits. We can see that in the first pattern both options fit the data extremely well. The comparison to the hand count, from table.5.5, shows that both overestimate the total counts slightly, 2.8% for the weighted fit and 0.1% for the non-weighted fit. In contrast, the weighted fit fails on the second pattern underestimating the total counts by 78.3%. It appears that when the pattern is almost random the intensity weighted fit works quite well, but that when there are large single pixel drops in the profile, the code attempts to find more than one line. On the other hand, the fit with equal weighting is within 0.8%.

In the majority of the weighted fits the errors in comparison with the hand count are within the estimated standard errors of the program and in the equal weighted cases this is always true. Also, the equal weighting fit is generally within 1% of the hand count. In fact, we only found one instance where this was not the case i.e. the line at 788.2Å. In general, the equal weighting fits were very good with the weighted fits not quite so good. We conclude that with judicious selection of lines, based on their patterns, we can fit the total counts in each to within our attempted statistical accuracy of 1%. Also, if necessary it is possible to take those lines that

Approx. Line λ (angstroms)	ESEF%	Comparison to hand count	Weighted Fit	Back-ground
171.0	9.6	2.8% +	Y	sloped
171.0	11.1	0.1% +	N	sloped
174.5	8.0	8.4% -	Y	flat
174.5	10.8	0.2% +	N	flat
188.2	51.9 & 51.8*	78.3% -	Y	flat
188.2	17.6	0.8% -	N	flat
305.3	20.1 & 11.0*	18.6% -	Y	sloped
305.3	27.6 & 11.0*	0.1% -	N	flat
393.5	17.2	12.9% -	Y	flat
393.5	14.5	0.7% -	N	flat
465.2	10.8	15.1% -	Y	flat
465.2	10.5	0.7% -	N	flat
770.4	13.1	5.1% -	Y	flat
770.4	15.3	0.8% -	N	flat
738.2	12.3	6.7% -	Y	flat
738.2	12.6	3.1% -	N	flat

Table 5.5: Comparison of line fitting options for GIS data. * denotes that two lines have been fitted, +/- denote that the fit was too high/low in comparison to the hand count.

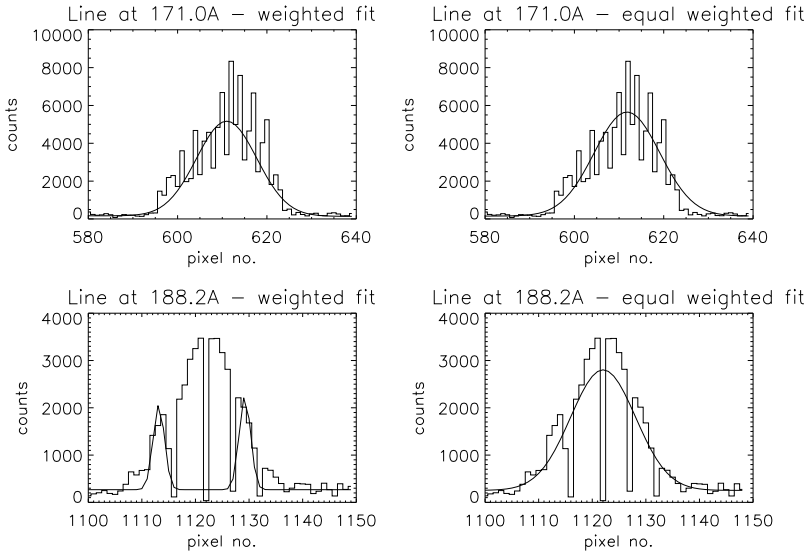

Figure 5.14: Weighted and non-weighted Gaussian line profile fits to the GIS1 lines at 171.0Å and 188.2Å.

cannot be fitted to sufficient accuracy and normalise them to the hand count in order to achieve the 1% statistics. This study is encouraging for all analyses reliant on intensity information from the GIS. In our case this is of major importance for the DEM study. Finally, we note that no attempt has as yet been made to retrieve line profile information, e.g. doppler components, and the above analysis assumed that in each case the line being dealt with was a single stationary Gaussian or a blend of two.

5.3.3 Modifications to Cosmic Ray Cleaning

The standard CDS-IDL cosmic ray cleaning routine (*avg_wo_cr*) was used successfully on the NISAT_S data. However, it automatically averages the data over one of the dimensions. If the data array consists of wavelength, slit and raster position dimensions then the routine reduces the data array to two dimensions, namely, the wavelength and slit. There is some flexibility here but contraction on wavelength is unsound (see below). The code works by locating cosmic rays as deviations of

greater than 3 σ in pixel count along the dimension to be contracted, marking their pixels, and then missing them out when the average is performed. However, it is quite possible, see fig.5.9, that cosmic ray hits may not occur perpendicular to the detector, that is, they leave a track across adjacent pixels. In such cases the routine is less effective and the choice of data dimension that can be worked over to locate them is constrained. In the case of a glancing hit, the slit dimension will not produce the best results (see fig.5.15 where the partially removed hit had smeared over pixels 60 to 89 in the y-direction along the slit) but contracting on the raster dimension means that the adjacent positional information is lost. For the NISAT_S study this was not a problem. We had to average in the raster direction to match the size of the CHASE slit. However, the aim of the RWPM_2 observations was specifically to map the intensity variations in time. As a result, we did not wish to lose time resolution by averaging over this dimension. Another approach was required.

One possibility is to write a new 'cleaning' routine that maintains the original array dimensions of the data. This would work, by finding values that deviate from those around them by more than 3 σ, and replacing them by some form of running average over, perhaps, three neighbouring values. In practice, we decided to make a modification to the existing routine to allow us to separate the data array dimension that was chosen for 'hit' location, from that chosen for averaging. This means that we can locate and mark cosmic ray hits in the most appropriate way for the particular observations and then average the data in a different way. It was felt that the method likely to be most successful was to locate hits in time, reasoning that the likelihood of a cosmic ray hitting exactly the same spot within the time frame of the observations was extremely small. This may not be true for long exposure times. To recap, for the RWPM_2 data we used the new cleaning code, temporal dimension for hit location and the spatial dimension for averaging. The method worked extremely well. Fig.5.15 shows the removal of a cosmic ray that had previously proved too stubborn when the original program was applied. The left hand diagram is a portion of the original spectrum. The centre frame shows the same portion after the original routine was applied and the right hand frame shows the results after application of the modified routine. Note how the hit at pixel no. 258, which was only partially removed by

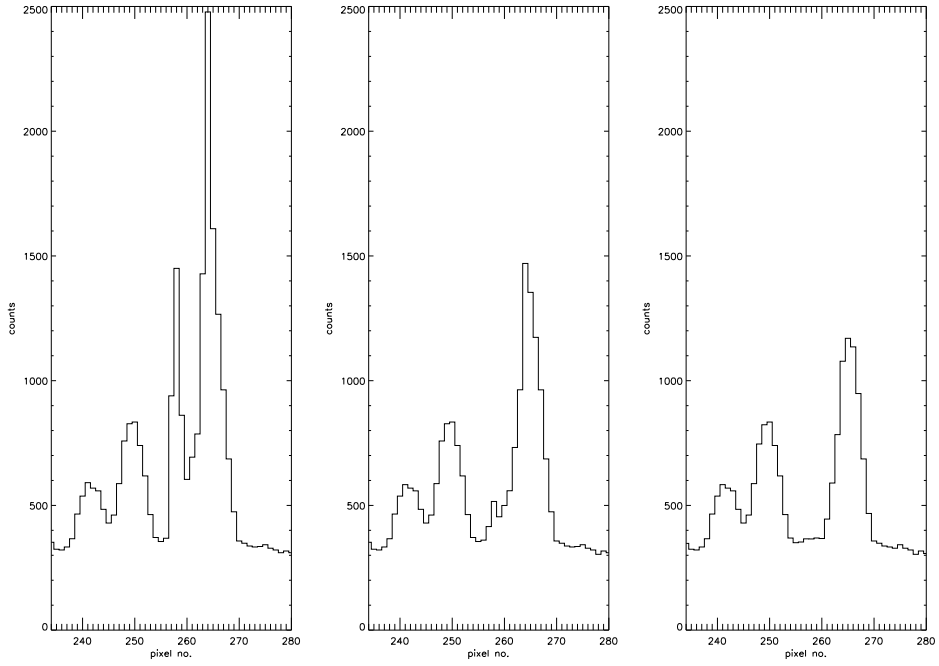

Figure 5.15: Application of cosmic ray removal routine to a hit between pixels 60 and 89 in the y-direction along the slit. The x-coordinate is pixel number along the wavelength dimension. The y-coordinate is recorded counts. Left - original spectral segment. Centre - segment after cleaning along y-direction with original routine. Right - segment after cleaning with modified code by location along teporal dimension and averaging over the y-direction as before.

the original routine, is completely removed by the new one. Note also that the 'real' spectral lines at 242 and 250 have count rates that are unchanged. Interestingly, it appears as though a cosmic ray lies atop the line at pixel no. 264. The routine has also been successful at differentiating it from the line itself. It is clear that this method is suitable for this particular data. Development of an array dimensionality maintaining cleaning code is deferred until the need arises.

As mentioned, for DEMST_1 the data for NIS were interleaved with GIS therefore only individual rasters were present in the datasets. More precisely, the data arrays were of the dimensions (1024,1,160) i.e. wavelength, raster, slit. We proceeded to test the cosmic ray cleaning on both the wavelength and slit dimension. Fig.5.16 shows

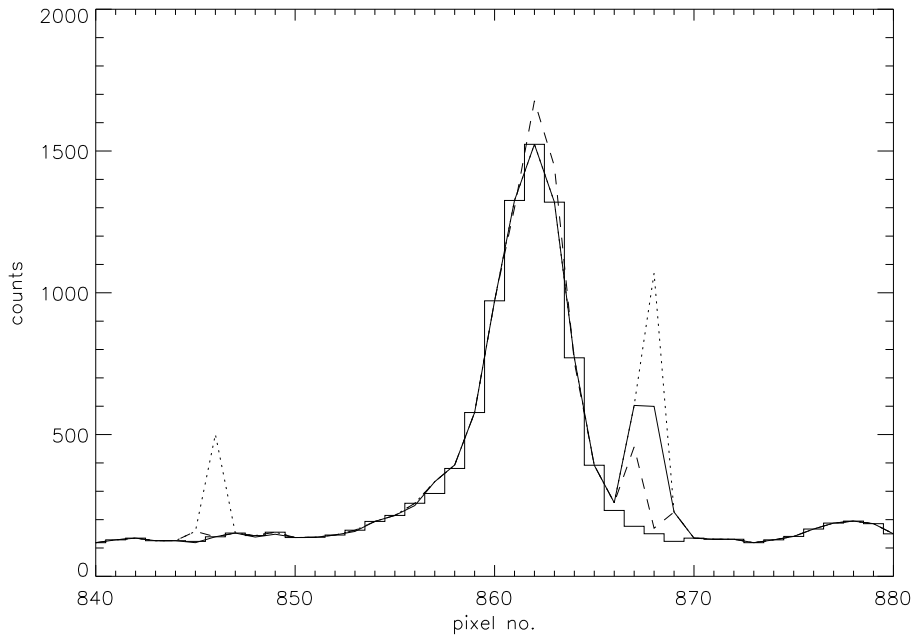

Figure 5.16: Example of improved cleaning as a result of collecting the DEMST_1 data together. Histogram - preferred method of cleaning over rasters. Dotted line - original data. Solid line - cleaned along slit. Dashed line - cleaned along wavelength. These are shown to highlight their inability to remove the event completely. Our method maintains the data and removes the spikes.

NIS1 data for fits file no. s4878r01. The data was extracted from pixels.840→880 along the wavelength dimension and 30→40 along the slit. The dotted line shows the original data summed over the slit dimension. Note the spikes at pixels 846 & 868 due to cosmic ray events. The solid line shows the result after locating hits on the spatial dimension. The dashed line shows the result after locating hits on the wavelength dimension. In both cases the data were averaged over the slit to produce the plot. We conclude that spatial location is a better method than wavelength location. Note that both methods almost completely remove the spike at pixel no.846, but that neither method has successfully removed the one at pixel no.868. Note also that locating by wavelength has added counts atop the spectral line at pixel no.862 and been marginally less effective in removing the line at pixel no.846. This method is clearly unsound. Given the success of the method used on the RWPM_1 data, despite appearing better, location spatially is unsatisfactory. We decided that location by comparing rasters would be more effective. Thus it was necessary to develop a procedure to read each dataset individually and stack the data arrays together. Then the cosmic ray location could be done over the raster dimension and the averaging performed over the slit. This retains the spatial components of the data. For our purposes we split the slit in two rejecting the redundant pixels at the ends as before. The method proved satisfactory. The histogram overplotted in fig.5.16 shows the result after separation of the stacked data.

5.4 Outline of Analysis Procedures and Preparation for the DEM

5.4.1 Coupling of the Observational Data to the DEM Code

Following the benchmark study of DEM programs by Harrison & Thompson (1992) it was agreed to adopt the inversion routine of Brown & Thompson (1991) as the standard preferred method. The core of the routine has been restructured and interfaced with ADAS, as routine ADAS601, by Summers et al.(1996). It has been thoroughly tested and validated on analysis of SERTS data (Lanzafame et al.(1997)). Following

discussions with the CDS team, Summers et al.(1996) also prepared a specific format for intensity files for entry to the DEM code. It is our wish to route the spectrally analysed, corrected and calibrated experimental data directly into files of this format.

The experience gained, during the work presented in the previous sections, has enabled us to develop a comprehensive analysis procedure and data archiving system that is both compatible with the CDS data and software and allows easy conversion to the ADAS DEM format files. In this section, the analysis path, and descriptions of software developments, are presented in detail.

The routines outlined below have been written to be flexible and applicable to different types of observing sequence. However, variety in all possible observing sequences is manifestly difficult for the *clean_data* routine to handle. For example, in the case of opacity or dynamic event studies, individual lines require to be analysed and mass automatic production of fits to them is not appropriate. Rather one wishes to fix certain lines and allow the positions of doppler shifted components to move. Therefore, although *clean_data* applies many important and necessary corrections to the data, it is not an all encompassing routine. Minor modifications may need to be made to accommodate individual observing sequences. The possibility of generalising it for all observing sequence data does arise through the standard format of the detector data arrays. All the data are collected in an array of the pattern; (wavelength, X, Y, time). However, gross averaging and reduction of data is not always necessary as exposure times may be such that good statistics can be obtained with small slit and raster sections. The principal point is that since it is not possible to account for or foresee every type of data, the initial data entry formats should not be strictly prescribed. Only after preliminary individual manipulations are the tighter data structures mandatory. In the case of the CHASE type analysis and DEM, the method and data use has been fairly well defined so it is possible to tighten and automate the initial manipulations.

Finally, all following routines prepare data for the line fitting program and store the results in a standard format so that any subsequent analysis procedures can easily be applied to it all. In addition, archiving of header information and identification tags is forced at each stage to allow the route to source data to be easily traceable.

5.4.2 Overview of the Analysis Path

Fig.5.17 is a flow chart showing the analysis path and archiving procedure. The manipulations discussed in the previous sections have been reduced to a number of small routines which can, if necessary, be tailored individually to any new developments. The routines are written in IDL and make use of a number of procedures provided by the CDS-IDL software. Therefore, the commands are typed interactively at the CDS software IDL prompt.

After starting *cidl* the routine *clean_data.pro* is invoked to separate selected data into segments suitable for the particular analysis. In the case of the analysis of statistical variance this refers to the spectral segments summed over half rasters and half slits corresponding to the size of the original CHASE slit. In the case of the DEM study, the spectral segments are untouched for GIS. For NIS the data are split along the slit, collected together, cleaned for cosmic rays on the time dimension and finally separated in time again (see sec.5.3.3). First, a CDS data fits file is selected by response to the prompt *'Enter data set for analysis'*. The chosen file is then read in by the standard *readcdsfits* routine. The program then checks, internally, to see whether the data was recorded by the normal incidence or grazing incidence spectrometer. In the case of the former, a number of standard corrections are performed to account for effects inherent in the detector. In the case of the latter, methods have been developed to deal with the data stream and investigation of the spectrum characteristics has been made (sec.5.3.3). Initial required corrections however are less well understood at this time and will be incorporated at a later data as they are not essential for the current study and demonstration which focuses on NIS.

For NIS the data has the *debias* correction imposed. The transmitted data will contain photon counts due to spectrum line radiation, continuum radiation, and possibly scattered light. In addition, there will also be a 'dark' current noise associated with the detector itself. However, the Viewfinder Detector Subsystem (VDS) CCD, of the NIS, adds a thermal background to the signal transmitted to the ground. This is because the temperature of the instrument is higher than was originally anticipated. This *bias* needs to be removed before analysing the spectrum (in extreme cases the bias can swamp the entire spectral signal (Harrison et al.(1995))). In order to correct

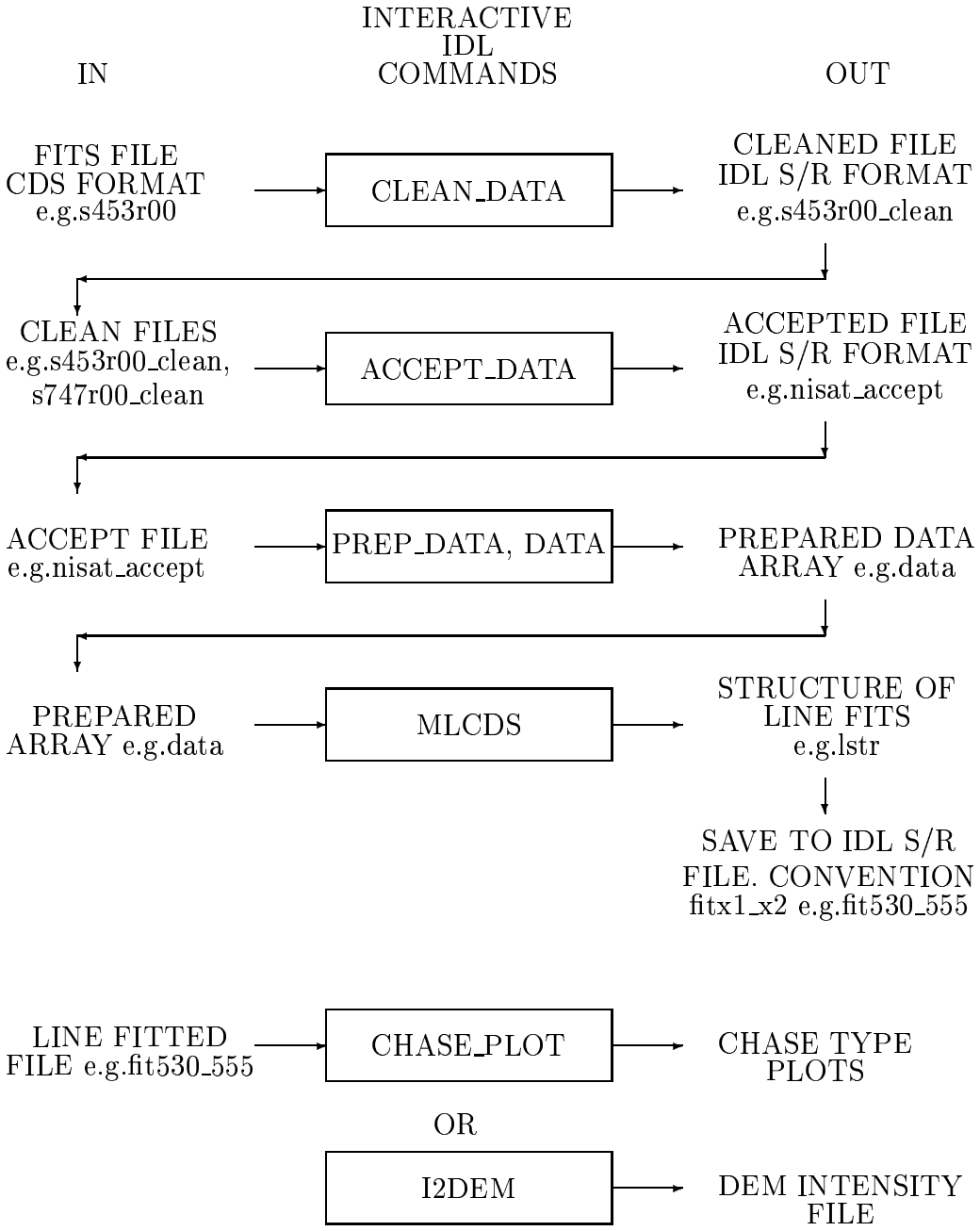

Figure 5.17: Schematic of CDS data analysis path and software components.

for the bias, data is transmitted from the four corners of the detector but outside the area of the two spectra. Thus it should only contain the bias, some scattered light and the inherent 'dark' current noise. It gives a measure of the magnitude of the bias together with an uncertainty, which can be subtracted from the spectral data. A CDS software routine *vds_debias* is available to do this and it is present in *clean_data.pro*.

Second, the routine *vds_calib* is applied to the data to convert it to photon events per pixel per second, rather than ADC's per pixel per sec. This conversion depends on the voltage of the detectors (Thompson (1994)). In addition, the routine divides the data by, and thus corrects for, the flat field image (or an appropriate part of it). It also takes account of any 'burn-in' of the detector due to the consistent appearance of strong lines e.g. HeI 584$\mathring{A}$. Finally, a correction term, to account for the nonlinear response of the detector, is applied if the count rate is high enough. This is introduced at 300 ADC/pixel/sec ($\sim$ 120 photon events/pixel/sec at 756V) but only becomes significant above a certain threshold ($\sim$ 5000 photon events/pixel/sec at all voltages (Thompson(1994) - CDS software note 13)).

For the DEM observing sequence the intensity calibration is then applied using *nis_calib*. This routine converts the data to physical units and for compatibility with ADAS we return the data as photons/cm^2/sec/steradian. The complete pre-flight calibration report is still under discussion so *nis_calib* should be subject to review after its publication.

The data for the two windows is then extracted from the structure and corrected for the fact that the slit images are not parallel to the edge of the detector. In addition, the spectral lines are slightly tilted. This 'skew' is wavelength dependent and varies between NIS1 & NIS2. For NIS1 the variation is approximately linear and averages to $\sim$0.004 pixels per pixel. For NIS2 the variation is approximately quadratic and of the same magnitude. A 0.004 'skew' corresponds to a slant along the spatial dimension of the slit of up to $\sim$0.64 of a pixel, for example. This in turn amounts to $\sim$ 0.045$\mathring{A}$ and $\sim$ 0.075$\mathring{A}$ for NIS1 and NIS2 respectively. A small routine was written to convert from pixel space to tilt factor and this was used to correct data when fitting the line profiles (see below). This correction is made for completeness and high precision though it is likely that, since the data are only binned to one

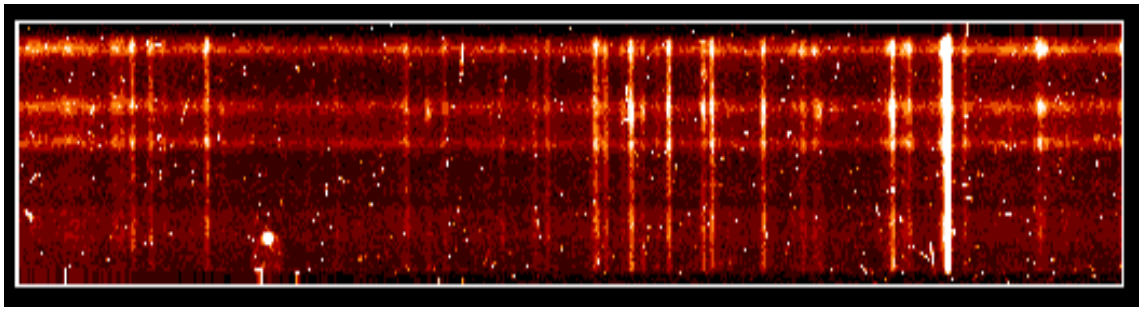

Figure 5.18: Example of the correction for spectrum slant applied to NIS1 dataset s4878r01. Note how the spectral lines now appear parallel to the slit edges and the redundant pixels at the lower edge are more clearly visible.

pixel, it will not improve our ability to separate lines within one pixel of each other. In addition, after testing we found that the difference in the flux in the lines was typically less than 2% and that this was within the estimated standard error of the fit. Fig.5.18 shows the same spectrum for NIS1 as in section.5.3.1 fig.5.9, but after application of the correction software. A comparison between the two shows the effect and the success of the correction.

clean_data then makes a check on the dimensionality of the data arrays to determine whether the data is from the DEM study (acronym DEMST_1) or the spectral atlas surveys (NISAT_S and GISAT_S). The data are then split and averaged as described above. For NIS, cosmic ray cleaning takes place at this point using the modified cosmic ray cleaning procedure described in sec.5.3.3. In addition, care is taken to ensure that missing pixels are accounted for correctly. Inadequate attention here initially caused some datasets to suffer major corruption. Data can sometimes be lost from individual pixels and pixels at the spatial extremes of the spectrum are often redundant (see section.5.3.1). These pixels are marked with a value of -100. This can obviously bias any averaging or totalling especially for NISAT_S where the intensity calibration is not applied and the values are consequently lower. For DEMST_1 the calibration affects the value that the missing pixels are marked with so a check is made to see whether any exist, prior to the calibration, in order to mark the value

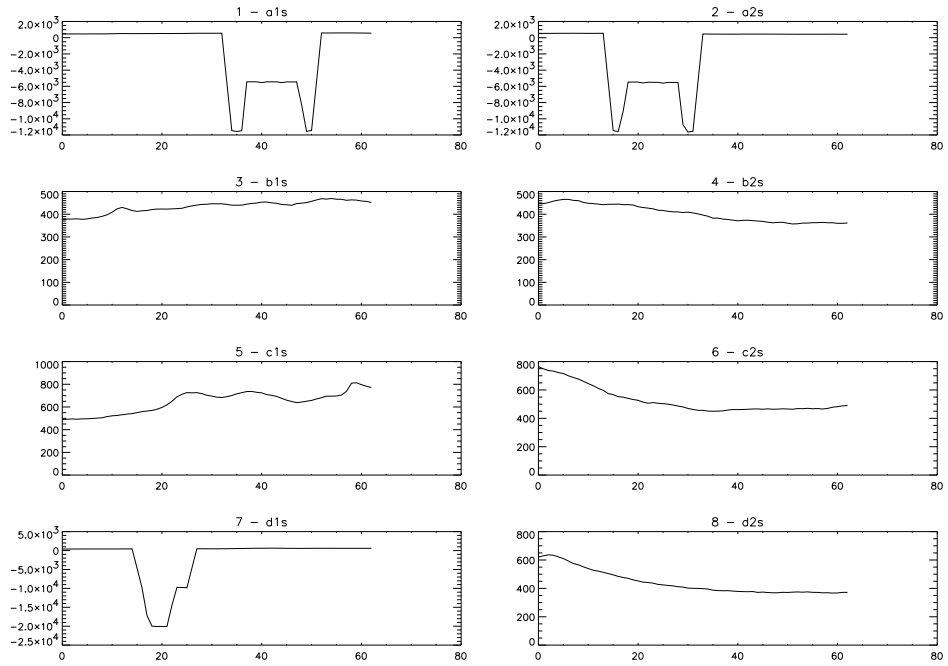

Figure 5.19: Example of the Display for Accepting Data segments. The x-coordinates are the pixel numbers in the y-direction along the spatial dimension of the slit. The y-coordinates are the recorded counts.

correctly. Subsequently, cosmic rays are marked with the same value so that the two features can be 'cleaned' simultaneously. The data are archived in IDL save/restore files with the naming convention tag (*_clean*) appended to the dataset name to distinguish it. Each individual spectral segment is given an index name corresponding to which portion of the rasters, slit and which detector it is. Data segments are also stored which are summed over wavelength, rather than slit, to aid subsequently in identifying signal drop outs. [1] In addition to data segments the header information, about the observing sequence, is also stored in the file.

The next step is to view the data segments to determine whether signal drop outs

[1]This works well for NIS but is problematic for particular sets of GIS observations. This is simply because the data arrays have only one dimension, or a wavelength dimension and 10 spatial locations, for the DEMST_1 and GISAT_S observations respectively. In either case, the data are effectively reduced to single values for each (if any) spatial raster.

Index	Detector window	Raster nos.	Slit Pixels
a1s	1	$0 \rightarrow 4$	$15 \rightarrow 77$
a2s	1	$0 \rightarrow 4$	$78 \rightarrow 140$
b1s	1	$5 \rightarrow 9$	$15 \rightarrow 77$
b2s	1	$5 \rightarrow 9$	$78 \rightarrow 140$
c1s	2	$0 \rightarrow 4$	$15 \rightarrow 77$
c2s	2	$0 \rightarrow 4$	$78 \rightarrow 140$
d1s	2	$5 \rightarrow 9$	$15 \rightarrow 77$
d2s	2	$5 \rightarrow 9$	$78 \rightarrow 140$

Table 5.6: Partitions of the NISAT_S data into segments.

occur and if there is evidence of other data corruption. This visual inspection is useful in convincing oneself that the cosmic ray cleaning has been performed successfully. A routine *accept_data.pro* is invoked which plots the cleaned spectral segments, summed over the dimension of wavelength dispersion, and allows the user to accept or reject them interactively. A dataset is entered in response to the *'Enter a CLEANED dataset for analysis'* prompt. This must be of the xxx_clean format output from *clean_data.pro*. An example plot for the dataset s453r00_clean is given in fig.5.19. The index numbers correspond, for this observing sequence, to the divisions given in table.5.6. A simple yes/no response to the question *'Accept plot 1 ?'* will stack the accepted plots into an array suitable for entry to the line profile fitting routine. After eight segments are plotted the option to *'Continue and analyse another CLEANED dataset ?'* is given. In this way, the array can be stacked with unlimited data segments. An internal check is made to ensure that, if a data segment is rejected, the corresponding segment for the other detector is also rejected. An identification array is created that stores the dataset name and segment letter designation to allow back tracing to the original header information in the xxx_clean file. Both the data array and identification array are stored in IDL save/restore format files with the naming convention *nis_accept* or *gis_accept* dependent on the spectrometer. In addition, a check is made every time a new dataset is analysed to ensure that the different xxx_clean datasets relate to the same spectrometer.

The data arrays stored in the xxx_accept files can be entered directly to *mlcds*. However, since it can only fit up to ten lines, it is usual to extract some segment of the array that covers only one or at most a few lines. This is aided by the routine *prep_data.pro*. A dataset is entered at the prompt *'Enter an xxx_accept IDL save/restore file :'* and a detector number is also specified at *'Enter a detector number :'*. The line or lines' pixel range can then be extracted by giving the lower pixel limit and then the estimated range in response to the questions *'Enter lower extreme pixel no. of line(s) to be fitted :'* and *Enter total pixel width of line(s) to be fitted :'*. The data array is restored to the *cidl* prompt by passing a variable, e.g. data, as a parameter in the call to *prep_data.pro*. All this requires that the pixel range of the line is known. A keyword */rotate* is available to allow the correction of tilted lines. This is done by the routine *vds_rotate* in conjunction with the routine *tilt_factor*. *tilt_factor* uses the central pixel of the entered range, along with supplied CDS software fits to the tilts of each detector, to calculate the parameters to pass to *vds_rotate*. Subsequently, the prepared data array is entered to *mlcds* which has the variety of options, allowing it to fit Gaussian profiles to the lines, described in sec.5.2.3. A comment is usually entered at this stage (in the header field - see sec.5.2.3) which gives the name of the user, the date of processing and the xxx_accept file that was used. This maintains the traceable route to source. The suggested convention is to give the output of the fits structure the name *lstr* and to save it to an IDL save/restore file, together with the minimum and maximum of the pixel range in the name e.g. fit530_555. This ensures that subsequent analysis routines, such as the 'intensities to DEM file' code and the statistical variance codes, can be used. The output structures are set up so that a series of lines can be stored in one file. It was thought, therefore, misleading to identify the file by one wavelength or pixel number and more appropriate to give a pixel range covering each line in the file. Also, a definitive statement of what the line is was thought impractical, anticipating the results presented in sec.5.5.1, so no attempt is made to introduce this in the naming convention. However, *mlcds* has a facility to make a preliminary identification if desired (see sec.5.2.3).

The structure based IDL save/restore files make the final fitted data compatible with the CDS software and easy to handle in subsequent analysis routines. Two

procedures for further application have been completed. Firstly, the routine which creates the CHASE type plots accesses the *fitx1_x2* files and makes use of any preliminary line identification so that it is easy to use. Invoked by typing *chase_plot* a *fitx1_x2* file is entered at the prompt and a *Preliminary Identification* list with an *Index* is displayed on screen. The program then asks the user to *Enter number of line in file for analysis :* whereupon the line fluxes and error are extracted, normalised to the average of the positions, and the plot displayed or written to a file. This routine was used repeatedly and successfully in sec5.5.1.

Finally, the code which writes the DEM intensity format file is started by typing *i2dem*. This routine prompts for the name of an output intensity file (*Enter a DEM file name :*) and then an input archive *fitx1_x2* file (*Enter an archive file name :*). The code determines how many datasets were used in the line profile fitting and displays a message on screen (e.g. *There are 40 datasets in this file*). The fits to the lines are stored in the data structures and so one of these is selected by response to the prompt *Choose a structure element to analyse (0,1,2...)*. From this the code extracts any preliminary line identifications to list on screen along with an index number. If no identification is available a *u* is displayed. Selection of a particular line is made by entering the appropriate index number. Further lines can be selected or alternatively lines from different datasets can be added. In this way the intensity file is built up. The line fluxes and estimated standard errors are then extracted. The estimated standard errors are converted from percentages to actual values and both are then written to the specific format of the DEM intensity file defined by Summers et al.(1996). An example is given in sec.5.6.1 fig.5.27. The line identifications can be given in two forms and are parsed to write out in the intensity file. The forms are e.g. 'OV 629' or 'O+4 629'and are entered while fitting the line profiles with *mlcds*. The *observed wavelength* is taken from this string and the fluxes and estimated standard errors are placed in the columns under *observed intensity* and *uncertainty*. A keyword option */wvspect* can be invoked to write the wavelengths into the *spectroscopic wavelengths* column also. This was found useful in practice. Other information has to be entered by hand as it relies on building up the $G(T_e)$ collection file as described in sec.5.6.1.

Note that the data stream is also compatible with the output of the SUMER

instrument. The IDL save/restore files that it produces are already in the correct format for *mlcds* and so can be directed to *fitx1_x2* archive files also.

5.5 Variability of Spectral Line Intensities from the CDS Data

5.5.1 Analysis of the Instrumental Accuracy and the Quality of the Observations

In order to obtain useful information regarding the physical nature of the solar atmosphere we must first overcome a number of problems associated with interpretation of the spectral line intensities. It is clear that the useable measurements, obtained by the spectrometer, depend on physical and observational factors. Included in the former category are changes in the structure of the solar atmosphere and in the physical conditions of the emitting plasma, during the time of the observations, along with changes in the intervening regions along the line of sight between the target and the spectrometer. In addition, the spectral reduction depends on the atomic model adopted. In the latter category, errors are introduced by the instrument, the methods of analysis and the instrumental sampling technique. These include random errors associated with the detection of photons, the accuracy of the intensity calibration and the instrumental transmission, the efficiency of the data communication system and transference to the ground and accuracy of the line profile fitting techniques. Also, the spectrometer will only 'see' a proportion of the emitted photons due to the finite width of the slit.

In this section we quantify the variation of spectral line intensities as we observe the solar atmosphere in different positions and at different times. Also, we make estimates of what Lang et al.(1990) call the reproducibility of the observations and which we prefer to refer to as the *observational accuracy*, i.e. that part of the analysis which produces errors purely due to the factors involved in determining spectral line intensities by using a spectrometer on a spacecraft.

Line Position (Å)	log T_e(K)	%	Line Position (Å)	log T_e(K)	%
HeI 515.617	4.1	12	HeI 522.213	4.1	9
HeI 537.030	4.1	10	HeI 584.334	4.1	7
HeII 303.78[2]	4.5	18	CIII 538.2[m]	4.9	29
OIII 525.797	4.9	20	OIII 599.598	4.9	11
OIV 553.329	5.3	7	OIV 554.076	5.3	7
OIV 554.513	5.3	4	OIV 555.263	5.3	4
OIV 608.397	5.3	7	NeIV 543.891	5.3	18
NeIV 541.127	5.3	42	NeIV 542.073	5.3	7
OV 629.732	5.4	17	NeV 569.830	5.5	18
NeV 572.106[b]	5.5	13	ArVII 585.75	5.7	24
NeVI 558.595	5.7	6	NeVI 562.7	5.7	10
NeVII 559.947	5.8	33	NeVII 561.378	5.8	17
NeVII 564.529	5.8	24	MgVIII 313.754	6.0	17
MgVIII 315.039	6.0	16	MgVIII 317.039	6.0	15
MgVIII 335.253	6.0	11	MgVIII 339.006	6.0	16
SiVIII 314.327	6.1	13	SiVIII 316.205	6.1	10
SiVIII 319.826	6.1	12	MgIX 368.057	6.1	12
AlX 332.789	6.1	23	AlXI 550.031	6.1	41
SiIX 341.949[b]	6.2	2	FeX 345.102[b]	6.2	9
FeX 345.723	6.2	10	FeX 365.543	6.2	10
CaX 557.74	6.2	12	CaX 574.01	6.2	13
MgX 609.76	6.2	13	MgX 624.94	6.2	6
SiIX 349.8[m]	6.2	7	FeXI 341.113	6.3	12
FeXI 352.662	6.3	9	FeXI 369.153	6.3	13
SiX 347.403	6.3	14	SiX 356.0[m]	6.3	14
FeXII 346.852	6.4	16	FeXII 352.106	6.4	13
FeXII 364.467	6.4	10	FeXI 358.621[b]	6.3	39
SiXI 580.92	6.4	8	SiXI 303.78[2]	6.4	34
SiXII 520.66	6.4	39	FeXIII 348.183	6.5	10
FeXIII 359.638	6.5	19			

Table 5.7: Lines selected for the study of statistical variance along with their temperature of formation and an estimate of the observational accuracy. Superscripts; m - multiplet, b - blend, 2 - second order line.

Table.5.7 presents the chosen line list and also shows the expected temperature of formation. This is taken as the peak of the ionisation balance curve for the emitting ion (Summers(1974)). Also shown in the table is a final estimate of the observational accuracy for each of the chosen lines (see below). The datasets used were the segments split and averaged as described in sec.5.3.1 and given in table.5.4.

For each line we plotted the log of the relative intensity against position number as given in table.5.4. That is, we normalised the uncalibrated intensities in counts, at each position number, to the average intensity of all position numbers. Note that the position numbers correspond to different summed sets rasters and different slit portions. Also, the different datasets were recorded on separate dates and varying times. The plots are presented in figs.5.20-5.22 and are ordered according to the temperature of formation of the line. For ions of the same element (assumed formed at the same temperature) they have been ordered by increasing wavelength. The line identifications and the window of the detector that recorded the data are given in the title of the individual plots. The plots are scaled appropriately for each line and so the y axis ranges are not all the same. This was done to allow any patterns to be more clearly visible. Also, error bars (output from the line profile fitting routine) are over plotted on each graph. In some cases the fits are so good that the error bars are difficult to see. These plots are similar to those presented by Lang et al.(1990) in their analysis of the CHASE measurements. Note that, as in table.5.7, some lines have superscripts denoting that they are multiplets or second order lines. Four lines are marked as blended. Their components are identified in sec.5.6.1 table.5.9. Each of these lines are included since the blended line's ions are formed at about the same temperature and so should show a similar pattern.

It is clear that a pattern of variation exists between lines formed at roughly the same temperature. This is not to say that the pattern reflects the temperature regime (that point will be discussed in sec.5.5.2) but simply that it may be possible to extend the CHASE analysis to CDS and so determine the statistical variation of the measurements. From fig.5.20-5.22 we can see a gradual development of the pattern from HeI 515.6$\mathring{A}$ through to NeVII 564.5$\mathring{A}$. This change is influenced mainly by the development of a sharp rise in intensity at position number 2 that remains high

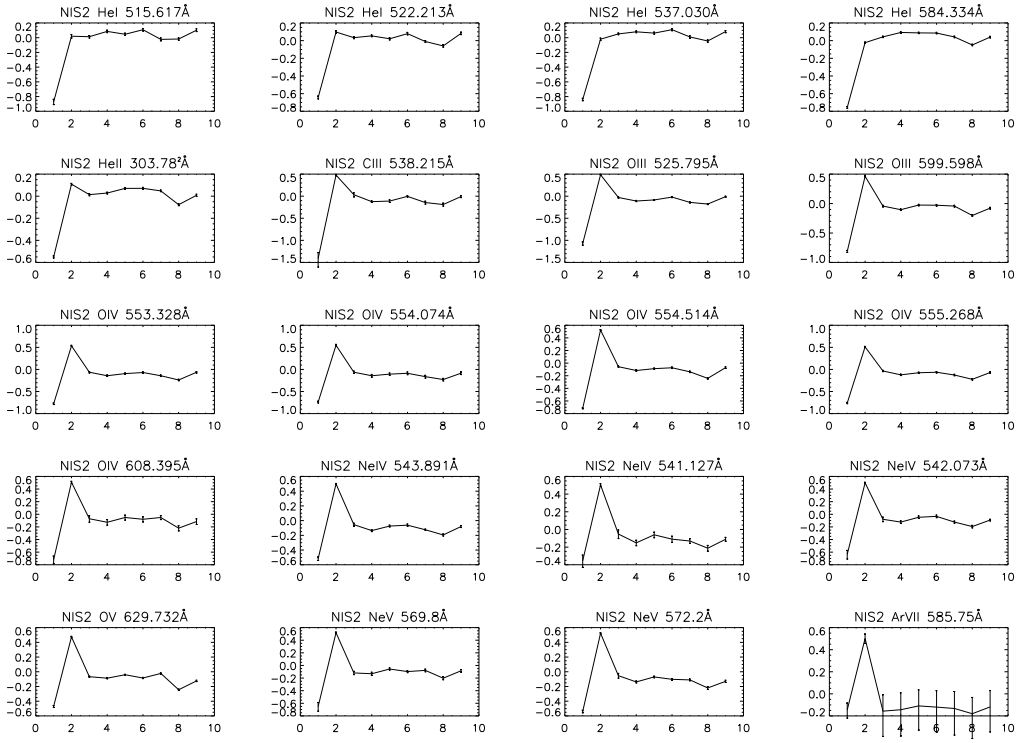

Figure 5.20: Plots of the logarithm of the relative intensity (see text) against position number (as defined in table.5.4). The line identification and the normal incidence extraction window that recorded it are noted above each individual graph. The plots are ordered by the temperature of formation of the line as given in table.5.4. Error bars are overplotted on each point and are largest for weak and blended lines.

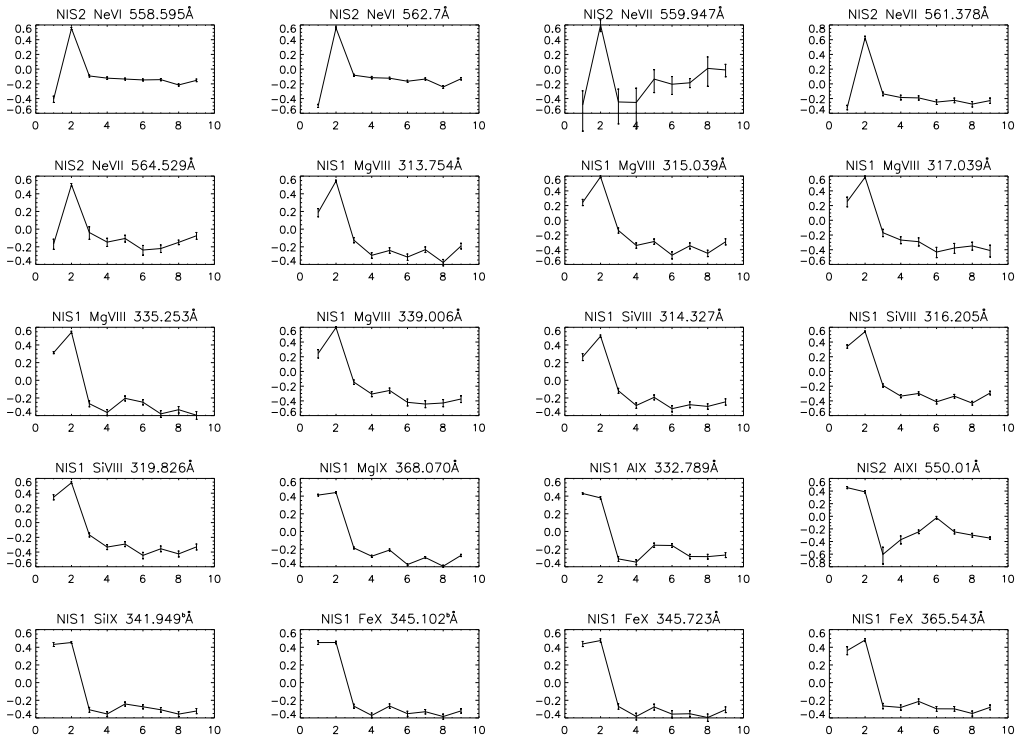

Figure 5.21: Plots of the logarithm of the relative intensity (see text) against position number (as defined in table.5.4). The line identification and the normal incidence extraction window that recorded it are noted above each individual graph. The plots are ordered by the temperature of formation of the line as given in table.5.4. Error bars are overplotted on each point and are largest for weak and blended lines.

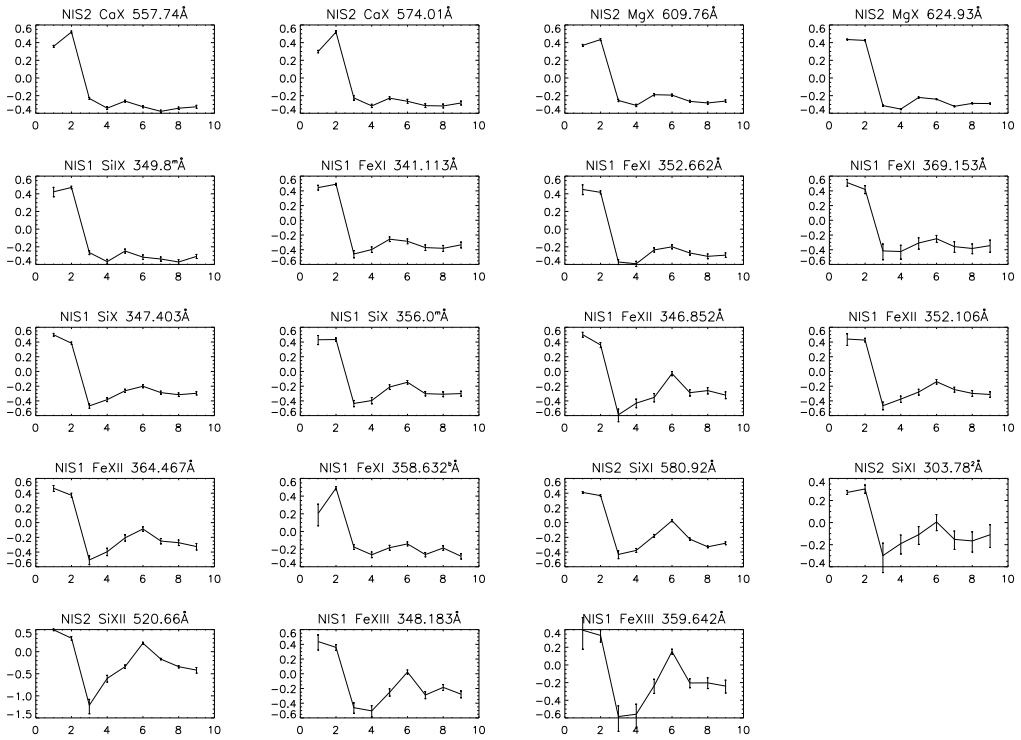

Figure 5.22: Plots of the logarithm of the relative intensity (see text) against position number (as defined in table.5.4). The line identification and the normal incidence extraction window that recorded it are noted above each individual graph. The plots are ordered by the temperature of formation of the line as given in table.5.4. Error bars are overplotted on each point and are largest for weak and blended lines.

through all the remaining plots. Position numbers 3 through 9 fluctuate around the mean up to HeII 303.8$\mathring{A}$ and then begin to be depressed to a slightly lower intensity. This is principally due to the influence, through the mean value, of the rise at position 2. Position number 1 varies more widely and in the plot of CIII 538.2$\mathring{A}$ is very much less intense despite the influence of position 2. By the time we reach the temperatures of the NeVII plots it has however begun to rise in intensity so that the sudden jump at MgVIII 313.7$\mathring{A}$ is not unexpected. From MgVII 313.7$\mathring{A}$ onwards the pattern has changed dramatically from HeI 515.6$\mathring{A}$ and position number 5 has also become more active. From here on there is a gradual development of the intensity of position number 6 until it rivals 5 in the AlX 332.7$\mathring{A}$ plot and briefly overcomes it in AlXI 550.0$\mathring{A}$. This latter pattern appears in greater evidence from FeXI 352.6$\mathring{A}$ onwards and raises the possibility that the temperature of formation of AlXI was wrongly assigned. In fact, results for AlX and AlXI were not presented by Summers(1974) and so results from ADAS were taken. From experience at looking at formation temperatures it is likely that had all the results been taken from ADAS the plots would have remained in order (except AlX and AlXI), but would have been shifted to slightly lower temperatures. From the plot of MgIX 368$\mathring{A}$ on, the intensity of position number 2 begins to drop slightly so that position 1 competes with it and dominates by the final four plots.

From the plots we see that the intensity of individual lines varies substantially from location to location and time to time with a typical variation being about a factor ten. However, variations of up to a factor fifty cannot be excluded, see for example, CIII 538.2$\mathring{A}$ or OIII 525.8$\mathring{A}$. In an attempt to be more quantitative and statistically accurate, we calculated the individual line's coefficients of count variation about their mean. We then then plotted these against the line's temperature of formation. This is simply the relative fluctuation of the counts about their mean, for a particular line, expressed as a percentage i.e.

$$\frac{\sqrt{\sum_i (F_i - \bar{F})^2 / N}}{\bar{F}} \times 100.0 \tag{5.5}$$

where F_i is the fitted flux for the line in the ith dataset, N is the number of datasets,

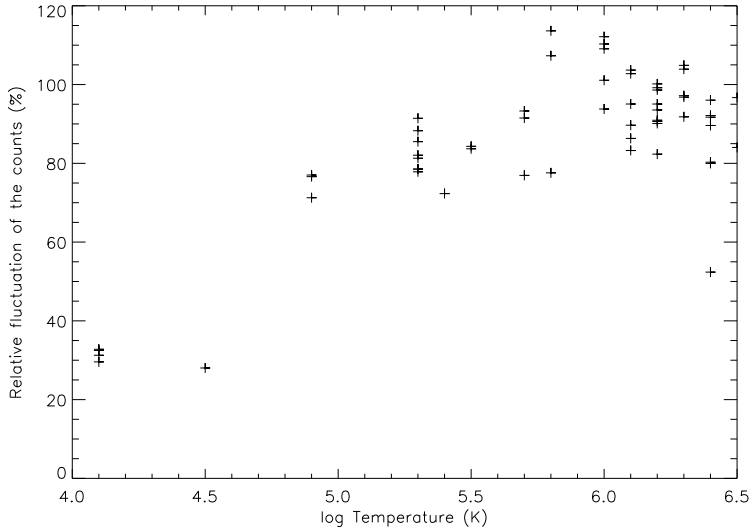

Figure 5.23: Relative fluctuation of the counts against temperature of line formation.

and the top line represents the standard deviation. Fig.5.23 presents the results. Statistically the meaning of this is that each point on the graph represents the percentage variability of the counts about their mean for a particular line. Therefore, we can see that the counts for individual lines can vary between $\sim 30\%$ and $\sim 110\%$ from their individual mean values.

Another way of expressing this variation is to take the standard error of the mean. For example, in the case of HeI 515.6$\mathring{A}$ the coefficient of variation is 32.8%, whilst the mean is 12496.8. Thus, the relative fluctuation is 0.328 and the standard deviation is $0.328 \times 12496.8 = 4098.9$, giving a standard error of the mean ~ 1366.3 (i.e.$\sigma/n^{1/2}$). Therefore, we can say that if we have a normal distribution of intensities, the mean value of intensity for HeI 515.6$\mathring{A}$ is $1.25 \pm 0.14 \times 10^4$ and that if we took a larger number of measurements the mean would lie within this range (i.e. between $\sim 1.11 \times 10^4$ and $\sim 1.39 \times 10^4$) with a probability of 68% (Topping (1962)). This single result is presented more as an example to help with our understanding rather than a quantitative statement about the intensity variation of HeI in the solar atmosphere. However, it might be argued that the distribution of intensities is in some sense normal

Pattern	No. of Lines	Ions Included
1	5	HeI, HeII
2	11	CIII, OIII, OIV, NeIV
3	9	OV, NeV, ArVII, NeVI, NeVII
4	11	MgVIII, SiVIII, MgIX, AlX, AlXI
5	14	SiIX, FeX, CaX, MgX, SiIX, FeXI, SiX
6	9	FeXII, FeXI, SiXI, SiXII, FeXIII

Table 5.8: Ions contributing to each averaged pattern.

or averaged in the quiet sun, even including *overactive* and *underactive* regions as these might cancel each other to some degree. In any case, it is often usual to make this assumption at least about the variance of intensity, see for example, sec.5.2.1.

Given that the patterns appear similar for lines formed at the same temperature we decided to separate groups of patterns, as was done for CHASE, and form average patterns to try to determine how much each individual pattern of the group varies from the average. We believe this variation gives us an indication of the observational accuracy of the results. We argue that since the lines of the groups are formed at the same temperature and they are responding in a similar way to the variations in the emitting plasma, variations from the average at each point are indicative of variations due to the observational technique. In reality, we expect that solar conditions and the atomic model still play some part in determining these variations and so we consider the results of this analysis to be upper limits to the observational accuracy. The ions whose lines were selected for each group are given in table.5.8. To form the averaged plots we took the members of the six groups and found the mean of the intensities from each member at each position. This gave us a mean value for each position number from which we then found the mean of these means. Finally, we divided the means at each position by this last mean and plotted the logs of these values. In this way we produced six averaged patterns which are shown in fig.5.24. Fig.5.24 also shows the temperature spread of these averaged patterns. The features described in detail above are more evident in these plots. The sharp rise at position 2 appears quite convincingly in the second and third plots with the jump at position 1 and the

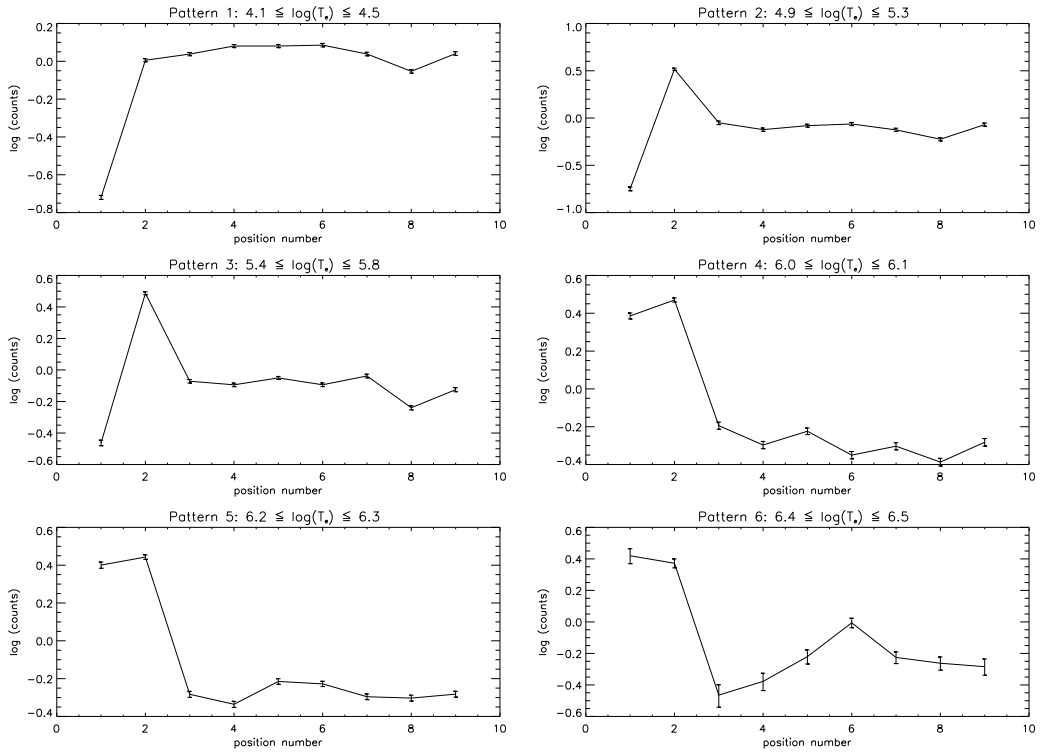

Figure 5.24: Averaged patterns corresponding to the groups of lines chosen (see table.5.8).

rise at position 6 evident in plots four and six respectively.

To calculate the observational accuracy we took the relative intensity values, used to produce the plots in fig.5.20-5.22, and calculated a mean from the values of the contributing patterns. This was done for each position. We then subtracted this mean from the relative intensities from the contributing patterns, at each position, and divided these by the mean. We then took the root mean square of these last values to give us our final results. The observational accuracy values obtained are shown in table.5.7 in the form of percentages. In addition, fig.5.25 shows the values plotted against line formation temperature. We can see that this measure of the observational accuracy varies between about 2% and 42% with the majority of values less than 20% and clustered around 10-15%. As mentioned these values are overestimates since it

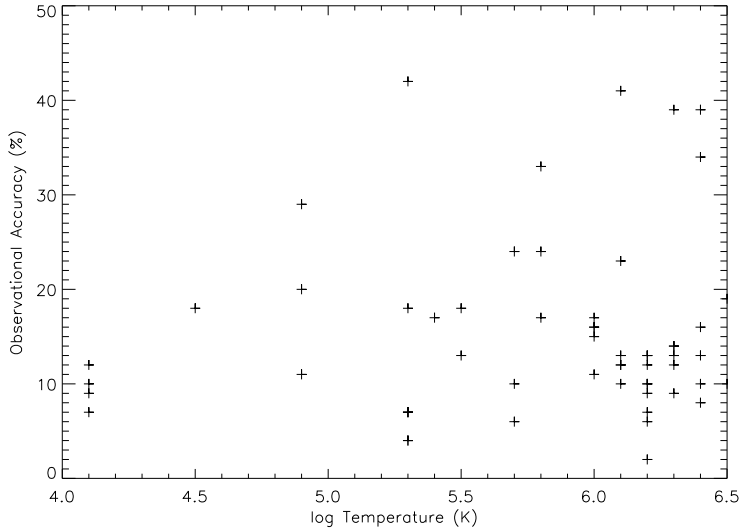

Figure 5.25: Observational accuracy of each line plotted against the log of the temperature of formation.

is difficult to completely exclude other influences (sec.5.5.1). Therefore, we conclude that the observational accuracy of the majority of these observations is in the region of 10-15% and we are cautiously optimistic that we may be able to work at around the 10% level or even better.

These results are similar to, or perhaps slightly better than, the conclusions of the CHASE analysis. In addition, it appears that the spectral line intensity variability is about the same as for CHASE. The determination of this observational accuracy is the main reason for looking at the raw data prior to any intensity calibration or atomic physics being applied. It would also be worthwhile to develop more accurate ways of determining the individual factors contributing to the observational accuracy.

Anomalies and Mis-Identifications

A number of important points arose during the above investigation. The original line identification list from the spectral atlas contained a further three lines which have been excluded from this study. These were identified as NeV 568.418$\mathring{A}$, MgVI 349.1$\mathring{A}$

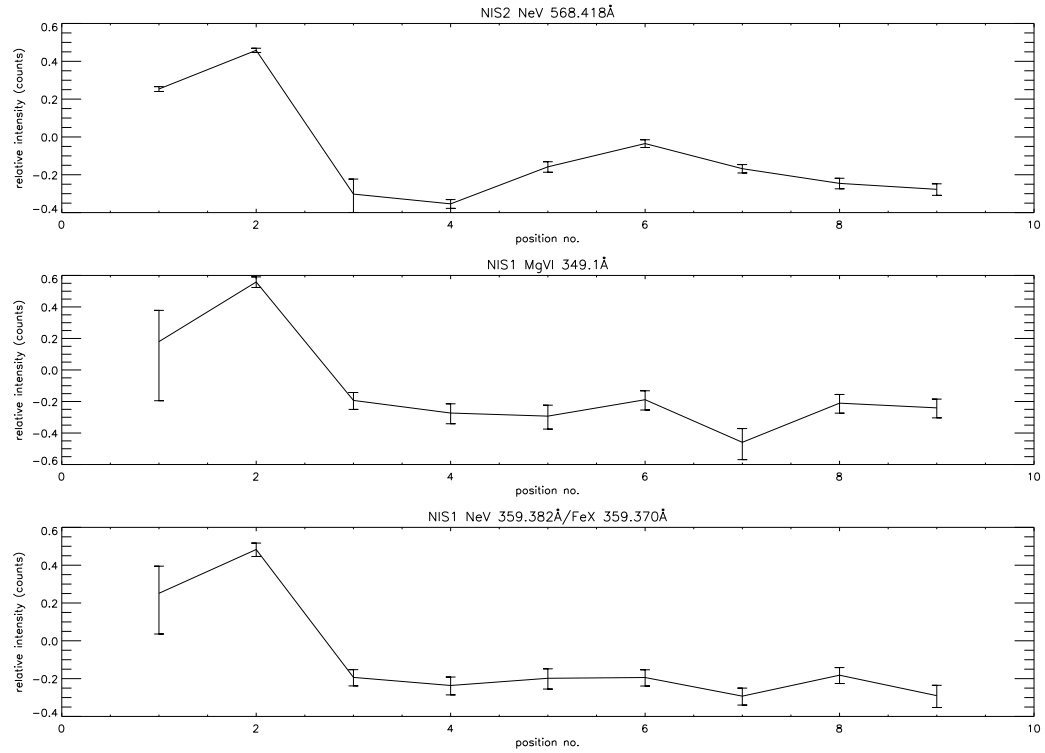

Figure 5.26: Three patterns which appeared odd for the reasons discussed in the text.

and a blend between NeV359.382$\mathring{A}$ and FeX 359.370$\mathring{A}$. The patterns of variation through the nine position numbers are given in fig.5.26. According to the temperatures of formation of NeV and MgVI (5.5 and 5.7 in the log respectively) the plots should appear between NeV 572.2$\mathring{A}$ and ArVII 585.75$\mathring{A}$ in fig.5.20. However, the high values of position number 1 suggest that the MgVI line should be associated with plots at a higher temperature of formation, perhaps closer to MgVIII or SiVIII i.e. 6.0 or 6.1 in the log. In addition, the rise in the intensity of position 6 in the NeV plot suggests that this line is formed at temperatures that are higher still (perhaps closer to MgX i.e. 6.2 in the log). For this reason we believe that these lines have been mis-identified. This points out a potentially valuable other use for the types of plots that we have presented. They may be able to confirm identifications and provide clues to the identity of unknown lines by allowing their temperatures to be

estimated. No suggestion for what these particular lines are is given here.

Note also that the blended line appears to be more closely related to the pattern of FeX than NeV. This raises the possibility that the FeX line is the dominant component. However, since this is the only line in the study that is a blend of two lines formed at radically different temperatures, it was decided to reject it.

5.5.2 On the Physical Significance of the Patterns and the existence of a Temperature Dependence of Variability

The main purpose of producing the plots was to attempt to discover the statistical variation in the measurements due to factors resulting from the sampling and analysis methods. We expected patterns, similar to those seen by Lang et al(1990), to exist and that this would aid us in our study by grouping together lines formed at similar temperatures. While we do not expect the patterns to be reproduced exactly for lines formed at the same temperature, since there are many solar and atomic influences on the intensities, we believe that their existence is indicative of them being determined by systematic factors. As pointed out by Lang et al(1990) this suggests that there is hope of interpreting the intensities if we can discover the proper physical processes that contribute to them.

The analysis of CHASE measurements by Lang et al(1990) show a number of interesting results. They identified three distinct types of pattern that appeared to change sharply at definite temperatures. They also found an increasing variability with temperature. The latter was seen both for relative intensities with position and also in deviations from the averaged patterns i.e. for the highest temperatures, despite the most obvious change, the averaged pattern was the least secure in terms of applicability to other lines. Given the much larger number of lines available in the present study it seems worthwhile to re-examine some of these issues.

On the question of a temperature dependence of the variability fig.5.23 should give an indication. However, this diagram is inconclusive due to the small number of lines observed in the $1.2 \times 10^4 K$ to $6.3 \times 10^4 K$ region. There is some indication of an increasing slope with temperature and if the five points in the lower left corner are

accepted then this idea is strengthened. There does appear to be a wider spread in fluctuation at higher temperatures but, again, this situation could be reversed if more points were added around the low temperature high variability region. We conclude that without more points it becomes a subjective exercise. It would be interesting to look again at this question with a specifically targeted set of lines that span a more controlled range of temperatures. Looking at the averaged patterns of fig.5.24 and the observational accuracies of fig.5.25 leads to the same conclusion. The variability appears higher for patterns 2 to 6 than for pattern 1 and there is a greater scatter in the values of observational accuracy at higher temperatures. However, if the lines contributing to pattern 1 are not a representative sample of the low temperature variability then much more cannot be said. In any case, the activity of points 1 and 2 partly controls the variability for this data collection.

It is interesting to compare the temperatures at which the averaged patterns change in the present work with the results presented by Lang et al.(1990). In their study they found a pattern change at $\sim logT = 5.5$ to 5.8 and a more distinct one at $\sim logT = 6.1$. They suggest that the patterns are associated with the physical structure of the atmosphere at different temperatures. That is, the first shows grossly the supergranulation structure of the network in the chromosphere and the second shows the loop structures of the higher temperature lines in the transition zone and corona. They also suggest that the third pattern may be evidence for an additional transition in the solar atmosphere at this temperature. With regard to this last point, they suggest that the discontinuity at $logT = 6.1$ could provide supporting evidence for the type of cool loop model proposed by Antiochos & Noci (1986). Indeed, a discontinuity of this type may be supportive of the arguments of Feldman & Laming (1994).

In this work, we found the most distinctive pattern changes between 1 and 2 and then between 3 and 4 of fig.5.24. As mentioned, these appear influenced by the activity of points 2 and 1 respectively. In addition, they are not as 'sharp' as those seen by Lang et al.(1990). These alterations occur at temperatures between $\sim logT = 4.5$ to 4.9 in the first case and between $\sim logT = 5.8$ and 6.0 in the latter case. The absence of a distinctive change at $logT$=4.5 to 4.9, in the CHASE

paper, and at $logT$=5.5 to 5.8, in the present work, suggests that there may be no deeper physical significance to the sharp pattern changes. However, the sharpest change occurred between $\sim logT = 5.8$ and 6.0 which is closer to that seen with CHASE. Also, if the changes correspond to particular features of the atmosphere it is possible that the temperatures at which the changes occur are dependent on the shapes and sizes of the features 'caught' by the spectrometer on the day. However, this is equivalent to saying that the pattern changes fall within the limits of the natural variation of the atmosphere. The observations with the grazing incidence spectrometer long slit should precisely match the observations done with CHASE and clear up these speculative queries. It is recommended that, for this purpose, the same source as used by Lang et al.(1990) is taken to decide the temperatures of line formation.

5.6 Demonstration of Method and Reconstruction of the DEM for CDS-NIS

As a demonstration and test of the analysis procedures we used the normal incidence spectrometer data from the DEMST_1 observations taken on September 22nd 1996. This demonstration provided an opportunity to re-assess each of the software components and to test their robustness. Modifications and adjustments were made as a result of this exercise that have subsequently been included in the routines described above. In addition, potential problems with atomic data and line blending were identified examination of which is now part of the final study.

5.6.1 Preparation of Intensity File

Each of the lines identified for the study of statistical variability in section.5.5.1 table.5.7 were considered for this preliminary DEM attempt. Fifty nine lines had been identified including three multiplets and four blends (see section.5.5.1). Using the preliminary spectral atlases for NIS1 & NIS2, completed as part of the initial study of the data (see section. 5.3.1), we identified those components of the three

Main Component	Actual/Other Contributors
SiIX 349.8^{m}Å	SiIX 349.795Å SiIX 349.617Å SiIX 349.873Å
SiX 356.0^{m}Å	SiX 349.05Å SiX 349.01Å
CIII 538.2^{m}Å	CIII 538.080Å CIII 538.149Å CIII 538.312Å
SiIX 341.949^{b}Å	MgVIII 342.062Å
FeX 345.102^{b}Å	SiIX 344.951Å SiIX 345.124Å
FeXI 358.621^{b}Å	SiXI 358.653Å
NeV 572.106^{b}Å	NeV 572.336Å

Table 5.9: Line components contributing to the make up of the blended lines and multiplets from table.5.7. Superscript m - multiplet, b - blend.

multiplets that contributed to the formation of the line shapes that were actually fitted. In addition, the atlases were used to identify those lines that were expected to contribute as components of the four blends. Table.5.9 lists the seven blends and multiplets and the components that were identified in each case. Due to the possibility of opacity affecting transitions within ions of moderate charge (Doyle & McWhirter(1980)), we rejected the five helium lines from the analysis. In addition, a second order intensity calibration was not available at the time of the analysis so the SiXI 303.78Åline was excluded. This left a total of fifty three lines, not including the blend/multiplet components.

The *s4878r03* data of the DEMST_1 observations was then processed, corrected and fitted as described in section.5.4.2. The routine *i2dem.pro* was used to create the intensity file, a segment of which is shown in fig.5.27. As mentioned in section.5.4.2, the ion identifiers, observed and spectroscopic wavelengths, observed intensities and uncertainties are printed directly by the routine. The *configurations* are not essential for further processing and are entered by hand. A blend index, *blnd*, is also entered

```
*
* CDS DEMST_1 observing sequence - Normal Incidence Data Only
*
|-------------------------------------------------------------------------------------------------------------------------------------------------------|
      spectr.          configuration              configuration          G-in  blnd  observed      observed          uncert.
    |       | wavelength |                          |                    |     |     | wavelength  | intensity     |
----|-------|------------|--------------------------|--------------------|-----|-----|-------------|---------------|---------------|--|
Fe    XIII      359.6380    3s2 3p2 (3)P( 1.0 ) -  3s 3p3 (3)D( 2.0 )     2     0     359.6380    1.1655e+13    8.9384e+11
Fe    XI        358.6210    3s2 3p4 (3)P( 0.0 ) -  3s 3p5 (3)P( 1.0 )     4     1     358.6210    2.1792e+13    1.6215e+12
Si    XI        358.6530      2s 2p (3)P( 1.0 ) -  2p2 (3)P( 2.0 )        10     1     358.6210
Fe    XII       346.8520    3s2 3p3 (4)S( 1.5 ) -  3s 3p4 (4)P( 0.5 )     3     0     346.8520    1.8233e+13    1.1201e+12
Si    IX        349.7950    2s2 2p2 (3)P( 2.0 ) -  2s 2p3 (3)D( 2.0 )    10     2     349.8000    5.2270e+13    2.5465e+12
Si    IX        349.6170    2s2 2p2 (3)P( 2.0 ) -  2s 2p3 (3)D( 1.0 )    15     2     349.8000
Si    IX        349.8730    2s2 2p2 (3)P( 2.0 ) -  2s 2p3 (3)D( 3.0 )    19     2     349.8000
Fe    XII       364.4670    3s2 3p3 (4)S( 1.5 ) -  3s 3p4 (4)P( 2.5 )     1     0     364.4670    4.6346e+13    1.7102e+12
..     .          .
Ne    VII       559.9470      2s 2p (3)P( 0.0 ) -  2p2 (3)P( 1.0 )        6     0     559.9470    1.8366e+12    1.4842e+11

-------------------------------------------------------------------------------------------------------------------------------------------------------|
```

Figure 5.27: Example of DEM intensity file format using DEMST_1 data.

by hand. Zeros are placed against every line that is to be treated separately, while blended lines are grouped together using the same index. The observed intensity for the blended lines is specified next to the main component and the contributing components' intensities are left blank (e.g. SiXI in figure). When the grouping of blended lines takes place the blanks are taken as zeros and the total remains as that of the main component. The same method is used for members of multiplets. Finally, an index number, *G-in*, referencing the appropriate $G(T_e)$ function in the 'kernel collection file' must be entered.

5.6.2 Preparation of Kernel Function Collection File

$G(T_e)$ functions must be available for each line in the intensity file. The $G(T_e)$'s are stored in 'collection files' which are output from ADAS routine ADAS506 (see Summers et al.(1996)). Each $G(T_e)$ in the collection file has a specific transition number and this is used to provide the connection with the observed intensity (the *G-in* index mentioned above). Collection files are built up by selecting the appropriate transitions from $G(T_e)$ functions stored in the ADAS database. $G(T_e)$ functions are stored for a wide range of ions at uniform electron densities and pressures. For this demonstration it was necessary to locate $G(T_e)$ functions for the radiative transitions

Ion
NeIV, ArVII, NeVI(558.595Å only), AlX, AlXI, FeX, CaX, FeXI, FeXII, FeXII

Table 5.10: List of ions where data was not available in ADAS and $G(T_e)$ functions had to be generated specifically. The data used were from lower quality Born calculations. Exceptions were FeXII, NeVI & FeXIII where high precision calculations of Tayal, Henry & Pradhan (1987), Zhang, Graziana & Pradhan (1994) and Fawcett & Mason (1989) became available.

forming each line in tables.5.7 and 5.9.

Given the problems associated with deriving plasma structure and the necessity for minimising errors in the atomic data, we wish to use only the highest quality data for our complete DEM study. However, for this demonstration we relax these constraints and ensure that we have adequate coverage for all the lines in the intensity file. This includes high precision electron collisional excitation data but also lower quality 'fill in' data generated by simpler methods. Most of the data were taken from ADAS where a large database of $G(T_e)$ functions (*adf20* files) have already been generated over a large range of constant densities ($1 \times 10^8 \rightarrow 1 \times 10^{12} cm-3$) and constant pressures ($1 \times 10^{10} \rightarrow 1 \times 10^{16} K cm^{-3}$). The electron collisional excitation and spontaneous radiative data sources are given in the relevant files and also by Summers(1996). For some transitions data is sparse and certainly not of the highest quality. Where necesssary we generated $G(T_e)$ functions specifically for this task based on Born approximation calculations carried out at JET. These data do not appear in the ADAS central database and the relevant ions are listed in table.5.10. The ionisation balance calculations of Arnaud & Rothenflug (1985) with a density dependent correction based on the collisional-radiative models were used in the generation of the G(T_e) functions.

Using ADAS506 a kernel 'collection file' was created for a uniform pressure of $3 \times 10^{15} K cm^{-3}$. This is shown in fig.5.28. The temperature coverage extends from a few tens of thousands to tens of millions of degrees kelvin. This is an adequate range for solar atmospheric studies, encompassing the upper chromosphere through

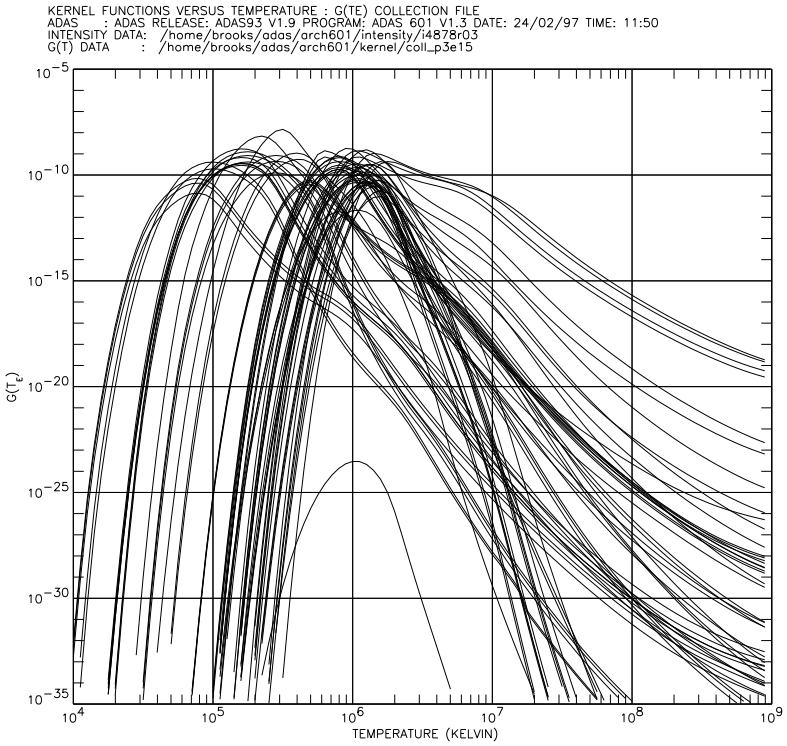

Figure 5.28: Kernel function (G(Te)) collection file for the DEM demonstration run.

the transition region to the corona. Note that there is particularly dense coverage around 10^6K. These lines come principally from the NIS1 extraction window and are thus more easily identifiable as a cluster in the DEM (see below). This allows us to make a more immediate judgement about the range of values associated with each window.

5.6.3 Sample Reconstruction of the DEM

To reconstruct the DEM distribution we require observed intensity, predicted intensity and elemental abundance information. These are input to specific ADAS format files and then used in conjunction with ADAS601 to perform the integral inversion. The prepared intensity and kernel collection files, described above, were used along with the photospheric abundances of Grevesse & Anders (1991). The values of these elemental abundances are shown in table.5.11.

Numerical Issues

Solutions to the bi-variate intensity integral equation (eq.2.61) are rare in astrophysics. However, many techniques have been developed and thoroughly tested to solve eq.2.62. ADAS601 uses the algorithm of Thompson(91) and the method is outlined in detail by Harrison & Thompson (1992) and by Summers et al.(1996). Here we give a brief overview.

Thompson used a *data adaptive smoothing approach* which required the equation 2.62 to be discretised as,

$$I_{i\to j} = \frac{1}{4\pi}\frac{N_{tot}}{N_H}\sum_{k=1}^{N}\phi_k^*\int_{t_{k-1}}^{t_k} G_{i\to j}(T_e)\phi_0(T_e)dT_e \tag{5.6}$$

where the transition is from the upper level i to the lower level j and we have ignored the dependence of the G functions on density. The G function is the kernel in this case. $\phi_0(T_e)$ is an initial estimate of of the expected gross behaviour of $\phi(T_e)$ which reduces the dynamic range of the problem before the full solution is obtained. $\phi_0(T_e)$ is named the 'prior' function. Also, ϕ_k^* represents a weighted average of the ratio of the

Element	Symbol	Abundance
Hydrogen	H	1.0
Helium	He	9.8×10^{-2}
Carbon	C	3.6×10^{-4}
Nitrogen	N	1.1×10^{-4}
Oxygen	O	8.5×10^{-4}
Neon	Ne	1.2×10^{-4}
Sodium	Na	2.1×10^{-6}
Magnesium	Mg	3.8×10^{-5}
Aluminium	Al	3.0×10^{-6}
Silicon	Si	3.6×10^{-5}
Sulphur	S	1.6×10^{-5}
Argon	Ar	3.6×10^{-6}
Calcium	Ca	2.3×10^{-6}
Iron	Fe	4.7×10^{-5}
Nickel	Ni	1.8×10^{-6}

Table 5.11: Table of photospheric abundances used in the DEM demonstration. The data are from Grevesse & Anders(1991) and only include elements whose abundance is greater than 10^{-6} of hydrogen. It is possible that some elements may have enhanced abundances in the corona (see discussion sec.5.6.5).

full solution $\phi(T_e)$ to the prior function, $\phi_0(T_e)$, between the temperature extremes of the components of the numerical integral i.e. t_{k-1} and t_k. Thus,

$$\phi_k^* \equiv \frac{\int_{t_{k-1}}^{t_k} G_{i\to j}(T_e)\phi(T_e)dT_e}{\int_{t_{k-1}}^{t_k} G_{i\to j}(T_e)\phi_0(T_e)dT_e} \tag{5.7}$$

The method effectively scales the solution using the prior function and has proven to be successful in preventing over-smoothing at high and under-smoothing at low values of the DEM.

The prior function is evaluated by approximating the G function as the product of its integral with the Dirac delta function of the difference between the temperature and the temperature of the maximum of the G function viz.

$$\begin{aligned} G_{i\to j}(T_e) &= \bar{G}_{i\to j}\delta(T_e - T_{i\to j}^{max}) \\ &\equiv \int_0^\infty G_{i\to j}(T_e)dT_e\delta(T_e - T_{i\to j}^{max}) \\ \bar{\phi}(T_{i\to j}^{max}) &= \frac{4\pi N_H}{N_{tot}}\frac{I_{i\to j}}{\bar{G}_{i\to j}} \end{aligned} \tag{5.8}$$

The values $\log(\bar{\phi}(T_{i\to j}^{max}))$ are the first approximations to the solution and a smooth representation of the prior function is obtained by fitting a cubic B-spline to them. This method is satisfactory only between the minimum and maximum values of $T_{i\to j}^{max}$ so a linear extrapolation is made to lower and higher temperatures. The methods used and further detail of the above description are given by Summers et al.(1996).

First Attempt

The sample DEM is shown in fig.5.29. The crosses are the first approximations calculated for each of the observed lines. The dashed line through these points is the prior function and the solid line is the final DEM. Note that the temperature maxima of the G(T_e) functions will not correspond exactly to the values quoted in table.5.7 for each line. Thus the temperature coverage extends from $\sim 5.0 \to 6.3$ in the logarithm only. Note also that the solution outside this temperature range has no physical meaning.

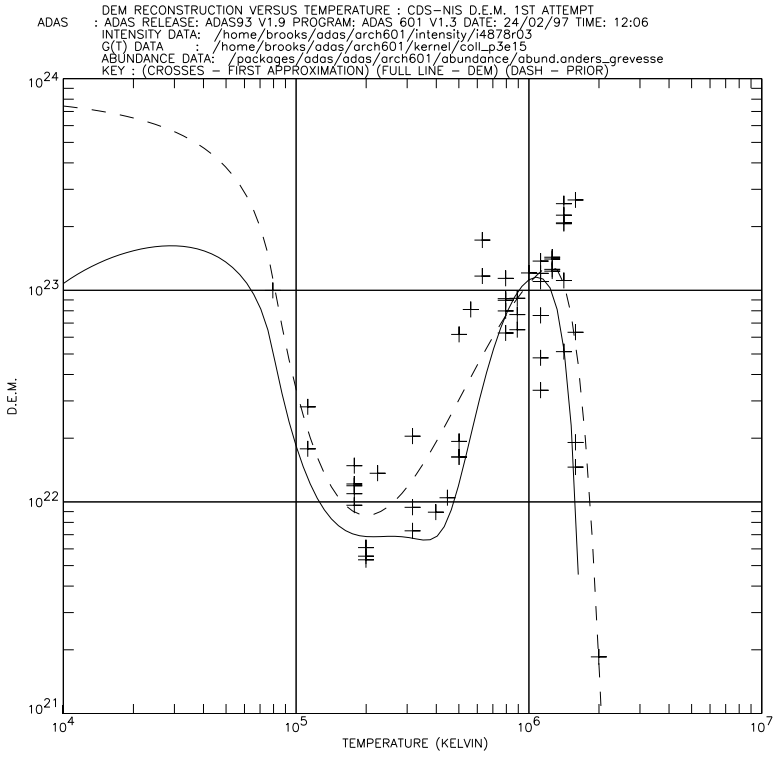

Figure 5.29: The emission measure differential in temperature computed from CDS-NIS data for a uniform pressure of $3 \times 10^{15} Kcm^{-3}$.

Within the range, the overall shape of the curve is largely familiar with the exception of the unphysical kink around $3 - 4 \times 10^5$K. Variations of this kind are unrealistic as we cannot reasonably expect to resolve structures that vary more sharply in temperature than the width of the G(T_e) functions used. The slope down from around 10^5K to form the shallow dip between 10^5 and 10^6K, followed by the peak around 10^6K is largely consistent with the results of previous authors although the actual numerical values of the DEM vary (see for example Brosius, Davila, Thomas & Monsignori-Fossi(1996)). The results of Lang et al.(1990) were consistent with this also except that they found a second 'hump' around 3×10^5K. However, as suggested by Thompson (1991) this 'hump' was overly influenced by the OVI($2s\ ^2S_{1/2} - 2p\ ^2P_{3/2}$) 1031.91Å line and he was able to remove the behaviour by giving this line less weight in the inversion. This is indicative of a significant error in the $G(T_e)$ function for that line. Errors in the G(T_e) functions may also be responsible for the kink in our curve. Alternatively, it may be due to the fact that the atomic data used, for some of the lines, was not of the highest quality.

We attempted to identify the line or lines responsible for this behaviour. By a process of line elimination and DEM re-evaluation we came to the conclusion that a smooth distribution, within the temperature range, could be recovered by excluding the two NeVI lines from the analysis. This might indicate again that there is some problem with the atomic data for this ion. It is essential to make a realistic assessment of the errors before attempting a proper DEM. In this demonstration we used the estimated standard errors output from the line profile fitting procedure. A more meaningful estimate would be to take the larger percentage between this value and the value of the observational accuracy for the line determined from the methods of sec.5.5.1.

5.6.4 Sensitivity of Spectral Lines Recorded by CDS-NIS

Thompson (1991) suggested that one way to ensure the G(T_e) functions do not contain significant errors would be to remove individual lines from the dataset and compute a DEM distribution from which the line intensity can be predicted. A comparison

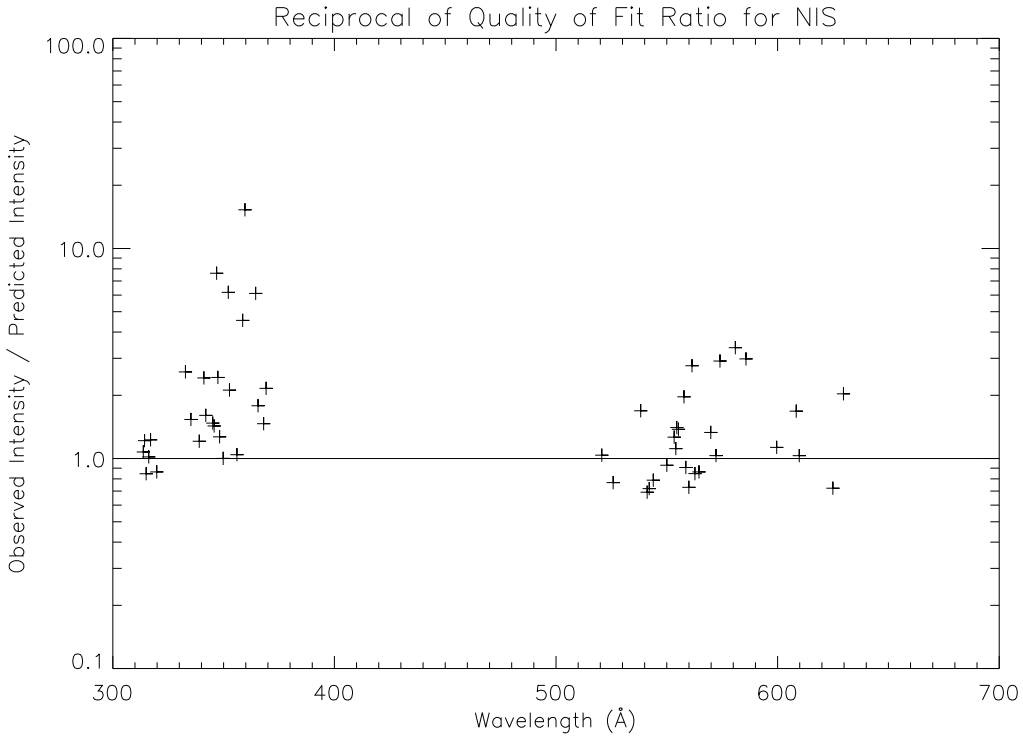

Figure 5.30: Ratio of observed to predicted intensities for NIS. NIS1 is the shorter of the two wavelength regions.

between the predicted and observed intensity would then show up any discrepancy which would identify any potential errors in the G(T_e) functions. Lang et al. (1990) presented something similar which they called quality of fit ratios, *qfr*. These are ratios of intensities predicted by the DEM code to the observed intensities and are calculated for all lines in the dataset without omission. These *qfr's* were used extensively by Lang et al.(1990) to try to obtain information on, for example, the correctness of the elemental abundances, errors introduced by the size of the recorded signal, errors related to the photometric calibration, etc.

We are also concerned with the possibility of a revision of the pre-flight intensity calibration (see sec.5.4.2). At time of writing there was some suggestion (Lang(1997) - private communication) that the NIS1 band was over sensitive. A glance at fig.5.29

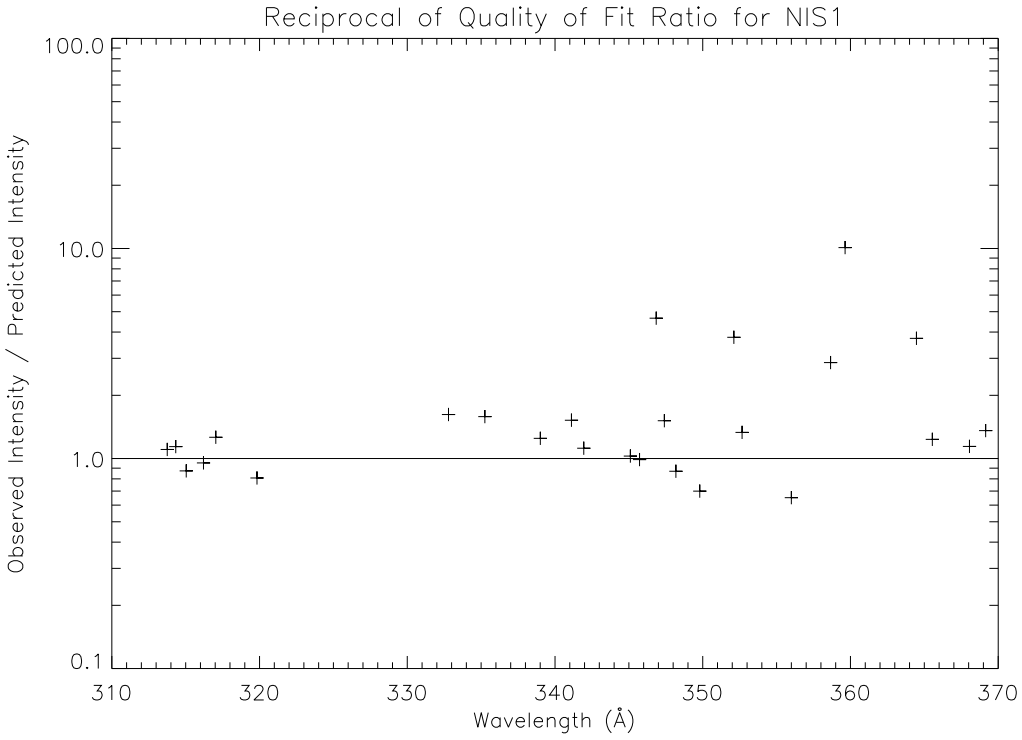

Figure 5.31: Ratio of observed to predicted intensities for NIS1.

shows a large cluster of values around 10^6K and $10^{23} cm^{-5} K^{-1}$ in the DEM. This temperature region corresponds mainly to the NIS1 data. Specifically, there is a large spread of values of the DEM for a group of lines formed at the same temperature (note the five points that cover the range $\sim 3 \times 10^{22} - 1.3 \times 10^{23} cm^{-5} K^{-1}$ and appear in a vertical line at $\sim 1.1 \times 10^6 K$).

To give clues to the accuracy of the calibration and the atomic data we plotted the reciprocal of the *qfr*'s against wavelength (see fig.5.30). The results for NIS2 are markedly better than for NIS1 and there does not appear to be any noticeable wavelength dependence of the *qfr*'s which might have helped in identifying any problems with the instrument sensitivity in particular spectral regions. Observed intensities from NIS1 appear too high by up to at least a factor ten while NIS2 is better showing an apparent overestimate of only up to a factor four. It is unlikely that this is a

true reflection of the sensitivity of the detector since the outliers may be affected by poor fits to the data, inadequate treatment of weak and blended lines that may remove counts from the total fluxes and poorer quality atomic data. For the final study such outliers will be investigated individually. As an example, fig.5.31 shows the same graph but excluding contributions from NIS2. That is, the approximate DEM is computed self consistently using the values for NIS1 only. Thus any disparity between the calibration of the two extraction bands should be removed. A group of five prominent outliers remain whose intensities are still too high compared to those predicted but, encouragingly, the disparity is reduced from previously. These were identified and are given in table.5.12 along with the reciprocal of the *qfr*'s for both examples. It is interesting that the largest discrepancies occur only for iron lines. This raises the possibility that there is some error in the elemental abundance. However, after investigation other more likely explanations arose. For example, the FeXII 352.106Åwas found to be blended with the MgV($2p^6\ ^3P_1 - 2s2p^5\ ^3P_0$) 352.201Å line which obviously causes an overestimation of the flux during the fit. Back tracking through the analysis procedures pointed up that there had been difficulty in unambiguously separating the FeXIII 359.638Åline from two neighbouring lines (FeX 359.37Å& NeV 359.382). Finally, the G(T_e) function used for the FeXI component of the blended line was generated from Born approximation data and so is not of the highest quality.

It is clear that some re-working and scrutiny of problem lines in conjunction with checks on predicted intensities and atomic data will be essential for dealing with such cases in the final DEM study. In this way we hope to close the gap as closely as possible between the theoretical and observed intensities. If we exclude the five lines from table.5.12, the observed intensities are well within a factor two of the predicted ones which is encouraging for this approach.

5.6.5 Comment on Solar Atmospheric Structure Determination

Since we have been able to derive an initial, and crude, differential emission measure distribution it is appropriate here to comment further on the objectives of the

Identification	1/qfr(using NIS)	1/qfr(using NIS1 only)
FeXIII 359.638Å	15.3	10.1
FeXII 346.852Å	7.6	4.7
FeXII 364.467Å	6.2	3.7
FeXII 352.106Å	6.2	3.8
Blend FeXI 358.621Å/ SiXI 358.653Å	4.5	2.9

Table 5.12: Ratios of observed to predicted intensities for the five outliers of NIS1. Results are quoted for the DEM computed with both NIS1 and NIS2 and also for NIS1 only.

complete study; what we hope to achieve and how to proceed. This follows from the discussion of chapter.2 section.2.2.3. With an accurate intensity calibration, best available atomic data and a realistic assessment of the errors we should ultimately be able to say definitively whether the DEM approach tells us some useful properties of the solar atmosphere. Clearly it does as much progress is likely to be made in areas such as line identification or radiative transfer computations by utilisation of the DEM technique. The expectation is however that disparities between observation and theory will remain independent of the quality and accuracy of the data and techniques applied. For example, Lang et al.(1990) found that the variability of their DEM 'solutions' that satisfied the integral inversion was greatest in the temperature regime where their confidence in the observational and atomic data was greatest.

Such a conclusion signals either the breakdown of assumptions underlying the theory of the DEM method, or mis-assessment of the errors in the observational and theoretical data. Lang et al.(1990) discussed the various experimental and theoretical factors that might cause one or other of the problems mentioned above. Subsequently these suggestions were revisited by Judge, Woods, Brekke & Rottman (1995). Here we will address some of these authors' points again.

In this chapter, and in the on-going study as a whole, we have tried to reduce the possibility that data errors (atomic and observational) have a significant effect on our analysis. The raw quality of the observational data was assessed in sec.5.5.1. Problems such as mis-identification of lines were partly eliminated through the CHASE

pattern analysis (see e.g. sec.5.5.1). Effects of the inaccurate treatment of blended lines and background signal subtraction cannot be completely avoided but the development of the maximum likelihood line profile fitting routine at least quantifies the errors associated with each fit. Also, as suggested above, the scrutiny of individual lines using an approximate DEM can be useful in this respect. In general, with the exception of badly blended lines, these effects were less than the statistical values of the observational accuracy found by the methods of sec.5.5.1. The assessment of these observational accuracies also partly eliminates many of the queries raised by Lang et al. with regard to spacecraft transmission errors etc. The routine adopted for the inversion procedure has been shown to be robust both in the assessment exercise (Harrison & Thompson (1992)) and in the analysis of SERTS data (Lanzafame et al. (1997)). Also, the data analysis procedures have now been well tested as a result of this thesis demonstration.

Many of the techniques developed will be used in much greater detail for the full study but there are a number of further points in this area that were not completely addressed. Clearly, there is an anxiety associated with the lack of a definitive pre-flight intensity calibration (see 5.4.2 and refsec:chap-564). A document is in preparation (Kent et al.(1997)) and some work is in progress investigating quality of fit ratios for the pre-flight calibration lines. Also, fig.5.30 is not indicative of any gross disparity between NIS1 and NIS2. Investigation of *qfr*'s for lines with highest quality atomic data may alter this situation. It is also possible that a definitive statement will not be made before the relaunch of the SERTS rocket, scheduled for autumn 1997. The problem of providing atomic data of best quality was not fully addressed. ADAS contains the best available data but further work may need to be done, for example on S-like and Cl-like Fe, where observations were available but atomic data was lacking. However, ADAS is in a uniquely advanced state to provide back up for this. It is also possible that errors in the elemental abundances used may affect the final study. There is a widely held view (see e.g. Laming, Drake & Widing(1995)) that the abundances of elements with a low First Ionisation Potential (e.g. sodium, calcium) are overabundant in the corona by $\sim$ factor of 3. These authors suggest there may be a diffusion process which tends to remove ions from the photosphere to the corona.

Elements that are difficult to ionise at the lower temperature of the photosphere would be partly left behind in this scenario. If this is correct then the abundances used in our demonstration DEM will be incorrect. However, this suggestion is not fully accepted and it is possible that the observational errors are too large to draw any conclusions on this so called FIP effect. Clearly if the errors are so large as to potentially obscure a physical process then more detailed analysis is required.

The possibility that there is a failure in one or more of the assumptions underlying the DEM method can only be concluded after the full study is completed with minimal errors. Of the explanations raised by the above authors we can however make some suggestions.

In the above DEM demonstration we excluded the helium lines on the grounds that their intensities may be altered by opacity. This is a concern for many observed lines. A paper is in preparation, Summers et al.(1997), which extends the analysis of Doyle & McWhirter(1980) from lines which show opacity effects as we view them across the solar limb, to the case of lines that are optically thick on the solar disc. Thus a complete prediction of the optical thickness of lines can be made allowing us to exclude these from the DEM analysis. Clearly there are optical thickness effects that must be considered for the cooler denser chromospheric region which may restrict the applicability of the DEM approach.

In the transition zone-corona region the results presented in sec.3.2.1 and sec.5.3.1 are consistent with a failure of the assumption of equilibrium for the ionisation balance. Dynamic effects clearly require that metastable states are fully accounted for in the atomic calculations but this falls short of computing a full nonequilibrium solution such as that of Spadaro and co-workers. As mentioned in chap.4 sec.4.7 we have the capability to examine such issues using the dynamic ionisation codes of ADAS. However, it has not yet been fully evaluated how such a model can be incorporated into the DEM method.

Evidence for disequilibrium in emission measure analysis of Li-like and Na-like isoelectronic sequences was reported by Judge et al.(1995). They observed that lines of these sequences are systematically underestimated by theoretical calculations. This is indicative of dynamics because Li-like and Na-like ions suffer from long recombination

times from He-like and Ne-like ions where larger than average temperature increases are required to open the closed $n = 1$ and $n = 2$ shells (see chap.3 sec.3.2.1). However, it is not clear whether this effect is significant as it was not seen by Lanzafame et al.(1997) in their analysis of SERTS data. A dynamical ionisation balance calculation is required but how large the disequilibrium is and whether it can be detected in the sort of 'averaged' structures of a DEM analysis is not yet known.

Invoking assumptions about surfaces of constant temperature and density in order to cast the integral in the form of eq. 2.62 is also questionable. Dynamic activity, flows, spicules etc. produce steep rapidly changing temperature gradients. In addition, Gabriel(1976) showed that there are strong magnetic fields around network features in the chromosphere which decrease in strength rapidly with height. The assumption that surfaces of constant plasma density and temperature both exist in the solar atmosphere and coincide is highly debatable.

Lang et al.(1990) and Judge et al.(1995) cite a failure of some aspect of the atomic model as another possibility. As mentioned by them, inaccurate treatments of dielectronic recombination and ionisation coefficients and, in particular, additional density dependences in them should be modelled more precisely. Judge et al.(1995) admit that they cannot completely discount an inadequate treatment of dielectronic recombination in their own work. One of the strengths of our work is in this area (see chap.4) so this problem has been and will continue to be addressed. Lanzafame et al.(1997) interestingly find density dependencies in lines where it would perhaps not be expected. The use of ADAS alleviates many of these difficulties as it provides a complete density dependent collisional-radiative model. Also, the SOHO-CDS & SUMER DEM study should provide new insight.

This leads us to another important point. Recent work by Judge et al.(1997) suggests it is debatable whether a solution to the formal mathematical extension of the DEM distribution to two independent variables, temperature and density, can be reconstructed from the observations at all. There is much to be investigated in this area. It remains to be seen whether a better inversion method than that of Hubeny & Judge(1995) would help in the derivation of the solution. As pointed out by Judge et al.(1997), some success has been achieved with inversion problems by

tailoring the approach to the individual problem. For example, Brown et al.(1991) showed that limits could be set on the form of DEM solutions for OIV and FeXI lines. Methods to deal with and determine the nature of the errors should be investigated. Judge et al. point out that the situation may be improved by using fewer lines in the analysis thus introducing fewer systematic errors or alternatively solving for the systematic errors as well. Alternatively, if the errors appear 'random' Judge et al. point out that the average of multiple inversions helps in the reconstruction. Judge et al.(1995) clearly believe the errors to be systematic as they discount the possibility of variations in abundances as a result. However, it may be more informative to check on this aspect as well, perhaps using the technique of Lang et al.(1990). Finally, the calculations of chap.2 sec.2.1.2 suggest that electron distributions will generally be Maxwellian and that this assumption is valid. However, the reappraisal with respect to the dynamic nature of the atmosphere suggests that departures from Maxwellians should be investigated further.

Of course, despite improving our understanding of the structure of the solar atmosphere over the last twenty years, it is not clear that the DEM method can provide the type of accurate description that will now take us a significant step forward. It tells us something about the volume distribution of emitting plasma globally but the solar atmosphere is continually changing on fine (perhaps unresolved) scales. Observations from SOHO (e.g. Harrison & Insley (1997), Pike & Harrison(1997)) show that bright points, spicules etc. are constantly dynamically evolving and it seems apparent that the idea of a plane-parallel static isothermal atmosphere is outdated. Given the difficulties of advancing the DEM method to two independent variables it may be that predictive modelling is the way forward. Future modelling we wish to attempt is presented as an overview in the next chapter.

Chapter 6

Outline of Future Plasma Models of the Solar Atmosphere and its Activity

We wish to synthesise the spectral observations by combining the atomic model of ADAS with a suitable plasma model. Cross-comparison with the instrumental measurements will allow progress to be made in defining realistic physical mechanisms for many of the observable solar features. SOHO is essentially a quiet sun observing station. However, it is clear that plasma dynamics play a significant role in prominence formation, x-ray bright points, sunspot activity and possibly also coronal heating. It is our intention to adopt a numerical hydrodynamic model that will allow us to investigate some of these phenomena. From the model we will obtain temperature, density and velocity information within a pre-defined plasma geometry that we can use in the production of $G(T_e, N_e)$ functions. Thus we can build up a time development of the atomic model that can be related to the expected evolution of some solar feature by the simulation of the hydrodynamic behaviour. Clearly it is an enormous computational task to develop a code separately and seems unnecessary when so many are currently in use. The most widely available, at present, are for computing solar flare loop hydrodynamics. Therefore, we obtained a copy of the flare hydrodynamic loop code of Peter MacNeice (1983) to use as a starting point. It has certain special

advantages discussed below.

Solar flares are not observable with SOHO, except through whole sun images such as those of EIT (Extreme Ultraviolet Imaging Telescope). Indeed, the detector saturation limit, of an instrument such as SUMER, is so low that flare enhanced lines would destroy it. This is in fact already a problem for bright lines such as Lyman α. As a result, it is not our intention, at least for planned SOHO observations, to attempt to develop the modelling duration or physical reality of the MacNeice code for flares. Our aim is to explore the applicability of the loop model to other plasma dynamics and energy balance questions such as prominence condensations (Antiochos & Klimchuk(1990)) or impulsive heating (Spadaro, Lanza & Antiochos (1996)). However, it was necessary to investigate the physical assumptions of the MacNeice model to see whether this could be done. Here we review the development of the physical basis for producing this type of numerical flare model. We also present results from a test run of the code and offer suggestions for future work. Finally, the concluding remarks of the thesis are presented.

6.1 Relevant Literature

EUV, XUV and X-ray observations by ground and space based instrumentation have shown that magnetic loop arcades dominate the observed structures of the low corona. This is as expected from an empirical view of the global processes contributing to energy transport from the solar interior to the atmosphere. We know that thermonuclear fusion takes place in the core of the sun, and that the nuclear furnace converts hydrogen into helium. The resulting energy released in each reaction is radiated outward towards the solar surface. As the temperature decreases towards its minimum, at the top of the solar photosphere, $\sim 10^7 K \rightarrow 4400K$, the free electrons of the highly stripped ions begin to recombine in the plasma. As a consequence, the escaping photons are more readily absorbed by the atoms and ions. Therefore, the plasma becomes optically thick and unstable, resulting in the appearance of large convection currents which transport the energy to the surface. Evidently, the permeating magnetic field lines are 'rolled up' into fluxtubes as the giant convection cells rise and fall. These

magnetic loops break through the surface of the chromosphere and into the corona.

In the low corona the ratio of the plasma pressure to the magnetic pressure, generally called β, is less than one (Spruitt(1981)). As a result, the plasma particles are confined to motion along the magnetic field lines. It is thus possible to model the hydrodynamic behaviour of a plasma by assuming that it moves along a one dimensional magnetic flux tube. The geometrical configuration of the tube is an open parameter. For flare modelling it is usual to assume that the loop structures, observed in the corona, are almost symmetrical semi-circles. If this assumption is made, it is sufficient to model one half of the loop. For models of suspended material in magnetic fields, it has been suggested (Poland, Mariska & Klimchuk (1986)) that a semi-circular loop with a long shallow symmetric dip is useful. Alternatively, for bright points and jets, a vertical flux tube may be all that is necessary. In any case, the principle is to model the evolution of the plasma in the tube, in response to some perturbation (perhaps an energy injection), by solving the equations of plasma transport theory. It is convenient here to rederive the equations of mass continuity, momentum conservation and energy balance.

6.1.1 Plasma Fluid Equations

To model a plasma it is necessary to know the distribution functions of all the particles. We denote these distribution functions by $f(\mathbf{x}, \mathbf{v}, t)$. At this stage we do not distinguish between the particle species. The function gives the particle density distribution at the position (**x,v**) in velocity space, where **x** is the (x,y,z) coordinate of the particles, and **v** are their velocities in each direction, i.e. (v_x, v_y, v_z). $f(\mathbf{x}, \mathbf{v}, t)dxdydzdv_xdv_ydv_z$ is then the particle density within the six dimensional volume element d**x**d**v**. In general, the particles in the plasma will move towards a Maxwellian distribution of velocities (eq. 2.1). A discussion of how quickly this process takes place is given in sec. 2.1.2. For a discussion of the influence of a non-Maxwellian tail in the electron distribution function in solar atmospheric models see MacNeice, Fontenla & Ljepojevic(1991). We restrict our present discussion to particle distributions that are Maxwellian.

If we could sample the particle distribution functions at every point in the plasma we would obtain a complete description of the plasma state. In reality this is not possible. However, we can acquire useful quantities by taking velocity moments of the distribution function.

$$\text{moment i} = \int f(\mathbf{v}) v^i d^3\mathbf{v} \tag{6.1}$$

Taking moments for $i = [0, \infty]$ would allow us to completely determine the distribution function but it is usually only necessary to investigate the lower order moments. There is a problem which occurs through taking increasing moments. Each successive one introduces the next higher order moment and at some stage an assumption must be made that will allow us to 'close' the set of equations. Usually it is sufficient to set the third moment, that of thermal conductivity, to zero.

Returning to the model plasma and taking the first three moments, we obtain,

1. $\int f(\mathbf{x}, \mathbf{v}, t) d^3\mathbf{v} \equiv n(\mathbf{x}, t)$
2. $\frac{1}{n} \int f(\mathbf{x}, \mathbf{v}, t) \mathbf{v} d^3\mathbf{v} \equiv \mathbf{u}(\mathbf{x}, t)$
3. $m \int (\mathbf{v} - \mathbf{u})(\mathbf{v} - \mathbf{u}) f(\mathbf{x}, \mathbf{v}, t) d^3\mathbf{v} \equiv \frac{3}{2} n k_B T$

where $n(\mathbf{x}, t)$ is the particle density, $\mathbf{u}(\mathbf{x}, t)$ is the mean particle velocity and $\frac{3}{2} n k_B T$ is the mean particle energy. We can obtain the plasma transport equations in analogous fashion by considering the Boltzmann kinetic equations,

$$\frac{\partial f}{\partial t} + \mathbf{v}.\frac{\partial f}{\partial \mathbf{x}} + \frac{\mathbf{F}}{m}.\frac{\partial f}{\partial \mathbf{v}} = 0 \tag{6.2}$$

This equation describes the evolution of the particle distribution functions. The Boltzmann equations are not specific to plasmas but can be made so by inclusion of the Lorentz force.

$$\mathbf{F} = q\left(\mathbf{E} + (\mathbf{v} \times \mathbf{B})\right) \tag{6.3}$$

The Lorentz force takes due account of the influence, on the particles, of the local magnetic and electric fields. From eqs. 6.2 and 6.3 we obtain,

$$\frac{\partial f}{\partial t} + \mathbf{v}.\frac{\partial f}{\partial \mathbf{x}} + \frac{q}{m}\left(\mathbf{E} + (\mathbf{v} \times \mathbf{B})\right)\frac{\partial f}{\partial \mathbf{v}} = \left(\frac{\partial f}{\partial t}\right)_c \tag{6.4}$$

which is the Fokker-Planck equation. In fact this derivation assumes no particle interactions in the plasma. This provides no problem provided we neglect short range reactions and postulate that because the electric and magnetic fields, $\mathbf{E}$ and $\mathbf{B}$, are due to all the other particles in the plasma, they adequately describe the particle interactions. This separation of long range and collisional interactions is only possible if plasma effects dominate over particle effects i.e. the plasma parameter, $\Omega = \frac{1}{n_\nu \lambda_D^3}$, is small, where n_ν is the particle density of the species ν, and λ_D is the debye length (i.e. the length at which a particles' potential is screened from the other particles in the plasma). The plasma parameter will be small if the Debye sphere surrounding the particle, contains large numbers of particles. This assumption is valid for the upper solar atmosphere (see MacNeice(1983)).

Taking moments of eq. 6.4 provides us with the fluid equations. These were originally derived by Braginskii(1965) and recent examples of the method were provided by Cuperman et al.(1981), Bittencourt(1986) and Elliot(1993). The resulting equations are,

$$\frac{\partial n}{\partial t} + \frac{\partial}{\partial \mathbf{x}} (n\mathbf{u}) = 0 \tag{6.5}$$

which is the equation of mass continuity,

$$mn \left(\frac{\partial}{\partial t} + \mathbf{u} \frac{\partial}{\partial \mathbf{x}} \right) \mathbf{u} = -\nabla p - \nabla . \mathbf{P} + qn \left(\mathbf{E} + (\mathbf{v} \times \mathbf{B}) \right) P_{ab} \tag{6.6}$$

which is the momentum conservation equation and

$$\frac{3}{2} n k_B (\left(\frac{\partial}{\partial t} + \mathbf{u} \frac{\partial}{\partial \mathbf{x}} \right) T + \frac{\partial}{\partial \mathbf{x}} (p\mathbf{u}) + \frac{\partial}{\partial \mathbf{x}} (\mathbf{P}\mathbf{u}) = -\nabla q + Q_{ab} \tag{6.7}$$

which is the energy conservation equation. In these equations, $\mathbf{P}$ is the stress tensor. The diagonal elements are the usual hydrostatic pressures, p, which have been separated out in eqs. 6.6 and 6.7. The off-diagonal elements represent the plasma viscosity and q is the heat flux, which is the next higher order moment. The term P_{ab} represents changes in the momentum density of the particles a, due to collisions with particles b. In eq. 6.7 the term Q_{ab} is the analogous expression for changes in the energy density due to collisions. This latter term can also include energy source and sinks, see sec.6.3.1.

6.2 Flare Loop Modelling: Background Literature

We focus here on the one dimensional symmetrical semi-circular loop problem. This approach was adopted for flare modelling by many workers in the early eighties. Interest was awoken due to the advent of the Solar Maximum Mission satellite. The energy balance, in the loop, is influenced by conduction, convection and radiation, and the plasma particles move under the control of gravity and the pressure gradients that develop. The flare energy is required to be conducted into the chromosphere where the higher densities can more easily radiate it away. Typically, authors adopted either a *Non-Thermal* or *Thermal* model. We describe briefly here the overall approach adopted for each model and the sorts of results obtained by the original modellers primarily to outline the results of the test (see section.6.3.1).

The non-thermal model investigated the coronal loops' hydrodynamic response to the injection of a highly energetic electron beam at the loop apex and was investigated by, for example, Nagai & Emslie(1984), MacNeice et al.(1984), Fisher, Canfield & McLymont(1985), Peres et al.(1987) and Mariska, Emslie & Li(1989). Essentially the model predicts that rising magnetic field lines break through into the corona and 'pinch' out plasmoids which they effectively carry upwards. Magnetic reconnection takes place in the wake of the rising material and the reconnection process produces electric fields which accelerate electrons spirally down the magnetic field lines. The electrons collide with ions as they go and emit thermal Bremsstrahlung before depositing the majority of their energy in the chromosphere by coulomb collisions. Brown (1973) coined the phrase *thick target* for the denser chromospheric collision point. Each of them assumed a power law distribution for the electron beam with a low energy cut-off point (usually 10-20keV).

All of the models of the authors mentioned above produced results that were qualitatively similar despite the differing energy inputs and durations (from repeated bursts of 1.8×10^{12} ergs $cm^{-2}s^{-1}$ every 2 secs. for 240s (Nagai & Emslie) to a 5 sec. burst of 3×10^{10} ergs $cm^{-2}s^{-1}$ for Fisher et al.). After the beam impacts on the chromosphere the temperature increases to that of the corona in less than a second. The plasma pressure increases and acts like a piston driving material up the

loop at speeds of up to 1,000kms^{-1}. Consequently diminished upward velocities are seen. A cooler denser compression wave is generated that propagates deep into the chromosphere towards the photosphere at supersonic speeds. Fisher et al. named the upward plasma motion, *chromospheric evaporation*, and the downward compression, *chromospheric condensation*. As a result of the condensation a shock wave is formed that travels ahead of the compression wave eventually slowing due to the increasing pressure and density. The coronal material increases in temperature and density to $> 10^7 K$ and $\sim 10^{12} cm^{-3}$ respectively. When the energy input ceases conduction and radiation act to re-establish the pre-flare atmosphere. The plasma in the low corona cools but the temperature and density at the loop top continues to increase principally due to the collision of the symmetric rising fronts. However, only the numerical model of Nagai & Emslie lasted long enough to model this event and this was partly due to the gross nature of the numerical grid they used compared with the others. Their model showed the atmosphere relaxing to its initial state by an oscillatory behaviour. As later pointed out by Gan, Fang & Zhang(1991) the collision of these symmetric fronts is extremely violent and results in drastic changes in the physical parameters. The collision causes a localised increase in temperature and density resulting in the formation of a new pressure peak which forces material back down the loop at hundreds of kms^{-1}. Their calculation terminated due to numerical instabilities associated with the ferocity of this collision. Clearly it would be interesting to follow this phenomenon more accurately.

The thermal model considered plasma motions initiated by heat fluxes from a high temperature thermal source deposited with a Gaussian distribution in the electrons at the loop top. Once again many authors investigated the problem. For example, Nagai(1980), Somov, Sermulina & Spektor(1982), Pallavicini et al.(1983), Cheng et al.(1983), MacNeice(1986), Kopp et al.(1986) and Gan et al.(1991). The source length was generally chosen so that the majority of the flare energy was deposited in the corona. An immediate temperature rise resulted causing a supersonic thermal wave to propagate down to the chromosphere. On arrival, it heats the cool chromospheric plasma. Subsequently the response is qualitatively similar to that of the non-thermal model i.e. a pressure peak develops which drives chromospheric evaporation and

condensation.

Resolution of the thermal wave entering the transition region is a major problem with these numerical models. For a chosen flare energy input of $2 \times 10^{11} ergscm^{-2}s^{-1}$ the minimum mesh spacing required is $\sim 10cm$. In addition, resolution of the steep temperature and density gradients that develop at the base of the transition zone is of concern. Prior to the work of MacNeice et al.(1984) this had always been insufficient. MacNeice(1986) achieved a resolution of under 100cm for the thermal wave front with their *adaptive regridding* technique which is outlines in section.6.3.1. Many of the other authors also developed such moving grids.

After the Solar Maximum Mission workshop in 1982 a flare dynamic modelling group was initiated to intercompare the various codes produced by the above authors. A *benchmark* calculation was defined against which all developing codes could be tested. Despite large discrepancies initially in some of the least sensitive parameters, for example the temperature at the loop top, close agreement was eventually achieved. The problem was of the thermal type and we use a modification of this as our test in section.6.3.1.

Many refinements to these models have been included to treat, for example, the problem of defining a realistic description of the conductive heat flux (MacNeice et al.(1984)) or particle return current effects (Karlicky & Henoux (1992)). Ultimately the aim of all the work was to use the models to predict observational signatures with critical differences that can be examined experimentally to discriminate between them. For example, Mariska et al.(1989) made a detailed examination of which ranges of electron beam parameters were better able to reproduce the observations. Much further research has also been undertaken in this area and much progress has been made during the lifetime of the YOHKOH satellite. However, we make no attempt to comment on the observational evidence or the numerical refinements here as the field of solar flare studies is enormous in itself and beyond the scope of our present work and this thesis.

6.3 MacNeice Flare Hydrodynamic Model

It is essential to develop confidence in the computer code before further developing it. This is non-trivial as it is likely that the code has been altered many times since its first use in 1983. To do this we have attempted to reproduce the results of the thermal conduction front model of MacNeice (1986). This should allow us to address the complexities of the adaptive rezoning techniques. This involves removing some of the more refined qualities of the code, produced in recent years.

6.3.1 The Benchmark Model

Essentially the problem was posed for the flare hydrodynamic modellers (see sec.6.2). We review here the parameters and expressions required for the original model and the necessary alterations we have made whilst maintaining the essence of the problem.

Our initial loop is slightly shorter than MacNeice used. This was dictated by the model atmospheres we obtained with the code. Thus the semi-circular symmetric loop has a length of $1.02 \times 10^9 cm$ and a cross-section constant in space and time. The effects of the curvature are ignored and this is justified since the ratio of the loop radius to internal radius is large, typically a factor 7 (Kopp et al.(1986)). The loop footpoints are rooted deep in the photosphere where no coronal disturbances can penetrate during the simulation. Therefore, the initial boundary conditions are,

$$\begin{aligned} \frac{\partial T}{\partial z} = v = \frac{\partial h}{\partial t} = 0 \qquad & \text{at} \qquad z = L_h \\ T = 8 \times 10^3 K, \;\; N = 8.255 \times 10^{13} cm^{-3}, \;\; v = 0 \quad & \text{at} \qquad z = 0 \end{aligned} \tag{6.8}$$

z is the spatial coordinate axially round the loop from 0 at the footpoint to $1.2 \times 10^9 cm$ at the loop top, L_h. The plasma is assumed to be a fully ionised single temperature one i.e. $T_p = T_e$, except as regards the radiative power loss which is dominated by light ion emission. $N_e = N_p$ and $N_H = 0$.

The thermal heat flux equations only account for contributions from electrons and are modelled by the Spitzer-Harm expression, viz.,

$$q = \kappa_0 T_e^{5/2} \frac{\partial T_e}{\partial z} \tag{6.9}$$

with units of ergs cm^{-2} s^{-1}. This expression assumes that the coulomb logarithm is approximately 20 and $\kappa_0 = 9.203 \times 10^{-7}$. The radiative power loss is assumed to be that of an optically thin plasma and is given by,

$$R = N_e N_p \Omega(T_e) \tag{6.10}$$

where,

$$\Omega(T_e) = \begin{cases} 3 \times 10^{-22} \left(\frac{T_e}{2\times 10^4}\right)^3, & T_e < 2 \times 10^5 K \\ 3 \times 10^{-22}, & 2 \times 10^4 \leq T_e < 2 \times 10^5 K \\ 3 \times 10^{-22} \left(\frac{T_e}{2\times 10^5}\right)^{-1/2} + 2 \times 10^{-23} \left(\frac{T_e}{10^8}\right), & T_e \geq 2 \times 10^5 K \end{cases} \tag{6.11}$$

A geometrical configuration of the loop is accounted for by the imposition of a pseudo-gravitational term for the acceleration i.e.

$$g(z) = g_0 \sin \frac{\pi z}{2L_h} C \tag{6.12}$$

$$C = \left(\frac{R_0}{r(z)}\right)^2 \tag{6.13}$$

where the correction factor C takes account of the variation with distance from the solar centre over the height of the loop and g_0 is the gravitational acceleration at the surface of the Sun. This correction is only minor since the minimum value of C is at the loop top and equals 0.978.

The heating function for the loop consists of two parts i.e.

$$H = H_{init} + H_f \tag{6.14}$$

An ambient heating function, H_{init}, maintains the initially static model atmosphere by balancing the initial radiative losses. This is expressed as,

$$H_{init}(z) = \begin{cases} 9.01 \times 10^{-3}, & z > 2 \times 10^8 cm \\ N_e^2 \Omega(T_{init}), & z < 2 \times 10^8 cm \end{cases} \tag{6.15}$$

where T_{init} is the initial temperature at a given height, z. The static atmosphere is perturbed by an energy injection at the loop apex. The flare heating function, H_f, is

Gaussian with a source length $\sigma = 5 \times 10^8 cm$. The expression used is,

$$H_f(z,t) = \begin{cases} E\exp(-(z - L_h/\sigma)^2), & 0 < t < 5s \\ 0 & t > 5s \end{cases} \tag{6.16}$$

where the integral over the whole loop gives a totalpower of $2 \times 10^9 ergscm^{-2}s{-}1$. In this test, we neglect the effects of viscosity and solve the plasma fluid equations of section.6.3.1.

As mentioned in section.6.2 one of the main difficulties is in resolving the steep temperature gradient that develops as a result of the flare injection. For this test we introduce the same *adaptive regridding* facility as originally defined by MacNeice (1983) in order to provide adequate spatial resolution and place it most advantageously. The method used was to construct the initial grid containing 250 points and initially place the finest resolution of $1.0 \times 10^4 cm$ at a height of $2 \times 10^8 cm$ where the starting temperature was $3 \times 10^4 K$. This is the lower transition zone boundary. The cell used was number 114. The grid cells expand uniformly away from this point with their size calculated to fill the rest of the loop. Thus we have two constant factors, one to describe the expansion up the loop into the corona and another to describe the expansion down into the chromosphere, the largest variation between neighbouring cells being 8%. At each integration timestep the temperature profile is checked in the region $3 \times 10^4 K$.

$$\left| \frac{T_{i+1} - T_i}{\min(T_{i+1}, T_i)} \right| < 1 \tag{6.17}$$

The constraint of equation.6.17 was applied and a check was made to ensure that the temperature of $3 \times 10^4 K$ was found within three cells of number 114. T_i denotes the temperature at the ith cell. If the temperature gradient is inadequately resolved or the cell has moved sufficiently then rezoning of the grid takes place. The minimum cell size required to satisfy equation.6.17 is calculated and placed at the height of the cell where the temperature of $3 \times 10^4 K$ is located. The grid is then reconstructed using the same method as above, with new expansion factors calculated. Thus the grid rezones only when it is required and unnecessary computations are avoided.

Timestep splitting techniques are employed to solve terms in the equations only over the timescales on which they vary. Thus conductive, radiative power loss and

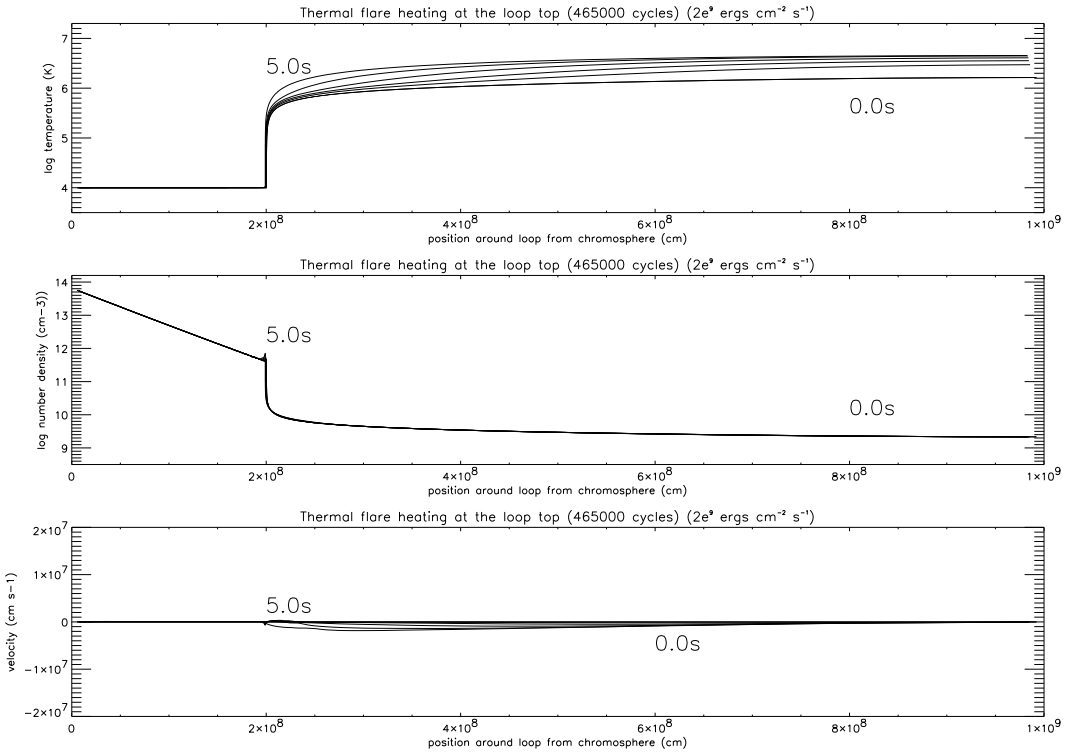

Figure 6.1: Temperature, density and velocity plots against position around the loop from the lower chromosphere as a function of time.

hydrodynamic terms are solved individually for example. More details are given by MacNeice(1983). Of course this helps in computational efficiency but is not so critical nowadays due to great advances in computational processing speeds.

Test Comparison

The results of the modified benchmark test run are given in figs. 6.1 and 6.2. The results satisfactorily reproduce those of MacNeice(1986) albeit within a shorter timescale due to the decrease in loop size and consequent increase in range and deposition of the energy distribution. Figure.6.1 shows the results for the first 5 secs and figure. 6.2 the subsequent development, around the transition region boundary, until termination of the calculation at 7.2 secs. The expected conduction front

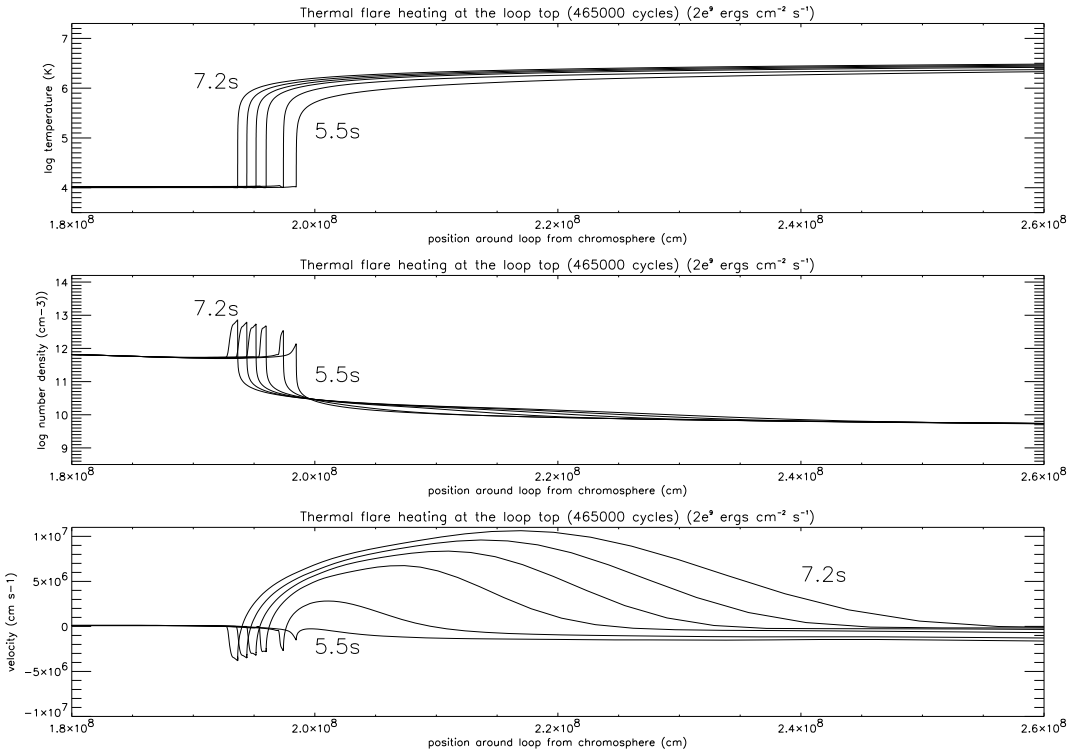

Figure 6.2: Temperature, density and velocity plots against position around the loop from the lower chromosphere as a function of time.

develops and moves down towards the transition region arriving there in under 5 secs. The coronal plasma expands downwards at a velocity of $\sim 2 \times 10^6 cm\ s^{-1}$. From fig.6.2 we see that the expected pressure enhancement does indeed develop and causes plasma motions both up and down the loop. The transition region begins to progress downward and pushes material ahead of it in a compression front. Due to considerations of momentum conservation and since the upward ablation of material has a larger velocity, a much larger mass of material is involved in this downward chromospheric compression. The upward evaporation accelerates quickly reaching a velocity of $\sim 1.0 \times 10^7 cm\ s^{-1}$ at the expansion front after 7.2s. The width of the chromospheric compression grew slightly as it progressed reaching about $\sim 9 \times 10^5 cm$ by the end of the simulation with a peak density of $\sim 6 \times 10^{12} cm^{-3}$. The temperature

at the loop top was $\sim 3.2 \times 10^6 K$. The temperature gradient of the transition region continually steepened to cope with the conducted heat flux from the corona. As a result the minimum grid cell size fell rapidly below 16cm requiring very short integration timesteps of $\sim 7 \times 10^{-7}$s. The computational resources available today are certainly improved compared to those available to MacNeice(1986). For example, in MacNeice(1986) his resources could no longer support the calculation once the grid size had fallen below 30cm and the integration timestep below 10^{-5}s. This in itself is less of a problem for us, we worked consistently at integration timesteps nearly two orders of magnitude smaller. However, the calculation eventually failed as it was unable to reconstruct the grid. The code uses a Newton-Raphson convergence scheme to calculate the grid expansion factors. In our test the scheme never converged. This problem should easily be overcome by an additional check in the program. That is, if the scheme does not converge after, say, 100 attempts, the expansion variables are taken from the previous cycle. This method is less accurate but should allow the computation to continue.

6.4 Applications to Quiet Sun Activity

The adaptive rezoning capabilities of the hydrodynamic model have proven effective in resolving shock fronts and extremely violent flare behaviour. We intend to adapt this model, by imposition of pseudo-gravity and alternative energy injections, to investigate the energy balance of coronal prominence condensation models (see for example Antiochos & Klimchuk(1991)) and impulsive bursts (see Spadaro et al.(1996)). We have undertaken some preliminary analysis of what is required and have some suggestions to offer here.

Antiochos & Klimchuk (1991) proposed a model for the formation of prominence condensations. They argued that a localized heating at the base of a coronal loop could form a condensation around the loop midpoint if the loop they considered was initially static with a shallow dip at the apex. The geometry of the loop was that of a semi-circle attached to a broad inverted Gaussian. Such a loop magnetic field configuration was imposed by a pseudo-gravitational term which can easily be

incorporated into our own code. The key idea was based on the expected response of the chromosphere to the localised heating. As with numerical simulations of flares (e.g. section.6.3.1), they anticipate that chromospheric evaporation causes material to rise up the loop and essentially become suspended in the shallow dip forming a cool dense condensation. The results of their simulations bore this out. However, their calculation terminated due to the formation of a steep temperature gradient around the edge of the dip in a transition region between the coronal material and the condensation. This was outside of the range of the finest resolution of their grid which they judged correctly would be required at the transition region itself.

Clearly there are a number of areas that we can immediately and speedily address. On the hydrodynamic side, imposition of the same geometric/gravitational configuration as that of Antiochos & Klimchuk (1991) and modification of the location and form of the transient heating source can be done easily. The development of a 'second' transition region requires an adaptive grid to calculate the required spatial resolution and place it correctly. This is already an inherent part of our code (see section. 6.3.1). It is our intention to construct a *double adaptive* grid that allows us to check the temperature gradient both above and below the maximum height of the loop. Thus we will be able to track the development of the condensation until it reaches approximately the width of observed condensations ($\sim 1000km$), something Antiochos & Klimchuk were unable to do.

On the atomic side, combining the model with ADAS will allow us to link effective emissivity coefficients with the time development of density, temperature and velocity data around the loop for observation prediction. There are several datasets relating to the connection between eruptive prominences and coronal mass ejections already available from SOHO and these should be of use in this respect. The formation of the cool dense condensation also raises the question of optical thickness effects. Through the study of opacity with the CDS & SUMER spectrometers our group has built up some expertise on excited population modelling for optically thick circumstances and simple escape factor treatments of photo-absorption. This should allow much progress to be made in probing the radiation emission of prominence condensations.

A preliminary analysis of the possibility of modifying the code to simulate impulsive bursts highlighted difficulties. Although alteration of the energy injection term proved easy it was not possible to match the magnitude and duration of observed bursts realistically. For example, a typical input energy rate for micro-flares is ~ 10 ergs $\mathrm{cm}^{-3}s^{-1}$ with a duration of $\sim 0.7s$ (Spadaro & Lanza(1995) - private communication). Thus a total pulse of 1.7×10^{23}ergs was injected at the footpoint of an initially static semi-circular symmetric loop (essentially the same as used in section. 6.3.1) for our test. This had no noticeable effect on the hydrodynamic evolution of the loop as it was smaller than the ambient heating function. This result may have been anticipated as micro-flares are essentially a candidate for a mechanism that purports to be responsible for coronal heating. Since our hydrodynamic model is initially that of a static atmosphere we effectively take due account of the coronal heating mechanism without defining what it is. This problem requires further attention.

Chapter 7

Thesis Summary and Discussion

This thesis addresses the problems associated with deriving information about the structure and dynamical nature of the solar upper atmosphere. We wish to extract as much information as possible from the spectral observations. In general, we require either an inversion or prediction approach. In the case of inversion, we must ensure that minimal errors are introduced by the observational and experimental techniques if we are to use the spectral intensities with confidence. Even if we can there are questions regarding the validity of the assumptions we make and in the interpretation of the results we obtain. The problems with this approach have been outlined throughout this thesis. For the predictive approach we are limited with the knowledge that even an exact match with our simulations does not definately tell us that the model is correct. It is only one possible solution. Despite these difficulties we hope to make substantial progress with improved instrumentation on SOHO, improvements to models and to numerical techniques. Of necessity we require a more accurate description of the radiating characteristics of atoms and ions in plasmas than has previously been applied in astrophysics.

Throughout the last decade extensive work has been done to define the difficulties with commonly used approaches and to attempt to address them in order to gain maximum output from the SOHO satellite. In the late eighties, Summers and co-workers began developing the ADAS package to provide the improved atomic model required. Harrison & Thompson (1992) reviewed the quality of differential emission

measure codes and that of Thompson(1991) was recommended and subsequently integrated with ADAS. Lang et al.(1994) reviewed the quality of fundamental data and made recommendations which have been used to expand the ADAS database. Lang et al.(1990) undertook a critical review of the differential emission measure technique and provided suggestions of how to test the various assumptions involved. Judge et al.(1995) revisited their work and attempted to narrow the choice of likely explanations for problems using data from the SOLar-STellar Irradiance Comparison Experiment (SOLSTICE) on the Upper Atmosphere Research Satellite (UARS), and the EUV Grating Spectrograph (EGS) which was flown on a sounding rocket on October 4th 1993. We are in the process of revisiting these questions again with the improved data from SOHO. Thus many workers have addressed each area of the subject and the results are only now starting to come to fruition.

Clearly the task is on going and it is unrealistic to expect this thesis to conclude the work. However, we have methodically set about the task and made significant inprovements at each stage of the work. We review these here.

Data handling utilities were introduced to ADAS to allow flexibility in the use of fundamental data between astrophysical and fusion applications. The ability to 'work at different resolution levels' within excited population structure allows us to avoid the duplication of effort in atomic collision calculations. In addition, the inclusion of a proper treatment of recombining ion metastables paves the way for a more realistic approach to ionisation-recombination models in transiently ionising plasmas (see sec.3.1.1).

The development of a numerical method for calculating a metastable resolved equilibrium ionisation balance was introduced (see sec.3.2.1). This allowed investigation of the effects of such states in line emissivities, contribution functions, radiated power etc. In addition, the explicit treatment of metastables allows use of the most sophisticated dielectronic recombination and ionisation data which is now becoming readily available for the first time. An in-depth analysis of this type was undertaken in chap.4 for oxygen. This included a critical review and upgrade of the existing fundamental database and production of results for solar targeted studies. This provides an example of the analysis methods for solar astrophysical applications which were

previously tested successfully in the fusion environment. It was shown there that a generalised collisional radiative model is essential for maintaining accuracy in the atomic modelling underlying the spectral reduction. This requires the inclusion of the substantial effects of finite density plasma and the influence of metastable states. If we are to attempt to improve on the two dimensional differential emission measure work of Judge et al.(1997), density dependent contribution functions will be required (see discussion of sec.4.6). Further, if we are to aim at the type of precision he requires in the 'kernel' functions metastable states must be included.

Although the effects of a dynamic ionisation were not included in the analysis of oxygen, it was shown in sec.3.2.1 and sec.5.3.1 that this effect is clearly important in the solar atmosphere. As mentioned in sec.4.7 it is clear that metastable states will play a significant role in this too. This is an area that has not been fully investigated.

Again nonequilibrium ionisation is clearly relevant for analysis of spectral intensities by differential emission measure. It is likely that at least this assumption in the formulation of the intensity integral equation is invalid. Its incorporation is an area we intend to investigate and the influence of metastables will be included.

Before improvement however we have to be sure of the limitations of the current approach. Hence the reason for our definitive differential emission measure study. To limit the observational and experimental inaccuracies a critical analysis was presented (chap.5) of the effects of instrumental problems (e.g. cosmic rays, fixed patterning etc.) and analysis methods (e.g. line fitting). We developed the maximum likelihood line profile fitting procedure of Lang et al.(1990) to ensure awareness of the magnitude of the errors associated with the line fitting. We developed further the methods of Lang et al.(1990) to quantify the observational accuracies of the measurements to produce meaningful errors for our differential emission measure analysis. In the course of this we made a statistical analysis of the variation of spectral line intensities and revisited the interesting point of variability pattern changes mentioned by Lang et al.(1990).

We developed an archiving scheme and set of analysis procedures to draw the CDS and SUMER data from their respective archives and link the data to the ADAS differential emission measure code via the line profile fitting procedure. The routines

and system were thoroughly tested and a demonstration DEM for CDS-NIS data was presented. The spread of observed to predicted intensities was then examined to constrain the variability of the DEM with temperature and also to investigate closely the normal incidence spectrometer calibration question. These results are preliminary but are proving helpful for the CDS team investigating the calibration issue. Atomic data was found to be lacking for some important lines, especially Iron in NIS1, and there appeared to be problems associated with the imperfect separation of badly blended lines and multiplets. These issues are under investigation for the final study. However, the number of strong identified lines available is encouraging for an extensive study which we also hope will include the grazing incidence spectrometer and SUMER in due course.

Finally, in chap.6 we initiated some work on predictive modelling using the hydrodynamic code of MacNeice (1983). This consisted mainly of a test run of the code to help in our understanding but some initial thoughts and investigations were presented in sec.6.4.

Many of the results presented here will be re-examined more comprehensively for the differential emission measure study, but the identification of lines, analysis of variability etc. is part of a larger work to be presented on the CDS spectrum. This presents the EUV spectrum comprehensively for the first time, as observed by CDS, and is analogous to the work of Feldman et al.(1997) on SUMER.

Associated with this work is an investigation of the role of opacity to help in exclusion of optically thick lines for the DEM study. An additional output from this has been investigation of the extension of ADAS to the optically thick case by integration of simple 'escape factor' models of radiation transfer. Further to this we intend to integrate opacity and differential emission measure studies with the aim of moving towards a more complete radiative transfer description of the radiation emission of ions such as SiII. Studies of photoabsorption and radiative transfer are essential for preparation for the upcoming deep space satellites AXAF (Advanced X-ray Astrophysics Facility) and XMM (X-ray Multiple Mirror satellite).

References

Abu-Salbi, N., Callaway, J.: 1981, *Physical Review A*, **24**, 237

Aggarwal, K.A.: 1983, *Astrophys. Journal Supp.Ser.*, **52**, 387

Aggarwal, K.A.: 1985, *Astronomy & Astrophysics*, **146**, 149

Aggarwal, K.A.: 1993, *Astrophys. Journal Supp.Ser.*, **85**, 197

Aitken, K.L., Harrison, M.F.A.: 1971, *Journal Physics B*, **4**, 1176

Allard, N.: 1990, *Astronomy & Astrophysics Supp.Ser.*, **84**, 563

Antiochos, S.K., Noci, G.: 1986, *Astrophys. Journal*, **301**, 440

Antiochos, S.K., Klimchuk, J.A.: 1990, *Astrophys. Journal*, **378**, 372

Arnaud, M., Rothenflug, R.: 1985, *Astronomy & Astrophysics Supp.Ser.*, **60**, 425

Athay, R.G.: 1981, *Astrophys. Journal*, **249**, 340

Badnell, N.R., Pindzola, M.S., Dickson, W.J., Summers, H.P.: 1993, *Astrophys. Journal Letters*, **407**, L91

Badnell, N.R., Gorczyca, T.W, Pindzola, M.S., Summers, H.P.: 1996, *Journal Physics B*, **29**, 3683

Bates, D.R, Kingston, A.E., McWhirter, R.W.P.: 1962, *Proc. Royal Society London*, **267A**, 297

Bell, K.L., Hibbert, A., Stafford, R.P., McLaughlin, B.: 1994, *Physica Scripta*, **50**, 343

Berrington, K.A.: 1994, *Atomic Data Nuclear Data Tables*, **57**, 71

Berrington, K.A., Eissner, W.B., Norrington, P.H.: 1995, *Computer Physics Comms.*, **92**, 290

Berrington, K.A. et al: 1979, *Journal Physics B*, **12**, L275

Berrington, K.A. et al: 1985, *Journal Physics B*, **33**, 195

Bhadra, K., Henry, R.J.W.: 1982, *Physical Review A*, **26**, 1848

Bhatia, A.K., Doschek, G.A., Feldman, U.: 1979, *Astronomy & Astrophysics*, **76**, 359

Bittencourt, J.A.: 1986, *Fundamentals of Plasma Physics, Pergamon, Oxford.*

Blum R.D., Pradhan, A.: 1992, *Astrophys. Journal Supp.Ser.*, **80**, 425

Braginskii, S.I.: 1965, *Reviews of Plasma Physics (Leontovich ed.)*, **205**

Bransden, B.H., Joachin, C.J.: 1992, *'Physics of Atoms and Molecules', Longman*

Breeveld, A.A., Edgar, M.L., Smith, A., Lappington, J.S., Thomas, P.D.: 1992, *Reviews Sci. Inst.*, **63**, 1

Brook, E., Harrison, M.F.A., Smith, A.C.H.: 1978, *Journal Physics B*, **11**, 17

Brooks, D.H., Badnell, N.R., lang, J., Summers, H.P.: 1997, *In Preparation*

Brosius, J.W., Davila, J.M., Thomas, R.J., Monsignori-Fossi, B.C.: 1996, *Astrophys. Journal Supp.Ser.*, **106**, 143

Brown, J.C.: 1973, *Solar Physics*, **31**, 143

Brown, J.C., Dwivedi, B.N., Sweet, P.A., Almleaky, Y.M.: 1991, *Astronomy & Astrophysics*, **249**, 277

Brown, J.C., Thompson, A.M.: 1991, *Rutherford Appleton Laboratory Report*, RAL-91-092

Brueckner, G.E., and 14 other authors.: 1995, *Solar Physics*, **162**, 357

Burgess, A.: 1964, *Astrophys. Journal*, **139**, 776

Burgess, A.: 1965, *Astrophys. Journal*, **141**, 1588

Burgess, A., Seaton, M.J.: 1964, *Mon. Not. R. Ast. Soc.*, **127**, 355

Burgess, A., Summers, H.P.: 1969, *Astrophys. Journal*, **157**, 1007

Burgess, A., Summers, H.P.: 1976, *Mon. Not. R. Ast. Soc.*, **174**, 345

Burgess, A., Tully, J.: 1992, *Astronomy & Astrophysics*, **254**, 436

Burgess, A., Summers, H.P., McWhirter, R.W.P., Cochrane, D.M.: 1977, *Mon. Not. R. Ast. Soc.*, **179**, 275

Burke, Burke, Scott.: 1992, *Computer Physics Comms.*, **69**, 76

Callaway, J.: 1994, *Atomic Data Nuclear Data Tables*, **57**, 9

Cheng, C.C., et al.: 1983, *Astrophys. Journal*, **265**, 1090

Christensen, R.B., Norcross, D.W., Pradhan, A.K.: 1985, *Physical Review A*, **32**, 93

Cowan, R.D.: 1981, *'The Theory of Atomic Structure and Spectra'.*

Craig, I.J.D., Brown, J.C.: 1976, *Astronomy & Astrophysics*, **49**, 239

Culhane, J.L., and 27 other authors.: 1991, *Solar Physics*, **136**, 89

Cuperman, S., Weiss, I., Dryer, M.: 1981, *Astrophys. Journal*, **239**, 345

Dere, K.P., Landi, E., Mason, H.E., Monsignori-Fossi, B.C., Young, P.R.: 1996, *Astronomy & Astrophysics Supp.Ser.*, *In press*

Dickson, W.J.D.: 1993, *Ph.D. Thesis, Univ. of Strathclyde*

Domingo, V., Fleck, B., Poland, A.I.: 1992, *Space Science Reviews*, **70**, 7

Doschek, G.A., Bohlin, J.D., Feldman, U.: 1976, *Astrophys. Journal*, **205**, L177

Doschek, G.A, Boris, J.P., Cheng, C.C., Mariska, J.T., Oran, E.S.: 1982, *Astrophys. Journal*, **258**, 373

Doyle, J.G., McWhirter, R.W.P.: 1980, *Mon. Not. R. Ast. Soc.*, **193**, 947

Dubau, J. : 1994, *Atomic Data Nuclear Data Tables*, **57**, 21

Elliot, J.A.: 1993, *'Plasma Physics' (Dendy Ed.), C.U.P.*

Emslie, A.G.: 1987, *Solar Physics*, **113**, 175

Fawcett, B., Mason, H.E.: 1989, *Atomic Data Nuclear Data Tables*, **43**, 245

Fleck, B., Domingo, V., Poland, A.: 1995, *Solar Physics - Special Edition*, **162**

Feldman, U., Behring, W.E., Curdt, W., Schuele, U., Wilhelm, K., Lemaire, P.: 1997, *Astronomy & Astrophysics Supp. Ser., Accepted*

Feldman, U.: 1983, *Astrophys. Journal*, **275**, 367

Feldman, U.: 1987, *Astrophys. Journal*, **320**, 426

Feldman, U., Laming, M.: 1994, *Astrophys. Journal*, **434**, 370

Fisher, G.H., Canfield, R.C., McLymont, A.N.: 1985, *Astrophys. Journal*, **289**, 414

Gabriel, A.H.: 1976, *Phil. Trans. R. Soc. London A*, **281**, 339

Gan, W.Q., Fang, C., Zhang, H.Q.: 1991, *Astronomy & Astrophysics*, **241**, 618

Gan, W.Q., Reiger, E., Fang, C., Zhang, H.Q.: 1993, *Solar Physics*, **143**, 141

Geesman, H., Hanne, G.F., Stauffer, A.D., Stauffer, J.A.: 1991, *Nucl. Inst. Methods in Phys. Res.*, **A307**, 413

Grevesse, N., Anders, E.: 1991, *Solar Interior and Atmosphere.* *Univ. Arizona Press*, **A92-36201 14-92**, 1227

Hahn, Y.: 1985, *Adv. Atomic Mol. Phys.*, **21**, 123

Harrison, R.A., Fludra, A.: 1995, *Rutherford Appleton Laboratory Report*, **SC-CDS-RAL-SN-95-0001**

Harrison, R.A., Insley, J.E.: 1997, *Solar Physics Special Edition, , In Press*

Harrison, R.A., Thompson, A.M.: 1992, *Rutherford Appleton Laboratory Report*, **RAL-91-092**

Harrision, R.A., and 38 other authors.: 1995, *Solar Physics*, **162**, 233

Hayes, M.A.: 1983, *Journal Physics B*, **16**, 285

Hayes, M.A., Nussbaumer, H.: 1983, *Astronomy & Astrophysics*, **134**, 193

Henry, R.J.W.: 1981, *Physics Reports*, **68**, 1

Ho, Y.K., Henry, R.J.W.: 1983, *Astrophys. Journal*, **264**, 733

Hubeny, V., Judge, P.G.: 1995, *Astrophys. Journal Lett.*, **448**, L61

Hutchison, I.H.: 1987, *'Principles of Plasma Diagnostics', C.U.P.*

Innes, D., Inhester, B., Axford, W.I., Wilhelm, K.: 1997, *Nature*, *Submitted*

Janev, R.K., Winter, H.: 1985, *State Selective Electron Capture in Atom - Highly Charged Ion Collisions*, *Physics Reports*, **117**, 265

Jordan, C.: 1969, *Mon. Not. R. Ast. Soc.*, **142**, 499

Judge, P.G., Hubeny, V., Brown, J.C.: 1997, *Astrophys. Journal*, **475**, 275

Judge, P.G., Woods , Brekke, Rottman : 1997, *Astrophys. Journal*, **475**, 275

Karlicky, M., Henoux, J.C.: 1992, *Astronomy & Astrophysics*, **264**, 679

Kato, T.: 1994, *Private Communication*

Kato, T., Lang, J., Berrington, K.: 1990, *Atomic Data Nuclear Data Tables*, **44**, 133

Kato, T., Nakazaki, S.: 1989, *Atomic Data Nuclear Data Tables*, **42**, 313

Kent, B.J., Breeveld, A.A., Bromage, B.J., Hollandt, J., Lang, J., Pike, C.D., Thompson, W.T.: 1997, *In Preparation*

Kingsburgh, R.L., English, J.: 1992, *Mon. Not. R. Ast. Soc.*, **259**, 635

Kohl, J.L. and 38 other authors: 1995, *Solar Physics*, **162**, 313

Kopp, R.A., Fisher, G.A., MacNeice, P., McWhirter, R.W.P., Peres, G.: 1986, *Proc. of SMM Flare Workshop*, *NASA-CP-2439*,

Laher, R.R., Gilmore, F.K.: 1990, *Journal Phys. Chem. ref. Data*, **19**, 277

Laming, J.M., Drake, J.J., Widing, K.G.: 1995, *Astrophys. Journal*, **443**, 416

Lang, J. (Special Editor): 1994, *Atomic Data Nuclear Data Tables*, vol.57

Lang, J., Payne, J.: 1987, *Rutherford Appleton Laboratory Report*

Lang, J., Summers, H.P.: 1994, *Atomic Data Nuclear Data Tables*, **57**, 215

Lang, J., Summers, H.P.: 1996, *ADAS Document*

Lang, J., Mason, H.E., McWhirter, R.W.P.: 1990, *Solar Physics*, **129**, 31

Lang, J., and 13 other authors.: 1992, *PASJ*, **44**, L55

Lanzafame, A.C., Brooks, D.H., Lang, J., Summers, H.P., Thompson, A.M.: 1997, *In Preparation*

Lennon, D.J., Burke, V.M.: 1994, *Astronomy & Astrophysics Supp.Ser.*, **103**, 273

Luken, W.L., Sinanoglu, O.: 1976, *Journal Phys. Chem. Ref. Data*, **64**, 1495

Maggi, C.F.: 1996, *Ph.D. Thesis, Univ. of Strathclyde*

Mann, J.B.: 1983, *Atomic Data Nuclear Data Tables*, **29**, 407

MacNeice, P.: 1983, *Ph.D. Thesis, Univ. of Cambridge*

MacNeice, P.: 1986, *Solar Physics*, **103**, 47

MacNeice, P., McWhirter, R.W.P., Spicer, D.S., Burgess, A.: 1984, *Solar Physics*, **90**, 357

MacNeice, P., Fontenla, J., Ljepojevic, N.N.: 1991, *Astrophys. Journal*, **369**, 544

Mariska, J.T., Emslie, A.G., Li, P.: 1989, *Astrophys. Journal*, **341**, 1067

McLaughlin, B.M., Bell, K.L.: 1993, *Astrophys. Journal*, **408**, 753

McLaughlin, B.M., Bell, K.L.: 1994, *Astrophys. Journal Supp.Ser.*, **94**, 825

McWhirter, R.W.P.: 1960, *Proc. Phys. Soc.*, bf 75, 520

McWhirter, R.W.P.: 1965, in *'Plasma Diagnostic Techniques'* , 201

McWhirter, R.W.P.: 1994, *Atomic Data Nuclear Data Tables*, **57**, 139

McWhirter, R.W.P., Summers, H.P.: 1985, in *'Applied Atomic Collision Physics* , 51

Mihalas, D.: 1978, *'Stellar Atmospheres' (Freeman) & Co.*, 26

Monsignori-Fossi, B.C., Landini, M.: 1994, *Atomic Data Nuclear Data Tables*, **57**, 125

Moore, C.E.: 1993, in *'Tables of Spectra of hydrogen, carbon, nitrogen and oxygen*

Nagai, F.: 1980, *Solar Physics*, **68**, 351

Nagai, F., Emslie, A.G.: 1984, *Astrophys. Journal*, **279**, 896

Noci, G., Spadaro, D., Zappala, R.A., Antiochos, S.K.: 1989, **338**, 1131

Pallavicini, P., Peres, G., Serio, S., Vaiana, G., Acton, L., Leibacher, J., Rosner, R.: 1983, *Astrophys. Journal*, **270**, 270

Peres, G., Reale, F., Serio, S., Pallavicini, P.: 1987, *Astrophys. Journal*, **312**, 895

Phillips, K.J.H.: 1992, *'Guide to the Sun', C.U.P.*

Pike, D., Harrison, R.A.: 1997, *Solar Physics Special Edition, , In Press*

Poland, A.I., Mariska, J.T., Klimchuk, J.: 1986, in *'Coronal and Prominence* , 57

Pradhan, A.K.: 1976, *Mon. Not. R. Ast. Soc.*, **177**, 31

Pradhan, A.K., Norcross, D.W., Hummer, D.G.: 1981, *Astrophys. Journal*, **246**, 1031

Robb, D.: 1980, in *Informal Report LA-6220-MS (Merts et al.)*

Sampson, D.H., Goett, S.H., Clark, R.E.H.: 1983,
Atomic Data Nuclear Data Tables, **29**, 467

Sampson, D.H., Zhang, H.L., Fontes, C.J.: 1994,
Atomic Data Nuclear Data Tables, **57**, 97

Saraph, H.E.: 1972, *Computer Physics Comms.*, **3**, 256

Saraph, H.E.: 1978, *Computer Physics Comms.*, **15**, 247

Saraph, H.E., Seaton, M.J., Shemming, J.: 1969, *Proc. R. Soc.*, **264**, A1149

Scott, N.S., Burke, P.G.: 1980, *Journal Physics B*, **13**, 4299

Seaton, M.J., Storey, P.J.: 1976, *UCL Dept. Phys. & Ast. Report*

Somov, B.V., Sermulina, B.J., Spektor, A.R.: 1982, *Solar Physics*, **81**, 281

Spadaro, D., Noci, G., Zappala, R.A., Antiochos, S.K.: 1990,
Astrophys. Journal, **355**, 342

Spadaro, D., Antiochos, S.K., Mariska, J.T.: 1991, *Astrophys. Journal*, **382**, 338

Spadaro, D., Lanza, A.F., Antiochos, S.K.: 1996, *Astrophys. Journal*, **462**, 1011

Spadaro, D., Lanza, A.F.: 1996, *Private Communication*

Spence, J.: 1987, *Ph.D. Thesis, Univ. of Strathclyde*

Spitzer, L.: 1956, *'Physics of Fully Ionised Gases', Interscience, NY*

Spruitt, H.C.: 1981, in *'The Sun as a Star'*, *NASA-SP 450*, 385

Summers, H.P.: 1973, *Appleton Laboratory Report*, **A1-R-5**

Summers, H.P.: 1974, *Mon. Not. R. Ast. Soc.*, **169**, 663

Summers, H.P.: 1992, *Unpublished*

Summers, H.P.: 1994, *JET Internal Report*, *JET-IR(94)-06*

Summers, H.P.: Dickson, W.J.: 1992, in *'Recombination of Atomic Ions'* , 31

Summers, H.P.: Hooper, M.B.: 1983, *Plasma Phys. Cont. Nucl. Fusion*, **25**, 1311

Summers, H.P.: McWhirter, R.W.P.: 1979, *Journal Physics B*, **12**, 2387

Summers, H.P., Brooks, D.H., Hammond, T.J., Lanzafame, A.C., Lang, J.: 1996,
Rutherford Appleton Laboratory Report, **RAL-TR-96-017**

Tayal, S.S., Kingston, A.E.,: 1984, *Journal Physics B*, **17**, 1383

Tayal, S.S., et al: 1982, *Proc. of ICPEAC Berlin*, 192

Tayal, S.S., Henry, R.J.W., Pradhan, A.K.: 1987, *Astrophys. Journal*, **319**, 951

Thompson, W.T.: 1994, *CDS Software Note*, **13**

Thompson, W.T., Poland, A.I., Sigmund, O.W., Swartz, M., Leviton, D.B., Payne, L.J.: 1992, *SPIE Proc.*, **1743**, 464

Topping, J.: 1962, *'Errors of Observation and their Treatment',*

Van Maanen, A.: 1982, *Unpublished*

Vernazza, J.E., Avrett, E.H., Loeser, R.: 1981, *Astrophys. Journal Supp.Ser.*, **45**, 635

Weise, W.L., Smith, M.W., Glennon, B.M.: 1966, *'Atomic Transition Probabilities 1'*, **NSRDS-NBS**, 4

Widing, K.G., Doyle, J.G., Dufton, P.C., Kingston, A.E.: 1982, *Astrophys. Journal*, **257**, 913

Wilhelm, K.: 1993, *Max Planck Institut Report*, **SUM-MPAE-RO-113000-02-00**

Wilhelm, K., and 15 other authors.: 1995, *Solar Physics*, **162**, 189

Winglee, R.M., Pritchett, P.L., Dulk, G.A.: 1988, *Astrophys. Journal*, **327**, 968

Woodgate, B.E., Shine, R.A., Poland, A.I., Orwig, L.E.: 1983, *Astrophys. Journal*, **265**, 530

Wolf, R.C.: 1993, *JET Internal Report*, *JET-IR(93)-08*

Zhang, H.L., Sampson, D.H.: 1994, *Atomic Data Nuclear Data Tables*, **56**, 41

Zhang, H.L., Graziana, M., Pradhan, A.K.: 1994, *Astronomy & Astrophysics*, **283**, 319

Zirker, J.B.: 1981, in *'The Sun as a Star'*, *NASA-SP-450*, 135